IDENTIFICATION OF ACTIVE SITES IN HETEROGENEOUS CATALYSIS AND SURFACE CHEMISTRY STUDY OF ALKANES ADSORPTION

A Dissertation
Submitted to the Graduate Faculty
of the
North Dakota State University
of Agriculture and Applied Science

By

Ashish Chakradhar

In Partial Fulfillment
for the Degree of
DOCTOR OF PHILOSOPHY

Major Department:
Chemistry and Biochemistry

March 2014

Fargo, North Dakota

North Dakota State University
Graduate School

Title

Identification of active sites in heterogeneous catalysis and surface chemistry study of alkanes adsorption

By
Ashish Chakradhar

The Supervisory Committee certifies that this ***disquisition*** complies with North Dakota State University's regulations and meets the accepted standards for the degree of

DOCTOR OF PHILOSOPHY

SUPERVISORY COMMITTEE:

Dr. Uwe Burghaus
Chair

Dr. John Hershberger

Dr. Pinjing Zhao

Dr. Chad Ulven

Approved:

03/24/2014
Date

Dr. Gregory R. Cook
Department Chair

ABSTRACT

Heterogeneous catalysis is considered the basis of the chemical industry. Surface science investigations on model catalysts have made significant contributions in gaining molecular level understanding of heterogeneously catalyzed reactions. Surface science studies involving the interactions of coal combustion gases such as CO and CO_2 on electron beam lithography (EBL)-fabricated CuO_x/SiO_2 nanoclusters to identify active sites and kinetics data characterizing the alkane adsorption on surfaces of alkaline earth metal oxides, metalloids, and metals are investigated in this dissertation. Diverse surface phenomena such as surface-adsorbate interactions, adsorbate-adsorbate interactions, chemical rearrangements of adsorbed reaction intermediates, identification of active sites, and formation of products have been studied utilizing surface science techniques. Thermal desorption spectroscopy (TDS) and molecular beam scattering (MBS) were utilized to study the adsorption kinetics and dynamics, respectively, of probe molecules on catalyst surfaces. The catalyst surfaces were characterized by various surface science techniques such as Auger electron spectroscopy (AES), X-ray photoelectron spectroscopy (XPS), X-ray diffraction (XRD), low energy electron diffraction (LEED), and scanning electron microscopy (SEM). Active sites on the catalyst surface of EBL-fabricated Cu/CuO_x nanoclusters (methanol synthesis model catalyst) were identified for CO and CO_2 adsorption. Experimentally, it was proven that CO_2 adsorbs preferentially along the clusters' rim site and CO on both the rim and terrace sites. Identifying the active sites on a catalyst surface forms the basis of systematic catalyst design strategies. Bond activation in alkanes is a crucial step in the catalytic processing of alkanes in application such as the catalytic combustion of natural gas, exhaust gas remediation, and the selective oxidation of alkanes to high demand products. Adsorption of small chain alkanes such as n-butane, n-pentane, and n-hexane on

CaO(100) surface resulted in bond activation to form mostly methane and ethylene via hydrogen abstraction. This production of hydrogen gas has significant economic and environmental benefits. Whereas, the adsorption of n-butane on Sb(111) and silica-supported Mo clusters was found to be molecular and non-activated. However, a strong hydrophobic property of Sb(111) surface was characterized by studying co-adsorption of n-butane and water. In addition, the adsorption sites for n-butane on Sb(111) and Mo nanoclusters were characterized.

ACKNOWLEDGMENTS

I would like to express my heartily gratitude to my adviser, Dr. Uwe Burghaus, for his excellent guidance, thorough support, patience, and understanding during my graduate studies at North Dakota State University. He not only provided me an excellent environment for conducting research but also made me grow as an experimentalist and a chemist with his mindful mentorship and moral support. His supervision and my dedication to research have brought me very close to my long-term career goals. For everything you have done for me in last (almost) half a decade, Dr. Burghaus, I thank you.

I would like to thank my wonderful committee members Dr. John Hershberger, Dr. Pinjing Zhao, and Dr. Chad Ulven for their continuous valuable guidance, thoughtful comments, and constructive criticism in every step of my graduate studies. I really appreciate their supervision and dedication to help me succeed in graduate school.

I would like to thank our collaborators Stefano Cabrini of The Molecular Foundry at Lawrence Berkeley National Laboratory and Lu Ming of Brookhaven National Laboratory for the fabrication and SEM imaging of model array nanocatalysts.

I would like to thank Dr. Angel Ugrinov at NDSU not only for conducting the X-ray diffraction of our model catalysts but also for training in successful operation of an XRD instrument, high resolution mass spectrometry, and software to analyze XRD data.

Importantly, I would like to acknowledge the financial support provided by DoE, NSF-Career, and DoE-EPSCoR. All the credentials that I have achieved, included in this dissertation, would not have been possible without these funding agencies.

I would like to heartily thank my past colleague Dr. Mallikharjuna Komarneni for providing me start-up training about the surface science experimental techniques in the laboratory. Also, he provided me a continuous insightful mentorship and support until the last day of his stay in the laboratory. I would also like to thank my past post-doctoral fellows Dr. Evgueni Kadossov, Dr. Zhongqing Yu, and Dr. Junjun Shan, visiting student from China, Yuan Li, and several fellow undergraduates Andrew Sand, Jordan Schmidt, Kyle Anderson, and Catherine Bartholome for mentoring and working with me on several projects covered in this dissertation.

I am grateful to my parents, Shyam Krishna and Chandra Kumari Chakradhar, my elder brothers Anil and Alesh Chakradhar, and my sister in law, Rita Chakradhar, for their love, support, and encouragement with their best wishes even though they are 10,000 miles away from me. Their encouragements and blessings motivated me every day to fulfill my ambition of getting doctoral degree in Chemistry.

Finally, and most importantly, I would like to thank my wife, Rashmi Dangol, who was always there kindly cheering me up and stood by me during my good and bad times for the last 7 years with love and unwavering support.

DEDICATION

This dissertation is dedicated to my parents Shyam Krishna Chakradhar and Chandra Kumari Chakradhar in appreciation to their infinite love and moral support throughout my life.

TABLE OF CONTENTS

ABSTRACT iii

ACKNOWLEDGMENTS v

DEDICATION vii

LIST OF TABLES xiv

LIST OF FIGURES xv

LIST OF ABBREVIATIONS xix

LIST OF SYMBOLS xxi

CHAPTER 1. INTRODUCTION 1

- 1.1. Heterogeneous catalysis 2
- 1.2. Adsorption 3
  - 1.2.1. Physisorption 3
  - 1.2.2. Chemisorption 4
- 1.3. Binding sites/active sites 5
- 1.4. Reaction mechanism 6
- 1.5. Model catalysts 7
- 1.6. Industrial or 'real world' catalysts 7
- 1.7. Single crystal system 8
- 1.8. Supported model system 9
- 1.9. Coal combustion gases 11
- 1.10. Methanol synthesis model nano-catalysts 12
- 1.11. Bond activation in alkanes 13

CHAPTER 2. EXPERIMENTAL TECHNIQUES 16

2.1. Ultra high vacuum 16

2.2. TDS chamber 17

2.3. Sample holder set up 19

2.3. Molecular beam scattering chamber 21

2.4. Kinetic measurements: thermal desorption spectroscopy 24

2.5. Theoretical description of TDS data 25

2.6. Desorption order 28

- 2.6.1. Zero-order desorption kinetics 28
- 2.6.2. First-order desorption kinetics 28
- 2.6.3. Second-order desorption kinetics 29
- 2.6.4. Pseudo second-order desorption kinetics 30
- 2.6.5. Fractional-order desorption kinetics 30

2.7. Molecular beam source 33

2.8. King and Wells method 36

- 2.8.1. Langmuirian adsorption model 38
- 2.8.2. Kisluik model 39
- 2.8.3. Adsorbate-assisted adsorption model 40

2.9. Capture zone model 41

2.10. Auger electron spectroscopy 42

2.11. X-ray photoelectron spectroscopy 46

2.12. X-ray diffraction 52

2.13. Low energy electron diffraction 55

2.14. Scanning electron microscopy 58

2.15. Electron beam lithography 60

CHAPTER 3. IDENTIFYING ACTIVE SITES IN HETEROGENEOUS CATALYSIS 62

3.1. Introduction 62

3.2. Brief literature survey 65

3.3. Sample fabrication 66

3.4. Sample cleaning and its chemical state 67

3.5. Blind experiments 68

3.6. Results and discussion 68

3.6.1. Sample morphology 69

3.6.2. Spectroscopic characterization of the chemical state of the Cu clusters 71

3.6.3. Oxidation state of the Cu clusters 74

3.6.4. Adsorption kinetics of CO and CO_2 on CuO_x clusters 75

3.6.4.1. Adsorption kinetics of CO on metallic and oxidic Cu clusters 76

3.6.4.2. Adsorption kinetics of CO_2 on CuO_x clusters 78

3.6.5. Adsorption dynamics of CO and CO_2 on CuO_x clusters 80

3.6.5.1. Adsorption dynamics of CO 81

3.6.5.1.1. CO adsorption transients on metallic and oxidic clusters 82

3.6.5.1.2. Energy dependence of initial adsorption probability - cluster size effects ... 84

3.6.5.1.3. Effect of oxidation state on initial adsorption probability 86

3.6.5.1.4. Coverage dependent adsorption probabilities 88

3.6.5.2. Adsorption dynamics of CO_2 89

3.6.5.2.1. Theoretical calculation of saturation coverages for rim and terrace sites 89

3.6.5.2.2. Experimental calculation of saturation coverages for rim and terrace sites . 90

3.6.5.2.3. Energy dependent adsorption probabilities 93

3.6.5.2.4. Temperature dependent adsorption probabilities 95

3.7. Summary 96

CHAPTER 4. SURFACE CHEMISTRY STUDY OF ALKANES ADSORPTION 98

4.1. Alkanes adsorption on CaO(100) 98

4.1.1. Introduction 99

4.1.2. Brief literature survey 99

4.1.3. Sample preparation and characterization 100

4.1.4. Results and discussion 102

4.1.4.1. Blind experiment 102

4.1.4.2. Molecular adsorption of alkanes 102

4.1.4.3. Bond activation in alkanes 106

4.1.4.4. Multi-mass TDS experiments results 107

4.1.4.4.1. Ethane multi-mass experiment 107

4.1.4.4.2. Long chain alkanes multi-mass experiments 109

4.1.4.5. Proposed mechanism 112

4.1.5. Summary 113

4.2. Alkane and water adsorption on Sb(111) surface 114

4.2.1. Introduction 114

4.2.2. Brief literature survey 115

4.2.3. Results and discussion 117

4.2.3.1. Sample characterization 117

4.2.3.2. Alkane adsorption 118

4.2.3.3. Water adsorption 121

4.2.3.4. Water and butane co-adsorption 123

4.2.3.5. Site blocking effect 124

4.2.4. Summary 125

4.3. Alkane adsorption on MoO_x nanoclusters 126

4.3.1. Introduction 126

4.3.2. Brief literature survey 127

4.3.3. Results and discussion 128

4.3.3.1. Sample morphology 128

4.3.3.2. Sample cleaning and characterization 130

4.3.3.3. Adsorption kinetics of n-butane 133

4.3.3.4. Adsorption dynamics of n-butane 135

4.3.4. Summary 138

4.4. Overall summary of the chapter 139

CHAPTER 5. SIDE PROJECTS: STUDY OF COAL COMBUSTION GASES ON MODEL CATALYSTS 140

5.1. Adsorption kinetics and dynamics of CO_2 on MgO(001) 140

5.1.1. Introduction 140

5.1.2. Brief literature survey 141

5.1.3. Results and discussion 144

5.1.3.1. Sample characterization 144

5.1.3.2. CO_2 adsorption kinetics 146

5.1.3.2.1. Parent mass TDS data 146

5.1.3.2.2. Multi-mass TDS data 149

5.1.3.3. XPS of CO_2 / MgO(001) 151

5.1.3.4. Adsorption dynamics of CO_2 152

5.1.3.4.1. Typical example of an adsorption transient 152

5.1.3.4.2. Energy dependence of adsorption dynamics 154

5.1.3.4.3. Temperature dependence of adsorption dynamics 156

5.1.4. Summary 156

5.2. Adsorption kinetics of coal combustion gases on selenium foil 157

5.2.1. Introduction 158

5.2.2. Brief literature survey 158

5.2.3. Sample cleaning 159

5.2.4. Results and discussion 159

5.2.4.1. Sample characterization by Auger electron spectroscopy 159

5.2.4.2. Sample characterization by X-ray diffraction 160

5.2.4.3. Adsorption kinectics of CO_2 161

5.2.4.4. Adsorption kinetics of NO 162

5.2.4.5. Adsorption kinetics of H_2/D_2 164

5.2.4.6. Adsorption kinetics of H_2O 168

5.2.5. Summary 169

5.3. Overall summary of the chapter 169

CHAPTER 6. CONCLUSIONS AND IMPLICATIONS 171

REFERENCES 175

LIST OF TABLES

Table Page

1. XPS Cu $2p_{3/2}$ line positions for Cu and Cu oxides 75

2. Binding energies of CO determined as compared to literature values.......................................77

3. Saturation coverages of CO and CO_2 on EBL fabricated CuO clusters 92

4. TDS peak temperatures and their binding energies for n-alkanes adsorption on CaO............106

5. Summary showing the results of short chain alkanes adsorption on model catalysts 139

6. CO_2 adsorption on various system, their binding energies and adsorption probabilities 148

7. XPS 1s line for adsorption of CO_2 on several systems...152

8. Summary showing the results of coal combustion gases adsorption on model catalysts 170

LIST OF FIGURES

Figure Page

1. Photograph of TDS ultra-high vacuum chamber 18

2. Photographs of sample holder 20

3. Photograph of the beam scattering chamber 21

4. Schematic of the beam scattering chamber 22

5. Schematic showing all the components of an UHV chamber 24

6. Computer-simulated zero-order desorption kinetics 28

7. Computer-simulated first-order desorption kinetics 29

8. Computer-simulated second-order desorption kinetics 30

9. Example of fractional-order desorption kinetics 31

10. n-Butane TDS on CaO(100) 32

11. Schematic illustration of King and Wells up-take beam scattering experiment 37

12. King and Wells experiment showing adsorption transients of CO 38

13. Schematic showing the coverage dependent adsorption probability curves 39

14. A set of coverage dependent adsorption probability curves at different impact energies 40

15. Schematic showing adsorption/desorption pathways 42

16. Schematic illustraing the Auger transitions 43

17. AES spectra of as received Cu clusters supported on silica 45

18. Schematic showing the photoemission process 47

19. Energy level diagram for an electrically conducting sample grounded to the spectrometer 49

20. Energy level diagram for an electrically insulated sample from the spectrometer 50

21. XPS spectrum of clean 12 nm Cu clusters supported on silica 51

22. Schematic showing cross-section of X-ray tube..53

23. XRD of MgO(100)...55

24. A schematic showing a LEED technique..56

25. LEED pattern for clean Sb(111) surface..57

26. Signals produced after high energy electron beam strikes on a surface 58

27. SEM image of 77 nm Mo clusters on silica support..59

28. 12 nm Cu clusters on silica support 61

29. SEM images of Cu EBL clusters showing size distributions 69

30. Cluster with probe molecules adsorbed on terrace and rim sites 71

31. AES and XPS spectra of as-received and clean 63 nm Cu EBL sample 73

32. XPS Cu 2p region for the metallic and fully oxidized copper..74

33. CO TDS on metallic and oxidic 63 nm Cu clusters..76

34. CO_2 and CO TDS on 63 nm CuO EBL clusters 79

35. Adsorption transients of CO on metallic and oxidic Cu clusters and bare supports................83

36. S_0 of CO vs E_i for 12 and 63 nm metallic Cu clusters compared to PVD Cu clusters 85

37. S_0 of CO vs Cu coverage for 12 nm and 63 nm metallic Cu clusters and PVD Cu clusters ..86

38. S_0 of CO vs E_i for 12 nm and 63 nm metallic and oxidic Cu EBL clusters............................87

39. S(Θ) curves for metallic and oxidic 63 nm Cu EBL clusters 89

40. Adsorption transients of CO_2 on bare supports and 12 and 63 nm oxidic Cu clusters...........91

41. Illustration of CO and CO_2 adsorption on different sites...92

42. Initial adsorption probability, S_0, of CO_2 as a function of impact energy, E_i.........................94

43. S_0 of CO and CO_2 as a function of T_s for 63 nm oxidic Cu EBL clusters 96

44. AES spectra of as-received and cleaned CaO(100) surface...101

45. TDS curves of n-butane and iso-butane as a function of exposure..103

46. TDS curves of n-pentane as a function of exposure 104

47. TDS curves of n-hexane as a function of exposure 105

48. Multi-mass TDS experiments of ethane on CaO(100) 108

49. Multi-mass TDS experiments of n-butane on CaO(100)...109

50. Multi-mass TDS experiments of n-hexane on CaO(100) 110

51. TDS data for m/e = 16 for n-butane and n-hexane on CaO(100) 111

52. AES spectra, LEED pattern, and XPS spectra of Sb(111)...118

53. n-Butane TDS as a function of exposure on Sb(111) 119

54. Adsorption transients of n-butane on Sb(111) at different impact energies 120

55. The initial adsorption probability of n-butane versus E_i on Sb(111).....................................121

56. Water TDS as a function of exposure on Sb(111) 122

57. TDS of n-butane on clean and water pre-covered Sb(111) 123

58. Adsorption transients of n-butane on water pre-covered Sb(111)...124

59. SEM images of 77 nm Mo EBL clusters with size distributions...129

60. Cleaning procedure curves for Ar^+ sputtering and O_2 annealing of Mo EBL clusters..........131

61. AES and XPS spectra of 77 nm Mo EBL clusters...132

62. TDS of n-butane on metallic and oxidic 77 nm Mo clusters 134

63. Multi-mass TDS of n-butane on metallic 77 nm Mo clusters..135

64. Adsorption transients of n-butane on metallic and oxidic Mo clusters 136

65. S_0 of n-butane on 77 nm metallic Mo clusters as a function of E_i..138

66. AES spectra, XPS spectrum, and LEED pattern for MgO(001) surface 145

67. CO_2 TDS on MgO(001) surface 147

68. Multi-mass TDS of adsorbed CO_2 on MgO(001) surface 150

69. XPS of C1s region with adsorbed CO_2 and after desorbed CO_2 from the surface 151

70. Adsorption transient of CO_2 and its integrated curve 153

71. S_0 of CO_2 as a function of E_i on MgO(001) compared to other surfaces 155

72. S_0 of CO_2 as a function of surface temperature 156

73. Auger spectrum for carbon and selenium regions 160

74. X-ray diffraction scan of the Se foil 161

75. CO_2 TDS data as a function of exposure on Se foil..162

76. NO TDS data as a function of exposure and coverage dependent heat of adsorption...........164

77. TDS curves of H_2 as a function of exposure on Se foil...165

78. Integrated TDS intensities of multi-mass TDS data for H_2 and D_2 166

79. Water TDS curves as a function of exposure on Se foil...168

LIST OF ABBREVIATIONS

AES	Auger Electron Spectroscopy
AFM	Atomic Force Microscopy
CMA	Cylindrical Mirror Analyzer
CVD	Chemical Vapor Deposition
CZM	Capture Zone Model
DFT	Density Functional Theory
EBL	Electron Beam Lithography
EDX	Energy-Dispersive X-ray Spectroscopy
ER	Eley Rideal
ESCA	Electron Spectroscopy for Chemical Analysis
FESEM	Field Emission Scanning Electron Microscopy
HDS	Hydrodesulfurization
HREELS	High Resolution Electron Energy Loss Spectroscopy
HV	High Voltage
IR	Infrared Spectroscopy
KE	Kinetic Energy
L	Langmuir
LASER	Light Amplification by Stimulated Emission of Radiation
LEED	Low Energy Electron Diffraction
LH	Langmuir Hinshelwood
LITD	Laser Induced Thermal Desorption
MBS	Molecular Beam Scattering

MCS	Monte Carlo Simulation
ML	Monolayer
MP2	Møller–Plesset Perturbation Theory
PID	Proportional Integral Derivative
PVD	Physical Vapor Deposition
RGA	Residual Gas Analyzer
RHEED	Reflection high Electron Energy Diffraction
RT	Room Temperature
SAR	Structure-Activity Relationship
SCF	Self-Consistent Field
SEM	Scanning Electron Microscopy
STM	Scanning Tunneling Microscopy
TDS	Thermal Desorption Spectroscopy
TOF	Time-of-Flight Spectroscopy
TPD	Temperature Programmed Desorption
UHV	Ultra-High Vacuum
XPS	X-ray Photoelectron Spectroscopy
XRD	X-ray Diffraction

LIST OF SYMBOLS

β	Heating rate
ε_{corr}	Correlation energy
ε_{k}	Orbital energy
ε_{rel}	Relativistic energy
ε_{relax}	Relaxation energy
Θ	Coverage
Θ_{M}	Coverage of adsorbate
Θ_{sat}	Saturation coverage
Θ	Bragg's angle
θ	Emission angle
λ	Molecular mean free path length
λ	Wavelength
λ_0	Optimum wavelength
ρ	Density of particles
υ	Frequency
υ_d	Pre-exponential factor
ϕ	Work function of the surface
ϕ_e	Energy of charge neutralization electron
ϕ_{sp}	Spectrometer work function
χ	Exposure
Δt	Time duration
c	Velocity of light

d	Diameter
dN/dE	Differentiated number of electrons with energy E
E	Energy
E_b	Binding energy
E_d	Energy of desorption
E_{des}	Activation energy for desorption
E_f	Fermi level
E_f^s	Fermi level of the sample
E_f^{sp}	Fermi level of the spectrometer
E_i	Impact energy
eV	Electron volt
E_{vac}	Vacuum level
F	Flux
h	Planck's constant
k	Desorption rate
k_d	Desorption rate coefficient
keV	Kilo electron volt
KL_1L_2	Auger transition
KV	Kinetic energy
L	Langmuir
M	Metal
M	Adsorbate
m/e	Mass to charge ratio

N	Number of molecules
n	Integer multiple
n	Order of the reaction
$N(E)$	Number of electrons with energy E
p	Pressure
P_0	Initial pressure
P_b	Base pressure
P_{sat}	Saturation pressure
r	Reaction rate
$S(\Theta)$	Coverage dependent adsorption probability
S_0	Initial adsorption probability
T or T_s	Surface temperature
T_0	Initial surface temperature
t_0	Initial time
T_{max}	Peak temperature
V	Valence band
V	Voltage

CHAPTER 1. INTRODUCTION

The motivation for the research described in this dissertation is to study chemical reactions on different surfaces in order to understand heterogeneous catalytic reactions. Heterogeneous catalysis is considered the basis of the chemical industry and it involves literally billions of dollars worth of economic activity. The chemical industry would not have existed if researchers had not been able to successfully implement and understand heterogeneous catalytic processes. Most of the heterogeneous catalytic reactions are initiated with the adsorption of probe molecules on the bulk catalyst, followed by diffusion on the surface to bind with active sites forming intermediate species, and eventually products desorb from the surface. The catalytic activity of model catalysts such as metal and metal oxide single crystals and supported metal and metal oxide nanoclusters has been extensively investigated. It has been well demonstrated that the catalytic activity depends on several parameters such as number of active sites with respect to particle size, quantum confinement effects, and metal-support interactions. The smaller active metal particles are expected to be catalytically more reactive due to their high surface area compared to the bulk catalyst which made most of the researchers work on nano-catalysts. Studying the effects of size, shape, and chemical composition of metal clusters on the catalytic activity is the current area of research and it leads to the optimization of the catalyst synthesis. Methanol synthesis model catalysts investigated in this dissertation include electron beam lithography (EBL)-fabricated silica-supported Cu and CuO_x clusters to identify the active sites for adsorption of CO and CO_2 probe molecules. The surface science studies allow one for the molecular level understanding of surfaces, surface-adsorbate interactions, adsorbate-adsorbate interactions, chemical rearrangements of adsorbed reaction intermediates, and desorption of products. In the model catalyst of oxide-supported metal clusters, the metal particle size influences the electronic and chemical structures, metal-support interactions, physical, mechanical, and thermal properties as well as overall catalytic activity and selectivity. Single crystals of considerable size can be grown from many materials including metals, semiconductors, and even insulators for surface science studies. Sb, Se, Ca, and Mg are among the trace elements formed in the combustion of coal and the safest way to characterize these systems in a model study is using single crystals and foils. Bond activation in alkanes has been a major topic of research for the last few decades; therefore, kinetics data characterizing the bond activation in such alkanes on the surfaces of CaO(100), Sb(111), and MoO_x nanoclusters are investigated in this dissertation.

1.1. Heterogeneous catalysis

Heterogeneous catalysis is one of the catalytic processes in which the catalyst is in a different phase from the reactants. Typically, the catalyst is a solid and reactants are either gases or liquids. The catalyzed reaction occurs repeatedly by a sequence of elementary steps that include adsorption, surface diffusion, chemical rearrangements of the adsorbed reaction intermediates (bond dissociation, bond formation, and other molecular rearrangements), and desorption of the products from the surface, where the catalyst is regenerated after each reaction cycle. Heterogeneous catalysis has a wide range of applications including oil refining, production of chemicals by hydrogenation, dehydrogenation, partial oxidation, and molecular rearrangements such as cyclization and isomerization to ammonia synthesis and fermentation processes. Usually, heterogeneous metal catalysts contain dispersed metal particles with active sites on a highly porous and high-surface-area oxide supports such as SiO_2, TiO_2, CeO_2, and Al_2O_3. Transition metals and their oxides, carbides and sulfides uniquely act as active heterogeneous catalysts and are used in most surface catalytic processes. The catalytic activity and selectivity of a heterogeneous catalyst is dependent on several factors such as the nature of the catalyst, its atomic and electronic configurations, its size, support effects, interaction between catalyst and support, use of promoters, and other reaction conditions.

Most of the chemical transformations in the chemical industry are promoted by heterogeneous catalysts. The chemical reaction occurs on surfaces, and the reactants are introduced as gases or liquids. Usually in the automotive industry, highly dispersed noble metals such as platinum, palladium, and rhodium supported on oxide supports are used for catalytic control of car emissions: unburned hydrocarbons, CO, CO_2, and NO. In petroleum refining, zeolites are widely used for cracking of various hydrocarbons in the presence of hydrogen. Similarly, hydrogenation processes primarily use nickel and palladium as heterogeneous catalysts. Several hydrodesulfurization (HDS) reactions utilize molybdenum, cobalt, and their sulfides on oxide supports as catalysts. Generally, steam reforming of natural gas and methanation processes is carried out using nickel as a catalyst for the production of hydrogen. Methanol synthesis from CO and H_2 is catalyzed by copper oxide and zinc oxide. These are the catalysts that are used in the largest quantity and serve as the basis of entire chemical technologies. Heterogeneous catalysis must proceed with adsorption of reactants on the catalyst surface.

1.2. Adsorption

When a molecule sticks to a surface, two main types of interactions are possible, namely a physical interaction (physisorption) and a chemical interaction (chemisorption).

1.2.1. Physisorption

Physisorption involves the balancing of a weak attractive force between the surface and the adsorbate. In other words, it involves the polarization of the adsorbate and surface rather than electron transfer between them. Any molecules can physisorb if the temperature is low enough. These weak forces, i.e. van der Waals forces, exist not only between adsorbates and substrates but also among adsorbates (lateral interaction). In fact, these lateral interactions between physisorbed molecules can be as strong as adsorbate-substrate interaction. Unlike chemisorption, physisorption is less site-specific and any atom or molecule can adsorb on any surface under suitable experimental conditions such as temperature and pressure.

1.2.2. Chemisorption

Chemisorption involves the formation of a chemical bond between the adsorbate and the substrate. Unlike physisorption, it involves the exchange of electrons between the adsorbing molecule and the surface and larger heat of adsorption is expected for chemisorption. Chemisorption is highly directional because adsorbates that are chemisorbed stick on specific sites. Therefore, they exhibit a binding interaction that depends strongly on their exact position and orientation with respect to the surface. The strength of adsorption is usually dependent on which crystal face is exposed to a crystalline adsorbent. For example, oxygen atoms bind strongly in the face centered cubic threefold hollow sites on Pt(111).[1] When the chemisorbed species are closely packed on the surface, the electrostatic coupling between adsorbates and repulsive forces also come into play.

Chemisorption between the adsorbates and the surface is termed as non-dissociative chemisorption if all the original inter-atomic bonds of the adsorbed molecule are retained in some form. For example, the non-dissociative chemisorption process for molecule AB is given by:

$$\mathrm{AB} \longrightarrow \mathrm{AB}_{ads} \tag{1.1}$$

Similarly, chemisorption between the adsorbates and the surface is termed as dissociative chemisorption if adsorption results in the dissociation of the molecule on binding to the surface. For example, the dissociative chemisorption process for molecule AB is given by:

$$AB \longrightarrow A_{ads} + B_{ads} \tag{1.2}$$

If additional energy is required to dissociate the molecule, then it is considered as activated dissociative chemisorption. Whereas if dissociation of the molecule is energetically favorable that occurs without any external energy, it is called non-activated dissociative chemisorption.

1.3. Binding sites/active sites

A significant aspect of the adsorption process is the nature of the site on which the adsorbate is bound. The binding energy of an adsorbate is dependent on its position on the surface. This means that the sites available have influence on the binding of the adsorbing molecule and on the charge transfer that takes place between the adsorbate and the surface. In fact, different faces of the same crystal may exhibit different properties with respect to certain adsorbates. For example, an fcc(111) surface does not offer any fourfolded bridging site, whereas a (100) face does not offer any threefold bridging sites. Therefore, an adsorbate has to hop from one site to another via pathways that overcome the energetic barriers. This pathway is called a diffusion barrier which separates the barriers between the binding sites. The diffusion barrier is not always uniform across the surface, especially when different adsorption sites are present such as terraces, steps, edges, kinks, rims, etc. Adsorbates diffuse anisotropically, i.e. adsorbates diffuse in different directions depending on availability of the activation energy for diffusion. Also, the diffusion of the adsorbate is dependent on the temperature of the substrate.

In this dissertation, active sites for CO and CO_2 adsorption are studied utilizing EBL-fabricated Cu or CuO_x clusters on a silica support.

1.4. Reaction mechanism

It is very crucial to have some idea of the mechanisms by which surface reactions undergo and much of the preliminary insight into these come from the study of their kinetics. It is a fact that not every collision between a molecule and a surface leads to adsorption. Therefore, based on this characteristic, the course of reactions at surfaces is affected and there are two generally accepted models for surface reactions, namely the Langmuir-Hinshelwood (LH) and the Eley -Rideal (ER) mechanisms. LH mechanism is the most common surface reaction mechanism in which both reactants adsorb on the surface, diffuse around, and then collide to form products. Adsorption, desorption, and surface diffusion play important roles in this mechanism. The reaction rate can be depicted once the complete reaction mechanism is understood, which is dependent on the surface coverage of both reactants and on other reaction conditions such as pressure and temperature. On the other hand, in ER mechanism, a gas molecule collides with an already adsorbed molecule leading to reaction and formed product escaping directly into the gas phase. The products formed after this reaction mechanism are supposed to be highly energetic unlike LH reaction products.

In the present study, most of the surface reactions are unimolecular therefore, adsorption on the surface, diffusion along the surface to find binding site, and finally desorption from the surface are expected as elementary steps. Only background residual gases that cover the entire surface can prevent incoming gas molecules to strike the surface. However, this is a very unlikely scenario in the present study considering the base pressure of the chamber at $2E10^{-10}$ mbar so Eley-Rideal reaction mechanism can be ruled out. Therefore, in this current study, a single species is adsorbed and either undergoes a rearrangement of decomposition to form a product which is eventually desorbed from the surface following LH reaction mechanism.

1.5. Model catalysts

Surface science studies allow the molecular level understanding of surfaces, surface-adsorbate interactions, adsorbate-adsorbate interactions, chemical rearrangements of adsorbed reaction intermediates, and desorption of products on model catalysts. The model catalyst acts as a suitable alternative for real-world industrial catalysts. Typically, metal or metal oxide single crystals, metal thin films, bimetallic or multimetallic thin films, oxide supported metals catalysts, and metal-supported oxide catalysts are used as model systems in surface science. Characterization studies conducted on these model systems focusing on structural, chemical, and electronic properties as a function of particle size and distribution have been related to parallel studies of relevant catalytic reactions, providing fundamental information into these processes at the atomic level. Pressure gaps and material gaps are two parameters that differentiate UHV investigations on model catalysts to 'real world' industrial catalysts. The surface science studies on the model catalysts are carried out at UHV conditions whereas the industrial catalysts are conducted at high pressures on a large scale. Recently, some experimental techniques have been designed which enable the kinetics reaction measurements to be done at high pressures on clean surfaces.[2-3]

1.6. Industrial or 'real world' catalysts

Many important 'real world' industrial catalysts consist of catalytically active metals finely dispersed on high surface area oxide supports to maximize the metal surface area. The reaction activity and selectivity are dependent on the cluster size of these active metals. In 'real world' industrial supported catalysts, there are a few complications in obtaining a detailed comprehensive description of their microscopic properties arising from porous, high surface area supports of poorly defined structure, uncertainty regarding metal particle size and morphology, and most importantly problems with surface contamination. All these factors serve as obstacles to obtain fundamental information of the catalytic process at the most primary level. Therefore, these problems are overcome by researchers with the utilization of model catalysts such as single crystals, thin films, or supported model systems.

1.7. Single crystal system

Single crystals of considerable size can be grown from many materials including metals, semiconductors, and even insulators for surface science studies. These materials are cut along specific orientations to yield surfaces with a high degree of order and simplicity. Thus, single crystal surfaces offer several types of site (terrace, steps, rims, edges, kinks, etc.) on which incoming molecules and molecular fragments can bind. Also, the relative simplicity of a single crystal system allows analysis of how the molecule or molecular fragment adsorbs on and interacts with the surface. The most important feature of single crystal systems is that they enable one to introduce certain structural characteristics of a catalyst surface in a well-controlled manner avoiding the full complexity of the real world catalysts. Sometimes, a well-defined single crystal surface mounted in UHV chamber is coupled with a high pressure reactor system. This set up allows high pressure kinetics studies to be combined with atomic level characterization of catalyst surfaces before and after reaction. Studies involving the interactions of small molecules like CO, CO_2, NO, O_2, and H_2O on clean single crystal metal surfaces give rise to the identification of a large number of adsorbed species that helps rationalizing diverse surface phenomena such as physical and chemical adsorption, lateral interactions in adsorbed layers, and chemical interactions on surfaces. These obtained results about the atoms and molecules can be used as basis for the improvement of the performance of catalysts. But, at the same time, well defined single crystals do not allow the investigation of intrinsic particle size, support, and structural effects. Therefore, the desire for a model catalyst that fulfills all the essential aspects of heterogeneous catalysis has led to the development of the supported model systems.

1.8. Supported model system

This model system is viable and acts as a complementary intermediate to bridge the material gap between single crystals and 'real world' catalysts addressing the important issues of intrinsic particle size and support effects.[4-5] In addition, the development of the planar model supported catalysts enables investigation of particle morphologies, growth modes, interactions with the support, and fundamental electronic structure by using techniques such as scanning tunneling, atomic force, scanning electron, and transmission electron microscopies.

When the catalytic reactions are conducted on metal single crystals or planar model supported catalysts at realistic conditions, the related surface chemistry and kinetics can be used to model the behavior of 'real world' industrial catalysts. For example, a kinetic model for methanol synthesis was based on the Cu(100) single crystal studies.[6] In catalysis, some reactions may exhibit kinetics that is dependent on metal particle size and surface orientations while some reactions may be surface-insensitive reactions. Examples of surface-insensitive reactions are CO oxidation on Rh, Pd, and Pt,[7-8] CO methanation,[9] and ethylene hydrogenation.[7] These are the cases where the reaction kinetics is determined to be very similar for the single crystals and 'real world' industrial catalysts. The structural insensitivity and independency in these cases may be mostly due to the poisoning of surface sites that are responsible for structure-sensitive activity by the reactants/intermediates. In fact, these metal catalyst particles are modified typically in the presence of impurities. In catalysis work, numerous studies are conducted to investigate the role of these impurities in either promoting or poisoning the catalytic reactions. Similarly, reactions such as ammonia synthesis on Fe,[7-8] alkane hydrogenolysis,[10] methanol synthesis on Cu,[11-12] CO oxidation by NO on Pd surfaces,[13] etc., are surface sensitive reactions. In these cases, the relative concentration of adsorption sites, such as terraces, steps, kinks, and defects on the metal particles, is dependent on the particle sizes and the way experimental procedures are carried out to fabricate the catalysts.[7-8] These factors can modify the coordination of surface atoms which can impact not only adsorbate binding energies but also the overall catalytic activities.

In the model system of an oxide-supported metal cluster, the metal particle size influences the electronic and chemical structures, metal-support interactions, physical, mechanical, and thermal properties, and overall catalytic activity and selectivity. A literature survey reveals hundreds of articles that explain several fabrication procedures for several model oxide films, including SiO_2,[14] Al_2O_3,[15] MgO,[16] CeO_2, and TiO_2,[17] which can be used as supports. At the same time, there are numerous ways to deposit metal clusters on oxide supports including physical and chemical vapor deposition (CVD),[18-20] electron beam lithography,[21] sputtering deposition,[22] high frequency laser vaporization,[23] mass-selective cluster deposition,[24-25] and nanolithography.[21,26-27]

In this way, a study starting with well-ordered single crystals under ultra high vacuum conditions (model catalysts) and then progressively increasing the gas pressure (real world catalysts) and complicating the catalysts under study from single crystals to planar supported model catalyst elucidates the structure-activity relationships (SAR) in heterogeneous catalysis.

This dissertation centers on the application of single crystal catalysts as well as oxide-supported metal catalysts under UHV conditions as a means for studying heterogeneous catalytic processes.

1.9. Coal combustion gases

Coal is considered as the largest source of energy for the power generation due to its relatively abundant reserves in comparison to the decreasing reserves of both petroleum and natural gas. At the same time, it is also one of the largest sources of carbon dioxide release. Coal is primarily composed of carbon along with other major elements such as oxygen, nitrogen, and sulfur. Along with these major elements, minor elements including Si, Al, Ca, Mg, K, Na, Fe, Mn, Ti, and trace elements which are the constituents with concentration below 100 ppm such as Se, Sb, Ce, Pb, Ni, As, Ba, Cu, Zn, Ga, Co etc. are evident during combustion in a larger power station. Practically each and every element of the chemical periodic table is present in coal.[28-30] The combustion of coal leads to the emission of gases such as carbon monoxide, hydrogen, carbon dioxide, nitrogen, methane, ethane and other volatile organic compounds. These pollutant emissions from coal combustion may cause serious environmental and health risks. Recently, the topic about these trace elements has drawn more and more research interest due to the great concern for their toxicological and environmental effects. Numerous studies have been carried out on the occurrence and distribution of such trace elements in coal, but studies show the trace elements' combination and contents vary from one coal type to another because of the different coalification processes. Therefore, motivated by environmental concerns, utilization, and sequestration of carbon monoxide and carbon dioxide; kinetics, dynamics, and spectroscopic studies of these coal combustion gases are investigated on model catalysts.

This dissertation includes studies involving the interactions of coal combustion gases such as CO and CO_2 on EBL-fabricated CuO_x/SiO_2 nanoclusters, MgO(100), and polycrystalline Se surfaces.

1.10. Methanol synthesis model nano-catalysts

Methanol is one of the most important feedstocks in chemical industries for many value-added products. It is the simplest alcohol which is produced in a catalytic industrial process directly using synthesis gases. Synthesis gases, 5% carbon dioxide, 5% carbon monoxide, and 90% hydrogen, are reacted over $Cu/ZnO/Al_2O_3$ catalysts at temperatures of 493-573 K and pressures of 50-100 bar.[31] The nature of the active site on Cu/ZnO based high-performance catalysts for methanol synthesis has been a matter of debate in literature and is still not completely understood.

Metallic copper is considered as the active phase of the catalyst since the catalytic performance correlates linearly with the surface area of copper.[32-33] This was later confirmed by in situ x-ray photoelectron spectroscopy[34] and surface x-ray diffraction studies.[35] The presence of Zn must be at the defective Cu surface which strengthens the binding of the intermediates and increases the catalytic performance of the catalyst. However, undistorted pure Cu and the flat Cu(111) surface were found to be quite inactive in the methanol synthesis experiment.[36] Furthermore, some prior studies reported that CO_2 is the essential component in synthesis gas for the production of methanol.[37] It was later confirmed by ^{14}C labeling experiments that methanol is mainly synthesized from CO_2 in the synthesis gas.[38] Furthermore, this was supported by measurements on the working catalysts.[39] These results suggested that methanol synthesis involves the following reactions:

$$CO + H_2O \rightleftharpoons CO_2 + H_2 \qquad (1.3)$$

$$CO_2 + 3H_2 \rightleftharpoons CH_3OH + H_2O \quad (1.4)$$

A literature survey revealed the synthesis of methanol mostly from H_2/CO_2 feedstock over Cu single crystals,[40] Cu/SiO_2, and $Cu/ZnO/SiO_2$.[41] In addition, the kinetic models for methanol synthesis were proposed by using UHV experimental data obtained on a Cu(100) single crystal.[6] It was found that the calculated methanol synthesis rates on model catalysts were in very good agreement with those obtained on a real world industrial catalyst. For this reason, the kinetic models based on model catalyst studies at UHV conditions can be useful to analyze the reaction mechanisms of industrial catalysts. However, this does not hold true for all the reactions. Sometimes, under industrially relevant conditions, a small fraction of the surface is significantly contributing to the chemical activity, which cannot be easily mimicked by simplified model approaches.

Methanol synthesis model catalysts investigated in this dissertation include electron beam lithography (EBL)-fabricated silica-supported Cu and CuO_x clusters.[42-44] Adsorption kinetics and dynamics of CO and CO_2 on EBL-fabricated Cu and CuO_x clusters were studied. The main objective of this project is to characterize the catalytic activity of silica-supported Cu nanoclusters (of different sizes) towards the adsorption of CO and CO_2. In addition, the results of CO adsorption on Cu PVD clusters are also compared to those obtained on silica-supported Au PVD clusters in order to understand the cluster size effects.[45]

1.11. Bond activation in alkanes

Bond activation in hydrocarbons has been a major thrust of research for the last few decades due to its potential applications in fuel generation. The bond dissociation of alkanes has been studied for decades, with a historic focus on metal single crystal surfaces such as Ir and Pt.[46-53] The high chemical activity of some metal oxides in this respect has been known for quite some time from catalysis studies on powders,[54-58] but only a few surface science projects about the adsorption of alkanes on nonmetallic systems have been conducted. Molecular adsorption has been seen for MgO,[59] ZnO,[60] rutile TiO_2,[61-62] silica,[63-64] and graphitic systems.[65-67] A bond cleavage on transition metal oxides, such as PdO thin films, was reported in a surface science study where a donor-acceptor mechanism has been proposed for alkane bond activation.[68-69] It utilizes multi-mass reactive TDS where C-H bond cleavage leading to adsorbed propyl/propoxy and hydrogen has been concluded for propane/PdO(101). Another study shows the bond activation in ethylene on O/Ni(111).[70] At present, apparently the only metal oxide single crystals/thin films studied in more detail with surface science techniques that promote alkane dissociation are Pd and Ca oxides. It is also evident that bond activation of alkanes was also seen for anatase TiO_2 thin films.[61] However, in this case, the alkanes decompose entirely, making a detailed characterization very cumbersome. In fact, two mechanisms of bond activation have been considered for metal catalysts.[46-53] At low impact energies, a precursor-mediated bond activation occurs where the alkanes are trapped in the physisorption well before dissociation. At high impact energies, a direct (impact-induced) bond breakage in alkanes is evident. It appears that basically the same mechanism explains the molecular beam scattering data gathered so far for the butane/CaO(100) system. Molecular beam scattering on CaO(100) provided the first evidence for the occurrence of bond activation of n-/iso-butane on this metal oxide surface.[71] The selectivity of the bond activation could be tuned by changing the impact energy and gas temperature of the probe molecules.

In this dissertation, bond activation in small chain alkanes is studied in model catalysts of alkaline earth metal oxide, i.e. CaO(100), single crystal of metalloid Sb(111), and silica-supported EBL-fabricated Mo metal clusters. As a result, adsorption kinetics study on a single crystal of CaO(100) provides the evidence for the occurrence of bond dissociation in small chain alkanes whereas only molecular adsorption is seen in the cases of Sb(111) and Mo nanoclusters.

CHAPTER 2. EXPERIMENTAL TECHNIQUES

A variety of experimental techniques are enclosed in an ultra high vacuum chamber for studying the model catalysts and other surface phenomena with gas phase molecules. Thermal desorption spectroscopy (TDS) was used to determine the kinetic and thermodynamic parameters of desorption processes and decomposition reactions on model catalysts surface. Molecular beam scattering was used to study the gas-to-surface energy transfer (adsorption dynamics) processes. Spectroscopic techniques such as Auger electron spectroscopy (AES) and X-ray photoelectron spectroscopy (XPS) were used to characterize the cleanliness as well as chemical and electronic state of the model catalysts. Low energy electron diffraction (LEED) was used to determine the surface structure of crystalline materials. X-ray diffraction (XRD) was used to investigate the structural properties of the surface. In addition, our collaborators at the Molecular Foundry, Berkeley, helped us fabricating EBL samples and Brookhaven National Laboratory helped us obtaining SEM images to further characterize the supported model catalysts. A description of each technique that was used in this research projects is presented hereafter.

2.1. Ultra high vacuum

Vacuum pressure below $1\text{x}10^{-9}$ Torr is considered as ultra high vacuum (UHV). Virtually, all surface studies are carried out under ultra high vacuum conditions. At a pressure of $1\text{x}10^{-6}$ Torr, it takes only one second for a surface to be covered with a monolayer of adsorbed gases. Therefore, UHV enables atomically clean surfaces to be prepared for study and maintains such surfaces in a contamination free state for the duration of the experiment. It allows the use of low energy electron, X-ray beam, and ion-based experimental techniques without any interference from gas phase scattering. At a UHV environment, the mean free path of probe and detected particles such as electrons, ions, atoms, and molecules must be considerably greater than the dimensions of the chamber in order that these particles may travel to the surface and from the surface to the detector without undergoing any collisions with the residual gas-phase molecules. Similarly, the UHV is also required to maintain high voltages in a surface analysis system without breakdown or glow discharges. Therefore, the UHV is indeed a necessity in order to carry out reliable surface science and surface analysis experiments.

There are two ultra high chambers in the lab at NDSU, one being called the thermal desorption spectroscopy chamber (TDS chamber) and another being called the scattering chamber for the molecular beam system. Figure 1 shows a picture of the TDS chamber whereas Figure 3 shows a picture for the scattering chamber. It should be noted that the projects mentioned in this dissertation are either conducted in the TDS chamber or the beam scattering chamber. The projects related to CaO and Se model catalysts were conducted in the TDS chamber, and the rest of the projects were conducted in the scattering chamber utilizing a molecular beam.

2.2. TDS chamber

The TDS chamber is equipped with two quadruple mass spectrometers (SRS RGA 100 and SRS RGA 300), low energy electron diffraction (LEED) optics combined with an Auger electron spectrometer (SPECS, ErLEED 3000D), a home-built metal doser, an atomic hydrogen source (a capillary doser with a hot W filament at the end), and a sputter gun (SPECS, IGE 11). The system is pumped by three turbo molecular pumps (two Leybold, NT 360 and one Varian) backed by a fore-line pump (Leybold) and an ion pump (Varian) with battery backup. Several pressure gauges are mounted within the chamber to measure the pressure readings. Two leak valves, connected to a gas line, are used to dose desired gases inside the chamber. Multiple leak valves allow for studying the co-adsorption of multiple gases on the surface at the same time. This gas line is further connected to a fore-line pump (Leybold) for cleaning purposes.

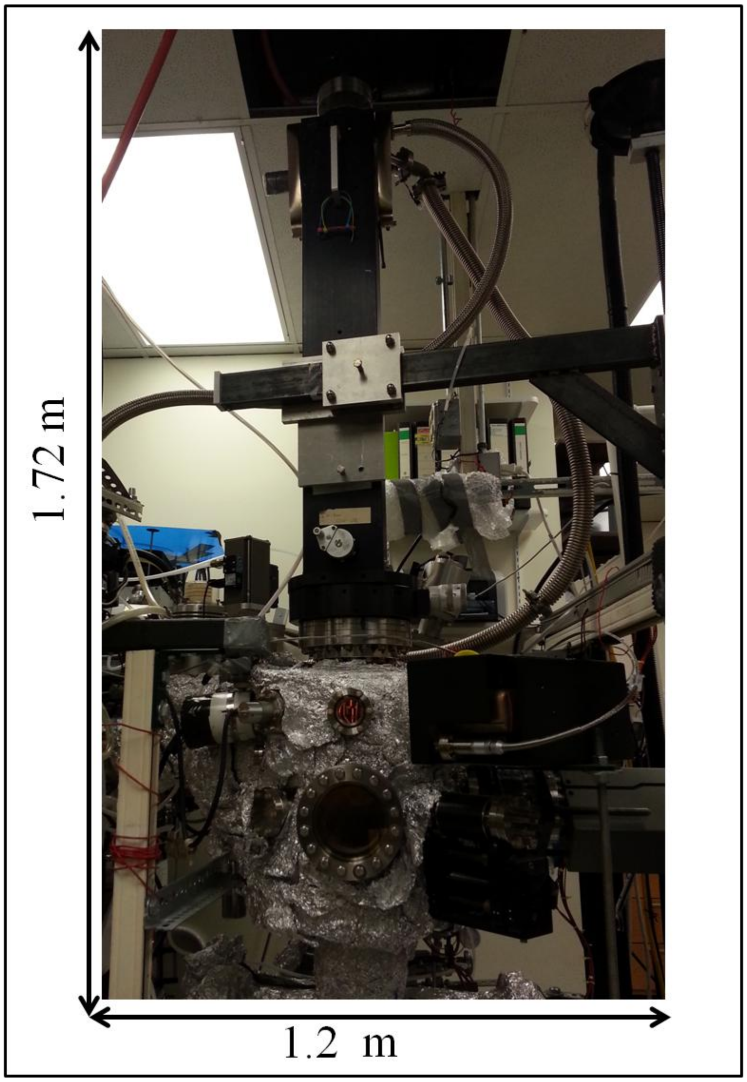

Figure 1. Photograph of TDS ultra high vacuum chamber at NDSU. Scales show the actual dimensions of the chamber.

An xyz manipulator (McAllister) with a differentially pumped rotary platform is also installed on the TDS chamber. With this manipulator, a sample can be moved in any direction within the chamber. A sample holder is mounted on the manipulator and can be rotated 360^{o} with a stepper motor. The rotary platform is pumped by a turbo molecular pump (Leybold, NT 360) backed by a fore-line pump (Leybold). The vacuum system can be baked above 150 °C using heating belts and surface heaters to achieve a base pressure of $2\text{x}10^{-10}$ mbar. The system is also equipped with UHV gate valves (VAT) to protect the vacuum in the event of power failure.

2.3. Sample holder set up

The sample holder consists of a stainless steel tube, one side (upper side) of which is welded to a through-hole conflat flange to form a dewar tube, and the other (lower side) is connected to a 4-pin molybdenum conductor CF 16 flange. The through-hole conflat flange is also equipped with two electrical feedthroughs, one for sample heating, and another for simultaneous temperature measurement (thermocouple). The reading of the thermocouple is calibrated (±5 K) *in situ* by TDS measurements of the condensed alkanes for every experiment. A picture of the body of the sample holder is shown in Figure 2A. Typically, the sample (10x10x1 mm) mounted on a tantalum plate (for non-conducting samples) is spot-welded to two front pins of molybdenum, as shown in Figure 2B. A chromel-alumel thermocouple is spot-welded on the back of tantalum plate which makes it possible for in-situ measurement of a sample temperature (T_s). A tungsten (W) filament (0.25-0.55 mm, Goodfellow) is spot-welded to two back pins right behind the tantalum plate as shown in Figure 2C. The air-side or upper side of the stainless steel tube acts as a dewar and can be filled with liquid nitrogen for cooling the sample to low temperatures (~ 93 K). The sample temperature can be further lowered (~ 87 K) by blowing He gas into the dewar.[72] An electron bombardment heating method is used for sample heating while performing TDS experiments and other cleaning procedures.

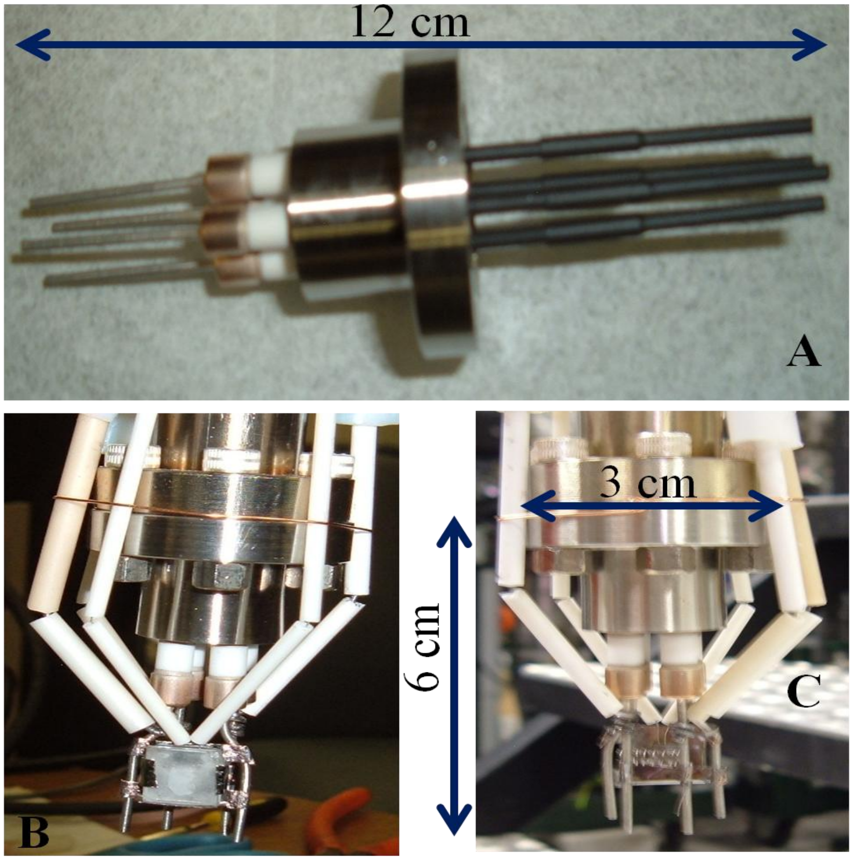

Figure 2. Photographs of sample holder A) a bare sample holder, B) mounted sample, front view and C) rearview of the mounted sample. Scales show the actual dimensions of sample and sample holder.

A tungsten filament is resistively heated to produce electrons by using a computer controlled power supply (HP 6433 B) that bombards the back of the sample. These thermal electrons emitted from the filament are further accelerated towards the sample by means of another computer-controlled high voltage (HV) power supply (Gassman PS/G59). A homemade data acquisition program driven by a proportional-integral-derivative (PID) controller is used to control the total heating power and attain a linear heating ramp (T_s vs. time) over a wide range of temperatures. PID uses the real time clock of the computer as its primary source of time.

2.3. Molecular beam scattering chamber

Molecular beam scattering technique is a well established tool to study the dynamics and kinetics of surface reactions. A molecular beam is a spatially well defined, directed, and collision-free flow of molecules. All the dynamics studies in this dissertation were conducted in a triple-differentially-pumped molecular beam system. Figure 3 and Figure 4 shows the photograph and schematic of the beam scattering ultra high chamber at NDSU, respectively. The first two pumping stages consist of varian diffusion pumps (a VHS-10 with a pumping speed of 6600 s^{-1} and a VHS-6 with 3000 s^{-1}) backed by a D25B/WSU500 rotary/booster pump (from Leybold). The aperture of the beam is adjustable by means of a linear motion combined with a tilter (Huntington,) and the nozzle is adjusted by a x-y-z-tilt-manipulator (McAllister).

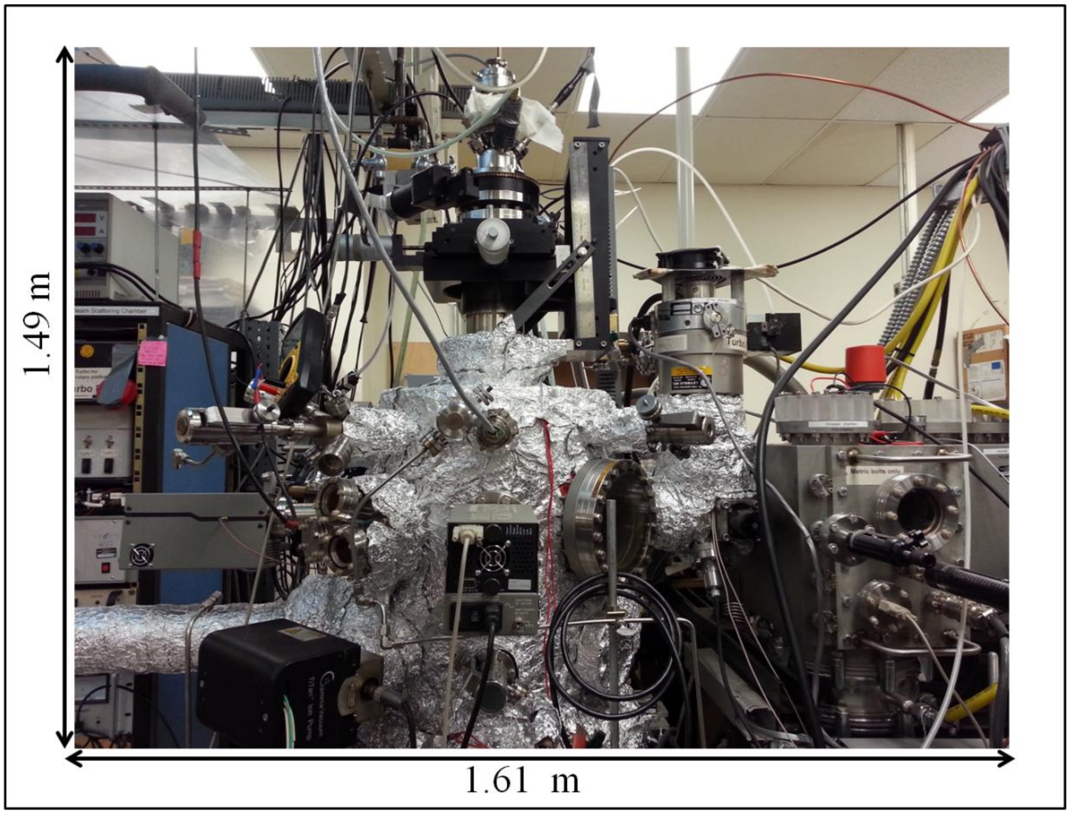

Figure 3. Photograph of the beam scattering ultra high vacuum chamber at NDSU. Scales show the actual dimensions of the chamber.

The nozzle contains steel tubing treated on top and a head counterpart for press fitting Pt/Ir nozzle plates (PLANO). The third beam chamber is pumped by a over head mounted 360 s^{-1} turbomolecular pump (Leybold, NT 360). The background pressure in the scattering chamber is below 2 × 10^{-8} torr. The supersonic molecular beam is attached to a scattering chamber pumped by 2 turbo pumps (Varian T-V551) with a 550 s^{-1} pumping speed and a Ti sublimation pump (Varian). This chamber is equipped with a dual Mg/Al anode X-ray source for X-ray photoelectron spectroscopy (XPS) and a double pass cylindrical mirror analyzer (CMA) with a coaxial electron gun for Auger electron spectroscopy (AES) measurements (all from Perkin-Elmer including an upgrade from RBD). In addition, this chamber is equipped with two mass spectrometers (SRS RGA 100): one of which is for time-of -flight (TOF) measurements, aligned collinearly with the molecular beam for beam characterization, and the other is for molecular beam and TDS experiments, aligned perpendicular to the molecular beam. Furthermore, the scattering chamber is equipped with a commercial electron beam evaporator (McAllister), a home-built metal doser, an atomic hydrogen source (Tectra GmbH), and a sputter gun (SPECS,IGE 11).

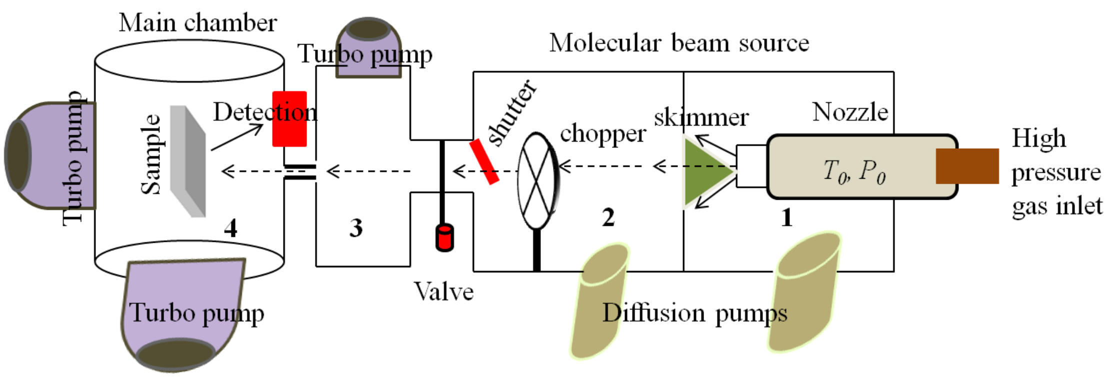

Figure 4. Schematic of the beam scattering ultra high vacuum chamber at NDSU.

The experiments are controlled by a homemade data acquisition program ("C" code, LABWINDOWS) including a software PID (Proportional-Integral-Derivative) controller for stabilizing the surface and nozzle temperature, and a beam shutter (miniaturized servo motor from pololu). An xyz manipulator (McAllister) with a differentially pumped rotary platform is also installed on the scattering chamber to move the sample in the desired direction. A sample holder is mounted on the manipulator and can be rotated 360^{o} with a stepper motor. The rotary platform is pumped by a turbo molecular pump (Leybold, NT 360) backed by a fore-line pump (Leybold). The vacuum system can be baked at 150 ^{o}C using heating belts and surface heaters to achieve a base pressure of $2x10^{-10}$ mbar. The system is also equipped with UHV gate valves (VAT) to protect the vacuum in the event of power failure. Several leak valves, connected to a gas line, are used to dose desired gases inside the chamber. Multiple leak valves allow for the study of co-adsorption of multiple gases on the surface at the same time. This gas line is further connected to a fore-line pump (Leybold) for cleaning purposes. Sample mounting and experimental procedures are the same as described above for the TDS chamber. Figure 5 shows the schematic of all the components attached to the molecular beam scattering chamber.

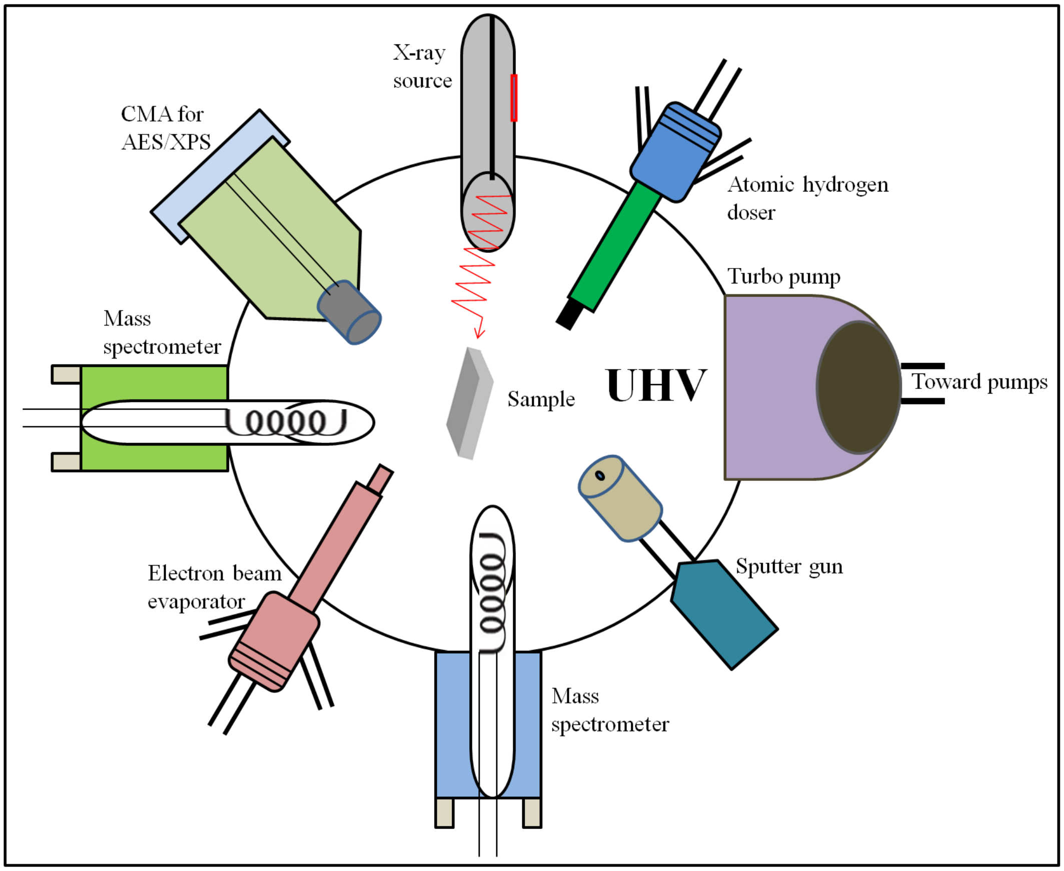

Figure 5. Schematic showing all the components of ultra-high vacuum chamber.

2.4. Kinetic measurements: thermal desorption spectroscopy

Thermal desorption spectroscopy (TDS), also known as temperature programmed desorption (TPD), is an important technique to determine the kinetic and thermodynamic parameters of desorption processes and decomposition reactions. The fundamental information such as the heat of adsorption, the desorption order, existence of multiple adsorption sites, evidence for the dissociative and non-dissociative adsorption, and even the nature of the adsorbate can be deduced. TDS experiments are performed using well defined surfaces of single-crystalline or polycrystalline as well as thin film or cluster samples in a continuously pumped UHV chamber. The samples are usually maintained at room temperature or cryogenic temperature around 90 K. A desired gas molecule is exposed to the clean surface; that way the adsorbed molecule is bound to the surface in a potential well of depth E_{des}. Then, this adsorbed gas molecule/atom is desorbed by heating the surface. The pressure rise is monitored and the desorbed gas molecules are detected by a quadrupole mass spectrometer. This mass spectrometer can acquire single or multiple mass-to-charge ratios (m/z) during heating. In principle, we can get information about heat of adsorption whether adsorption and desorption are reversible/non-dissociative processes, quantitative coverage information of dissociative and non-dissociative adsorption, energetic information about the interadsorbate interactions, several adsorption sites, and kinetic information about desorption processes and decomposition reactions. TDS measurements are carried out by varying the surface coverage of the adsorbate. The gas exposures are given in Langmuir (1 L = 1 s gas exposure at 1×10^{-6} mbar). The Polanyi-Wigner equation, which is derived below, can be used to describe the dependence of surface temperature on the desorption behavior.

2.5. Theoretical description of TDS data

Consider an adsorbate M on a surface which is desorbed into a gaseous state upon heating

$$M_{ads} \xrightarrow{k_d} M_{gas} \tag{2.1}$$

where k_d is the desorption rate coefficient.

The desorption rate (k) is expressed by a rate law of the nth order and is given by the negative rate of change of the coverage of adsorbate molecules:

$$k = k_d[M_{ads}]^n \tag{2.2}$$

$$k = -\frac{d\Theta_M}{dt} = k_d\, \Theta_M{}^n \tag{2.3}$$

where Θ_M is the instantaneous coverage of adsorbate molecules in monolayers. The rate of desorption follows Arrhenius-type behavior. Therefore, we can write:

$$k_d = \upsilon_d \, e^{-\frac{E_{des}}{RT}} \tag{2.4}$$

Here υ_d is the frequency factor, E_{des} is the activation energy for desorption, R is the universal gas constant, and T is the surface temperature. By combining equations 2.3 and 2.4, the desorption rate law can be obtained:

$$-\frac{d\Theta_M}{dt} = \upsilon_d \, e^{-\frac{E_{des}}{RT}} \, \Theta_M{}^n \tag{2.5}$$

This equation is referred to as the Polanyi-Wigner equation which can lead to information of the kinetic parameters governing the reaction. Assuming linear increase of T with time during TDS, we can write:

$$T = T_0 + \beta t \tag{2.6}$$

where T_0 denotes the initial temperature in Kelvin, β is the heating rate ($K.s^{-1}$), and t is the time in second (s).

Heating rate β is the derivative of temperature with respect to time, so it can be written as:

$$\frac{dT}{dt} = \beta \Rightarrow dt = \frac{1}{\beta} dT \tag{2.7}$$

By substituting the value of dt in equation 2.3, we get

$$k = -\frac{d\Theta_M}{dt} = -\frac{d\Theta_M}{\frac{1}{\beta} dT} = -\beta \frac{d\Theta_M}{dT} \tag{2.8}$$

This term is substituted into the Polanyi-Wigner equation, mentioned above, to get the following equation:

$$-\beta \frac{d\Theta_M}{dT} = \upsilon_d \, e^{-\frac{E_{des}}{RT}} \, \Theta_M{}^n \Rightarrow -\frac{d\Theta_M}{dT} = \frac{\upsilon}{\beta} \, e^{-\frac{E_{des}}{RT}} \, \Theta_M{}^n \tag{2.9}$$

The pressure rise of desorbing gas in a TDS experiment is directly proportional to the derivative of adsorbate coverage with respect to temperature. The activation energy for desorption is calculated by determining the peak in pressure which corresponds to the maximum desorption rate or peak temperature (T_{max}). Peak pressure is determined by taking the second derivative of adsorbate coverage with respect to temperature and making it equal to zero.

$$p \propto \frac{d\Theta_M}{dT} \Rightarrow \frac{d}{dT}\left(\frac{d\Theta_M}{dT}\right) = \left(\frac{d^2\Theta_M}{dT^2}\right) = 0 \qquad (2.10)$$

$$\frac{d}{dT}\left(- \frac{\upsilon}{\beta}\, e^{-\frac{E_{des}}{RT}}\, \Theta_M{}^n\right) = \left(\frac{d^2\Theta_M}{dT^2}\right) = 0 \qquad (2.11)$$

One can use the product rule for differentiation of the left side of equation 2.11 to get the following equation:

$$\frac{\upsilon}{\beta}\left(n\Theta^{n-1}\, \frac{d\Theta_M}{dT}\, e^{-\frac{E_{des}}{RT_{max}}} + \frac{\Theta^n\, E_{des}}{RT^2{}_{max}}\, e^{-\frac{E_{des}}{RT_{max}}}\right) = 0 \qquad (2.12)$$

By rearranging the terms in equation 2.12, one arrives at the following equation:

$$n\Theta^{n-1}\, \frac{d\Theta_M}{dT} = - \frac{\Theta^n\, E_{des}}{RT^2{}_{max}} \qquad (2.13)$$

After substituting the value of $\frac{d\Theta_M}{dT}$ from equation 2.9 in the above equation and rearranging the terms, the following equation is created:

$$\frac{\upsilon}{\beta}\, n\Theta^{n-1} e^{-\frac{E_{des}}{RT_{max}}} = \frac{E_{des}}{RT^2{}_{max}} \qquad (2.14)$$

This equation is called the Redhead equation which assumes that activation parameters are independent of surface coverage. For the first order desorption, the estimated desorption activation energy, E_{des}, can be calculated using an approximated Redhead equation as follows:

$$E_{des} = RT_{max}\left[\ln\left(\frac{\upsilon T_{max}}{\beta}\right) - 3.64\right] \qquad (2.15)$$

The Redhead method is often used to determine the activation energy from a single desorption spectrum by choosing the pre-exponential factor as 10^{13} s^{-1}. The shape of desorption spectra and the number and position of the peaks help in understanding the details of the adsorbate-surface interaction.

2.6. Desorption order

2.6.1. Zero-order desorption kinetics

TDS curves corresponding to different surface coverages have a common leading edge which looks exponential as shown in Figure 6. T_{max} moves to higher T with an increase in surface coverage, and the peak intensity drops immediately after reaching the maximum.

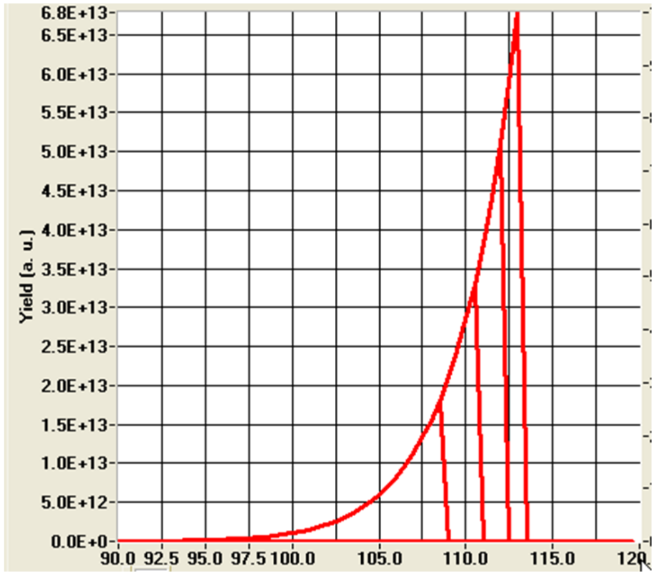

Figure 6. Computer simulated zero-order desorption kinetics.

2.6.2. First-order desorption kinetics

TDS curves corresponding to different surface coverages have a characteristically asymmetric peak shape. Desorption rate is proportional to surface coverage, but T_{max} is independent of surface coverage as shown in Figure 7.

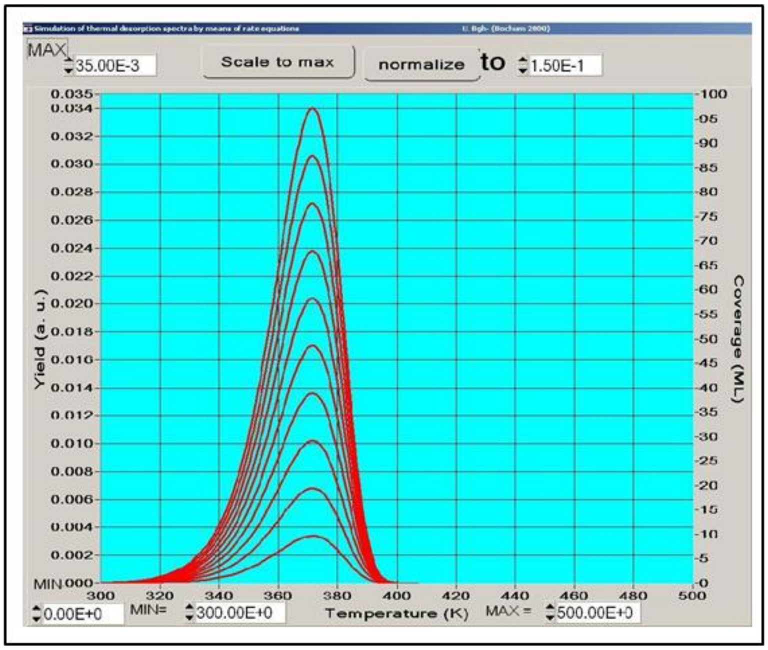

MAX 35.00E-3
to 1.50E-1
0.00E+0
MIN= 300.00E+0
MAX = 500.00E+0

Figure 7. Computer-simulated first-order desorption kinetics.

2.6.3. Second-order desorption kinetics

TDS curves corresponding to different surface coverages have a characteristically nearly symmetric shape. TDS curves corresponding to different surface coverages have a common trailing edge. T_{max} moves to lower T with an increase in surface coverage. Desorption rate is proportional to the surface coverage. Multiple peaks corresponding to different adsorption sites on the surface are often observed in the second-order desorption process.

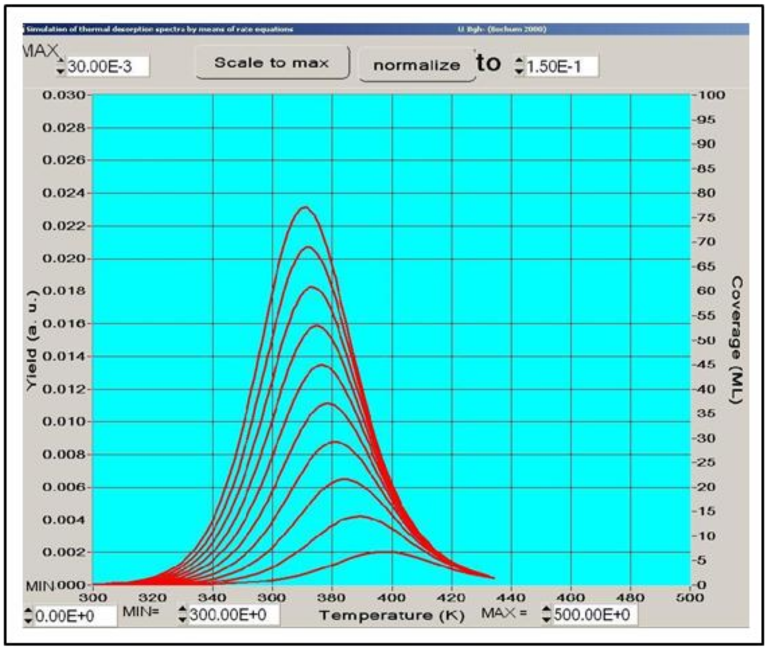

Simulation of thermal desorption spectra by means of rate equations U. Bgh- (Bochum 2000)

MAX 30.00E-3

to 1.50E-1

MIN 0.00E+0

MIN= 300.00E+0

MAX = 500.00E+0

Figure 8. Computer-simulated second-order desorption kinetics.

2.6.4. Pseudo second-order desorption kinetics

Sometimes, strong repulsive interadsorbate interactions at different surface coverages lead to a common trailing edge. This repulsion increases with coverage which lowers average desorption temperature.

2.6.5. Fractional-order desorption kinetics

Desorption order of $0 < n < 1$ is considered as fractional-order. TDS curves corresponding to different surface coverages do not have a common leading edge. T_{max} increases with an increase in surface coverage, and the peak intensity does not drop immediately after reaching the maximum unlike in zero order kinetics. Usually, desorption from the edges of 2D or 3D clusters possesses fractional-order desorption. Figure 9 shows the example of fractional order desorption kinetics where appearance of α_2, α_3, and α_4 peaks are primarily due to the desorption of Zn from the perimeter of islands or clusters.[73]

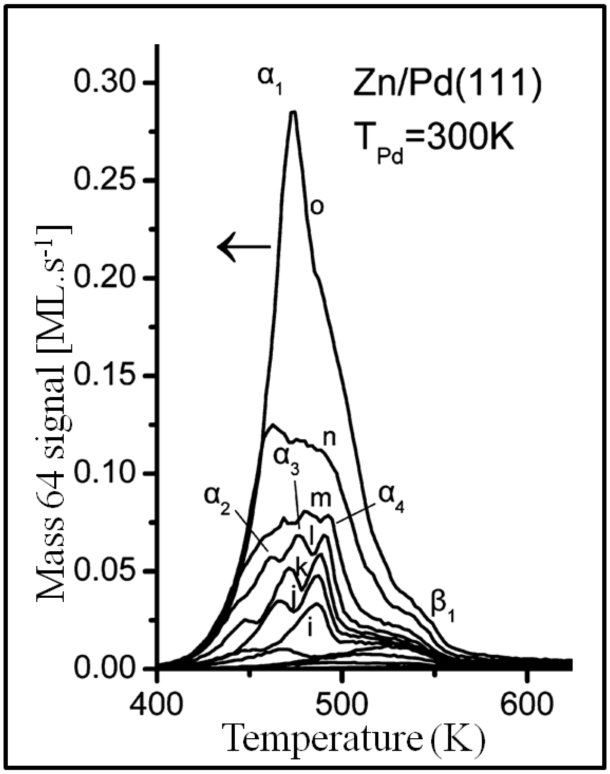

Figure 9. Example of fractional-order desorption kinetics. Desorption of ultrathin Zn layers from Pd(111) surface. Ref.[73]

Therefore, the shape and size of the desorption peak in TDS spectra varies with reaction order, coverage, E_{des}, and pre-exponential factors. The desorption spectra can be analyzed as a function of heating rate and coverage. The activation energy for desorption can be determined by using the Redhead equation if a pre-exponential factor is known. Two conditions have to be fulfilled to utilize the Polanyi-Wigner equation to achieve an accurate spectral interpretation. The first condition is that the mass spectrometer signal is proportional to the rate of desorption. This condition is only met when the pumping speed is high enough to prevent the re-adsorption of desorbed particles on the sample. Similarly, the second condition is that the desorption process consists of at least one rate-limiting elementary step. In fact, the activation parameters such as the desorption order, pre-exponential factor, and the activation energy generated by Polanyi-Wigner equation will only be applicable to such a rate-limiting step. Also, these activation parameters are dependent on the surface coverage and the sample temperature. Sometimes, Monte-Carlo simulations are considered as the alternatives to the interpretation by means of the Polanyi-Wigner equation. Therefore, thermal desorption spectroscopy is considered as the beauty as well as the beast of surface kinetics measurements. Its beauty lies in its simplicity that leads to an approximate understanding of what is going on in surface kinetics. The beast lies in the accurate and unambiguous interpretation of the data.

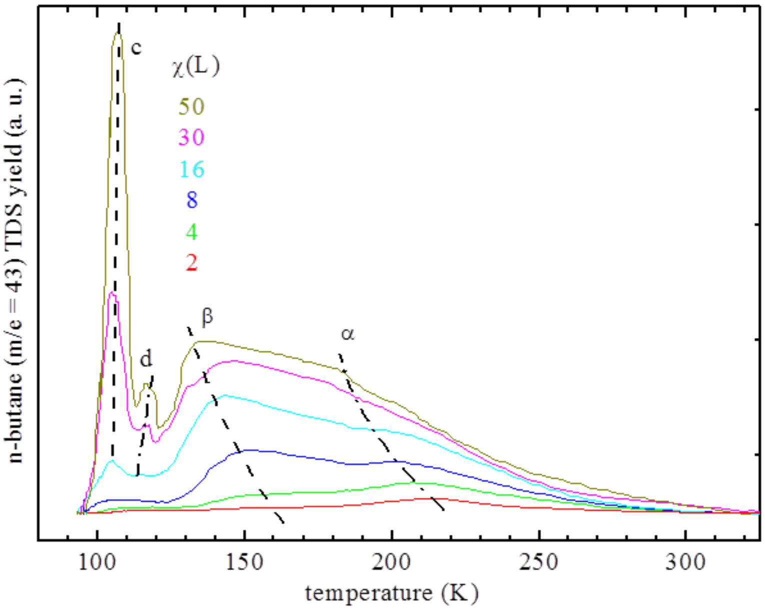

Figure 10 . n-butane TDS on CaO(100) (α and β: different adsorption sites, c: multilayer formation, and d: condensation). The different curves represent TDS data at coverages, χ.

An example of TDS spectra of n-butane on a single crystal of CaO (100) is shown in Figure 10.[74] Four distinct peaks α, β, c, and d, are observed in the TDS spectra. Low exposures TDS spectra consist of only one TDS peak (α peak). With increasing exposure, a second structure grows in intensity (β peak), and at very large exposures a low-temperature TDS peak appears (c peak). They indicate the presence of kinetically different adsorption sites on the surface of CaO. The α and β TDS peaks arise from different adsorption sites/configurations including possibly the effect of surface defects. The c peak is assigned to a multilayer formation of condensed alkanes. The low temperature edges of the TDS curves line up to form a peak d, an adsorption (and system) unspecific condensation peak of n-butane. The Redhead equation can be used to calculate the corresponding binding energies of n-butane on these adsorption sites.

It should be noted that the background pressure in the scattering chamber, with a pure beam running, does amount to 2×10^{-10} mbar. Thus, it takes approximately 5000 sec or 1.29 hours to dose one Langmuir onto the surface from the residual gas ambient (assuming a 50% measuring error of the ion gauge would reduce that time to 3000 sec). This is the time required to saturate the surface with gas-phase species having an adsorption probability of one from the background gases inside the chamber. In contrast, a typical TDS experiment requires about 10-15 minutes, including cooling the surface from room temperature to 90-100 K range and ramping up the temperature again. Similarly, besides probe molecules, no other species appear above the background level with the beam system running. Therefore, it is very unlikely that any large uptake of gas-phase species from the residual vacuum did take place while conducting kinetics or dynamics experiment in this study.

2.7. Molecular beam source

Molecular beam scattering is a well-established tool in surface science to study the kinetics and dynamics of surface reactions. It provides a unique way of performing detailed, quantitative and systematic experiments on the kinetics and dynamics of surface reactions.[25,75-77] Molecular beam methods have helped to elucidate many aspects of the kinetics and dynamics of adsorption/desorption phenomenon in great detail on single crystals as well as on supported model catalysts.

A detail description of the scattering chamber is already given in the previous section. The first and second chambers of the molecular beam system are respectively connected to Varian diffusion pumps backed by a D25B/WSU500 rotary/booster pump combination. The third chamber is pumped by a turbo molecular pump backed by a foreline pump. The second and third chambers are separated by a screw valve. The nozzle is mounted on a xyz-tilt-manipulator in the first chamber. The nozzle consists of a steel tube onto which a Pt/Ir µm nozzle plate is press fitted. The nozzle is wrapped with small ceramic beads strung on a nichrome wire for heating purposes. A conical skimmer is mounted on the wall of the first chamber facing towards the nozzle as shown in Figure 4. A linear drive (Huntington) combined with a tilter is used to adjust the second aperture of the beam chamber. The second chamber consists of a beam chopper and a light sensor for the time of flight (TOF) analysis of the supersonic molecular beam. A beam shutter driven by a miniature servo motor is also mounted in the second chamber. This sophisticated supersonic molecular beam system is attached to a scattering chamber for a dynamics study. Molecular beam scattering experiments are controlled by a homemade data acquisition computer program called LabWindows.

Simply, a molecular beam is a spatially well-defined collision-free flow of molecules directed towards the sample. Usually it is generated in a beam source as shown in Figure 4. The nozzle beam is created by expanding a gas from a so called stagnation state (p_0, T_0) and this expanded gas travels through a pinhole from a high pressure nozzle into a vacuum with a series of rapidly pumped chambers. In fact, the dynamic properties of the molecules in this expansion depend on the specific conditions of the experiment. This beam is collimated as it passes from one chamber to the next and eventually forms a well collimated beam. A mechanical chopper is used to prepare the desired temporal structure by modulation. At the early stages of the beam, many collisions occur, and random thermal motion is converted into translational motion, with a relatively narrow velocity distribution, in the beam direction. Similarly, a beam of light gas such as hydrogen or helium can be seeded with a heavy reactant, to achieve very high reactant translational energies, along the beam direction. By doing so, the reactant is dragged along at the same velocity as the light gas towards the sample. In addition, the velocity or kinetic energy of the reactant can be varied by varying the fraction of the reactant in the beam and the temperature of the nozzle. At the same time, its rotational and vibrational energies are considerably reduced in the general conversion of thermal into directed motion. The directed beam can be separated from the effusive background of molecules by implementing several differential pumping stages. Finally, the beam enters the scattering chamber from the last differential pumping stage and collides with the sample at the desired angle of incidence. The so-called Knudsen number (Kn) is used to differentiate the type of beam produced from the source. It is defined as the ratio of the molecular mean free path length (λ) to the effusion hole/nozzle diameter (d). Simply, a high pressure gas (small λ) and a μm nozzle (small d) combination produces a supersonic molecular beam. An effusive beam will be produced when the molecular mean free path length is comparable to the effusion aperture size. Typically, the efficiency of the gas cooling during an adiabatic expansion can be characterized using the Mach number (M). The Mach number is the ratio of the average velocity of the expanding gas to the local speed of sound of the expanding gas. Therefore, the higher Mach number means narrow speed or energy distribution of the gas molecules and low beam temperature and vice versa. Typical beam temperatures of ~ milli K can be obtained in supersonic molecular beam formation.

2.8. King and Wells method

The measurements of adsorption probabilities (S_0) or sticking coefficients for surface reactions are performed based on experimental procedures originally proposed by King and Wells, detecting the relative pressure change in an ultra high vacuum chamber. This method (shown in Figure 11) relies on a sufficiently quick response of the vacuum system. Before exposing the vacuum chamber with a beam, the chamber has a certain base pressure (P_b). Once the shutter is opened, the beam enters the chamber resulting in pressure rise to P_0 (assuming the beam is not hitting the sample surface). Now, as the beam is directed towards the sample, the pressure, p(t), changes as a function of time t, as gas molecules adsorb onto and eventually increase the pressure in the chamber to a saturation level (P_{sat}) as shown in Figure 11. Typically, the sample temperature is adjusted in such a way that the incoming beam adsorbs to a monolayer range on the surface, avoiding condensation of gas molecules. In fact, the initial rise of pressure in the vacuum chamber is because of the scattered gas molecules. Therefore, initial adsorption probability (S_0) is calculated by taking the ratio of the initial pressure rise (P_0) to the saturation pressure (P_{sat}). The fact that the incident flux is known makes it possible to determine the adsorbed number of molecules by considering the area above the transient and below the saturation level. Similarly, coverage (Θ) dependent adsorption probability $S(\Theta)$ can be obtained by integrating the pressure transient. The determination of adsorption probabilities opens up the possibility to directly compare reaction rates as a function of the surface structure for heterogeneous and nanostructured surfaces. This King and Wells method is typically appropriate for detecting adsorption probabilities in the range between about 10^{-2} and 1.

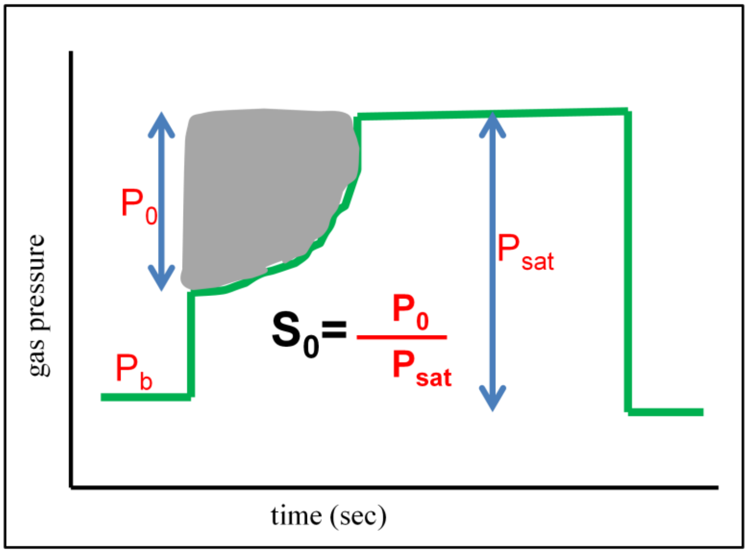

Figure 11. Schematic illustration of King and Wells uptake beam scattering experiment. P_b is the base pressure in the vacuum chamber. The molecular beam entering the vacuum chamber saturates the sample's surface with time.

An example of the King and Wells type uptake curves for CO on SiO_2 (Silica) and 63 nm Cu clusters supported on silica are shown in Figure 12. The pressure transient for CO on silica reveals no adsorption of CO. However, the pressure transient of CO on 63 nm Cu clusters approaches the saturation level much slower compared to bare silica. This indicates the adsorption of CO on Cu clusters. The area above the pressure transient and below the saturation coverage can be integrated to calculate the number of molecules of CO adsorbed, if the beam flux is known. Adsorption probability is typically a function of surface coverage and surface temperature. Depending on the shape of coverage dependent adsorption probability curves, various types of adsorption processes are categorized as discussed in the following.

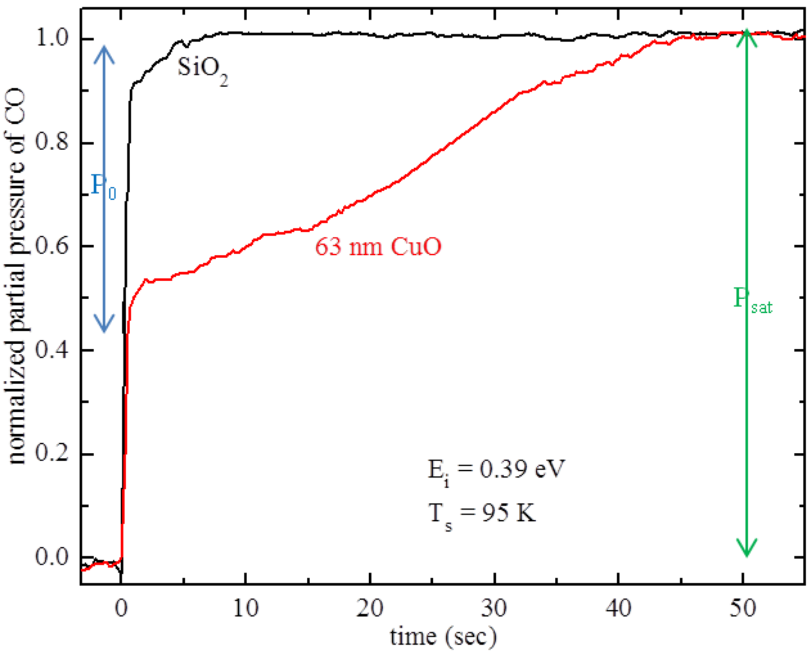

Figure 12. King and Wells experiment showing the adsorption transients of CO on clean silica and 63 nm Cu clusters supported on silica. The initial adsorption probability (S_0) is equal to the ratio of the initial pressure rise (P_0) to the saturation pressure (P_{sat}). T_s is the sample temperature and E_i is the impact energy of CO.

2.8.1. Langmuirian adsorption model

In the Langmuirian adsorption model, it is assumed that $S_0 = 1$ on vacant sites and $S_0 = 0$ on filled adsorption sites. This means the gas molecules arriving on the surface will only adsorb on vacant adsorption sites and not on the molecules already adsorbed on the surface. Therefore, the initial adsorption probability decreases linearly with surface coverage as shown in Figure 13A. This property is an indication that the adsorption probability decreases due to simple site blocking rather than due to any chemical or electronic effects. It should also be noted that this model does not mean that the adsorbing molecule sticks where it hits. Also, the observation of Langmuirian adsorption does not rule out the possibility of transient mobility after the initial collision with the samples' surface.

2.8.2. Kisluik model

The Kisluik model is also known as precursor-mediated adsorption for the reason that the adsorption is mediated by a precursor state through which the adsorbing molecule passes on its way to the vacant sites. Precursor states can be categorized as either extrinsic or intrinsic. An extrinsic precursor state is associated with the presence of adsorbates on the surface, whereas an intrinsic presursor state is associated with the clean surface. In other words, an intrinsic precursor state is formed on a vacant active site, whereas the extrinsic precursor state is formed on an occupied chemisorption site. According to this model, the adsorption probability stays above the value predicted by the Langmuirian model because the adsorbing molecule can roam or diffuse around the surface and hunt for a vacant site. Therefore, the adsorption probability is greatly enhanced because an adsorbed molecule has a certain probability of sticking even if it collides with an occupied site, unlike in the Langmuirian model. Typically, the initial adsorption probability remains almost constant at the beginning and drops quickly to zero in approaching the saturation coverage as shown in Figure 13B.

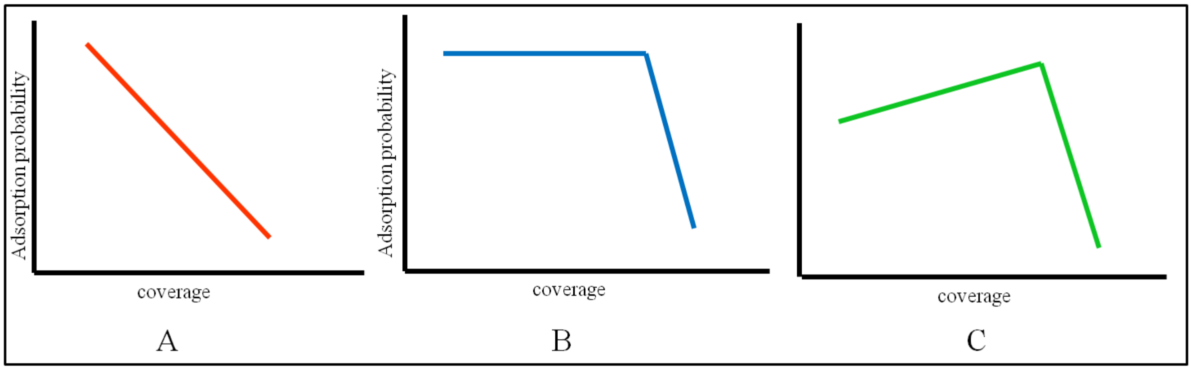

Figure 13. Schematic showing the coverage dependent adsorption probability curves depicting the A) Langmuirian, B) Kisliuk, and C) adsorbate-assisted adsorption. The coverage is expressed in monolayers (ML).

2.8.3. Adsorbate-assisted adsorption model

In this model, the incident gas molecules stick more efficiently to the pre-adsorbed molecules than to the vacant sites. As a result, the initial adsorption probability increases with an increase in surface coverage, but eventually drops to zero when the adsorption approaches saturation, as illustrated in Figure 13C. This phenomenon is usually seen where the incident molecules have a better mass-match with the pre-adsorbed molecules, which leads to efficient energy transfer between them. This adsorbate-assisted adsorption is more significant at high impact energies of impinging gas molecules, but less significant at high surface temperatures.

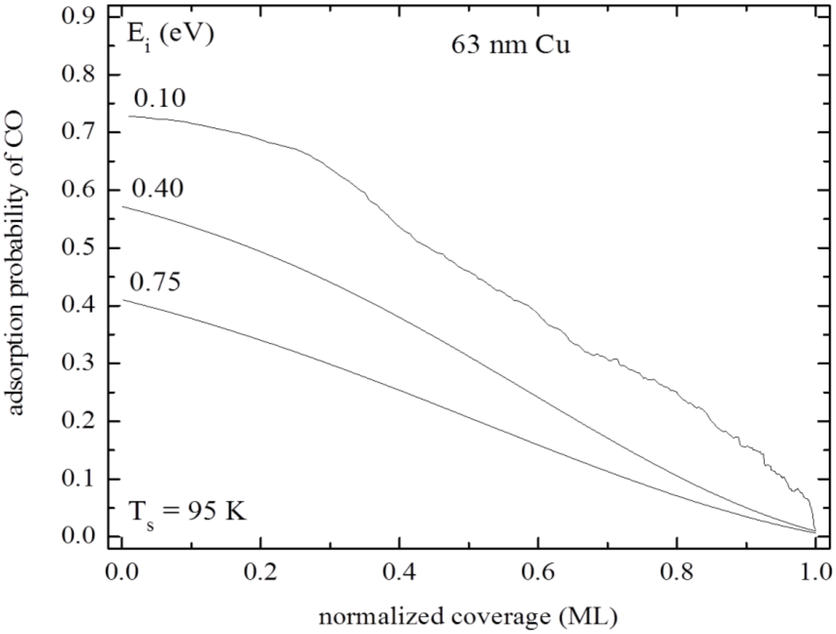

Figure 14. A set of coverage dependent adsorption probability, S(Θ) curves at different impact energies (E_i) for CO adsorption on 63 nm Cu clusters supported on silica. The coverage of CO is expressed in monolayers (ML).

As an example, the coverage dependent adsorption probability of CO on 63 nm Cu clusters is shown in Figure 14 to illustrate the presence of Langmuirian and Kisluik adsorption models. At low E_i, S(Θ) obeys the traditional Kisliuk shape, as S(Θ) remains the same up to the saturation coverage of the catalyst and eventually drops to zero. This type of curve shape indicates the effect of precursor states, as expected from the capture zone model. Alternatively, for large E_i, $S(\Theta)$ decreases about linearly with Θ, resulting in Langmuirian-like adsorption dynamics. This cross-over from precursor-mediated Kisliuk-like dynamics to direct Langmuirian-like dynamics is commonly also seen for CO on planar catalysts which simply reflect the decrease in the trapping probability in the precursor state with increasing E_i.

2.9. Capture zone model

The concept of capture zone model (CZM) is typically used to model the kinetic effects in supported cluster systems. This model has been applied by Rumpf, et al., and others in their respective studies.[78-79] In supported cluster systems, beam scattering experiments are conducted at an adsorption temperature where the coverage of the probe molecule on the support is negligible. Nevertheless, even in that case, the lifetime of the probe molecule on the surface can be sufficiently long enough allowing diffusion of the gas-phase species from the support to the metal deposits. Therefore, four different adsorption/desorption pathways are considered in supported cluster systems as shown in Figure 15: 1) thermal desorption from the deposits and/or the support, 2) direct adsorption on the metal deposits and/or the supports, 3) trapping of the adsorbates on the support and subsequent diffusion to the deposits, and 4) trapping of the adsorbates on the deposits and subsequent diffusion to the support. The diffusion zone is called the capture zone. The size of the capture zone decreases with the increase of surface temperature due to decrease of the surface residence and diffusion lifetime.

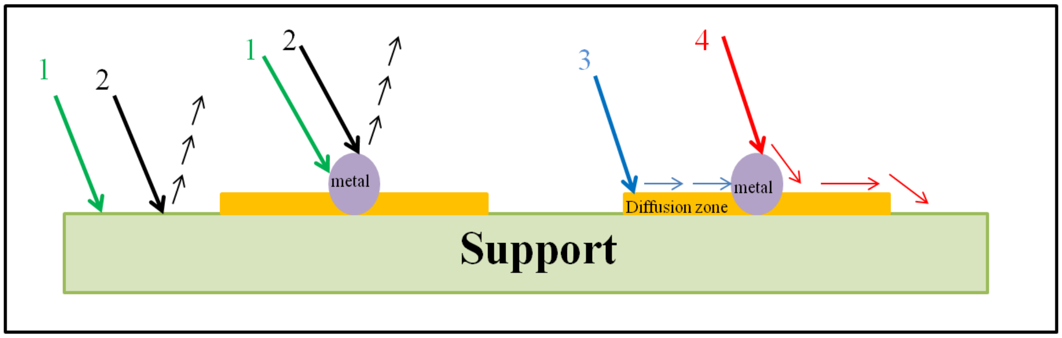

Figure 15. Schematic showing adsorption/desorption pathways in supported cluster systems.

2.10. Auger electron spectroscopy

Auger electron spectroscopy (AES) is one of the most widely used analytical techniques for obtaining information on the chemical composition of solid surfaces. This technique offers advantages such as: its high sensitivity for chemical analysis, its high-spatial resolution, a rapid data acquisition speed, and its ability to detect all elements above helium. The Auger phenomenon was first seen in 1925 by Pierre Auger.[1] An Auger transition can be excited by the bombardment of electrons, photons, and ion. Typically, the primary electron bombardment at energies in the range of 3000-5000 eV is used for surface analysis. The Auger electrons emitted from the surface form small peaks in the total energy distribution function, N(E), as shown in Figure 17A. The incident electrons striking a solid material are scattered both elastically and inelastically. The elastically scattered electrons can give the crystal structure information for a crystalline material, which is explained in the low energy electron diffraction (LEED) section. The peaks due to Auger electrons are superimposed on a sloping background caused by the secondary electrons. These peaks become more distinct by electronic spectral differentiation which removes the large sloping background as shown in Figure 17B.

In the Auger process as shown in Figure 16, an incident electron with high energy displaces an electron in a low-lying energy level, such as the K shell, in the atom, leaving a hole which results in a very unstable ionized species. In order to relax, an electron from a higher lying electron in either the core shell or valence shell drops down to fill the hole created in the orbital. Therefore, energy is released, which is taken up by another electron in another energy level and gets ejected as shown in Figure 16 or can be released as X-rays. The emitted electron with energy $E = E_K - E_{L1} - E_{L2} - \Phi$ is called an Auger electron where Φ is the work function of the surface. The electron must overcome this work function to get ejected into the vacuum. This Auger transition is labeled as a KL_1L_2 transition because the Auger electron energy is a characteristic of these three energy levels involved and hence of the element from which it is produced. The Auger electron energies are characteristic of the target material and independent of the incident beam energy.

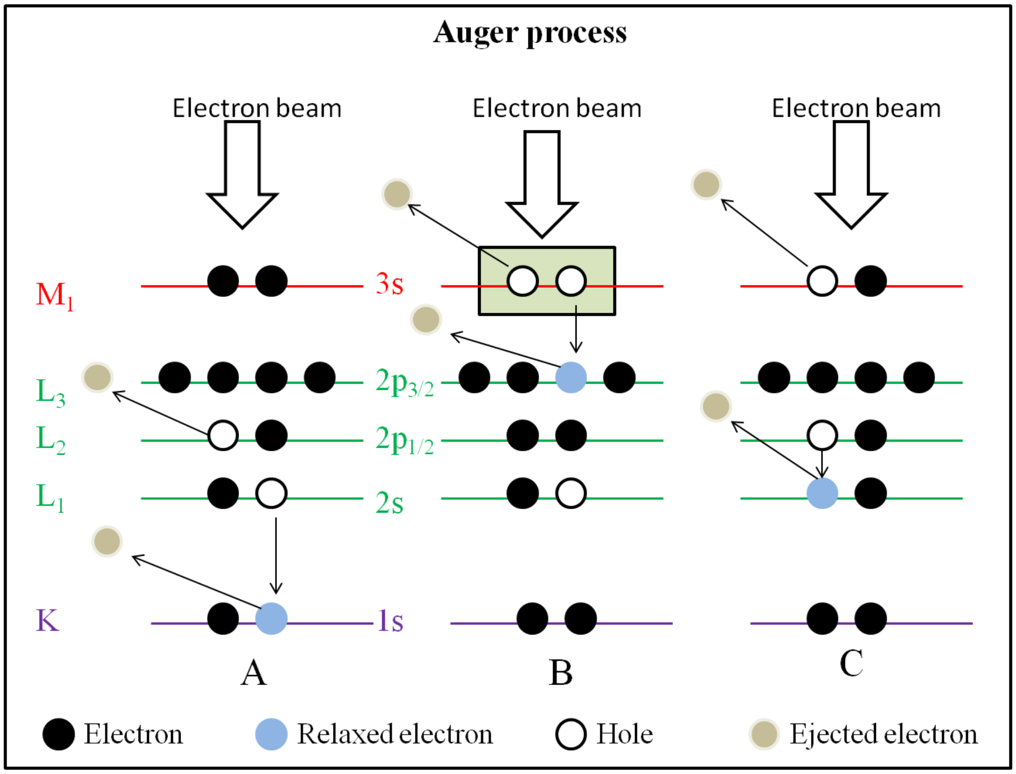

Figure 16. Schematic illustrating the Auger transitions involving A) three core levels, B) a core level and the valence band, and C) Coster-Kronig transition.

Figure 17 shows a typical Auger spectrum of as-received Cu clusters supported on silica, plotted as count rate N(E) against the electron energy. The sloping background in the Auger spectrum is because of the secondary electron background. The desired Auger peaks are superimposed on the secondary electron background and appear as sharp peaks. The signal is differentiated to minimize such secondary electron background leading to an observation of pronounced peaks.

The Auger spectrum in Figure 17 carries significant information about the target material. Auger peak positions provide qualitative information about the elemental composition in the solid surface and near surface region by comparing it with reference spectra. The peak height in the Auger peak is directly proportional to the atomic concentration of the particular element, which can be used to get quantitative information about surface concentrations.

Similarly, chemical state information can be obtained from Auger peaks that arise from transitions involving the valence electron states. Another common use of AES is in the analysis of depth profile. The mean escape depth for Auger electrons is in the order of 1 nm.[80] The sputtering process can be used where the surface is bombarded with ions to remove material slowly from the surface. Then, Auger spectra are recorded repeatedly to determine the way in which the concentrations of the several elements present on the surface change with depth. This process is repeated several times and the peak-to-peak height of the derivative feature (Auger yield) for each element is plotted against ion bombardment time. This plot can give information about the depth profile below the original surface. In addition, AES can be used to perform non-destructive angular resolved analysis for layers of thickness ≤ 2-3 nm. This process involves the measurement of Auger intensity as a function of the emission angle (θ) of the Auger electrons with respect to the surface normal.

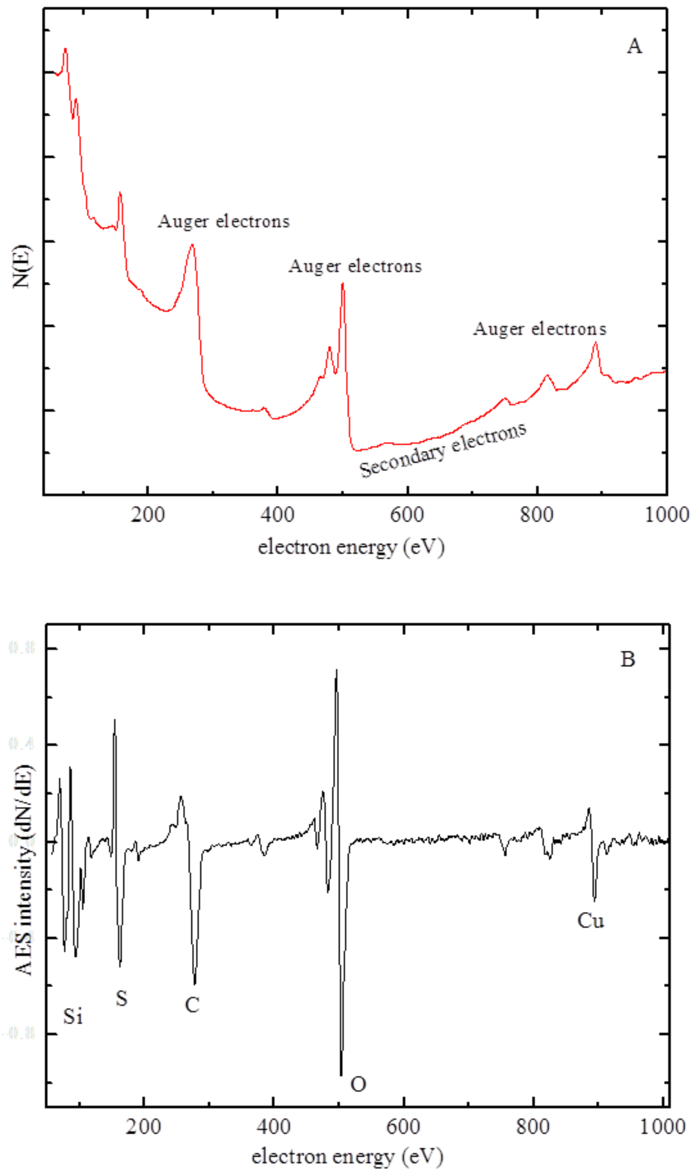

Figure 17. Auger spectra of as received Cu clusters supported on silica: A) plot of N(E) as a function of energy and B) plot of dN(E)/dE as a function of energy. N(E) represents the number of electrons that possess an energy E.

All the projects covered in this dissertation utilize AES for surface analysis. The morphology and cleanliness of supported Cu and Mo clusters, CaO, MgO, and Sb single crystal, and selenium foil were characterized by AES. The electron energy for AES amounted typically to 2 keV with a modulation voltage of 2 eV for all the samples studied in this dissertation.

2.11. X-ray photoelectron spectroscopy

X-ray photoelectron spectroscopy (XPS), also known as electron spectroscopy for chemical analysis (ESCA), is a surface analytical technique commonly used to investigate the chemical composition and electronic state of the surface region of a sample. XPS was developed in the mid-1960s by Kai Siegbahn and his research group at the University of Uppsala, Sweden. Kai Siegbahn was awarded the Nobel Prize in 1981 for his contributions.[1] The XPS technique works under the principle of the photoelectric effect.

In XPS, an incident photon of energy hν (h is Planck's constant, and ν is the photon frequency) is absorbed by an atom in a solid, a photoelectron is emitted and the kinetic energy of the photoelectron is related to the energy of the photon. A photon must have energy in excess of the binding energy of an electron for ionization and the emission of a core electron. The number of photoelectrons emitted will be proportional to the intensity of incident light. The kinetic energy of the photoelectrons will be independent of light intensity, but linearly proportional to the frequency of the incident photons. Time between excitation and emission is extremely small (10^{-16} s). The absorption of an incident photon of energy hν causes the emission of an electron having an energy given by:

$$E_b = h\nu - E_{kin} \tag{2.16}$$

where E_{kin} is the kinetic energy of the photoelectrons and E_b is the binding energy of the electronic level excited by the absorption of the photon. The binding energy is referenced to the vacuum level, the photoemission peaks of gold are conventionally used as a standard to calibrate the energy scale, and Φ is the work function for spectrometer.

The photoemission process is illustrated in Figure 18. Here an atom in a n-electron initial state is considered. The incident x-ray photon causes photoemission with a total energy transferred to a core-level electron.

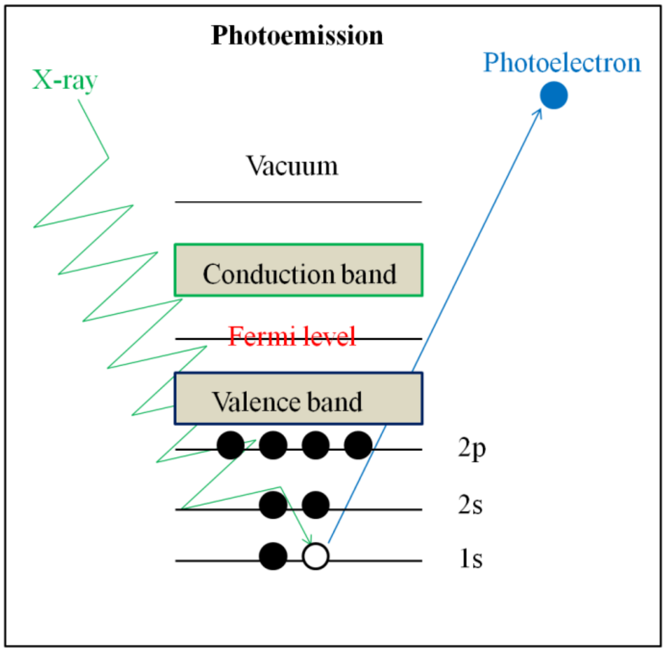

Figure 18. Schematic showing the photoemission process with the bombardment of X-ray.

The binding energy of an electron is equal to the energy difference between initial (i) and final (f) states of the atom which is given by:

$$E_b = E_f(n - 1) - E_i(n) \tag{2.17}$$

where $E_f(n - 1)$ is the final state energy, and $E_i(n)$ is the initial state energy. E_B will be equal to the negative orbital energy ($-\varepsilon_k$) for the ejected photoelectron if there is no electronic rearrangement after photoemission. This approximation is known as Koopmans' theorem and is written as:

$$E_b = -\varepsilon_k \tag{2.18}$$

Usually, ε_k values are within 10-30 eV of the E_b values and are calculated by the Hartree-Fock method. However, the other electrons in the sample will undergo rearrangement to minimize the energy of the ionized atom. Such energy reduction is called the 'relaxation energy.' Relaxation is a final state effect which can occur in two ways: atomic relaxation or extra-atomic relaxation. A more accurate expression of the binding energy is given by considering relaxation, electron correlation, and relativistic effects and is written as:

$$E_b = - \varepsilon_k - \delta\varepsilon_{relax} + \delta\varepsilon_{rel} + \delta\varepsilon_{corr} \qquad (2.19)$$

where $\delta\varepsilon_{relax}$, $\delta\varepsilon_{rel}$, and $\delta\varepsilon_{corr}$ are correction factors for relaxation, relativistic effect, and electron correlation, respectively.

Metals are electrically conducting materials and are electrically contacted with the spectrometer and grounded which is shown in Figure 19. In metals, the Fermi levels (E_f) of the sample and the spectrometer will be aligned ($E_f^s = E_f^{sp}$) so that the binding energy (E_b) is referenced with respect to E_f. There exists a minimum energy required to knock out an electron from the highest occupied level into a vacuum which is called work function (Φ_s) and is written as:

$$\Phi_s = E_f - E_{vac} \qquad (2.20)$$

where E_{vac} is the vacuum level. Therefore we can write:

$$E_b^f = h\upsilon - KE - \Phi_{sp} \qquad (2.21)$$

where E_b^f means E_b is referenced with respect to E_f. The measurement of E_b is independent of material work function (Φ_s) but dependent on the spectrometer work function (Φ_{sp}).

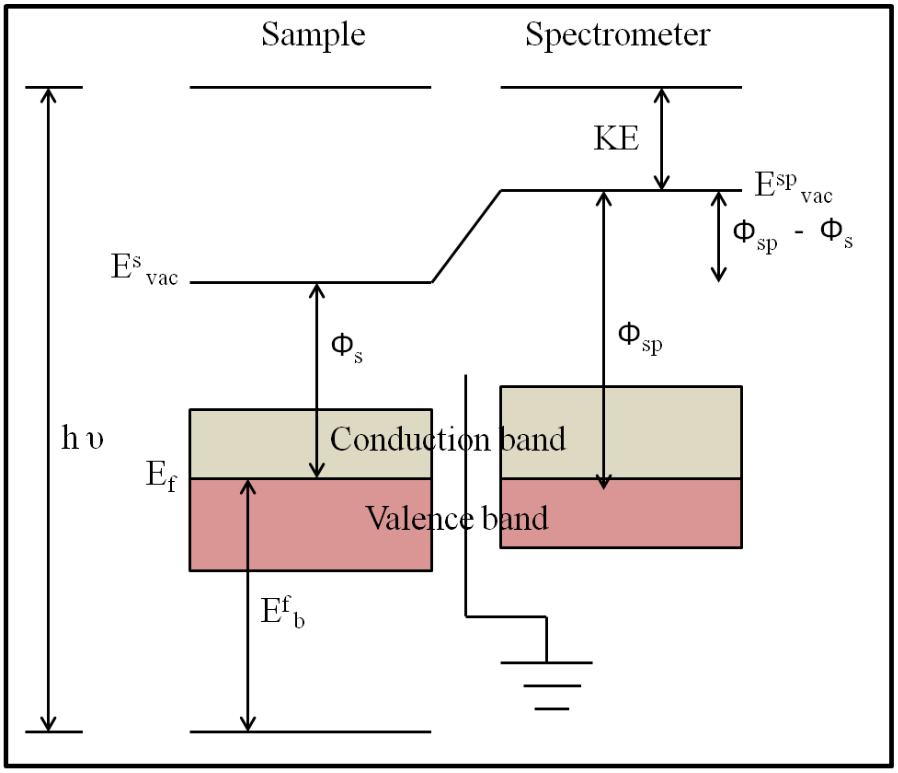

Figure 19. The energy level diagram for an electrically conducting sample that is grounded to the spectrometer where E_f is the Fermi level, E_{vac}^{s} and E_{vac}^{sp} are the vacuum levels of the sample and the spectrometer respectively, ϕ_s and ϕ_{sp} are the work functions of the sample and the spectrometer respectively; E_b^f is the binding energy (E_b) referenced with respect to E_f, hυ is the energy of the excitation x-ray photon, and KE is the kinetic energy of the emitted photoelectron.

On the other hand, insulators are materials with low electrical conductivity which cannot be electrically contacted with the spectrometer. These materials acquire a positive charge after the emission of photoelectrons. This positive charge can be compensated by an external source of monoenergetic electrons from a flood gun. Ultimately, the vacuum level of the sample (E_{vac}^{s}) and the energy of the charge neutralization electrons (Φ_e) are aligned as shown in Figure 20 and the binding energy (E_b) is referenced with respect to Φ_e. Here, the measured E_b depends on the sample work function (Φ_s) and the energy of the charge neutralization electrons (Φ_e) and can be written as:

$$E_b^{vac} = E_b^f + \Phi_s = h\nu - KE + \phi_e \quad (2.22)$$

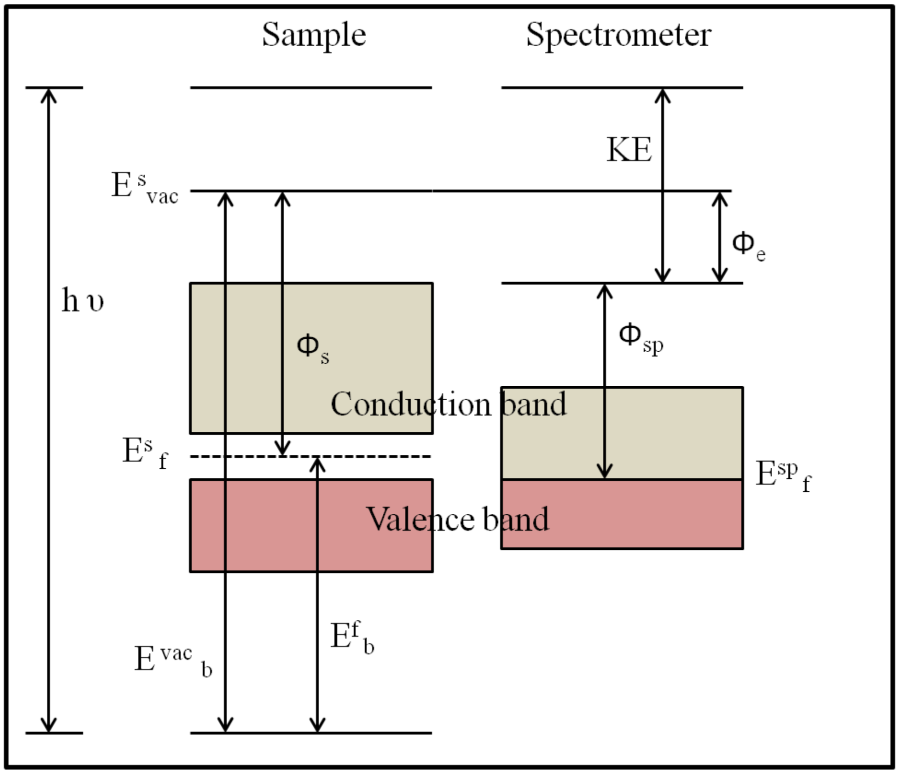

Figure 20. The energy level diagram for an electrically insulated sample from the spectrometer with E_f^s and E_f^{sp} are the Fermi levels of the sample and the spectrometer respectively, E_{vac}^s is the vacuum level of the sample;,ϕ_s and ϕ_{sp} are the work functions of the sample and the spectrometer respectively, ϕ_e is the energy of charge neutralization electron, E_b^{vac} is the binding energy (E_b) referenced with respect to E_{vac}, E_b^f is the binding energy (E_b) referenced with respect to E_f, hυ is the energy of the excitation x-ray photon, and KE is the kinetic energy of the emitted photoelectron.

In fact, it is difficult or almost impossible to measure accurate values of E_b for insulators, as it is referenced to E_{vac} and ϕ_e. An internal reference is typically used to accurately determine the value of E_b.

For the orbitals with l > 0 (p, d, or f), two energetically equivalent final states, 'spin up' or 'spin down', are possible after photoemission which leads to a coupling between the magnetic fields of spin (s) and angular momentum (l). This coupling can split the degenerate state into two components. This process is called spin-orbit coupling. Spin-orbit coupling often results in the splitting of photoemission peaks into sub-peaks.

A survey scan spectrum of 12nm Cu clusters supported on silica is shown in Figure 21. The intensity in counts of photoelectrons is plotted against the binding energy. Half of the projects covered in this dissertation utilize XPS for chemical composition and electronic state analysis. Mg-K_α is used as a primary source for the generation of X-ray photons.

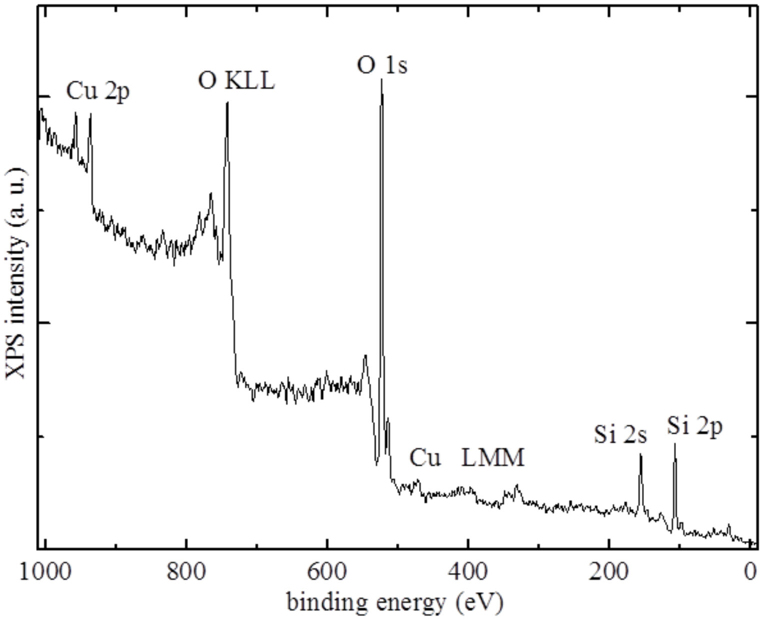

Figure 21. XPS spectrum of clean 12nm Cu clusters supported on silica. XPS peaks of O, Si, and Cu are observed. AES peaks (KLL) of O are also observed.

In this dissertation, the Mg Kα line (at 1253.6 eV) was used with a pass-energy of 100 eV (survey spectrum) and 50 eV (individual peaks) of the analyzer for XPS. XPS analysis is typically performed by first collecting a survey scan spectrum with a binding energy range of 0-100 eV. Later, high-resolution spectra of specific features observed in the survey scan spectrum are collected.

2.12. X-ray diffraction

X-ray diffraction (XRD) is one of the successful methods capable of revealing the structure of crystals. The X-ray was first discovered in 1895 by M.K.Roentgen during one of his experiments, but the nature of X-rays was not known at that time. Later in 1912, Max Von Laue came up with the crucial finding during his X-ray diffraction experiment where he considered x-ray as both electromagnetic wave as well as particle like theory. And this discovery of the X-ray was recognized with the first Nobel Prize in physics to Max Von Laue. Moreover, the importance of structural determination, measurement of the spacings between layers of atoms, identification of the orientation of a crystal, measurement of the size, shape, and internal stress of crystalline materials has led to the conclusion that X-rays are actually electromagnetic waves as pointed out by Braggs (father and son).[81] Since X-rays discovery, science has taken a easy route to determine crystal structure of an unknown material and has brought about revolution in medical treatment.

To understand X-ray diffraction it is convenient to consider light as an electromagnetic wave with a wavelength related to the energy of the light given by the equation $E = hc/\lambda$, where h is Planck's constant, c is the velocity of light, and λ is the wavelength of light. X-ray lies between ultraviolet light and gamma radiation in the electromagnetic spectrum and has an approximate wavelength range of 0.1-100Å. The interference patterns formed in x-ray diffraction are produced by rapidly decelerating fast-moving electrons converting their energy of motion into a quantum of radiation. Electrons are accelerated by an electric field toward a metal target to generate X-rays as shown in Figure 22. Most of the electrons are not brought to a full stop by a single collision, rather undergo multiple collisions, and give rise to a continuum of radiation. The targets can be Cr, Fe, Co, Ni, Cu, Mo, Ag, W, and Al and the wavelengths of emitted X-rays depend on the energy of the electrons.

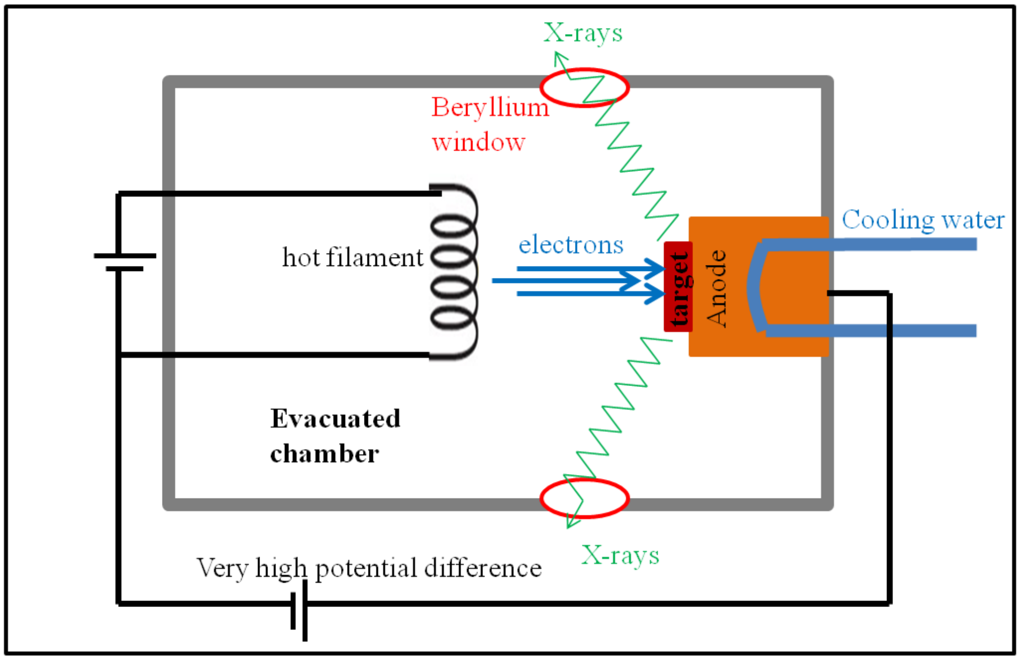

Figure 22. Schematic showing cross-section of X-ray tube.

The optimum wavelength of the characteristic radiation is determined by the accelerating voltage and is given by the formula:

$$\lambda_0 = \frac{1.24}{\mathrm{V}}\,(\mathrm{nm}) \qquad (2.23)$$

As the voltage increases, not only the peak intensity moves to shorter wavelength, more penetrating wavelengths, but also the total intensity increases even though the electron current remains the same. The characteristic radiation that originates from X-ray diffraction is directed against a crystalline solid to characterize the crystal properties. A crystalline solid is a collection of atoms, well definely packed together to form a crystal lattice. The simplest case would be the unit cell of a cubic structure because all of the edges of the cube are equal and the corners are perpendicular to each other. Now, let’s consider a cubic structure and draw imaginary planes through the nuclei. The incoming x-ray is now scattered by the electrons of each of these imaginary planes of atoms giving rise to a set of parallel partial mirrors which is called the "reflected beam." The relative phases of scattered x-rays depend on the angle of the incident x-ray and the separation distance between these imaginary planes. It is obvious that the x-rays that penetrate deeper travel more distance within the crystal lattice before they are reflected. As a result, the wave that is reflected by the imaginary second plane travels a distance of $2d\sin\Theta$. Constructive interference is produced only when the path length difference between reflected waves is an integer multiple of the wavelength (λ) and gives rise to Bragg's equation: $n\lambda=2d\sin\Theta$, where d is the space lattice and Θ is the Bragg's angle. The planes of atoms can be constructed in various ways by using Miller indices.

The Miller index is the combination of three numbers h, k, and l, one for each coordinate in three dimensional spaces. The diffraction pattern is obtained once Bragg's law is satisfied at the Bragg's angle. If Bragg's angle Θ is known for different diffraction lines, it is easy to find out the various d spacing values using Bragg's equation. Rewriting Bragg's equation, we get $\sin^2\Theta = \lambda^2/4d^2$ where $d = a/(h^2 + k^2 + l^2)$ for a given simple cubic crystal (a = lattice parameter). Now solving the above two equations we get,

$$\sin^2\Theta = \lambda^2 (h^2 + k^2 + l^2) /4a^2 \tag{2.24}$$

Powder diffraction is a scientific technique in which x-rays are directed toward the powder or microcrystalline samples to characterize the structural properties of the materials. Powder consists of a large number of crystallites with all possible orientations of the crystal. Finally, a plot of intensity as a function of the scattering angle (2Θ) is created which enables one to identify the arrangement of atoms within the unit cell and the distances between consecutive atoms.

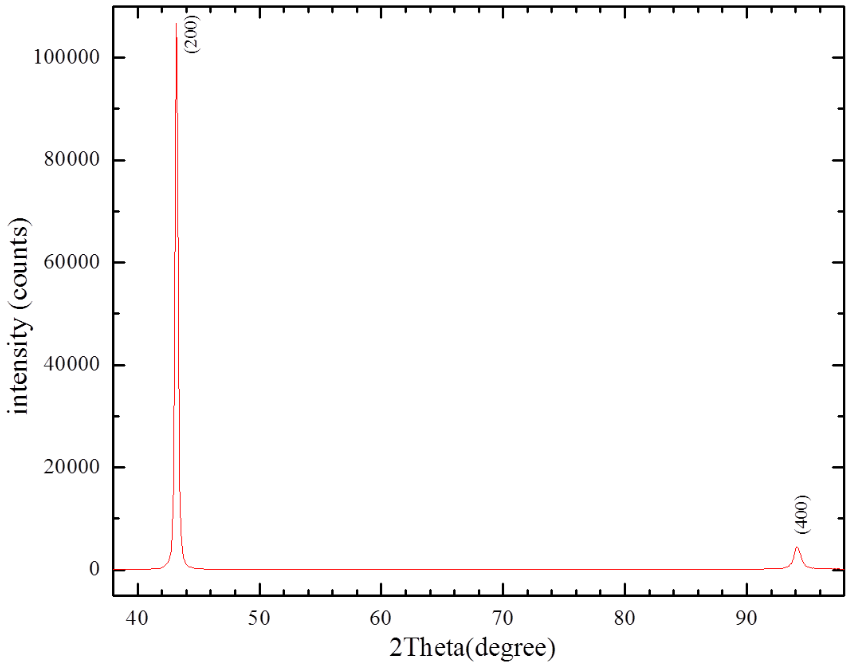

Figure 23. XRD of MgO(100). Miller indices represent planes of atoms.

An XRD spectrum of a single crystal of MgO(100) is shown in Figure 23. The diffracted intensity is plotted as a function of the scattering angle 2Θ. All the data in this dissertation were collected with a Panalytical X'Pert MPD system equipped with Cu Kα X-ray source (1.54060 Å). Only a few projects included in this dissertation, such as Selenium foil and MgO single crystal projects, utilize XRD for crystal structure analysis.

2.13. Low energy electron diffraction

Low energy electron diffraction (LEED) is the principal technique for the determination of the surface structure of crystalline materials. Davission and Germer, in 1927, observed diffraction pattern for the first time when they bombarded low-energy electrons at a crystalline nickel target.[1] However, LEED crystallography was in practice for surface analysis only after adequate vacuum techniques were developed in the early 1970s.

Certain conditions must be fulfilled to carry out the successful LEED experiment, such as the environment must be ultra high vacuum (pressure < 10^{-9} Torr) and the sample surface must be well-oriented, planar, and, importantly, clean. A LEED consists of three main parts enclosed in an UHV chamber: the electron gun to generate the collimated electron beam, the goniometer to hold and orient the sample and the detector to monitor the diffracted beams. A collimated beam of low energy at the range of 20-200 eV is bombarded on the surface and these electrons are very easily scattered, both elastically and inelastically, by atoms within the material. They get absorbed if they penetrate into a solid for more than four to five atomic layers. However, if they survive absorption in the first two or three atomic layers, they are back scattered out of the crystal and these diffracted electrons are observed on the fluorescent screen as spots. A simple schematic of LEED technique is shown in Figure 24.

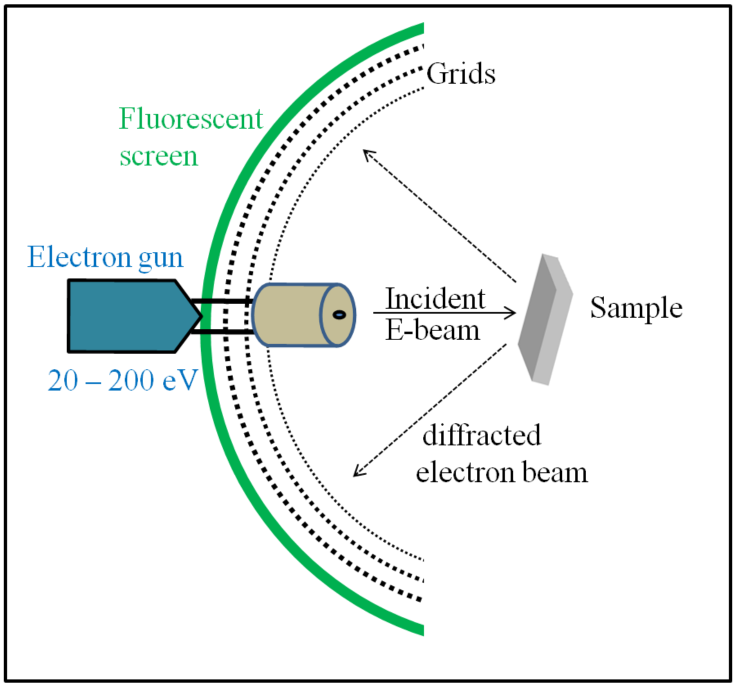

Figure 24. A schematic showing a LEED technique.

Typically, a number of diffracted beams of electrons with the same energy as the incident ones are backscattered. The analysis of the spot positions qualitatively yields information on the symmetry, size, and rotational alignment of the adsorbate unit cell with respect to the support unit cell. For the quantitative purpose, the intensities of diffracted electron beams can be recorded as a function of the incident electron beam energy to generate so-called I-V curves. These curves are compared with theoretical curves which can provide precise information on atomic positions within the solid surface. The brightness of the LEED spots is proportional to the intensities of the corresponding diffracted beams which can be monitored using a suitable brightness-measuring external detector. A hexagonal LEED pattern of a Sb(111) single crystal as an example is shown in Figure 25.

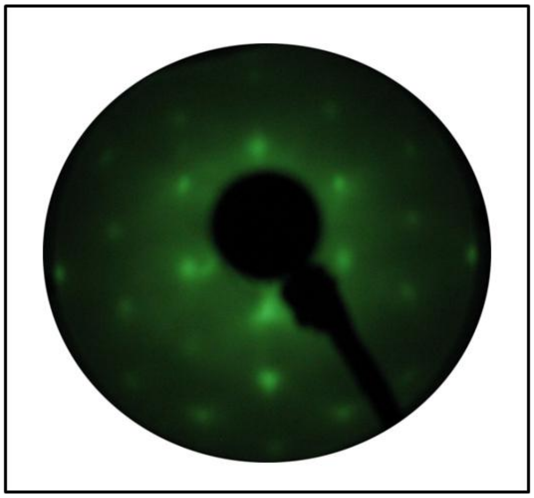

Figure 25. LEED pattern for clean Sb(111) surface showing hexagonal pattern.

The LEED pattern contains valuable information about the symmetry and the periodicities of surface structures, and about the atomic arrangements in such structures. In this dissertation, LEED patterns for Sb (111) and MgO (100) single crystalsare included to reveal the atomic arrangements in surface structures.

2.14. Scanning electron microscopy

A scanning electron microscope (SEM) is one of the most advanced electron microscopes that produces images of solid specimens by scanning over it with a focused beam of high energy electrons. The signals that arise from electron-sample interactions reveal information about the specimens' topography, chemical composition, morphology, crystalline structure, and orientation of materials making up the sample. In a SEM, electrons with a certain kinetic energy coming out of the cathode are directed towards the sample with the use of electromagnetic lenses and apertures. The electron-specimen interactions produce signals when the incident electrons are decelerated by the sample. These signals could be secondary electrons, backscattered electrons, Auger electrons, characteristic X-rays, transmitted electrons, elastically scattered electrons, and inelastically scattered electrons as shown in Figure 26.

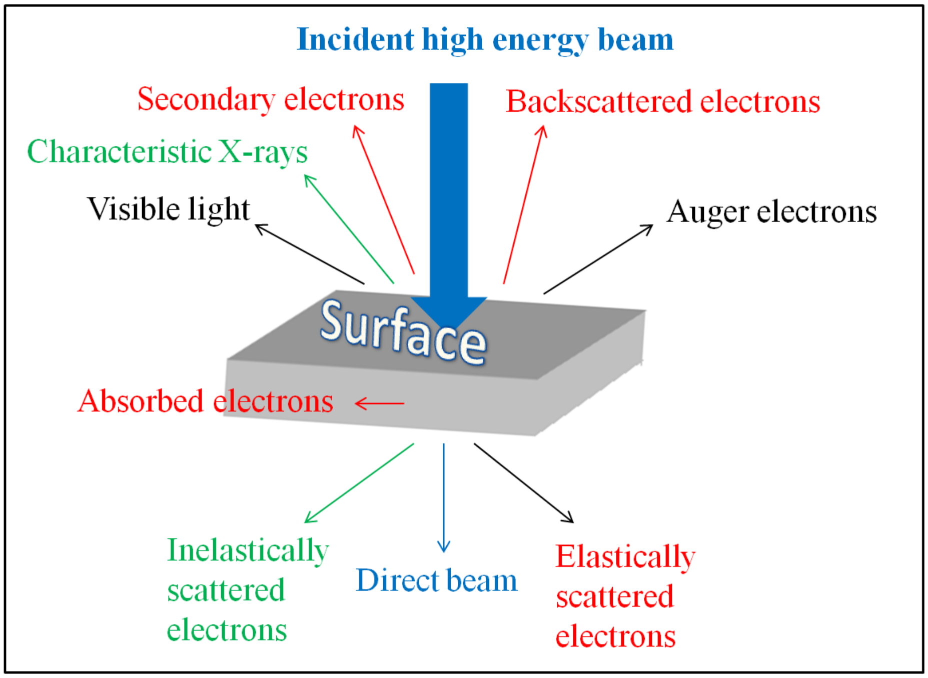

Figure 26. Signals produced after high energy electron beam strikes on a surface.

The signals produced primarily by the secondary electrons and backscattered electrons are used to obtain SEM images. Secondary electrons determine the topography and morphology of the specimen whereas backscattered electrons generate the contrast in SEM images. The main application of SEM is to generate high resolution images of the specimens and to reveal spatial variations in chemical compositions. The quality of the images can be improved by making adjustments to the accelerating voltage, working distance, and aperture size. Precise measurement of even small features and objects down to 10-50 nm in size is also accomplished using the SEM. Usually SEM is interconnected with energy dispersive X-ray spectroscopy (EDX or EDS) which is used to analyze the chemical composition of the specimen.

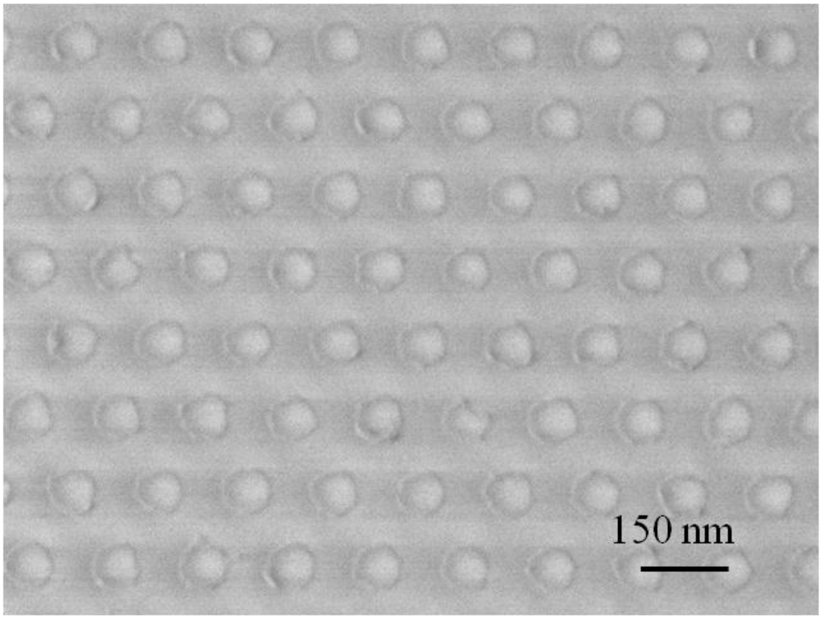

Figure 27. SEM image of 77 nm Mo clusters on silica support.

A SEM image of 77 nm Mo clusters on a silica support is shown in Figure 27. These clusters were fabricated by EBL with a lattice constant of 150 nm. In this dissertation, the copper and molybdenum nanoclusters projects include SEM images to characterize the samples' morphology.

2.15. Electron beam lithography

Electron beam lithography is a modern nanofabrication technique in which a focused beam of electrons is used to draw a custom pattern for the fabrication of desired clusters with sub-10 nm resolution. This technique allows the nanofabrication of supported clusters with predetermined morphology such as cluster size, shape, rim length, and height. Nanofabrication is a technique of building up new materials of tiny size which behave differently than their bulk or macroscopic counterparts. In fact, nanofabrication has an ability to fabricate these tiny materials and manipulate its structures to characterize their performance. Among different techniques of nanofabrication, electron beam lithography is one of the most fundamental techniques used to fabricate devices at the nanometer scale. Lithography is a process of transferring pattern from one medium to another medium by subsequent steps. The process involves exposure of the sensitive material, development of the resist, and finally pattern transfer. In the last few decades, different forms of particles beams like light beams, electron beams, and ion beams have been used in lithography. Using electrons as a source has the advantage of having high resolution and limited diffraction unlike photolithography. Also, it has versatile pattern formation due to the successive development of different components and elements in the system.

The nanostructures developed utilizing EBL have applications in several fields such as engineering, catalysis, surface science, and material science. EBL could be coupled with other techniques like chemical vapor deposition and electrochemical deposition to develop different nanostructures such as nanowires, nanopillars, nanofluidic channels, gratings, and nanopatterning with potential industrial applications.[82-84] Semiconductor nanowires developed by EBL have attracted most of the industries for their potential use in high-density electronics. Similarly, nanowires could be used as sensors due to their smallest possible size being extremely sensitive to the current transport. The nanofluidic channels patterned through EBL have been considered as well established nanostructure for genetic sequencing, tissue engineering, and drug discovery. These channels have the capability to manipulate and analyze the biomolecules such as DNA and proteins at a single molecule resolution. The nanopattern is one of the suitable methods to study quantum confinement effects. Due to these diverse applications, this technique is gaining more and more attention for nanofabrication.

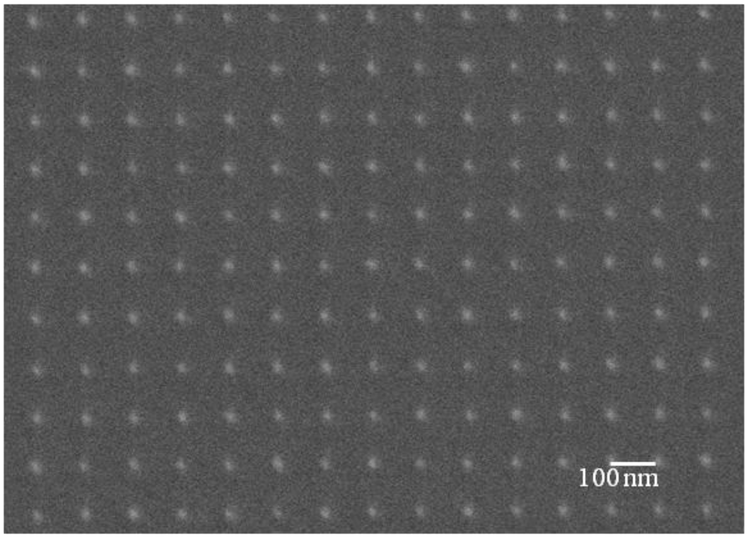

Figure 28. 12 nm Cu clusters on silica support fabricated by EBL method. A uniform nano-array pattern is shown.

A SEM image of EBL-fabricated 12 nm Cu clusters on silica support is shown in Figure 28. These clusters were fabricated by using EBL method. The copper and molybdenum nanoclusters studied in this dissertation are fabricated utilizing electron beam lithography at Molecular Foundry in Lawrence Berkeley National Laboratory.

CHAPTER 3. IDENTIFYING ACTIVE SITES IN HETEROGENEOUS CATALYSIS

This chapter includes the study of CO and CO_2 adsorption kinetics and dynamics on the surface of methanol synthesis model catalysts. This project characterizes the catalytic activity of EBL-fabricated Cu nanoclusters of different sizes on a silica support towards the adsorption of CO and CO_2. Taking advantage of the unique feature of EBL samples, the active sites of a methanol synthesis model catalyst are identified with simple surface science techniques. In addition, cluster size effects on adsorption of CO molecules are also studied. An introduction to the significance of electron beam lithography along with a brief literature survey about CO and CO_2 interactions with several metal or metal oxide catalysts are also presented. Similarly, the importance of identifying active sites in chemical transformations is mentioned in this chapter.

3.1. Introduction

The use of nanoparticles for promoting catalytic processes has been the major focus of attention for several decades. The effects of the size, rim, shape, and the chemical composition of metal clusters on their catalytic activity are the major topic of research currently under investigation.[85] The supported cluster systems, referred to as model or inverse model catalysts, are typically considered as more realistic models of technical catalysts compare to single crystals and polycrystalline films, which can still be handled experimentally and theoretically. In early days, rather simple techniques, such as physical vapor deposition (PVD) in an ultra-high vacuum (UHV) environment, were utilized to fabricate model catalysts with little or no control over the morphology. As a result, sophisticated and time consuming morphology characterization was required. But today in surface science and catalysis, more and more emphasis is placed on utilizing nanofabrication techniques in order to gain better a priori control over morphology and composition at the atomic level. One interesting approach for model studies is employing electron beam lithography (EBL).[86-87] EBL is utilized to nano-fabricate nearly mono-disperse cluster samples, forming a regular pattern on a substrate, and these samples are called model nano array catalysts.[19,21,87-89] These model-nano-array samples, consisting of reasonably small cluster sizes, can now be fabricated at various research facilities within a reasonable processing time (<12 h) over a macroscopic area of at least a few mm^2.[90] EBL allows the fabrication of nano-clusters with predetermined cluster size, shape, rim length, and height. Therefore, with EBL, a time consuming characterization of the sample's morphology can be avoided, nevertheless, the samples studied in this project have been inspected by scanning electron microscopy (SEM). Moreover, spectroscopic tools such as Auger electron spectroscopy (AES) and x-ray photoelectron spectroscopy (XPS) were used for sample characterization. Although the smallest size of the clusters which can be made by EBL over a macroscopic surface is still technically limited, cluster size effects can be studied in a unique way by utilizing EBL.

The identification of active sites in chemical transformations is a major topic in disciplines such as anti-cancer drug synthesis and heterogeneous catalysis because the knowledge about the active sites allows for the development of structure-activity relationships (SAR). SAR rules can pave the way for system optimizations while gaining a mechanistic understanding of catalytic processes at the molecular level.[91] It should be noted that the concept of active sites in heterogeneous catalysis was explicitly introduced back in Langmuir's days around 1925.[92] However, clear identification of the catalytically active sites on a solid catalyst surface still remains scientifically challenging. Very few unambiguous examples of determining active sites based on sophisticated microscopic techniques exist in the literature.[93-94] On contrary to these microscopic techniques, a novel kinetics technique is presented in this study which could easily be applied to diverse systems. Model catalysts have been extensively studied where desired nano-size clusters are deposited on particular supports. These cluster systems serve as models for industrial or real-world catalysts. One proposal claimed that the rim along these clusters is catalytically active site whereas the terrace site along the top surface of the clusters is catalytically less reactive. This idea was detailed in the discussion concerning the formation of minute Schottky junctions at the interface between metals and oxides and their correlation with catalytic activity in the case of methanol synthesis model systems.[95] However, a clear experimental proof is still a matter of debate for most systems as far as we are aware from the literature. In this study, experimental evidence is presented based on a kinetics technique for catalytically active rim sites along Cu cluster samples, which serve as methanol synthesis model catalysts.

Silica is typically used as a support to grow nanostructures. SiO_2 supported catalysts are commonly used in reactions such as methanol steam reforming[96] and hydrogenation reactions.[97] There are few scientifically interesting complications for copper clusters due to the fact that different oxides (Cu, CuO, and Cu_2O moieties) exist even at ultra high vacuum conditions. However, different oxides have been characterized both before and after each kinetics/dynamics experiment by means of XPS and AES peak analysis in this study. Thus, the chemical state of the Cu clusters has been well-documented, which allows one to compare directly the chemical activity of metallic-like and oxide-like Cu clusters. It is a well known fact that the electronic structure of clusters affects kinetics and dynamics properties.[98-99] The dynamics study provides a better insight to mechanistic aspects of gas-surface interactions with Cu clusters. Besides, Cu as a catalyst, being readily available and cheap, has many applications including methanol synthesis,[6,100] water splitting catalysis under visible light irradiation,[101] water-gas shift reactions,[102] and low temperature CO oxidation.[103] Similarly, it has applications in materials science including surface plasmon resonance,[104] solar cells,[105] and high-T_c superconductors.[106] In this study, CO and CO_2, which are considered as the simplest probe molecules, are used as the adsorbate due to its importance for a number of practical catalytic processes (environmental, alternative fuels, etc.).[107] The gas-to-surface energy transfer processes (adsorption dynamics) were characterized using molecular beam scattering techniques. This beam scattering technique is particularly useful for the study of small clusters with a large dispersion (small total coverage) for the reasons that the beam can be directly focused onto the surface which can avoid any sample holder effects and keep the background pressure low.

3.2. Brief literature survey

The copper system has a variety of applications due to its importance in the field of heterogeneous catalysis. A brief literature survey reveals that the Cu cluster literature is dominated by studies on various Cu nanoparticle powders, synthesized by a variety of "wet chemistry"/electrochemistry techniques.[104,108-110] Most investigations on powder samples focus on surface reactions; however, kinetics/dynamics adsorption studies of small molecules on these systems at UHV conditions are rare. These supported powders are typically characterized by XRD, XPS, SEM, and infrared spectroscopy (IR). The traditional Blyholder model for CO adsorption on metal surfaces has to be modified for metal oxides.[111] It is evident from the TDS data of CO on $Cu_2O(100)$ that the differences in the electronic structure lead to larger binding energies.[112] CO adsorbs/desorbs molecularly on Cu metal oxide single crystals without CO_2 formation.[112] However, CO_2 formation has been detected for silica supported Cu_2O nanoparticles powder[108] and copper single crystals.[113]

In contrast to CO that chemisorbs on most metal surfaces, CO_2 physisorbs and interacts rather weakly with most metal surfaces. In addition, CO_2 dissociation at ultra-high vacuum

(UHV) was also reported for Ni and Fe surfaces. On silver, carbonates (CO_3^{ads}) are formed from CO_2 when coadsorbed with oxygen, whereas carbonate formation was never reported on copper. So far, molecular beam scattering experiments with CO_2 have only been conducted for Pt(111), Pd(111), Cu(110), and Ni(100).[114-117] For all of these systems except Ni(100), non-dissociative and non-activated molecular adsorption was observed. Also, at large impact energies, E_i, of CO_2 and low adsorption temperatures, T_s, the adsorption dynamics were dominated by the effect of an extrinsic (trapping above occupied sites) precursor state. The binding energy of CO_2 on metal oxides is typically much greater than on metals. In this regard, the effect of defects is widely discussed; i.e., CO_2 is trapped on oxygen vacancy sites of metal oxide surfaces.[118-119] CO_2 beam scattering on PVD Cu clusters supported on ZnO has been studied previously by our group.[43,120-121]

The so-called capture zone model (CZM) is considered to explain the dependence of S_0 on cluster size of the nanoparticles. The size of the capture zone is given by the ratio of the lifetime of the adsorbates on the support or in the precursor state to the diffusion (hopping) time. In some cases, depending on the binding energies, the size of the capture zone can be significant, even at larger surface temperatures.[78-79,121] The adsorption dynamics of CO and CO_2 have been studied in detail on Cu/ZnO and copper single crystal systems.[116,121-123] Surface chemistry studies utilizing a molecular beam scattering technique on Cu (oxide) cluster systems are rarely available in the literature. In addition, the concept of utilizing electron beam lithography (EBL) has still not been applied very often.[19,21,87-89]

3.3. Sample fabrication

The nanofabrication of Cu clusters was conducted at the Molecular Foundry in the Lawrence Berkeley National Laboratory. Detailed nanofabrication procedures of the EBL samples are described elsewhere.[19] Cu clusters with diameters of $d_s = 11.9 \pm 0.3$ nm, $d_m = 35 \pm 2.6$ nm, and $d_l = 63 \pm 2$ nm were made (suffixes s, m, l refer to small, medium, and large size). Their lattice constants amounted to $a_s = (100 \pm 1)$ nm (square), $a_m = (100 \pm 2)$ nm (hexagon), and $a_l = (150 \pm 4)$ nm (square). A $h = (5 \pm 2)$ nm thick Cu layer was used in the fabrication process and a 5 by 5 mm area on a 10 by 10 mm silica support was covered with the Cu clusters. SEM images have been collected with a Zeiss Ultra 60 equipped with a field emission gun (shown in Figure 29). The FESEM has a nominal resolution of ∼1.2 nm with 20 keV for the electron beam acceleration voltage.

3.4. Sample cleaning and its chemical state

The challenges in cleaning EBL samples without affecting morphology and/or the chemical composition have been discussed by Somorjai and Kasemo in their pioneering works.[87-88] The 12 nm and 63 nm Cu/SiO_2 model nano array catalysts used in this study were initially cleaned by annealing them in a flux of atomic hydrogen [$p(H_2) = 7\times10^{-8}$ mbar, $T_s = 480$ K] using a commercial thermal hydrogen doser. This cleaning procedure was used for previous projects of Au EBL clusters by our group.[19,124] As a result, carbon containing impurities are removed from the surface which is evident in the Auger spectrum in Figure 31. In some cases, sulfur impurities were present which could be removed by annealing the surface in 2×10^{-5} mbar of molecular oxygen at $T_s = 500$ K.

Metallic and oxidic-like Cu clusters were studied in this project. The CuO_x cluster samples were remarkably stable for weeks at UHV conditions judged by well reproducible XPS, AES, and beam scattering data. Oxidic-Cu was reduced to the metallic Cu by annealing the Cu/SiO_2 sample in the presence of molecular hydrogen at 420 K ($p(H_2) = 5\times10^{-5}$ mbar). At times, the chemical state of copper was monitored by XPS. The absence of oxide satellite features indicates elemental copper, which will be discussed in more detail later. Note that the samples were never annealed above 500 K to avoid sintering of the clusters as the bulk Tammann temperature of Cu amounts to 678 K.[125] Sintering effects were induced on purpose in one of our prior works on Au EBL samples.[126] In this case, EBL samples were annealed above 600 K and beam scattering data resulted in reduced adsorption probability of probe molecules on the surface. This means annealing temperatures play an important role in sintering of the samples, however, these effects have not been observed for the Cu clusters in this study.

3.5. Blind experiments

In the present study for the nanofabrication, silica is used as a support. It is necessary to confirm that the results obtained from the support do not interfere with the experimental results from the Cu/SiO_2 system. Therefore, blind experiments were collected on silica supports which underwent cleaning procedures identical to those employed for the EBL samples. The cleaning procedures of the nano model array catalysts may also affect the chemical composition of the support which was determined by AES and XPS before and after each beam scattering experiment. In addition, fully oxidized and partially reduced silica supports were studied. In both cases, no significant uptake of CO was seen in beam scattering experiments at the lowest surface temperature. More details are described below, and some blind data are depicted together with the data on the Cu clusters.

3.6. Results and discussion

The morphological characterization of EBL-fabricated silica-supported Cu clusters will be presented in this section, followed by a spectroscopic characterization of the chemical state of Cu clusters. Adsorption kinetics and dynamics of CO and CO_2 on Cu EBL samples will be presented in detail along with the identification of catalytically active sites on the samples' surface.

3.6.1. Sample morphology

The sample morphology of Cu clusters was studied by SEM. Figure 29A and 29C shows an image of 12 nm and 63 nm Cu clusters forming a predetermined square pattern, and the dots are separated by a_s = 100 nm and 150 nm respectively. Figure 29B and 29D show the size distribution of 63 nm and 12 nm clusters, respectively, obtained by analyzing a 1.4 μm by 1 μm section using the pixcavator software tool.

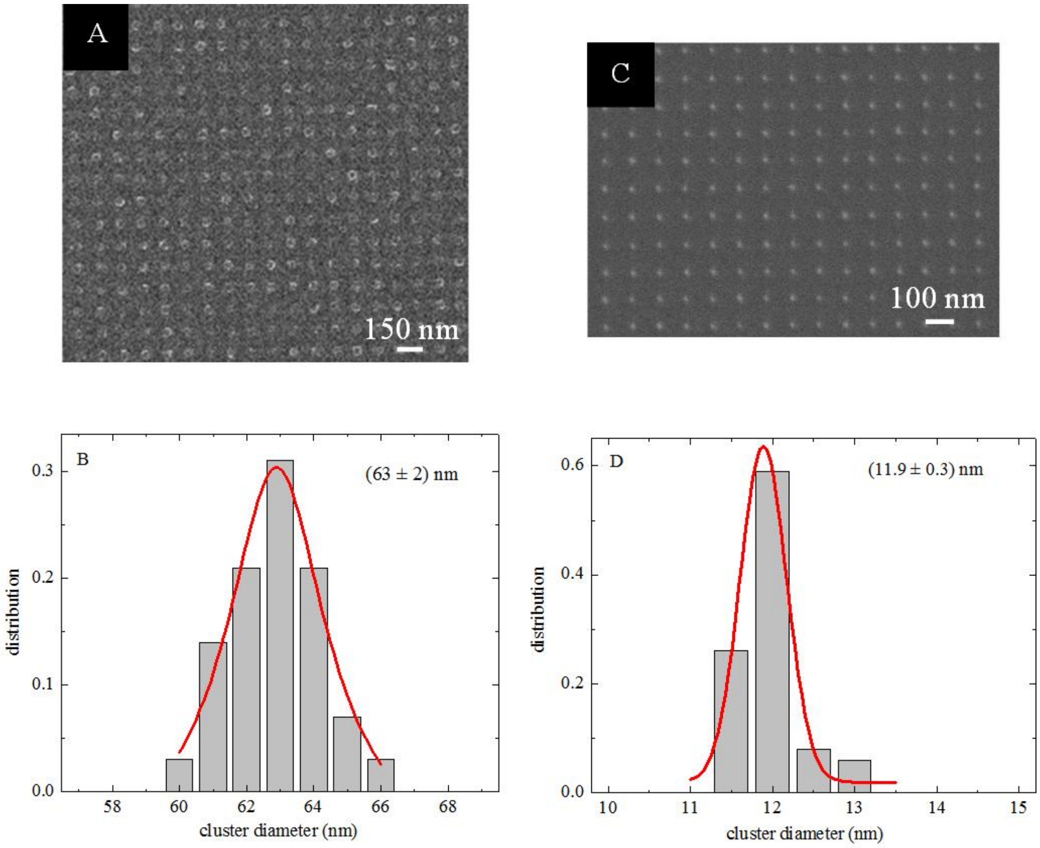

Figure 29. SEM images of Cu EBL clusters showing size distribution. A) SEM of the 63 nm and C) 12 nm clusters sample. B) Size distribution of the 63 nm and D) 12 nm clusters sample. The size distribution depicts the number of clusters (normalized with respect to the total cluster number in the SEM image) vs. the cluster diameter as, obtained from the SEM images.

As a result, the most possible cluster size (diameter) for the small (s) and large (l) clusters amounts to $d_s = 11.9 \pm 0.3$ nm and $d_l = 63 \pm 2$ nm with a lattice constant of $a_s = 100 \pm 1$ nm and $a_l = 150 \pm 4$ nm, respectively. A very narrow cluster size distribution was observed for EBL samples, e.g., $0.3/11.9 \approx 2.5\%$, using the full width at half maximum of the Gaussian fit shown in Figure 29D.

Assuming circular clusters, the calculated Cu coverage (Cu area vs. support area) amounts to 0.011 ML ($= \frac{1}{4}\pi d^2/a^2$) for small 12 nm and 0.139 ML for large 63 nm clusters, which corresponds to a factor of 12.6 ± 1.0. Therefore, CO saturation coverages, Θ_{sat}, for large clusters should be higher by the factor of 12.6 ± 1.0 compare to small clusters if the adsorption dynamics is dominated by terrace sites. Note that the uncertainties in the theoretical predictions are related to the cluster size variations. Relative Θ_{sat} can be determined by analyzing beam scattering data which is described later. However, the total rim length is given by $\rho A\ \pi d$ where A is the total area covered by the clusters and ρ is the cluster density (particles per area). Therefore, the ratio (large/small clusters) of the rim length equals to $d_l\rho_l/ d_s\rho_s = 2.3 \pm 0.4$. This means Θ_{sat} should increase only by a factor of 2.3 when increasing the clusters' size from 12 nm to 63 nm for the dynamics dominated by rim effects. A trivial assumption is made that the rim length and surface area is proportional to the number of adsorption sites and that the rim is a one-dimensional (1D) structure. The latter may be a good assumption considering the small aspect ratio of the clusters. The cluster density ($=1/a^2$) decreases from $\rho_s= 1\text{x}10^{-4}/\text{nm}^2$ to $\rho_l = 4\text{x}10^{-5}/\text{nm}^2$ while comparing the 12 nm and 63 nm cluster samples.

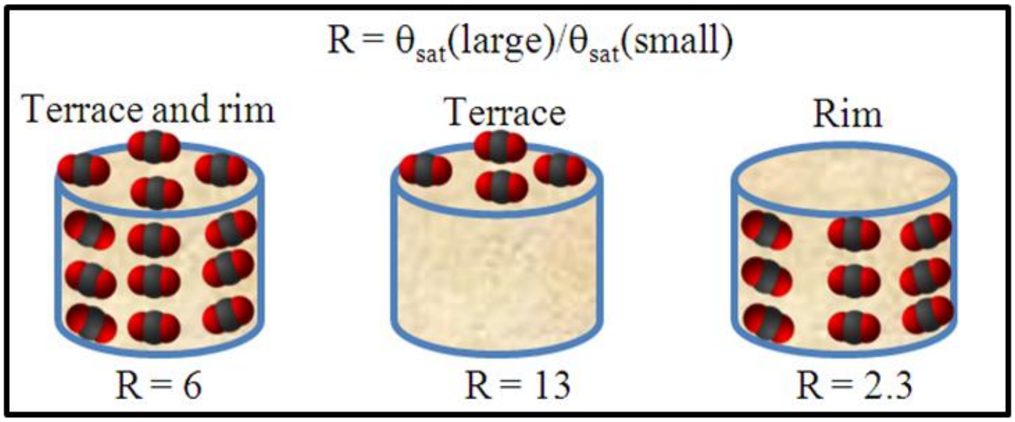

Figure 30. Clusters with probe molecules adsorbed on terrace only, rim only, and terrace and rim both. Theoritical calculations of saturation coverages ratios for 63 nm and 12 nm clusters are mentioned.

Similarly, if we assume that CO adsorbs on both rim and terrace sites as shown in Figure 30, Θ_{sat} should increase by a factor of 6 ± 0.8 when increasing the clusters' size from 12 nm to 63 nm. In order to do such estimation, a 2D rim with a height of h = 5 nm was assumed. It is possible that this assumption might have overestimated the area of rim sites. The total area of terrace and rim sites was given by $\pi A\rho d(¼d + h)$. Similarly, the calculated ratio only for the rim (= $4h/d$) of the 12 nm and 63 nm clusters amount to 1.66 and 0.32, respectively. Therefore, if rim adsorption sites have special properties, then these should be most distinct for the smaller cluster sample which has additionally a greater cluster density. Hence, EBL samples have the advantage for model studies because these simple estimates are possible without very time consuming sample characterization such as scanning tunneling microscopy (STM).

3.6.2. Spectroscopic characterization of the chemical state of the Cu clusters

AES and XPS were used to characterize the chemical state of the Cu clusters. Table 1 summarizes the XPS line positions. A literature survey reveals extensive XPS studies on copper systems that are available. In the present study, XPS has only been used to characterize the state of the catalyst before and after the reactivity tests with CO. Bulk CuO (powders, single crystals) is characterized by intense Cu 2p XPS shake-up satellites and a broad O 1s peak, however, each of the Cu oxides has its distinct LMM AES peak position.[127] In contrast, Cu_2O and metallic Cu show weaker/no Cu 2p satellites and a narrower O 1s peak in an XPS scan. It is experimentally challenging to assign the oxidation state of Cu based on the LMM AES peak position because of the charging effects. Unfortunately, whether or not the inspection of the LMM AES signature is required to distinguish Cu_2O and Cu is rather a controversial matter in the literature. According to the XPS study of Cu oxides, the Cu 2p shake-up satellites are caused by a charge transfer into 3d bands which are filled in the case of Cu^0.[128] Therefore, small Cu 2p satellite peaks would be characteristic of Cu_2O and their complete absence would indicate the presence of Cu^0. The same holds true for Cu clusters, however, the XPS peak positions of Cu^0 also depend on clusters' morphology (primarily on coverage) and support. Therefore, a correct assignment of the Cu clusters' oxidation state based on XPS/AES peak positions is still quite challenging.[129-130] In this study, the presence of very intense satellite peaks indicate fully oxidized (CuO-like) clusters whereas the absence of satellite peaks indicates nearly metallic (Cu^0-like) clusters.

AES survey scans of as received and cleaned 63 nm Cu dot samples are shown in Figure 31A. Similarly, XPS of the cleaned sample is shown in Figure 31B. The inset depicts the XPS Si 2p region. It is evident from the figure that no other peaks were seen after cleaning the samples besides support (silica) peaks and Cu peaks. The XPS spectra were referenced with respect to the Si 2p XPS peak corresponding to a binding energy of 103.4 eV and are in agreement with prior experiments[131-138] and reference data.[139-140] Only one peak is evident for fully oxidized silica whereas two features are seen for partially reduced silica in the Si 2P XPS region.[140] Thus, the cleaning procedures only affected highly reactive Cu clusters but not the support. This is a very important result because some studies about silica supported cluster systems have shown that silicon (Si) is more reactive than silica (SiO_2) at least for some probe molecules (as seen for hydrogen). Therefore, silica is considered chemically inert which allows one to distinguish between support and cluster effects.

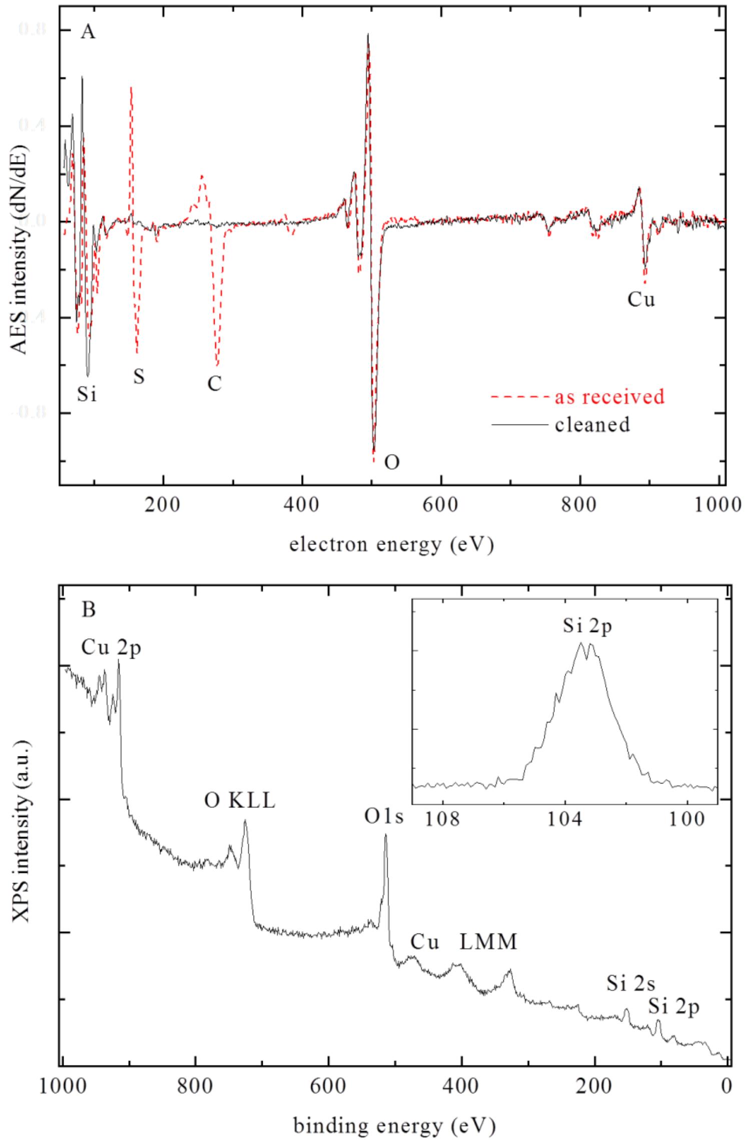

Figure 31 . A) AES spectra of as-received and cleaned 63 nm Cu EBL sample. B) XPS survey spectrum of the clean 63 nm Cu EBL sample and the inset shows the Si 2p XPS peak.

3.6.3. Oxidation state of the Cu clusters

Figure 32 depicts the Cu 2p XPS region of the silica-supported 63 nm Cu clusters which clearly distinguish metallic, partially, and fully oxidic states. Very similar results are observed for the 12 nm Cu clusters as shown in Figure 32B.

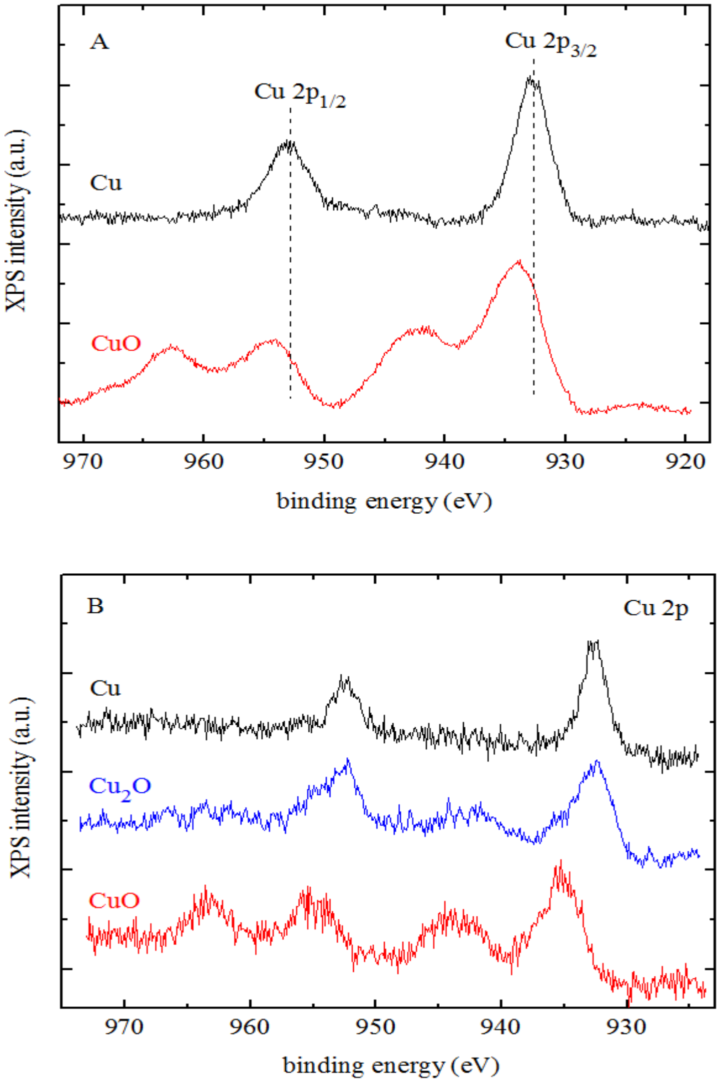

Figure 32. A) XPS Cu 2p region for the 63 nm sample B) for 12 nm sample. No satellite peaks are present for metallic Cu; whereas appearance of tiny or intense XPS satellite peaks is consistent with Cu_2O or CuO clusters.

The results are in good agreement with the literature that is shown in Table 1. At least it is confirmed that nearly metallic Cu clusters, partially oxidized, and fully oxidized Cu clusters could be prepared depending on the cleaning procedures. The oxidation and reduction of the Cu clusters were reversible as evident from AES and XPS data.

Table 1. XPS Cu $2p_{3/2}$ line positions for Cu and Cu oxides.[a]

	This work	**Other studies**	**System**	**Ref.**
Cu	932.7	932.8	Single crystal	[128]
		933.1-932.7	Cu/Zr	[129]
		932.6	Metallic Cu	[127]
Cu_2O	932.8	932.6	Single crystal	[128]
		932.3	Thin films	[141]
		933.0-932.4	Cu_2O/SiO_2	[129]
		932.4	Nanocrystals	[142]
		932.4	Powder	[127]
CuO	934	933.8	Single crystal	[128]
		933.9	Thin films	[141]
		935.5-933.8	CuO/SiO_2	[129]
		933.5	Nanocrystals	[142]
		933.6	Powder	[127]

[a]The Cu_2O data refers to 12 nm Cu clusters sample, and the rest of the data is for 63 nm Cu sample.

3.6.4. Adsorption kinetics of CO and CO_2 on CuO_x clusters

The thermal desorption spectroscopy results on the silica-supported EBL cluster samples for CO and CO_2 are presented in this section.

3.6.4.1. Adsorption kinetics of CO on metallic and oxidic Cu clusters

Figures 33A and 33B summarize CO TDS data on 63 nm Cu EBL samples for metallic and fully oxidized Cu clusters, respectively. CO was dosed by the molecular beam system to avoid sample holder effects and the intensities are given in arbitrary units.

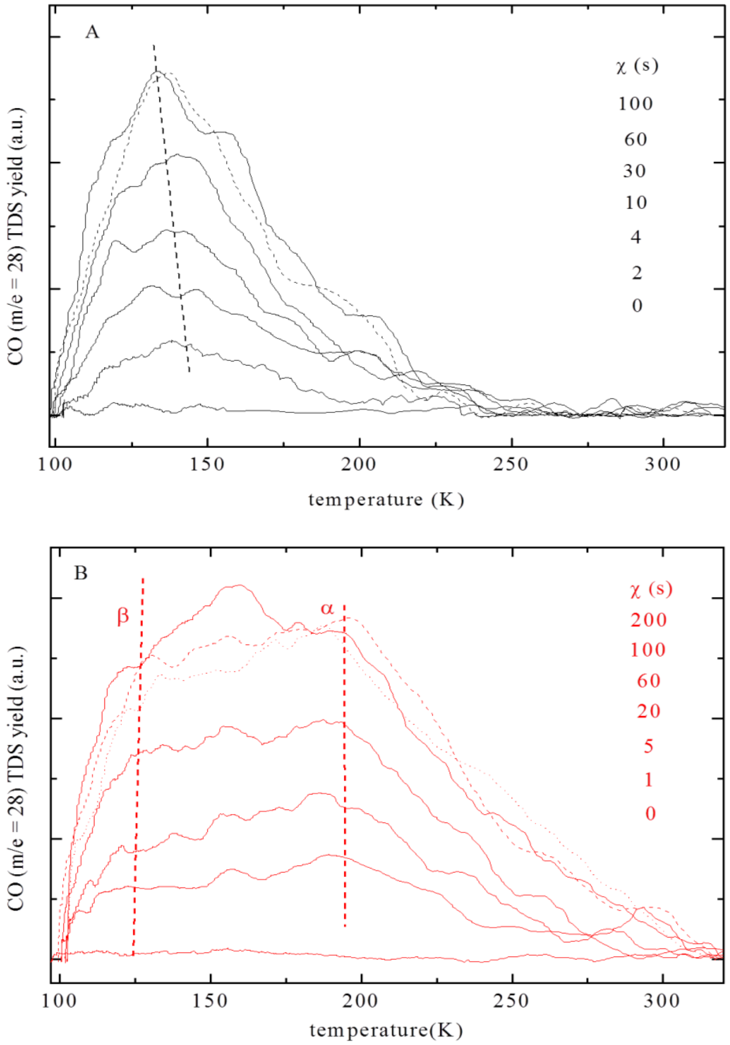

Figure 33. A) CO TDS on metallic 63 nm Cu clusters. B) CO TDS on silica-supported oxidic 63 nm Cu clusters.

A very broad feature which shifts slightly to smaller temperatures with increasing exposure is evident for the metallic clusters as shown in Figure 33A. It is obvious that the TDS signal is weak due to the small overall Cu coverage. The peak width and shift would be consistent with kinetically distinct adsorption sites, repulsive interactions, or a combination of both. An effect from lateral interactions can be ruled out because the total CO coverage even on the larger Cu clusters seems to be small. However, small clusters have a large rim-to-surface area ratio which supports the conclusion that mostly different adsorption sites are responsible for the peak broadening. Binding energies were calculated considering the TDS peak positions with the use of the Redhead equation (assuming a pre-factor of $1^{x}10^{13}$/sec) which are given in Table 2.

Table 2. Binding energies of CO determined from TDS peak positions as compared to literature values.[a] Ref.[42]

	T_{peak} (K)	**E_d (kJ/mol)**	**System**	**Ref.**
Cu^0	203	49.4	Cu(311)	[143]
	430	107.5		
		58.6	Cu(110)	[144]
		54.3	Cu(111)	[145]
CuO	132-143	33.6-36.5	63 nm EBL clusters	This work
	195 (α peak)	50.2	63 nm EBL clusters	This work
	125 (β peak)	31.7		

[a] The uncertainty in temperature calibration amounts to ± 5K, which results in an uncertainty of ± 1.3 kJ/mol in binding energies.

The TDS peak width seems similar to prior data collected for Cu PVD clusters, however, peak position appears at a significantly lower temperature.[18,121] The only logical explanation is morphological differences in details of the clusters' structure and electronic properties. Similar deviations in kinetics data were also seen when comparing Au PVD and Au EBL cluster systems.[19] As already mentioned in prior studies,[121] a clear assignment of TDS features to certain crystallographic phases is rarely possible.

TDS experiments of CO on oxidic Cu clusters are depicted in Figure 33B. Very broad TDS peaks with two structures (α and β peaks) are evident unlike one feature in metallic Cu. No adsorption kinetics studies of CO on CuO_x are available in the literature, but adsorption of CO on oxidic single crystals such as TiO_2 and ZnO also shows two TDS peaks.[119,146] The standard model is to assign the different TDS peaks to different adsorption sites. In this case, the high temperature (larger binding energy) feature may be related to defect sites (rim sites, edges, etc.) and the low temperature peak may correspond to pristine (terrace) sites. Similarly, the binding energies of CO on oxygen and Cu sites of the oxidic clusters would be different. In the case of iron oxide clusters, different CO TDS features were assigned to different Fe oxides.[147-148] The presence of different Cu oxides was ruled out by the XPS results. There was no indication of CO_2 formation in TDS and molecular beam scattering studies of CO.

3.6.4.2. Adsorption kinetics of CO_2 on CuO_x clusters

Figure 34A depicts thermal desorption spectroscopy (TDS) data of CO_2 on the larger size cluster sample. CO_2 was dosed onto the surface using the molecular beam system which suppresses contributions from the sample holder. In addition, CO TDS data from previous study are shown in Figure 34B as a reference.[18] Evidently, only one low temperature desorption feature was seen for CO_2, whereas two TDS peaks (labeled as α and β peaks) were detectable for CO. AES/XPS after these TDS experiments did not indicate any carbon residuals. Additionally, no other gaseous desorption products besides those related to molecular species were seen, leading to the conclusion that the adsorption of CO and CO_2 is molecular. Condensation temperatures of CO and CO_2 at UHV are well below 100 K.[149-150] Thus, the TDS peaks observed are related to adsorption in the monolayer range.

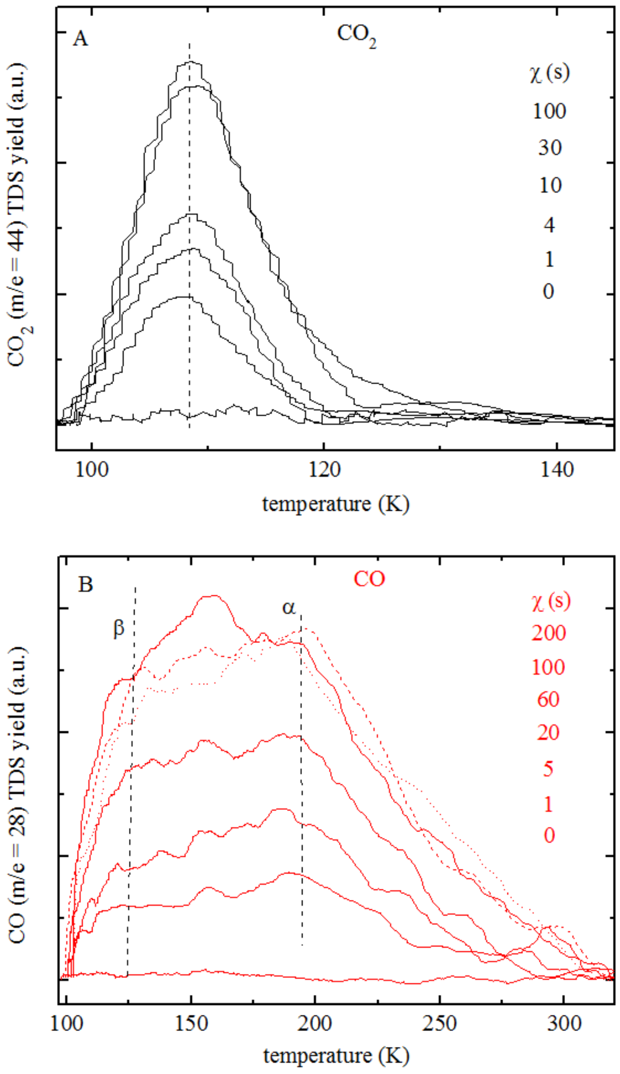

Figure 34. A) CO_2 TDS on 63 nm CuO cluster. B) CO TDS on 63 nm CuO cluster. The two different CO TDS peaks are consistent with two kinetically distinguishable adsorption sites. The missing second peak in CO_2 TDS would be consistent with adsorption solely on rim sites.

The appearance of two TDS features is typically indicative of the adsorption of the probe molecules on different adsorption sites rather than the effect of lateral interactions.[151-152] Considering the small coverages, the latter can indeed be ruled out. Furthermore, it is known that CO and CO_2 are ideal probe molecules to distinguish defect and pristine adsorption sites on oxides.[146,153] Therefore, it is plausible to assign the lower temperature CO desorption peak (β peak) to pristine (terrace) sites and the high temperature structure (α peak) to defect sites (step edges, rim sites, vacancies, etc.). Interestingly, only one low temperature TDS feature was evident for CO_2. It is known that CO_2 does not adsorb (at $T_s = 90$ K) on the close-packed surfaces of copper.[154-155] The terrace sites of our clusters likely have that close-packed structure. Therefore, indeed only one CO_2 TDS peak would be expected. Copper oxides will consist of Cu and O adsorption sites. The interaction of CO_2 with oxygen sites will likely be repulsive[156] and carbonates will not be formed on copper oxides.[116,157-158] Therefore, it is plausible that CO_2 adsorbs solely on defect sites which could be the rim of the clusters, consistent with the observation of only one CO_2 TDS peak.

The peak temperatures corresponded to binding energies of (27.1 ± 1.3) kJ/mol for CO_2 as well as (31.7 ± 1.3) kJ/mol and (50.2 ± 1.4) kJ/mol for the α and β CO TDS peaks respectively, assuming a standard pre-exponential factor of $1\text{x}10^{13}$/s for first order molecular adsorption/desorption. The CO binding energies are rather low; however, they are close to the binding energies obtained on a stepped copper surface which would be in line with clusters consisting of a large defect density.[159] It is known from studies of metal oxides such as TiO_2 and ZnO that the adsorption of CO on defect sites (oxygen vacancies) is characterized by greater binding energies as compared with pristine sites.[146] Therefore, the assignment of the β peak to defect sites is plausible. CO_2 interacts weakly with metal surfaces.[116,157-158]

3.6.5. Adsorption dynamics of CO and CO_2 on CuO_x clusters

The molecular beam scattering results on the silica-supported EBL cluster samples for CO and CO_2 are presented in this section.

3.6.5.1. Adsorption dynamics of CO

The adsorption dynamics study for metallic and oxidic Cu EBL clusters is presented along with blind experiments on the clean silica supports and Cu PVD clusters data. The PVD deposition of Cu on silica has been studied before with spectroscopic and kinetic techniques according to the literature survey.[6,100,160] The morphology of Cu PVD clusters was characterized using STM.[17,131-134] The data indicate that Cu PVD clusters nucleate on the silica support for low Cu exposures, forming highly dispersed and small clusters. This nucleation phase is followed by a cluster growth regime. To the best of our knowledge, only one beam scattering project on that system is reported in the literature where the Cu PVD clusters did remain metallic at UHV conditions.[18] The adsorption dynamics of CO could be modeled with the CZM. S_0 decreases with impact energy, as expected for molecular and non-activated adsorption. In some prior studies regarding CO adsorption on ZnO(0001)-supported Cu PVD clusters, a crossover from direct adsorption dynamics (Langmuirian-like) to more precursor assisted adsorption dynamics (Kisliuk-like) has been observed, which clearly depends on the size of the metal deposits.[121,123] Some of the observed trends are consistent with simple CZM, but interestingly not the shape of the $S(\Theta)$ curves, which are obtained at small Cu coverages and at large impact energies. These results suggest a weak effect of precursor states that shorten the lifetime of trapped particles either because of large diffusion activation energies or non-thermal precursor states. Clean copper surfaces have been studied using molecular beam scattering techniques.[161] However, no beam scattering data are available on Cu oxide single crystals, supported CuO_x clusters, or any Cu EBL system.

3.6.5.1.1. CO adsorption transients on metallic and oxidic clusters

As mentioned earlier, the probe molecule was dosed by using a supersonic molecular beam. The beam flux was determined by measuring the equivalent beam pressure using the mass spectrometer aligned with the beam which resulted F = (1.8 ± 0.1) x 10^{13} CO molecules cm^{-2} s^{-1} for the seeded CO beam. The beam flux was kept constant (within 6%). Typical examples of CO adsorption transients (CO pressure vs. exposure time) of the silica-supported 12 nm and 63 nm Cu EBL clusters, blind experiments on silica, and partially reduced silica are shown in Figure 35. The top panel displays results for metallic Cu and the bottom panel for oxidic Cu EBL clusters. The curves are normalized such that 1-S(t) vs. t is depicted where t is the exposure time of the seeded molecular beam and S(t) is the adsorption probability. In fact, the adsorption probabilities can directly be read from these figures. For example, S_0 can be determined at t = 0 where the CO beam starts to strike the surface and slowly approaches the saturation level. Integrating these transients give one the CO coverage dependent adsorption probability, S(Θ).

It is evident that the transients approach the saturation level (where S = 0 or 1 - S = 1) much slower on the supported cluster samples than on the supports only. Thus, the clusters indeed affect the adsorption dynamics and CO adsorbs on the clusters and/or along the clusters' rim. It is seen that the CO coverage on the clean silica, as well as reduced silica supports, is negligible at the given adsorption temperature. The area above the transient and below the saturation level equals the amount of adsorbed probe molecules. Therefore, with the known CO flux, the total CO uptake (or saturation coverage Θ_{sat}) amounts to $\Theta_{sat} = \int FS(t)dt \approx 1.8 \times 10^{14}$ molecules/cm^2 (or 1.8 x 10^{14}/1.9 x 10^{15} = 0.09 ML) for 63 nm Cu clusters. Using the bulk lattice constant of Cu (3.6 Å), the calculated Cu atom density of e.g. a (111) plane amounts to 1.9 x 10^{15} atoms/cm^2. The experimental saturation coverage (0.09 ML) appears reasonable since the calculated theoretical Cu coverage of the 63 nm clusters was found to be 0.139 ML. The calculated CO coverage amounts to 0.07 ML = (0.139 x 0.52). A saturation coverage of 0.52 ML for CO adsorption on Cu(111) was determined experimentally.[162]

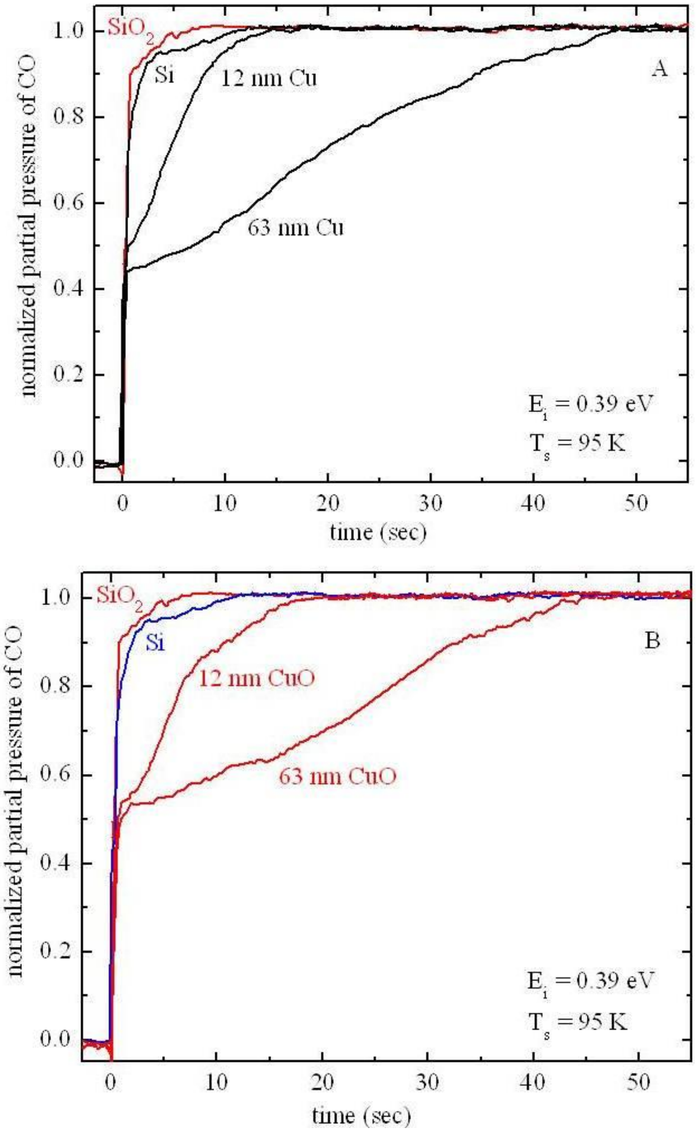

Figure 35. A) Adsorption transients of CO on metallic and B) oxidic Cu clusters depicted together with the blind experiments on clean bare supports of Si and SiO_2 (T_s = 95 K and E_i = 0.39 eV).

More interestingly, when comparing large and small clusters, the experimental ratio of $\Theta_{sat,\,l} / \Theta_{sat,\,s}$ amounts to 5.5 ± 0.9 and 4.5 ± 0.7 for metallic and oxidic clusters, respectively. The experimental uncertainties are obtained from averaging independent experimental runs. As described earlier considering its simple geometry, the ratios of 2.3 ± 0.4, 12.6 ± 1.0, and 6.0 ± 0.8 would be expected if the gas-phase species adsorb only along the rim sites, terrace sites, or both rim and terrace, respectively. These results lead to the following conclusions:

Nearly the same saturation coverage ratios were obtained independent of the oxidation state of the Cu clusters. Hence, it appeared that geometrically similar adsorption sites might be present on both metallic and oxidic Cu clusters. The experimentally determined ratio matched the prediction for adsorption on rim sites and terrace sites within small margin of uncertainty. Therefore, CO indeed adsorbed not only on the clusters' terrace but also on clusters' rim as expected. This result may also imply that the rim sites on Cu clusters do not show special behavior besides simple geometrical effects. Although CO molecules were dosed with a molecular beam system, the saturation coverage was determined by the adsorption kinetics. It should be noted that the rim sites on the EBL clusters provide additional adsorption sites which, however, do not appear to behave kinetically much differently than terrace sites. If the kinetics was dominated only by rim sites (as it is for Au clusters[45,163]), a different ratio of the saturation coverages would have been expected. Similarly, variations in S_0 are seen depending on the cluster size and oxidation state which is described next.

3.6.5.1.2. Energy dependence of initial adsorption probability - cluster size effects

The initial adsorption probability (S_0) of CO as a function of impact energy (E_i) at constant adsorption temperature is shown in Figure 36. This figure summarizes the results of S_0 of Cu PVD data[18] as a function of Cu exposure, as well as provides a comparison of S_0 of small and large EBL Cu clusters. In all cases, S_0 decreases with $E_{i,}$ consistent with non-activated and molecular adsorption. This is in agreement with the absence of carbon after dsorption/desorption cycles, as verified by XPS/AES. At small E_i, the adsorption probabilities of CO are large, which is typical for CO as seen in a variety of other systems.[164-166] Cluster size effects are consistently evident in several data sets. The arrow in Figure 36 represents the increment of S_0 with increasing cluster size. The CO impact energy and surface temperature were kept constant. It is evident that the results obtained on Cu EBL and Cu PVD clusters match. For large exposures (PVD), S_0 appears to approach the values determined in other studies for Cu single crystals or Cu films.[161,164] The same trend has been seen for ZnO supported Cu PVD clusters.[121] This means, Cu clusters with a total coverage in the percent range are as reactive as Cu single crystals, which is a typical result of the capture zone effect.[78] Even if the coverage of the probe molecules on the bare support is negligible, the probe molecules are trapped on the support and diffuse from their landing site to the metal clusters where they adsorb.

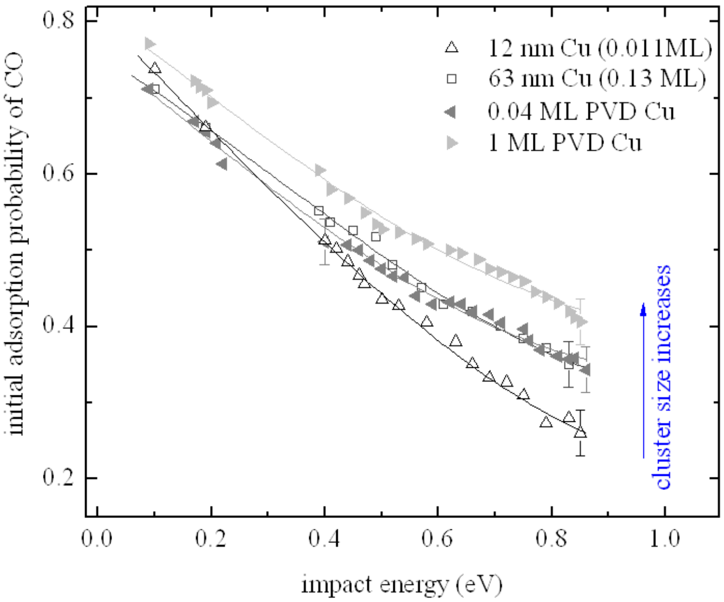

Figure 36. S_0 of CO vs E_i for 12 and 63 nm Cu clusters (metallic) as well as for selected Cu PVD depositions. (T_s = 95 K).

The adsorption probabilities for supported cluster systems may be larger than is expected for their geometrical size. The initial increase in S_0 with cluster size/coverage is caused by the increase in available adsorption sites. However, for large cluster densities (large Cu exposure) in the PVD experiments, the capture zones around the clusters overlap with each other. At that point, increasing the cluster size and dispersion cannot increase S_0 anymore, as shown in Figure 37. Therefore, the initial adsorption probability in S_0 vs. exposure plots levels out.

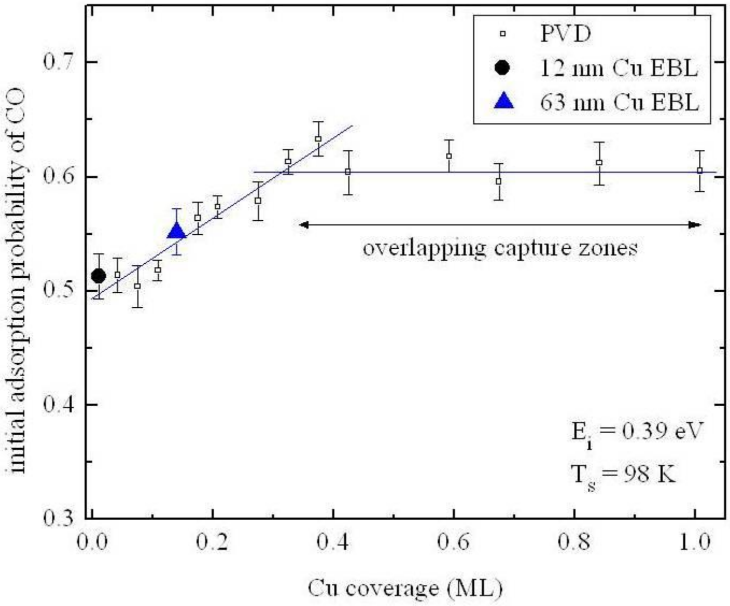

Figure 37. S_0 of CO vs Cu coverage (T_s = 95 K and E_i = 0.39 eV) for 12 and 63 nm Cu clusters (metallic) as well as for selected Cu PVD depositions.

3.6.5.1.3. Effect of oxidation state on initial adsorption probability

Figure 38 depicts the S_0 of metallic and oxidic EBL clusters as a function of impact energy. Differences in S_0 are evident, depending on the oxidation state of the clusters. Metallic Cu clusters are more reactive than oxidic Cu clusters in terms of adsorption probability of CO. This trend is seen very clearly for large E_i, where details in the adsorption dynamics are naturally more important than at low impact energies. This trend is consistent with simple mass matching models when taking site blocking effects into account. A CO molecule can interact only with Cu adsorption sites on the metallic clusters whereas with Cu and O adsorption sites on the oxidic clusters. The CO-to-Cu mass match is worse than the CO-to-O mass match which should result in more efficient gas-to-surface energy transfer processes (and larger S_0) in the latter case. Therefore, simple mass-matching models would predict larger S_0 values for the oxidic clusters, contrary to the results obtained in this study. However, this may suggest that CO does not adsorb on oxygen sites of the oxidic clusters. Since the adsorption probability is basically the ratio of adsorption rate to impinging rate, and site blocking effects (or poisoning) result in smaller S_0 values. The O-sites on the oxides where CO cannot adsorb would act as poisoned adsorption sites, decreasing S_0, as indeed observed. Therefore, with these assumptions, the available number of adsorption sites on the oxidic clusters is simply smaller than on the metallic clusters. Also, CO adsorption on oxidic structures may in principle also be influenced by defects such as oxygen vacancy sites or even carbonate formation.

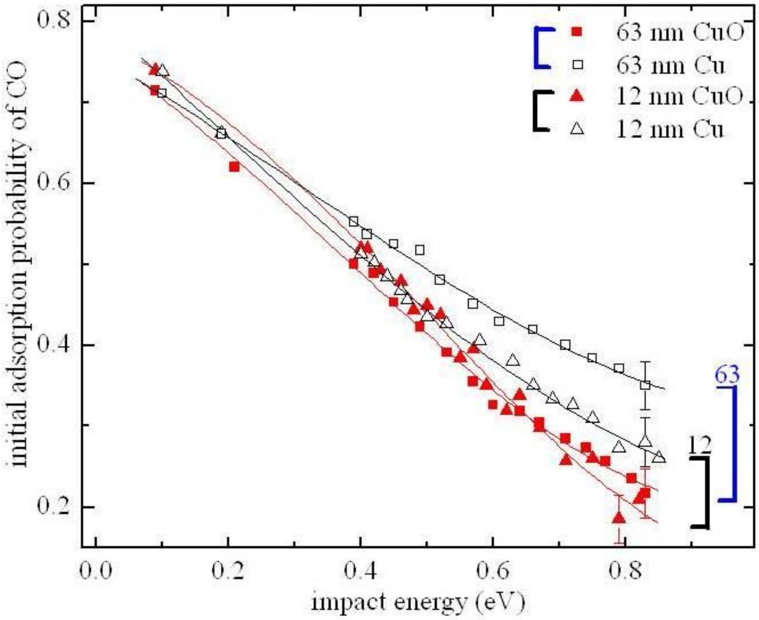

Figure 38. S_0 of CO vs E_i for 12 and 63 nm metallic and oxidic Cu EBL clusters (T_s = 95 K).

It is clearly seen that S_0 (within experimental uncertainties) is independent of cluster size for the oxide considering cluster size effects for the oxidic clusters as shown in Figure 38, unlike for the metal clusters where S_0 depends on cluster size (Figures 37 and 38). The database for the oxides is limited and electronic effects should be present. However, when oxidizing Cu clusters, the overall clusters' size should increase. The crystallographic phase which dominates the clusters is unknown, but the unit cell of Cu(111) amounts to 6.5 Å^2, whereas the unit cell of bulk CuO is 16 Å^2, making it larger by factor of 2.5.[167] Therefore, in the case of oxidic clusters, the capture zones would most likely already overlap and no effect of cluster size on S_0 would be expected. In addition, the CO binding energies on the oxide is larger than for the metal (Figure 4), i.e. the precursor lifetimes and therefore the capture zones will be larger and overlap early.

3.6.5.1.4. Coverage dependent adsorption probabilities

Integrating the adsorption transients determines the coverage, Θ, dependent adsorption probabilities, S(Θ). Figure 39A and 39B depict S(Θ) as a function of E_i for CO adsorption on 63 nm Cu clusters and CuO-like clusters at constant T_s, respectively. The coverage was normalized to 1 ML which corresponds to 1.8×10^{14} molecules/cm^2 as determined earlier. At low E_i, S(Θ) obeys the traditional Kisliuk shape. Here, S(Θ) remains initially large up to saturation of the catalyst, where S(Θ) drops to zero. This type of curve shape indicates the effect of precursor states, as expected from the capture zone model. Whereas for large E_i, S(Θ) decreases about linearly with Θ, resulting Langmuirian like adsorption dynamics. This cross-over from precursor-mediated Kisliuk-like dynamics to direct Langmuirian-like dynamics is commonly seen for CO also on planar catalysts, which simply reflects the decrease in the trapping probability in the precursor state with increasing E_i.[166]

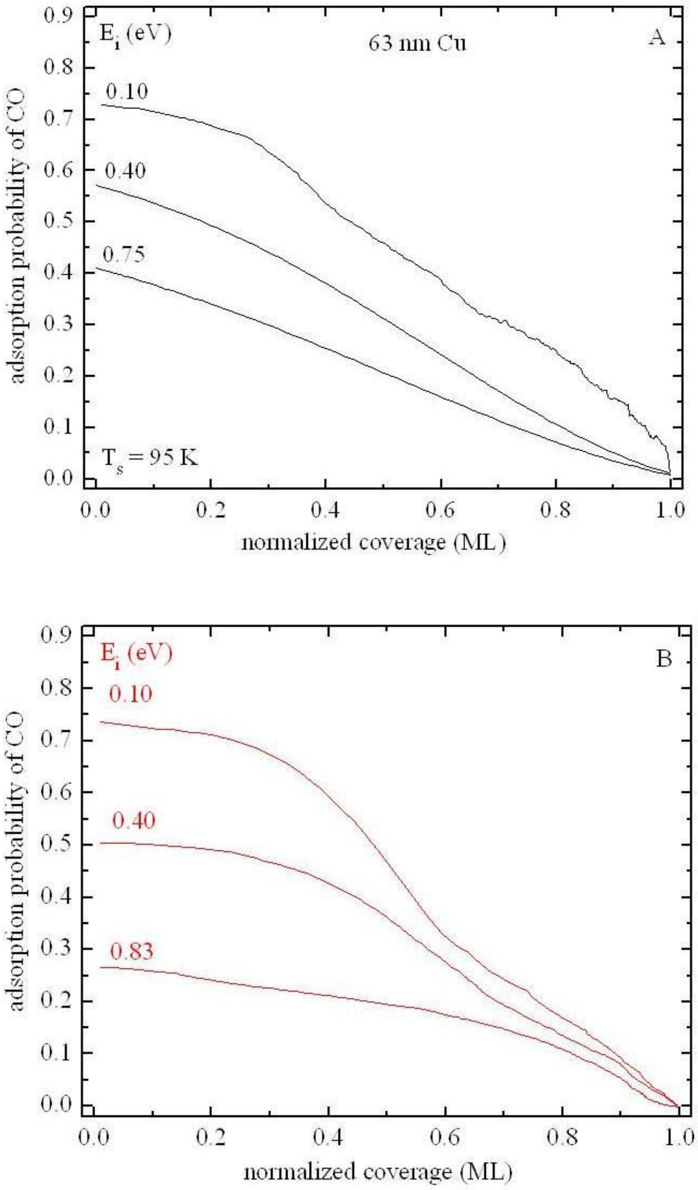

Figure 39. S(Θ) curves for A) metallic and B) oxidic 63 nm Cu EBL clusters (T_s = 95 K). The impact energy (E_i) was varied as indicated.

3.6.5.2. Adsorption dynamics of CO_2

3.6.5.2.1. Theoretical calculation of saturation coverages for rim and terrace sites

EBL samples with predetermined structure allow for calculating further geometrical parameters, in particular expectation values of terrace and rim sites. Saturation coverages can be determined precisely by using molecular beam scattering techniques. Hence, relative numbers of adsorption sites can be determined experimentally at UHV conditions.

As mentioned earlier, considering the large (63 nm) and small (12 nm) Cu clusters, the ratio of terrace sites increased by a factor of 13.0 ± 1.0 as the clusters' size increased from 12 nm to 63 nm. Similarly, the total rim length increased by a factor of 2.3 ± 0.4. It is assumed that the rim length and surface area were proportional to the number of adsorption sites. In addition, the rim was viewed as a one-dimensional (1D) structure. For simultaneous adsorption on 2D terrace and rim sites, a factor of 6.0 ± 0.8 would be expected. These ratios would not change if considered a 2D rim since the clusters' height was kept constant. Similarly, an expansion of the clusters while oxidizing them would conserve the ratios when assuming that the expansion factor (e.g. ratio of unit cell areas) was independent of cluster size. In other words, comparing saturation coverages of CO_2 on the small and large clusters, ratios of 2.3 ± 0.4, 13 ± 1, and 6.0 ± 0.8 would be predicted (see Tab. 1) when CO_2 adsorbs only along the rim sites, on terrace sites, or on both, respectively. EBL samples have the advantage for model studies that these estimates are possible without very time consuming sample characterization.

3.6.5.2.2. Experimental calculation of saturation coverages for rim and terrace sites

Relative saturation coverages were obtained from adsorption transients while dosing CO_2 onto the surface with a molecular beam. Typical traces of CO_2 impinging on the surfaces starting at exposure time t = 0 are shown in Figure 40. For clean silica support (partially reduced or fully oxidized) nearly a step function was detected since CO_2 does not adsorb on silica at temperatures as low as 90 K. However, the adsorption transient approaches a saturation level (for t > 35 s) much slower for the Cu nanoclusters catalysts. Once the surface is saturated, the CO_2 pressure levels out (t > 35 s); accordingly a new equilibrium pressure builds-up in the scattering chamber.

In order to demonstrate the reproducibility of these experiments, a number of transients are shown for 12 nm and 63 nm clusters, as indicated in Figure 40. In fact, the area above the transient and below the saturation level amounts to the number of adsorbed species on the surface. Relative saturation coverages (small cluster vs. large clusters) can be obtained by keeping the CO_2 flux constant.

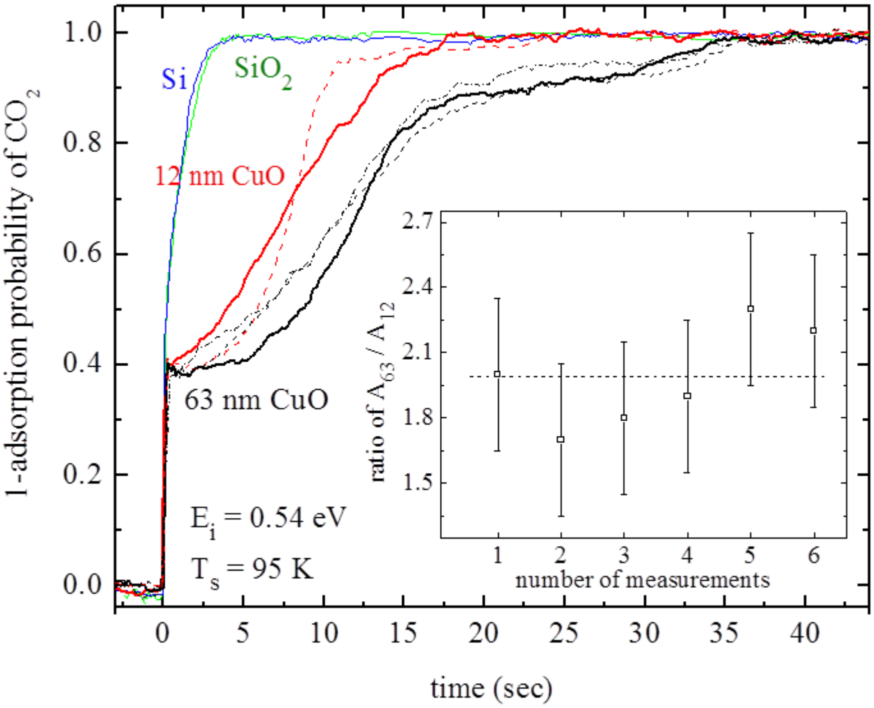

Figure 40. Adsorption transients of CO_2 on Si, SiO_2, 12 nm, and 63 nm CuO clusters supported on SiO_2. The inset shows saturation coverage ratios of six independent measurements. Impact energy and adsorption temperature are indicated.

Determining saturation coverages from different samples by TDS would require sophisticated calibration procedures, whereas using beam scattering, variations in the sensitivity of the mass spectrometer do not affect the results. The ratio of the CO_2 saturation coverage obtained from these transients amounted to 2.0 ± 0.3 for 63 nm and 12 nm clusters. The results for the 35 nm sample are also shown in Table 3. These ratios were obtained by averaging 6 independent experimental runs, as shown in the inset of Figure 40. This numerical value is indicative of adsorption of CO_2 primarily on rim sites along the clusters as shown in Figure 41, which is consistent with the detection of only one CO_2 TDS peak. Previous experiments for CO adsorption gave a saturation-coverage-ratio of 4.5 ± 0.7, indicating that CO indeed adsorbs not only along the rim of Cu clusters, but also on terrace sites as shown in Figure 41.[18] Density functional calculations could perhaps provide a more detailed explanation which is still not available in literature.

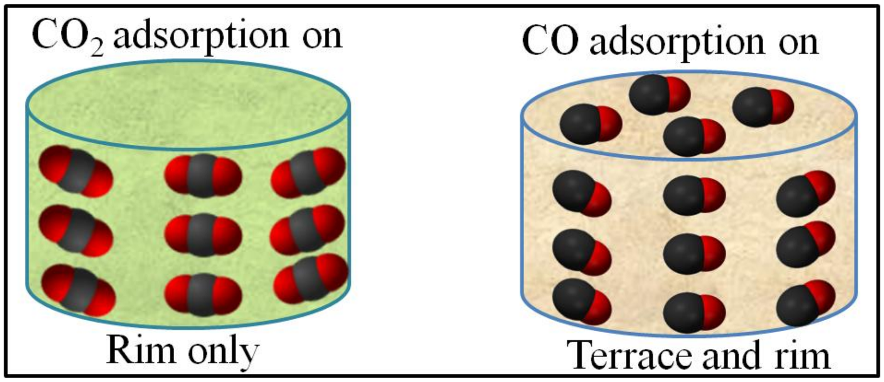

Figure 41. Illustration of CO adsorption on both terrace and rim sites and CO_2 adsorption on rim site only.

Table 3 . Saturation coverage ratios for three different EBL samples. Note that also the lattice constants differ. (Theoretical [**black**], Experimental CO_2/CuO **[red]**, Experimental CO/CuO **[green]**) Ref.[43]

Adsorption site	63 nm/12 nm	63nm/35 nm	35nm/12 nm
Terraces	**13 ± 1**	**1.2 ± 0.3**	**10 ± 2**
Rims	**2.3 ± 0.4** **2.0 ± 0.3**	**0.6 ± 0.1** **0.8 ± 0.2**	**3.9 ± 0.6** **2.7 ± 0.3**
Both	**6.0 ± 0.8** **4.5 ± 0.7**	**1.0 ± 0.2** **1.2 ± 0.3**	**6 ± 1** **4.0 ± 0.6**

Literature survey reveals the unique properties of rim sites that was evident from scanning tunneling microscopy experiments with thiophene on MoS_x clusters.[94] Similarly, it is known that CO_2 does not adsorb on the closely packed surfaces of copper which likely constitute the terrace sites of our clusters.[154-155] Hence, it is plausible that CO_2 adsorbs solely along the rim of the clusters. The data base for copper oxide clusters is unfortunately very limited. However, CuO will consist of Cu and O adsorption sites. The interaction of CO_2 and CO with oxygen sites will likely be repulsive and carbonate formation has never been seen for copper oxides. For CO, the rim sites on Cu clusters provide additional adsorption sites which kinetically behave more or less like terrace sites.[42] This is consistent with data on various Cu single crystals where CO adsorbs efficiently independent of the crystallographic orientation.[161] Nearly the same saturation coverage ratios were obtained independent of the oxidation state of the Cu clusters. Therefore, it appears that for CO, kinetically similar adsorption sites on metallic and oxidic clusters exist.

3.6.5.2.3. Energy dependent adsorption probabilities

Molecular beam scattering experiments on cluster samples are typically conducted at experimental conditions which assure negligible concentration of the probe molecule on the support.[49,51,79,158,168-170] Therefore, the transients on the clean support were just step functions as shown in Figure 40. It is an experimental fact that the lifetime of the probe molecule on the surface can be sufficiently long, which allows the diffusion of the molecules from the support to the clusters. This effect is referred as the “capture zone” (CZ) model because the clusters capture the diffusing probe molecules. The size of the capture zone is given by the ratio of the surface residence time and the hopping (diffusion) time. Therefore, it is completely dependent on adsorption temperature, T_s, and cluster size.[78-79,118] In the simplest case, the CZ size would increase with cluster size and decrease with T_s. However, the CZs can overlap for high cluster densities and sizes at low T_s. The impact energy, E_i, dependence of the initial adsorption probability, S_0, parametric in cluster size, is depicted in Figure 42. The surface temperature (and precursor life time) was kept constant in this study.

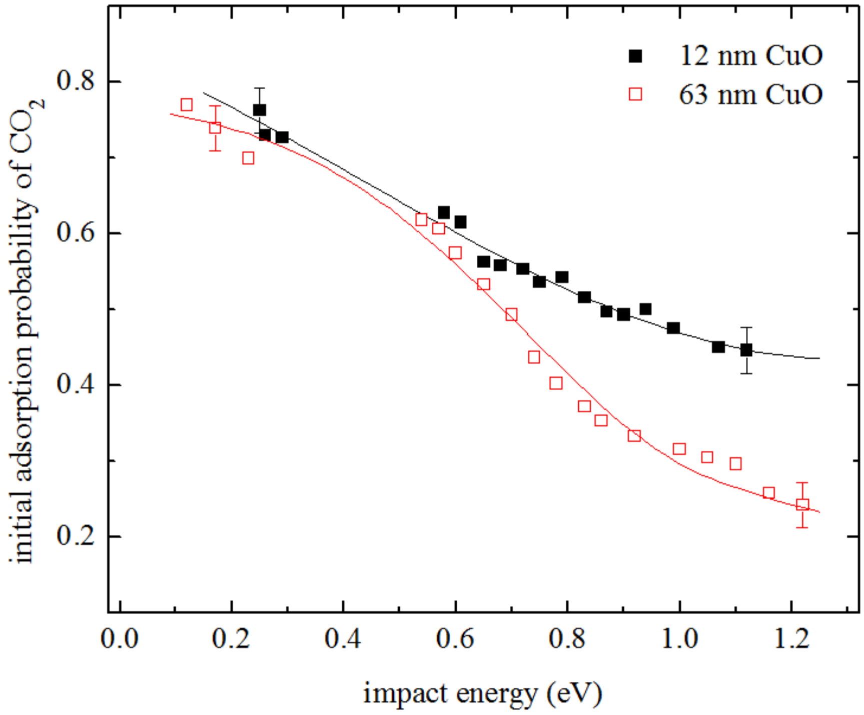

Figure 42. Initial adsorption probability, S_0, of CO_2 as a function of impact energy, E_i. Results for two different cluster sizes are shown. The result indicates molecular and none-activated adsorption.

It was evident that the trapping probability in precursor states was decreased with E_i for molecular and non-activated adsorption. Therefore, the decrement of S_0 with E_i is consistent with the TDS and XPS results which indeed indicate molecular adsorption. Usually, details in the adsorption dynamics become evident at large E_i since the trapping probabilities in precursor states are generally large at low E_i. Unexpectedly in the framework of the CZ model, smaller clusters were found to be more reactive than larger clusters (Figure 42). However, oxidic clusters were considered in our experiments. The terrace sites on the initially metallic clusters are most likely closed packed Cu surfaces which is similar to Cu(111). The unit cell of Cu(111) amounts to 6.5 Å^2 whereas the unit cell of bulk CuO is much larger and amounts to 16 Å^2 (=a $_x$ b).[167] Therefore, when oxidizing the 63 nm clusters, the cluster size will increase such that the sample is dominated by terrace sites. Terrace sites are less reactive for CO_2, as discussed above. Therefore, it is not too surprising that the large Cu-oxide clusters would be less reactive (smaller S_0) than the small clusters. In addition, due to the large size of the 63 nm oxidic clusters, the total CZ would be small which means S_0 would be small, too. On the other hand, for small 12 nm clusters, when these clusters are expanded to form oxide, the CZ effect would still be active, allowing diffusion-mediated adsorption of CO_2 along the rim of the small clusters.

3.6.5.2.4. Temperature dependent adsorption probabilities

A typical example of the temperature dependence of S_0 for CO_2 adsorption on the 63 nm clusters is shown in Figure 43 and is compared to the temperature dependence of S_0 for CO adsorption. In fact, for non-activated and molecular adsorption, S_0 would actually be independent of adsorption temperature, T_s. However, as briefly summarized above, the capture zone's size decreased with T_s and therefore S_0 decreased as well. In addition, the binding energy of CO_2 on the EBL clusters was found to be smaller than for CO. When approaching the desorption temperature of the adsorbates, a kinetic adsorption probability will be determined which is governed by an adsorption/desorption equilibrium. Therefore, for CO_2, $S_0(T_s)$ approaches zero at lower temperatures than for CO. This result also independently confirms the kinetics data presented earlier in Figure 34.

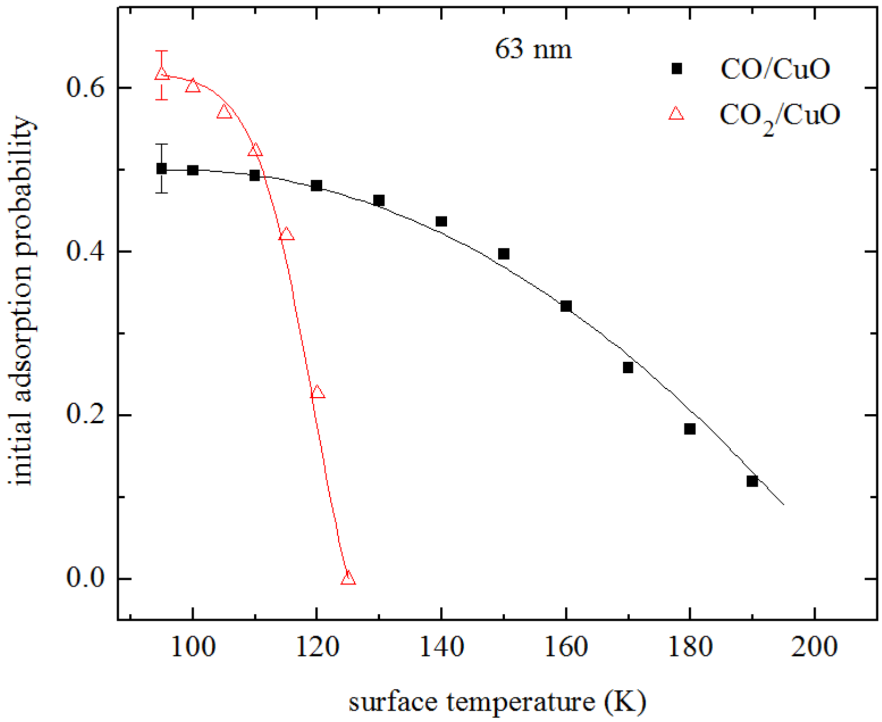

Figure 43. S_0 of CO and CO_2 as a function of surface temperature, T_s, for 63 nm oxidic Cu clusters. The temperature dependence is a consequence of the capture zone effect.

3.7. Summary

In this study, kinetics (TDS), dynamics (molecular beam scattering), microscopic (SEM), and spectroscopic (AES, XPS) techniques were used to characterize the reactivity of Cu and CuO_x clusters toward CO and CO_2 adsorption. The silica-supported 12 nm, 35 nm, and 63 nm Cu cluster samples were fabricated using EBL. Interestingly, the saturation coverage of CO did not simply scale with the area of the clusters, but, rather, the rim effects clearly increased the saturation coverage. The non-activated molecular adsorption of CO was concluded due to the decrease in S_0 of CO with an increase in E_i , and no indication of surface carbon by AES/XPS after CO experiments. S_0 of metallic Cu clusters, depended on cluster size, was described by considering the framework of the capture zone model. Furthermore, the adsorption dynamics of CO was found to be different depending on the oxidation state of Cu clusters explained by simple mass matching models. S_0 of CO on the metallic clusters was larger than on oxidic clusters. It is evident from the experiment that distinct cluster size effects were only present in the case of metallic clusters, but not in the case of oxidic clusters due to cluster size expansion during the oxidation process and larger binding energies. Similarly, the nonactivated molecular adsorption of CO_2 was also concluded due to the decrease in S_0 of CO_2 with an increase in E_i and no indication of surface carbon by AES/XPS after CO_2 experiments. The hypothesis that rim sites along catalysts show special properties is perhaps evident in this study.[118] Similarly, the capture zone's size decreased with T_s and therefore S_0 did as well. Identifying the active sites on a catalyst surface forms the basis of systematic catalyst design strategies. EBL allows for nanofabricating model catalysts with predetermined morphology which is utilized for a methanol synthesis model catalyst in this study. By measuring CO and CO_2 saturation coverages on different cluster sizes, it was experimentally proven that CO_2 adsorbs preferentially along the clusters' rim and CO on both rim and terrace. The implications for catalysis may be to optimize the catalyst synthesis such that the rim length of the supported clusters is maximized.

CHAPTER 4. SURFACE CHEMISTRY STUDY OF ALKANES ADSORPTION

This chapter is comprised of three projects that relate to the surface chemistry study of small chain alkanes adsorption on the surface of several model catalysts. Different categories of model catalysts such as an alkaline earth metal oxide (i.e. CaO), a transition metal (i.e. Mo), and a metalloid (i.e. Sb) for alkane adsorption are studied in this dissertation. Alkanes adsorption on metals and metal oxide surfaces has been studied intensively utilizing surface science techniques. However, research efforts have been devoted to the design and fabrication of new catalysts that can have an effect on bond activation in alkanes. Bond activation in alkanes has been a focus of attention in research for the last few decades due to its potential applications in fuel generation and other energy related fields. The first project includes the study of bond activation in alkanes such as n-butane, n-pentane, and n-hexane on the catalyst surface of an alkaline earth metal oxide, i.e., CaO. Taking the advantage of a simple surface science technique i.e. thermal desorption spectroscopy, the bond activation in alkanes is characterized. The second project concerns the study of co-adsorption of n-butane and water to characterize the formation of a porous water film as expected for a hydrophobic surface. Similarly, the final project in this chapter concerns the study of catalytic activity of n-butane adsorption on EBL-fabricated metallic Mo and oxidic Mo nanoclusters.

4.1. Alkanes adsorption on CaO(100)

A brief literature review regarding the importance of bond activation in alkanes on various metal and metal oxide surfaces is presented in the first part of this section. Then, the adsorption kinetics of small chain alkanes on CaO(100) studied by multi-mass thermal desorption (TDS) spectroscopy is presented. Both molecular and dissociative adsorption pathways, which are evident in this study, are explained in the results and discussion section.

4.1.1. Introduction

The bond dissociation of alkanes has been studied for decades on metal single crystal surfaces such as Ir and Pt.[46-53] Although the high chemical activity of some metal oxides in this respect has been known for quite some time from catalysis studies on powders,[54-58] only a few surface science projects about the adsorption of alkanes on nonmetallic systems have been conducted. Molecular adsorption has been seen for MgO,[59] ZnO,[60] rutile TiO_2,[61-62] silica,[63-64] and graphitic systems.[65-67] Theoretical studies predict an increase in the catalytic activity along the group of the alkaline earth oxides.[171-172] Therefore, a higher activity of CaO compared to MgO is expected. Despite the importance of catalytic importance of bond activation in alkanes, relatively few studies of alkane dissociation on well-defined oxide surfaces have been reported.

4.1.2. Brief literature survey

A brief literature survey reveals bond activation of butane on an alkaline earth metal oxide single crystal such as CaO(100).[71] Also, bond cleavage on transition metal oxides, such as PdO thin films, was reported in a surface science study.[68] Another study shows the bond activation in ethylene on O/Ni(111).[70] At present, apparently the only metal oxide single crystals/thin films studied in more detail with surface science techniques that promote alkane dissociation are Pd and Ca oxides. It is also evident that bond activation of alkanes was also seen for anatase TiO_2 thin films.[61] However, in this case, the alkanes decompose entirely, making a detailed characterization very complex. In fact, two mechanisms of bond activation have been considered for metal catalysts.[46-53] At low impact energies, a precursor-mediated bond activation occurs where the alkanes are trapped in the physisorption well before dissociation. At high impact energies, a direct (impact-induced) bond breakage in alkanes is evident. It appears that basically the same mechanism explains the molecular beam scattering data gathered so far for the butane/CaO(100) system. Molecular beam scattering on CaO(100) provided the first evidence for the occurrence of bond activation of n-/iso-butane on this metal oxide surface.[71] The selectivity of the bond activation could be tuned by changing the impact energy and gas temperature of the probe molecules. No evidence for the oxidation of the alkane or catalyst poisoning was present.

Similarly, a donor-acceptor mechanism has been proposed for alkane bond activation on transition metal oxide films such as PdO.[68-69] It utilizes multi-mass reactive TDS where C-H bond cleavage leading to adsorbed propyl/propoxy and hydrogen has been concluded for propane/PdO(101). C_3H_7 is subsequently oxidized without dehydrogenation. Besides molecular propane, only desorption of CO_2 and water were evident. Propyl appears to form below 200 K via a precursor-mediated process, but the subsequent reactions were only evident above 400 K. Density functional theory (DFT) calculations suggest the formation of dative bonds with coordinatively unsaturated Pd atoms. This weakens the C-H bonds via a donor-acceptor mechanism leading to alkane bond activation on PdO. In addition, TDS of the parent mass of the alkane leads to two features which is also seen in this study. The lower temperature TDS feature is assigned to physisorbed alkanes and the higher temperature feature is discussed in conjunction with dative bonding and coordinatively unsaturated Pd atoms. It is proposed that surface defects appear not to directly affect the dissociation of alkanes on PdO(101), but coordinatively unsaturated (cus) cus-Pd/cus-O sites may act similarly to O-vacancy sites.[68-69] On the other hand, an O-vacancy site based mechanism for methane decomposition on other PdO surfaces has been proposed.[173]

4.1.3. Sample preparation and characterization

A single crystal of as-received CaO(100) surface (~10 × 10× 2 mm) was immersed in petroleum for storage (CaO is hygroscopic) and rinsed in acetone and ethanol prior to mounting in the vacuum chamber. The sample was cleaned by UHV annealing at 1000K for 90 minutes. Auger electron spectroscopy was used to characterize the cleanliness of the surface. AES spectra of an as-received and cleaned CaO(100) sample are shown in Figure 44. For as-received sample, carbon contaminations were initially evident (see C AES peak at 278 eV) and were removed by the UHV annealing at higher temperatures. A literature survey reveals that $Ca(OH)_2$ or $CaCO_3$ layers can form on CaO which passivate the surface.[156,174-175] It was evident from the prior study that UHV annealing helps remove this passivating carbonate layer.[156] Besides a charging related peak shift (~20 eV), the AES spectra finally obtained agreed well with the reference data[176] (see the Ca AES line at 300 eV and O AES peak at 520 eV).

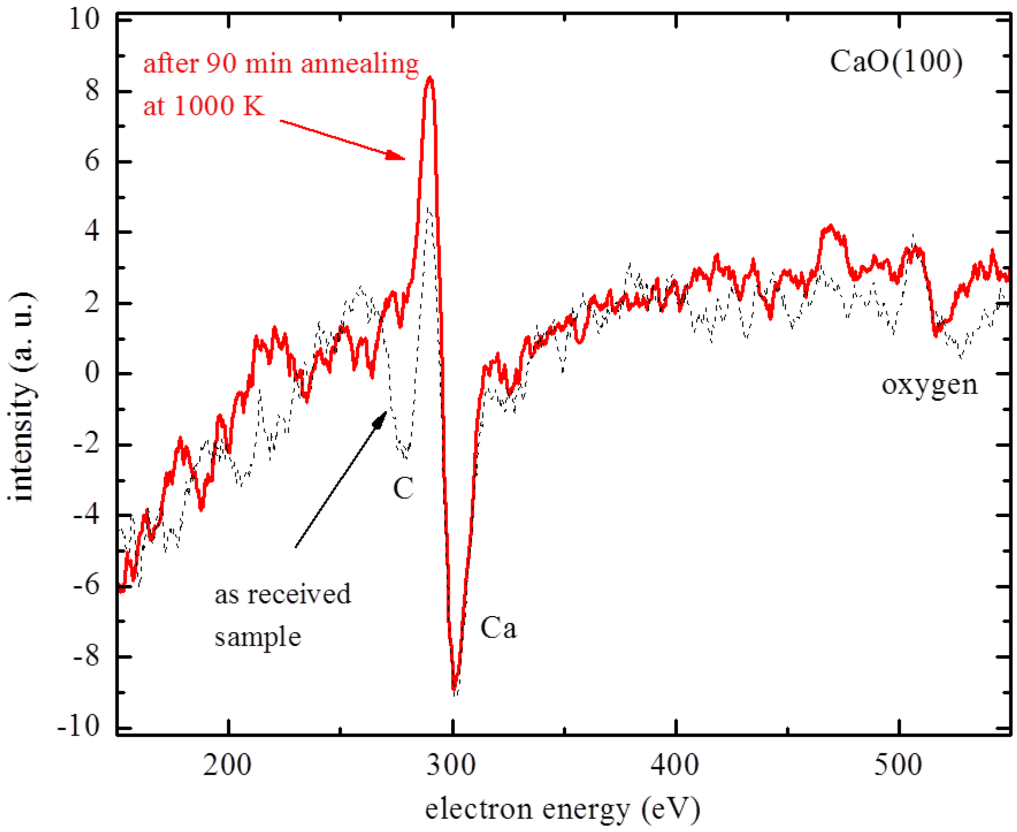

Figure 44. AES spectra of as-received and cleaned CaO(100) surface. Ref.[74]

4.1.4. Results and discussion

4.1.4.1. Blind experiment

It is worth mentioning that blind experiments have been conducted where the sample was removed from the sample holder. The Mo pins were replaced by tantalum and TDS data were then collected for the bare sample holder. By doing so, the TDS background signal observed from the bare sample holder dropped below the detection limit. Furthermore, the samples were mounted on a small (non-bulky) sample holder as a precaution to prevent unnecessary contributions from the sample holder during TDS experiments.

4.1.4.2. Molecular adsorption of alkanes

TDS curves of the parent mass of n/iso-butane, n-pentane, and n-hexane, which were collected as a function of exposure (χ), are shown in Figure 45, Figure 46, and Figure 47, respectively. The parent mass must relate to molecular adsorption/desorption of the alkanes. Thus, a molecular adsorption pathway exists. However, the exact bonding type is unknown at present. Desorption temperatures appear somewhat large to be considered for a pure physisorption. However, for PdO thin films, a system where similarly large binding energies were present, a dative bond formation has been proposed.

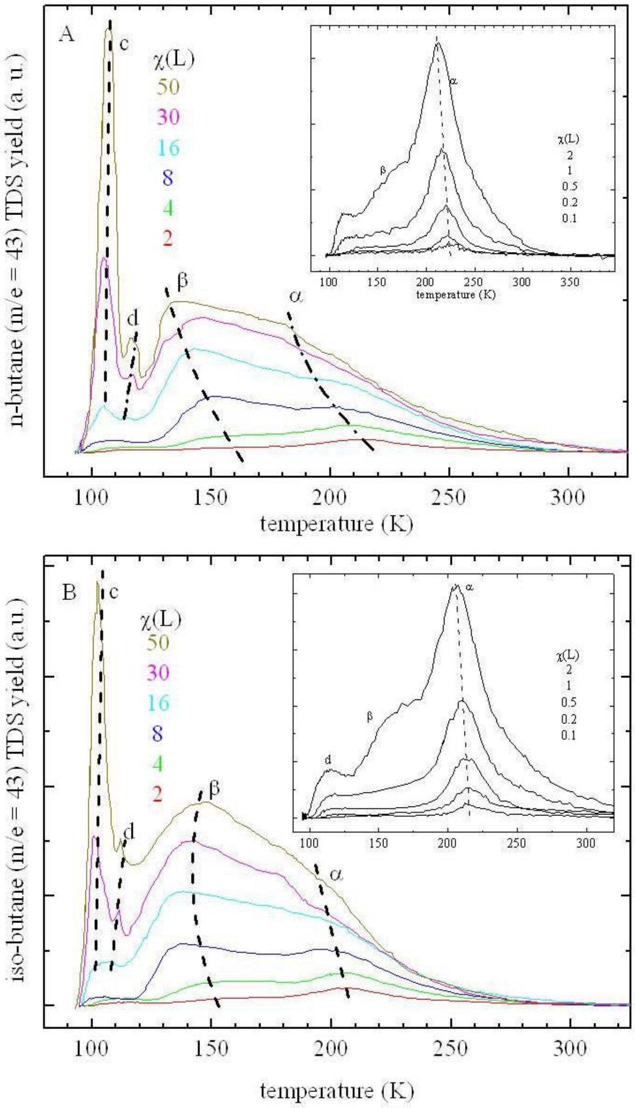

Figure 45. Thermal desorption spectroscopy (TDS) curves of the parent mass of n-butane and iso-butane as a function of exposure, χ. (c: condensation; b: bilayer; α, and β are assigned to different adsorption sites/configurations). Ref.[74]

Low exposures TDS spectra consist of only one TDS peak (α peak). With increasing exposure, a second structure grows in intensity (β peak), and at very large exposures a low-temperature TDS peak appears (c peak).

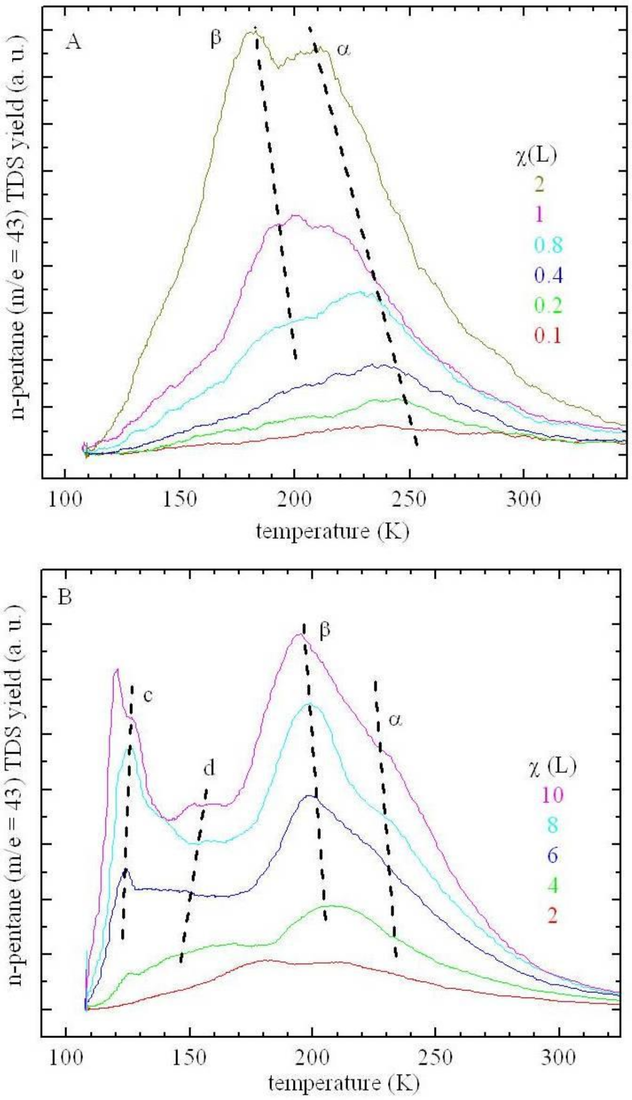

Figure 46. TDS curves of the parent mass of n-pentane as a function of exposure, χ. Ref.[74]

In addition, for butane and pentane, a second low-temperature TDS feature (d peak) is clearly evident. The c peak is assigned to multilayer formation of condensed alkanes. The d peak detected just before the onset of the condensation peak is assigned to bilayer formation. Note that the c and d peaks shift to greater temperatures with increasing exposure, whereas the α and β peaks shift in the opposite direction. The peak shifts of the c and d peaks are consistent with 0th order kinetics. The c and d peaks are typical for condensed alkanes (multilayer and bilayer).[59-]

[60,62,66-67] α and β TDS peaks are rather uncommon for alkane adsorption kinetics, except that similar TDS data is reported for PdO.[68-69]

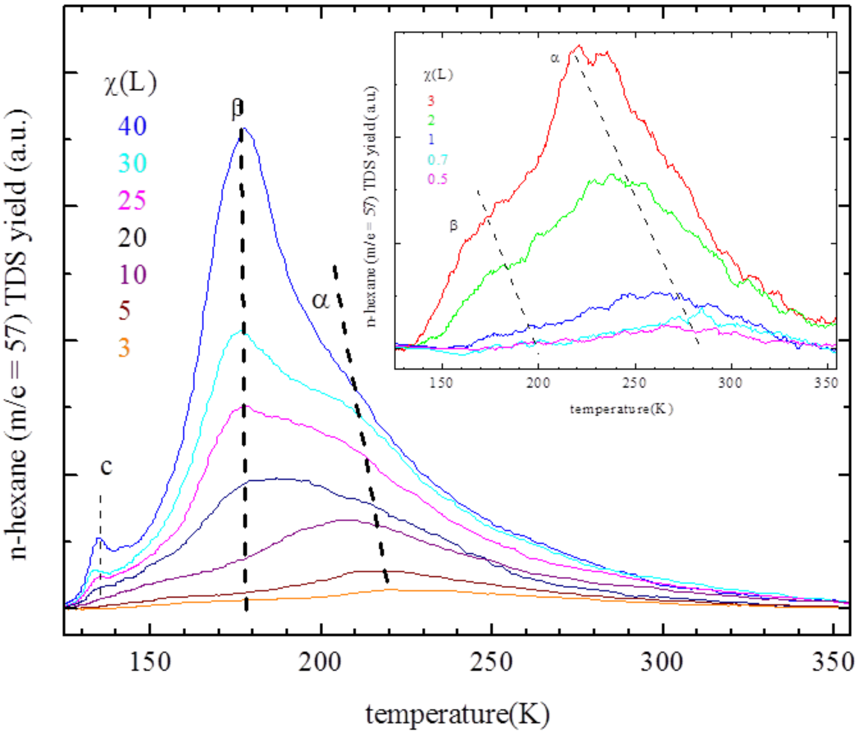

Figure 47. TDS curves of the parent mass of n- hexane as a function of exposure, χ. Ref.[74]

Typically, only one TDS feature is seen in the monolayer range as per literature search.[46-53] Both structures shift to lower temperatures with increasing exposure, which is consistent with repulsive lateral interactions and/or overlapping features resulting from different adsorption sites and/or configurations. Unfortunately, these different effects cannot be easily distinguished. In the simplest case, attractive lateral interactions would be expected, although the opposite has also been reported for metal oxides and was explained by substrate-induced polarization effects.[177] Different adsorption sites as the reason for the rather small peak shifts appear unlikely, considering the presence of two monolayer TDS features. Most alkanes commonly adsorb flat on surfaces, but they can be found in different adsorption configurations. Therefore, it is concluded that the α and β TDS peaks arise from different adsorption sites/configurations including possibly the effect of surface defects, whereas the shifting of peaks is due to repulsive lateral interactions. As expected, the TDS peak temperatures increase with the chain length of alkanes which is shown in Table 4.

Table 4. TDS peak temperatures and their corresponding binding energies. Ref.[178]

Probe molecule	**Peak temperature (K),** $\Theta_{low} \rightarrow \Theta_{high}$		**Peak temperature (K),** $\Theta_{low} \rightarrow \Theta_{high}$ $\nu = 1\text{x}10^{15}$/s		**Binding energy (kJ/mol),** $\Theta_{low} \rightarrow \Theta_{high}$ ν from ref.[59]	
	α	**β**	**α**	**β**	**α**	**β**
Ethane	223	168	66.4	49.7	66.0	49.3
iso-butane	215-194	150-140	64.0-57.6	44.2-41.2	66.9-60.2	46.2-43.0
n-butane	224-182	156-133	66.8-53.9	46.0-39.1	69.8-56.4	48.1-40.8
n-pentane	247-230	200-197	73.8-68.6	59.4-58.5	78.1-72.5	62.9-61.9
n-hexane	279-210	183-177	83.7-62.5	54.2-52.4	89.0-66.5	57.7-55.8
benzene	323 - 290	248 - 224	97.2-87.0	74.1-66.8	---	---
estimated errors	± 20		± 6		± 6	

The TDS peak temperatures were within the range of 170-280 K. Therefore, assuming a pre-exponential factor (independent of chain length) of $1\text{x}10^{15}$/sec (see ref.[59]), for first order kinetics, the binding energies were found within the range of 50-84 kJ/mol. These binding energies of alkanes on CaO were larger than MgO,[59] but were comparable to PdO.[68-69] On PdO thin films, desorption temperatures of ~150 K for methane were reported. The apparent discrepancy of CaO and PdO to MgO may be expected because alkanes adsorb only molecularly on the latter surface, whereas bond activation has been evident on PdO and CaO.

4.1.4.3. Bond activation in alkanes

The simplest way to experimentally distinguish molecular and dissociative adsorption is to record TDS traces for m/e ratios besides the parent and fragmentation masses of the gaseous species and to look for possible desorption of reaction products. If the TDS mass pattern does not match with the expected fragmentation pattern of the gaseous probe molecule, the occurrence of bond activation is predicted. The intensities may deviate from the fragmentation pattern, and/or new fragment masses, not observed for the gaseous species, may be present. The latter is a simpler means of qualitatively identifying a dissociative adsorption pathway.

4.1.4.4. Multi-mass TDS experiments results

Multi-mass TDS experiments for ethane, n-butane, and n-hexane are shown in Figures 48-50. Although the sample was not cold enough to observe the condensation of ethane, adsorption in the monolayer range was evident from the TDS experiment. The top panels in the Figures 48-50 show the mass spectra of the gaseous alkanes measured with our mass spectrometer. Similarly, the center panels depict the integrated intensities which resulted from the multi-mass TDS experiments where a constant exposure of 4 L was used. The intensities were normalized with respect to the signal at m/e = 43. Finally, the bottom panels display the difference spectra of the center panels and the top panels (TDS minus gas phase intensities, respectively). The mass scans and TDS data were not corrected for sensitivity factors that depend on a given mass. For the sake of comparison, the inset of Figure 50 depicts gas phase spectra of methane measured with our mass spectrometer and ethylene downloaded from the NIST database.

4.1.4.4.1. Ethane multi-mass experiment

It is evident from this experiment that ethane adsorbed molecularly because the mass scans for the gaseous molecules more or less matched those of the multi-mass TDS data. In other words, the difference spectra (bottom panel) consisted of close to zero intensity peaks.

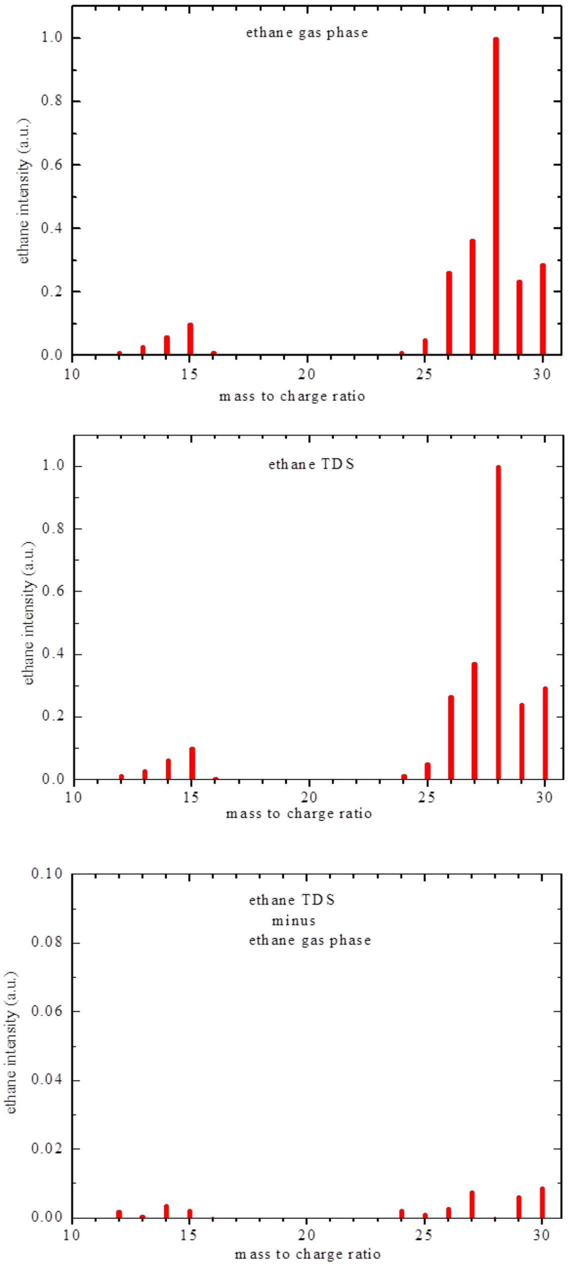

Figure 48. Multi-mass TDS experiments of ethane. Top panel: gaseous molecules; middle panel: integrated TDS peak intensity; bottom panel: difference spectra. (4 L exposure).

This result is perhaps expected, because the literature survey reveals that the bond activation in smaller alkanes such as methane and ethane on metal surfaces requires a much larger activation energy than bond-breaking in longer chain alkanes.[49,179]

4.1.4.4.2. Long chain alkanes multi-mass experiments

Besides ethane, multi-mass TDS experiments were conducted for n-butane and n-hexane as shown in Figures 49 and 50.

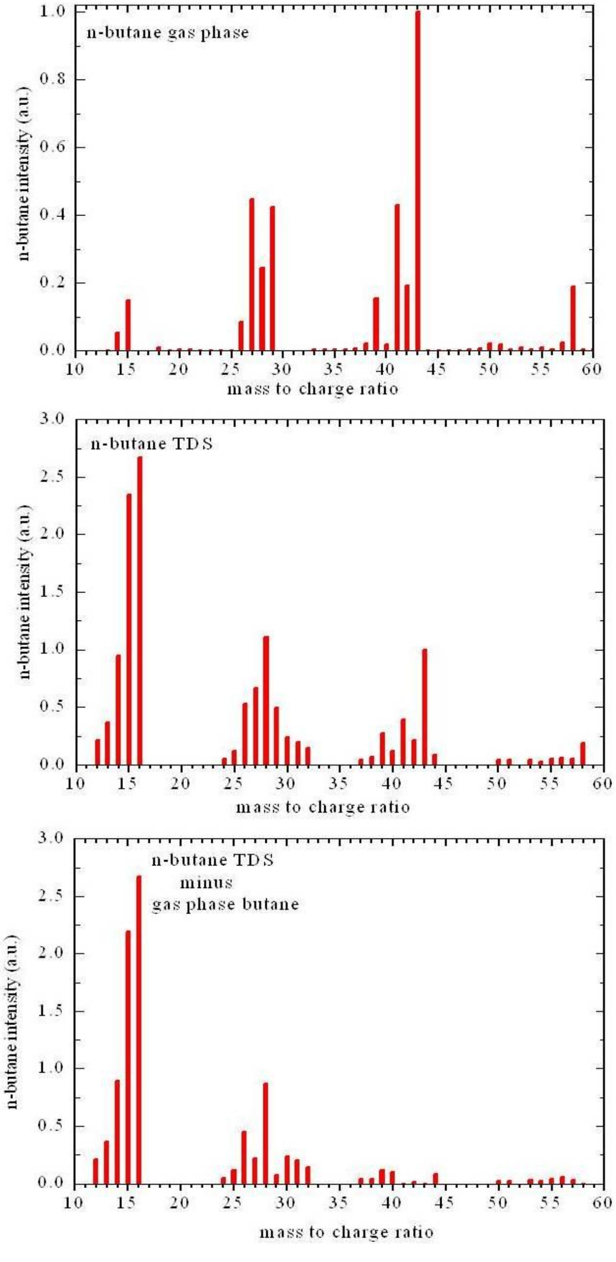

Figure 49. Multi-mass TDS experiments of n-butane. Top panel: gaseous molecules; middle panel: integrated TDS peak intensity; bottom panel: difference spectra. (4 L exposure).

Bond activation was evident for these probe molecules for the reason that the multi-mass TDS data deviate significantly from the data of the gaseous molecules. The relative intensities of the fragmentation pattern of the gaseous molecules did not match those obtained in multi-mass TDS scans.

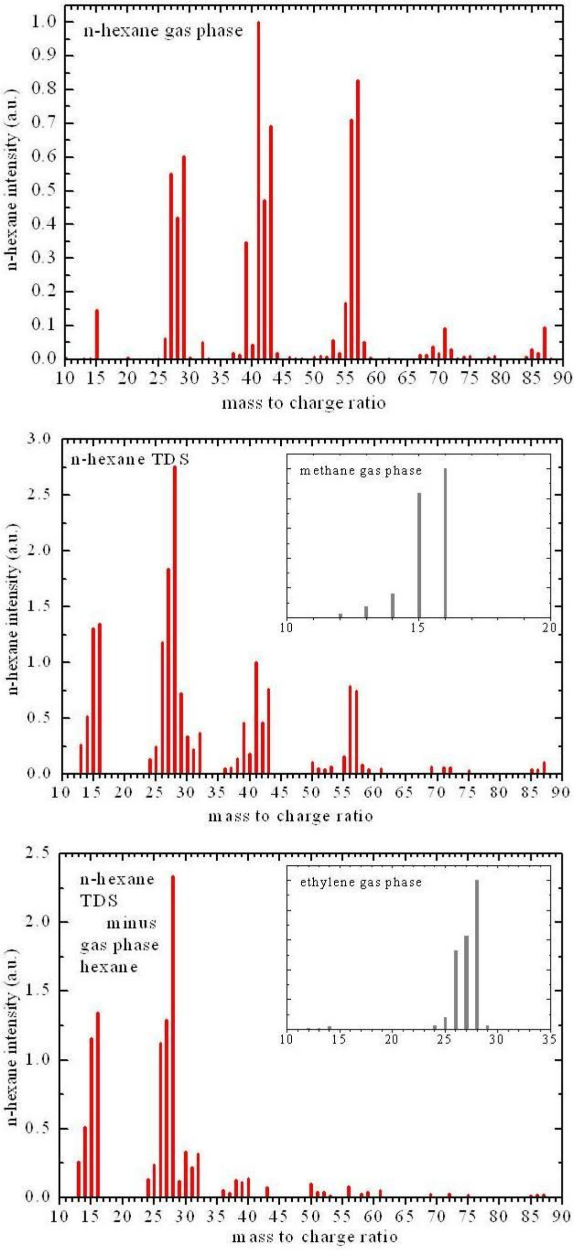

Figure 50. Multi-mass TDS experiments of n-hexane. The insets depict the mass scans of gaseous methane and ethylene.

Also, new masses that were not present at all in the fragmentation pattern of the gaseous molecules appeared in the multi-mass TDS scans. For example, no signal at m/e = 16 was present for gaseous n-butane and n-hexane, but it appeared in their multi-mass TDS data. The signal detected at m/e = 16 while dosing various exposures of n-butane and n-hexane on the surface is shown in Figure 51.

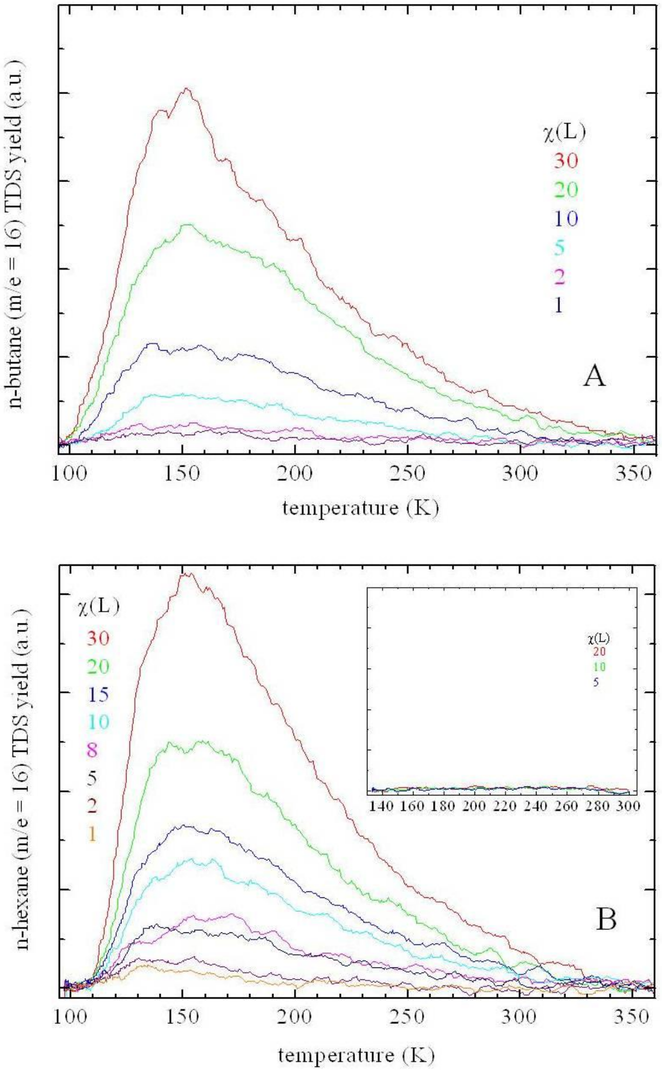

Figure 51.TDS data for m/e = 16 when dosing **A)** n-butane and **B)** n-hexane. The exposures have been varied. The inset in B shows results of blind experiments

Interestingly, only one TDS feature appeared for this fragment mass unlike the features in TDS of parent mass. Taking sensitivity factors of the mass spectrometer into consideration, the ratio of signals at m/e = 16 to the parent mass of hexane amounted to about 0.15, approximately independent of exposure. Therefore, the desorption signals of the fragmentation masses are fairly large as compared with the parent mass. However, conversion rates cannot be easily determined using TDS data. Importantly, a signal at m/e = 16 was below the detection limit of the mass spectrometer when removing the sample and conducting TDS experiments on the bare sample holder, as shown in the inset of Figure 51B.

4.1.4.5. Proposed mechanism

The deviations seen in the mass pattern and gas phase spectra (determined with the same mass spectrometer) were similar for all the longer chain alkanes studied. Most significant is the appearance of TDS peaks at m/e = 13 to 16, which more or less matches the mass spectra of gaseous methane (see the inset of Figure 50B). This draws a conclusion that mostly methane is formed. The m/e = 16 and 28 ratios do not match with CO. Likewise, strong contributions from background adsorption of CO_2 can be ruled out. The peak at m/e = 28 and m/e = 30 could possibly result from fragmentation into either ethane or ethylene. Hydrogen desorption was seen in the TDS experiments. Therefore, besides methane, it is likely that mostly ethylene is formed via hydrogen abstraction. This would lead to the following scheme of reactions for the bond activation in n-butane:

$$\mathrm{Surface\text{-}O + CH_3\text{-}CH_2 - CH_2\text{-}CH_3 \rightarrow Surface\text{-}OH + \bullet CH_2 - CH_2\text{-}CH_2 - CH_3} \qquad (4.1)$$

$$\mathrm{\bullet CH_2 - CH_2 - CH_2 - CH_3 \rightarrow CH_2 = CH_2 + \bullet CH_2 - CH_3} \qquad (4.2)$$

Equation 4.1 describes the result of the hydrogen abstraction and equation 4.2 depicts the C-C bond activation. A similar mechanism has been proposed in previous catalysis studies on n-hexane/MoO_2.[180] This mechanism suggests that the lattice oxygen is involved in bond activation. For example, the formation of carbonates on CaO by CO_2 involving lattice oxygen is an established mechanism for CaO powders[181] and single crystals.[156,182]

Similarly, the existence of features at m/e = 29, 39, and 41 might be due to the formation of reaction products such as propane, propylene, and butene during the process. However, we can rule out a number of other possibilities at this point due to insufficient proof to support their formation. AES did not detect carbon residuals on the surface, and catalyst deactivation was absent. Thus, the alkanes do not undergo complete bond activation, seen in the anatase TiO_2 system[61] or often observed for metal catalysts.[52] No distinct signal was present for m/e = 18, which would be expected for an oxidation of the alkanes, as seen for the PdO system.[58,68]

The effect of defects has always been a difficult question to address in this regard. The CaO single crystal used in this study certainly might have a large, but not precisely known, intrinsic density of defects. In a prior study, CO_2 TDS was used to estimate a 40% density of defects.[156] Therefore, it appears plausible that defects influence adsorption kinetics. However, definite proof would require a precise study of a nearly defect-free surface. Unfortunately, this type of system is presently not available for CaO to the best of our knowledge.

4.1.5. Summary

The adsorption kinetics of small chain alkanes on CaO(100) single crystal was studied by multi-mass TDS experiments. Two reaction pathways were evident, namely: molecular adsorption and bond activation for the linear alkanes larger than ethane. The molecular adsorption pathway in the monolayer range leads to the detection of two features in TDS data that were assigned to different adsorption sites/configurations. Bond activation in longer chain alkanes led to the formation of mostly methane and ethylene via hydrogen abstraction. Only gaseous reaction/decomposition products were seen in this study whereas oxidation of the alkanes can be ruled out. This is a rare example showing bond activation in alkanes by a metal oxide single crystal.

4.2. Alkane and water adsorption on Sb(111) surface

An introduction to the importance of studying metalloid like Sb is presented first, followed by the brief literature survey about the applications of antimony (Sb). A combined results and discussion section about the distinct hydrophobic character of the antimony surface is presented along with the co-adsorption of water and n-butane on the Sb (111) surface.

4.2.1. Introduction

Antimony is a semiconductor which can be present in natural coal and can be released with the plume in coal power plants.[183-184] Therefore, it is important to study the interactions of coal combustion gases with the antimony model system. Surface science investigations about the adsorption kinetics of small molecules have apparently not been published for any Sb surface. Unexpectedly, our results show that neither H_2, CO, CO_2, nor NO appear to adsorb on Sb(111) down to adsorption temperatures of 85 K. Besides alkane adsorption, only water seems to adsorb on the Sb surface and significant hydrophobic character is evident. The alkane adsorption on Sb(111) studied in this dissertation, has never been reported in the literature. However, the focus of this research is on adsorption of water and its co-adsorption with n-butane to characterize the hydrophobic property of Sb(111) surface. Recently, hydrophobic surfaces have attracted significant interest in the surface science, catalysis, and engineering communities due to unusual physico-chemical properties and numerous applications (in catalysis, electrochemistry, medicine, geology, etc.).[185-186] The term “lotus effect” is used to describe superhydrophobicity since the leaves of lotus plants are water repelling. A large number of studies focus on various nanostructured surfaces of complicated morphology.[185] For example, antimony oxide nanoparticles supported on glass substrates are super-hydrophobic in nature.[187] Similarly, octane or hydrogen terminated Pt and Ni surfaces, respectively, show hydrophobic properties.[188-189] It is evident that nonwetting ice crystallites can be formed on Pt single crystals when covered first with a complete monolayer of water ice.[190]

Water desorption is often discussed in regard to submonolayer and multilayer formation while amorphous or crystalline water layers are formed only at large exposures. Water condensation peaks are evident in TDS at the temperature range of 150-160 K, whereas monolayer desorption occurs typically at about 170 K.[186,191-193] Usually, recombinative H_2O desorption of OH and hydrogen can result in higher temperature features.[186] Interestingly, for hydrophobic surfaces, a monolayer feature in TDS will be missing and only one desorption peak is seen that obeys 0th order kinetics.[189-190] Therefore, TDS can be used to distinguish hydrophobic (non-wetting) and hydrophilic (wetting) surfaces based on the feature present in TDS. In fact, a hydrophobic or nonwetting interaction results in porous water films, whereas wetting or hydrophilic interaction leads to layer-by-layer growth.

In this study, an example of a single crystal surface by itself, without any apparent functionalization showing strong hydrophobic (nonwetting) properties is reported. The only other known hydrophobic single crystal systems until now are surfaces of Au, Ag, and Cu. Among these systems, gold is the only system being the clear example.[190,194]

4.2.2. Brief literature survey

A systematic literature search revealed, perhaps unexpectedly, numerous surface science publications about antimony. Mostly Sb thin films and clusters have been studied in surface science,[195-196] motivated by applications in the semiconductor industry, but supported Sb oxide nanoparticles recently revealed super-hydrophobic effects.[187] Despite its toxicity, Sb finds applications in materials science (ceramics, alloys, paint) and even medicine. Vapor depositing these highly toxic elements (using crucibles and pure materials or, e.g., H_2Se gas[197]) on supports such as silica/silicon in order to form thin films or clusters has been applied by a number of groups.[195-196] Since metalloids crystallize in rather complex structures and show unusual electronic properties, it makes their study interesting from a fundamental perspective. However, nearly all of the studies focus on characterization of the geometrical and electronic structure. Techniques such as Auger electron spectroscopy (AES),[198] low energy electron diffraction,[199] reflection high energy electron diffraction (RHEED),[200] high resolution electron energy loss spectroscopy (HREELS),[198] x-ray photoelectron spectroscopy (XPS),[201] photoelectron diffraction,[202] and scanning tunneling microscopy[203] have been used to characterize Sb single crystals. Sb is a rhombohedral bulk structure which means Sb(111) has a truncated hexagonal structure.[203] Although bulk Sb is a semi-metal, the surfaces apparently show a metallic character.[202]

Thermal desorption spectroscopy, molecular beam scattering, Auger electron spectroscopy, and X-ray photoelectron spectroscopy have been used to characterize n-butane and water adsorption on antimony single crystal surface. Perhaps the safest way to characterize these systems in a model study is by using single crystals. In addition, coadsorption experiments of water and n-butane have been studied to characterize the hydrophobic character of the antimony surface.

4.2.3. Results and discussion

4.2.3.1. Sample characterization

AES spectra for as-received and cleaned Sb surface are shown in Figure 52. The surface was initially covered by a layer of carbon containing impurities. This layer was sputtered off by Ar^+ bombardment; several additional cleaning cycles were required to remove an intrinsic oxide layer. Finally, AES spectra in agreement with the reference data[176] were obtained, indicating a chemically clean surface. In addition, a presence of LEED pattern further reveals a cleanliness of the surface and shows a hexagonal pattern as expected for Sb(111).[199]

Similarly, XPS spectra of the cleaned surface reveals no indication of impurities and only shows the expected Sb lines.[204] For XPS, a Mg Kα line (at 1253.6 eV) was used with a pass-energy of 50 eV of the analyzer. The XPS spectra were referenced with respect to the C1s peak at 284.5 eV (using carbon contaminations of the as-received surface).

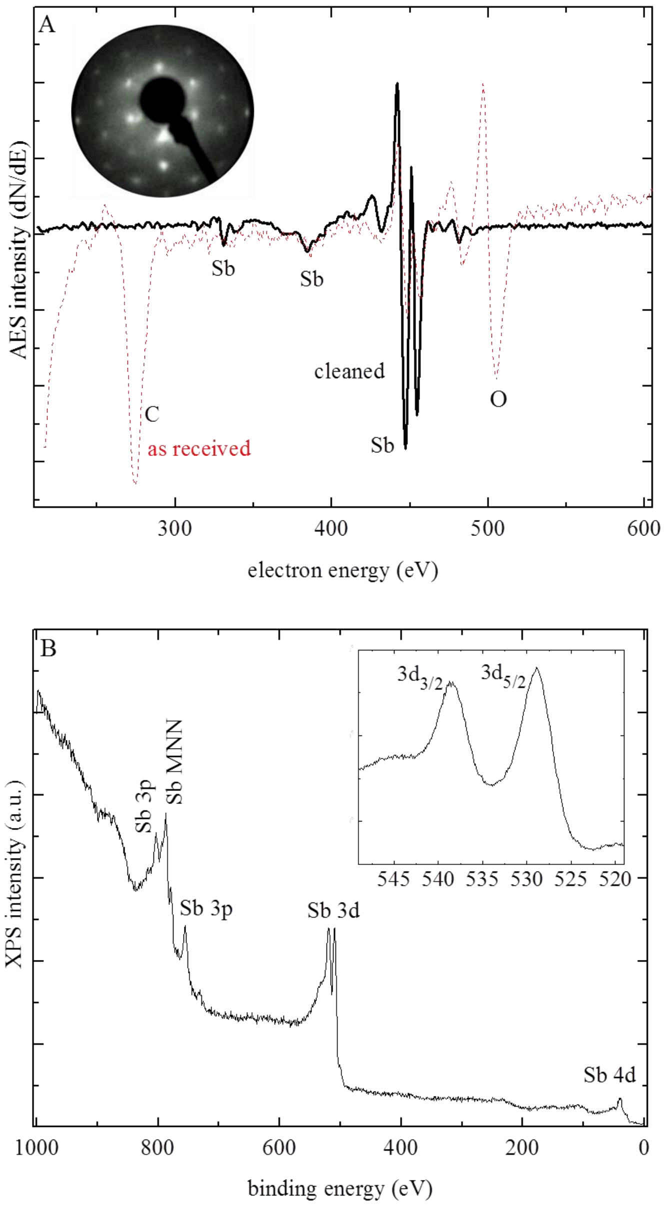

Figure 52. (A) AES spectra of Sb(111) before cleaning (dashed line), and after cleaning (solid line). The inset shows the LEED pattern of the Sb(111) surface after cleaning. (B) XPS spectra of Sb(111) after cleaning. The inset shows XPS Sb 3d peaks after cleaning.

4.2.3.2. Alkane adsorption

A set of n-butane TDS curves collected as a function of exposure, χ, is shown in Figure 53. A pure n-butane is dosed using a molecular beam and the exposure time is given in sec. The inset depicts data for small exposures. Only one TDS peak (α peak) is evident at lower exposures with its position at approximately 123 K independent of exposure.

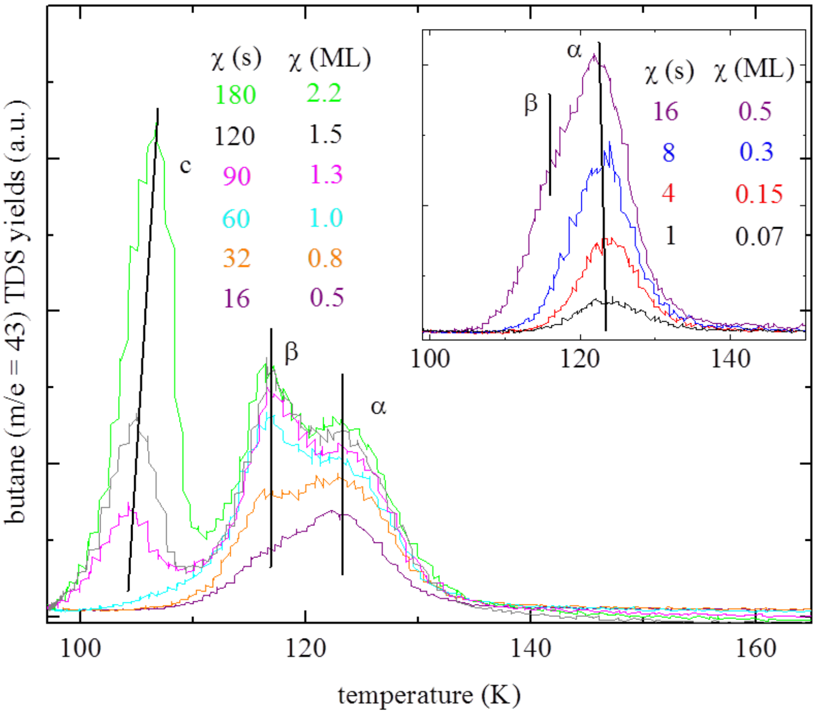

Figure 53. n-butane TDS as a function of exposure on Sb(111). Exposure time and the corresponding coverage are indicated. The inset shows TDS for small exposures.

With increasing χ, first a structure at 118 K (β peak) emerges, and then at large exposures a peak at 105 K (c peak). The c peak intensity does not saturate, and the peak position shifts to greater temperatures with increasing χ, while the leading edges of the TDS curves line up. These properties identify the c peak as a condensation peak. The β structure may be related to lateral interactions or bilayer formation. Strong lateral interactions of non-polar alkanes are unlikely, but bilayer desorption features have been seen before[205] in studies of alkane adsorption. Therefore, we assign the β TDS peak to desorption from bilayers. The structure evident at the smallest exposures is commonly seen and assigned to n-butane adsorption within the monolayer range. A Redhead analysis results in a binding energy of 34.4 kJ/mol with 10^{15} s^{-1} as the pre-exponential factor.[205] Integrating the TDS curves and normalizing the area at the onset of the c peak to 1 monolayer (ML) results in the coverage calibration which is also given in Figure 53. Here coverage of 1 ML simply indicates saturation of the surface with n-butane at 85 K; the absolute particle density is not easily available. AES or XPS did not reveal any carbon after the TDS experiments and no new fragments were evident from the multi mass TDS experiments which led us to conclude that the adsorption of the alkane is molecular.

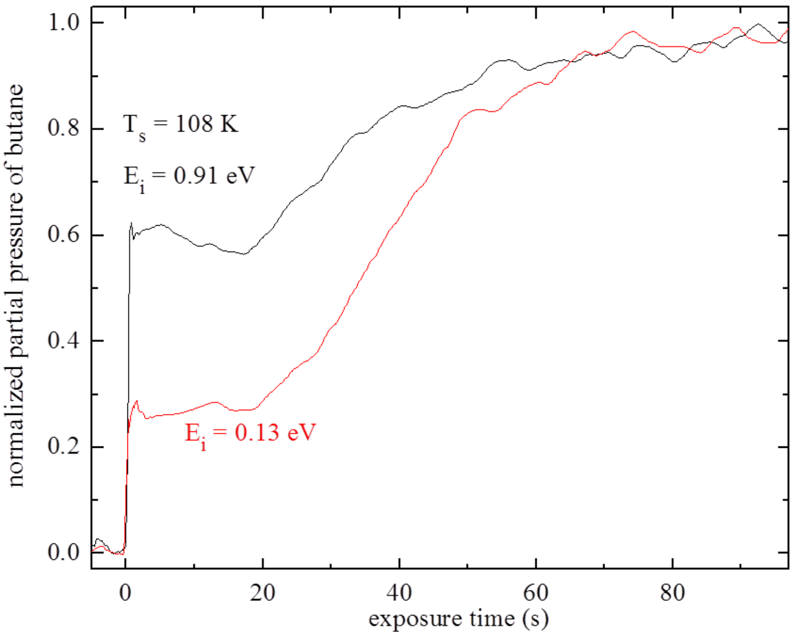

Figure 54. Adsorption transients of n-butane on Sb(111) at two different impact energies.

A typical adsorption transients[206] of n-butane for two different impact energies is shown in Figure 54. N-butane was dosed on the surface at 108 K to prevent the condensation of n-butane, with the beam exposure starting at a time of t = 0 sec. A typical Kisliuk-like shape of the transients is evident, since the adsorption probability remained essentially constant up to saturation of the surface. Therefore, standard precursor-mediated adsorption was obeyed.[207] Figure 55 depicts the initial adsorption probability, S_0, as a function of impact energy, E_i, at 108 K. S_0 decreases with increasing E_i implying the adsorption was molecular and non-activated adsorption. This trend simply reflects the decreasing efficiency of the gas-to-surface energy transfer with increasing E_i (and decreasing interaction time).[52]

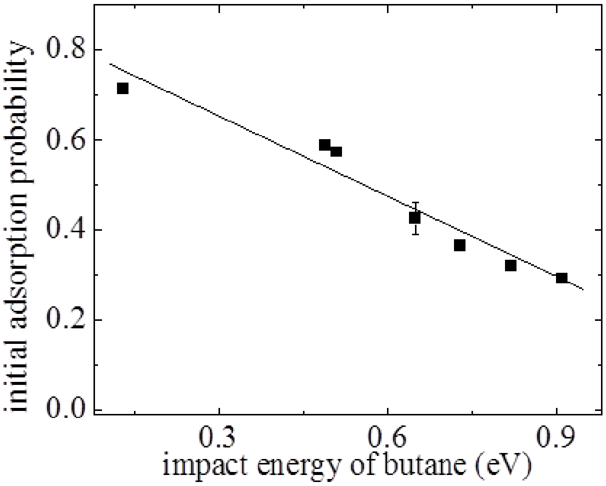

Figure 55. The initial adsorption probability of n-butane as a function of the impact energy.

4.2.3.3. Water adsorption

A set of water TDS curves collected as a function of exposure, χ, is shown in Figure 56. Water was also dosed on the surface using a molecular beam to prevent any background effect from the sample holder. The exposure, χ, is given as the beam exposure time in sec and in Langmuir (1 Langmuir = 1 L = $1\text{x}10^{-6}$ mbar sec). TDS data collected by backfilling the chamber and by beam exposure are compared to estimate the water exposure in Langmuir. As evident from the experiment, only one water TDS peak is seen, which shifts from 140 to 152 K with increasing exposure. The low temperature edges of the TDS peaks line up perfectly. The peaks are asymmetric, with a sharp step-like decrease at the greater temperature edges. No monolayer TDS peak was seen at any exposure. All of these features are consistent with (near) 0^{th}-order kinetics and water condensation on a hydrophobic surface.

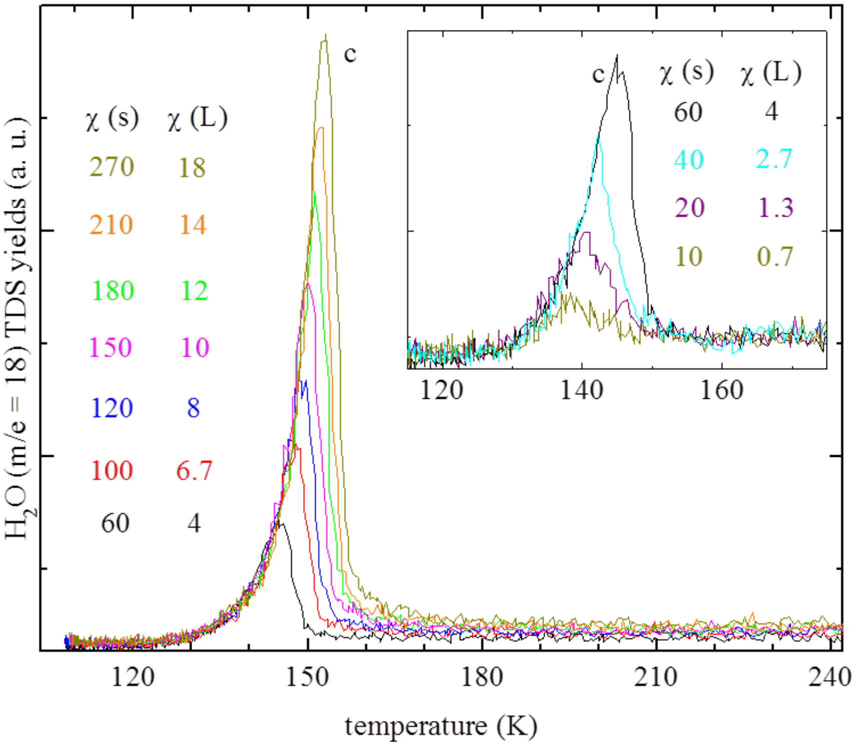

Figure 56. H_2O TDS as a function of exposure on Sb(111). The exposure time in sec and corresponding exposure in Langmuir are indicated. The inset shows TDS for lower exposures.

Therefore, it is concluded that water already forms multilayer islands on Sb(111) within an exposure range where monolayer desorption at greater temperatures would be seen for “hydrophilic” surfaces. In other words, the water-water interactions dominate the kinetics rather than the water-surface interactions. Similarly, no further water TDS peaks were evident up to 300 K and multi mass TDS experiments did not provide evidence for H_2 desorption when heating the water molecules. Water adsorbed molecularly on the Sb(111) surface. There was no apparent “functionalization” of the surface, which appeared clean when inspected by XPS and AES after the TDS experiments. In addition, a large uptake of H_2 from the background seems unlikely due to the inertness of the surface. Therefore, all these results reveal that Sb(111) is intrinsically hydrophobic in nature. This has rarely been seen that clearly before in TDS experiments except for inert gold surfaces.[190,207] Unexpectedly H_2, CO, CO_2, and NO did not adsorb on Sb(111) down to adsorption temperatures of 85 K.

4.2.3.4. Water and butane co-adsorption

The growth of water is further characterized by co-adsorption experiments of water and fairly inert n-butane as shown in Figure 57. It is evident from a study about water adsorption on octane films that water does not adsorb efficiently on closed alkane films deposited on a Pt(111) support, which shows its hydrophobic character.[188]

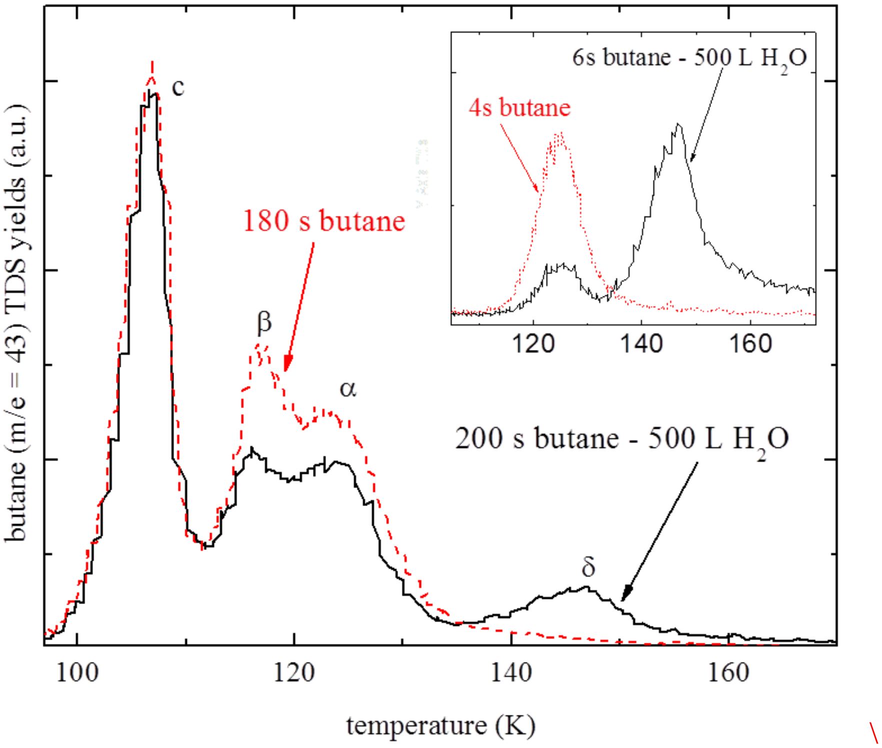

Figure 57. TDS of n-butane on clean and 500 L water pre-covered Sb(111) (exposures at 85 K).

Adsorption transients are shown in Figure 54 and 58 (solid lines as well as dashed lines). Note that the area above the transients and below the saturation level in these figures equals the number of adsorbed species (saturation coverage). Figure 58 depicts n-butane adsorption transients for a Sb(111) surface pre-covered with different amounts of water at 108 K. At small water exposures (10 L), the transients of the clean and water-covered surface coincided perfectly. In addition, the TDS spectra of n-butane were identical to the clean surface. Thus, the water pre-covered surface appeared basically as clean when co-dosing n-butane, as perhaps expected for a hydrophobic surface. Previous water TDS experiments certainly confirm that water was indeed adsorbed. This confirms that there was no site blocking for n-butane adsorption by water at exposures lower than 500L.

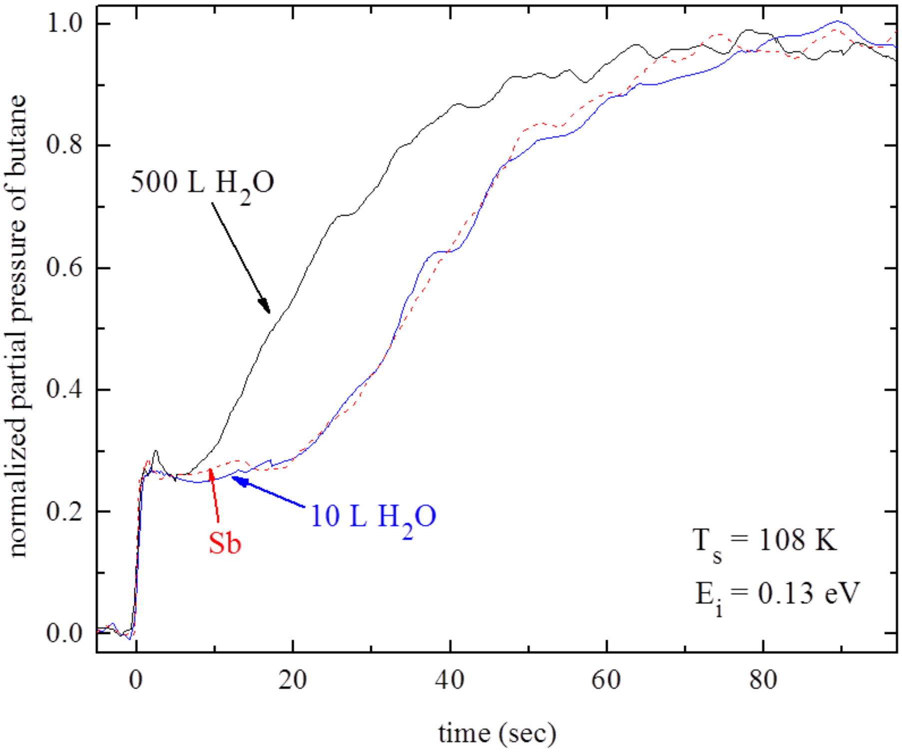

Figure 58. Adsorption transients of n-butane on different amounts of water pre-covered Sb(111) dosed by backfilling at 108 K. (The dashed line indicates the saturation level.)

4.2.3.5. Site blocking effect

Site blocking for n-butane adsorption by water was observed at exposures greater than 500L according to the experimental results. At exposures as large at 500 L H_2O, all nucleation sites were blocked by water, and most likely a rather thick and porous water film was formed. In this case, site blocking of butane by water was evident, since the butane saturation coverage was smaller than for the clean surface (Figure 58). A part of the n-butane appeared to be trapped inside the water film. These transients were collected at a constant surface temperature of 108 K, which appears sufficient to freeze out diffusion to a large extent. The n-butane was indeed partially encapsulated by the water film as evident from the TDS data shown in Figure 57. Depicted are butane TDS data for the clean (solid line) and water pre-covered (dashed line) surface. The inset depicts data for small butane exposures. A higher temperature n-butane TDS peak (δ) at ~148 K appears for the water pre-covered surface in addition to the monolayer (α), bilayer (β), and condensation (c) peaks seen for the bare surface. Surprisingly, the position of this δ peak coincides well with the water TDS peak as seen Figure 56. This led to the conclusion that when the water layer started to desorb, the trapped butane was released. The area of the δ TDS peak equaled, however, only 0.17 ML (see main panel of Figure 57), whereas the n-butane saturation coverage in the transients (Figure 58) was reduced by nearly 50%. It should be noted that not all pores in the water film will allow diffusion down to the surface layer, and the TDS data will be more strongly affected by diffusion than the isothermal transients. Although the mechanistic details of the coadsorption experiment are not entirely known at this point, it is clear that the alkanes still adsorbed on the surface even when pre-covered by large amounts of water. This indicated the formation of a porous water film, as expected for a hydrophobic surface. Also, none of these probe molecules dissociated on the surface which would have led to perhaps irreversible side blocking effects.

4.2.4. Summary

In summary, the adsorption of n-butane on Sb(111) surface was found to be molecular and non-activated. Two TDS features were assigned to desorption from monolayer and bilayer ranges. A distinct hydrophobic character of Sb(111) surface was indicated through experimental results. In addition, antimony surfaces appeared inert towards the adsorption of small molecules such as H_2, CO, CO_2, and NO. Site blocking for n-butane adsorption by water was evident at exposures greater than 500L of water. Neither water nor n-butane were dissociatively adsorbed on the surface of Sb(111).

4.3. Alkane adsorption on MoO_x nanoclusters

The importance of molybdenum and molybdenum based catalysts are discussed in the first section followed by a brief literature survey about Mo-based catalysts and bond activation in alkanes. Detailed results and discussion about the difference of catalytic activity of butane adsorption on metallic Mo and oxidic Mo are presented next, followed by the summary of this study.

4.3.1. Introduction

Mo single crystals have been studied extensively as a hydrodesulfurization (HDS) catalyst for the last few decades.[208] Similarly, Mo clusters and inorganic nanotubes have also been considered as HDS catalysts.[209-211] Mo clusters can decompose small organic molecules such as methanol (MeOH) and thiophene. Decomposition of even CO, and CO_2 on Mo has been reported due to its reactive nature.[212-213] Therefore, it is interesting to characterize the surface chemistry of small organic molecules interacting with Mo-based catalysts. In the present study, we characterized the adsorption of alkanes on a Mo clusters sample which were fabricated utilizing electron beam lithography. Scientifically, it is interesting to compare the chemical activities of metallic and oxidic clusters. It is a known fact that the properties of catalysts can be dramatically altered by surface oxidation which can be used to tune the catalytic behavior of a given system or to prevent catalyst deactivation.[214-216] To understand the underlying mechanism, molybdenum and oxidic molybdenum have been extensively studied in recent years, as an important example.[217-219]

4.3.2. Brief literature survey

Historically, Mo catalysts were used for HDS of coal[220-221] and raw oil[208] while Mo oxides were used to catalyze oxidations.[222-223] The decomposition of methanol has been investigated on metallic and oxygen-modified Mo single crystals.[224] It has been found that methanol decomposes on clean Mo(100) and desorbs without decomposition from oxygen-saturated Mo(100).[217,224] The saturation coverage for methanol on Mo(100) and Mo(110) decreases with the extent of surface oxidation.[225] These studies suggest that although Mo is quite reactive, complete oxidation makes the Mo surfaces inert. Most early studies were conducted on various Mo single crystals; however, supported Mo and Mo oxides clusters have been recently considered.[226-228] Berkó et al. deposited Mo clusters on TiO_2(110) by PVD.[226] The clusters were stable up to annealing temperatures of 900 K and partial oxidation by lattice oxygen occurred at 900 - 1050 K. Mo clusters supported on SiO_2 through PVD were oxidized by annealing at 600 K in $1x10^{-6}$ mbar molecular oxygen.[221] In contrast, oxidizing Mo single crystals requires significantly extreme reaction conditions.[225,229] Therefore, one may speculate that real-world catalysts are strongly affected by oxidation which leads to catalyst deactivation.

Similarly, bond activation of alkanes has been studied for decades as a model system with a historic focus on metal single crystal surfaces.[47,230-236] Only a few surface science projects about the adsorption of alkanes on non-metallic systems have been conducted. Only molecular adsorption has been seen for MgO,[237] ZnO,[238] rutile TiO_2,[61-62] silica,[239-240] and graphitic systems.[241-243] In a recent study, for an alkaline earth metal oxide single crystal, CaO(100), bond activation of butane was evident.[178] Later, bond cleavage on transition metal oxides, PdO thin films, was also reported.[244] Therefore, at present, the only metal oxide single crystals/thin films studied in more detail with surface science techniques that promote alkane dissociation are Pd and Ca oxides. Palladium is quite rare and expensive which makes it a poor choice for a sustainable economy. Note that bond activation of alkanes was also present for anatase TiO_2 thin films, however, the alkanes were decomposed entirely in this case making detailed characterization very cumbersome. In addition, the TiO_2 catalyst is poisoned in that process.[245]

In this study, the discrepancy in catalytic activity on Mo and oxidic Mo clusters was characterized using an alkane (butane) as the probe molecule. The model catalyst was nanofabricated by electron beam lithography using silica as a support.

4.3.3. Results and discussion

4.3.3.1. Sample morphology

The EBL sample of Mo clusters on silica support was nanofabricated at Molecular Foundry (Lawrence Berkeley National Laboratory).[246] Mo clusters with a diameter of $d_s = (77 \pm 2)$ nm were arranged in a hexagonal pattern with a lattice constant of $a_s = 150$ nm and a height of about 5 nm. A 5 mm by 5 mm area was covered with the Mo clusters on a 10 by 10 mm silica support. Although the Mo cluster size, shape, and height, as well as lattice constant were predetermined in the EBL fabrication, the sample was still inspected by scanning electron microscopy (SEM) as shown in Figure 59A. SEM images of the samples were collected before the UHV experiments at Lawrence Berkeley National Laboratory with a Zeiss Ultra 60 equipped with a field emission gun. Similarly, SEM imaging after the experiments was conducted at Brookhaven National Laboratory with a Hitachi S-4800 UHR.

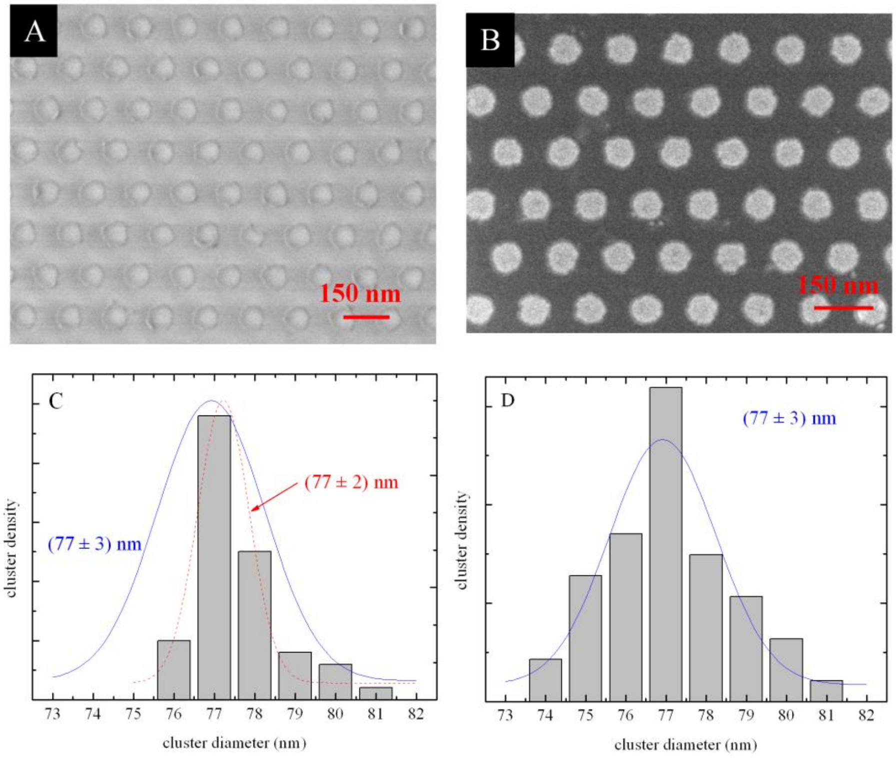

Figure 59. A) SEM images of 77 nm Mo EBL clusters supported on silica before B) after the UHV experiments. C) and D) represent corresponding cluster size distributions. Ref.[247]

The size distribution of the clusters is depicted in Figure 59C as a bar diagram and was determined by using a pixcavator software tool. The cluster size distribution is with 2/77 = 2.5% narrow (using the FWHM of the Gaussian fit shown in Figure 59C as a solid line). Figure 59B depicts SEM images collected after the UHV experiments showing unchanged morphology of the sample. The cluster size distribution (shown in Figure 59D) was also unaltered, i.e., significant sintering was absent. In order to better compare the cluster size distributions, Figure 59C depicts the Gaussian fits together. However, a slight broadening of the distribution was evident for the used model catalyst. This could indicate the capture of small metal residuals from the lift-off process by the larger Mo clusters, caused by the sample annealing.

4.3.3.2. Sample cleaning and characterization

Mo single crystals are usually cleaned by a thermal treatment at rather high temperature, e.g., annealing at ~1700 K under O_2 atmosphere followed by flashing to 2300 K.[217,219,224-225,229,248-251] Unfortunately, this standard cleaning procedure is not applicable to EBL samples. Therefore, the Mo EBL sample studied here was initially cleaned by mild room temperature sputtering/annealing cycles (one minute each, sample current 2 μA), followed by annealing at 700 K in oxygen (1×10^{-8} mbar), and a flash to only 750 K. During this cleaning procedure, the sample was inspected regularly by AES which is shown in Figure 60A. The carbon impurities did act as a buffer layer protecting the Mo clusters. Afterwards, cycles of oxygen annealing at 700 K for 10 minutes were applied which finally brought the carbon impurities below the detection limit of the AES system as shown in Figure 60B. Unfortunately, this procedure will also likely oxidize the Mo clusters.[221] Again, the high-temperature (1050 K)[252] annealing used to reduce Mo single crystals does not work for EBL clusters. Therefore, as a final cleaning step, the EBL sample was annealed in a flux of atomic hydrogen ($p(H_2) = 1 \times 10^{-7}$ mbar, $T_s = 750$ K, for two hours). It should be noted that the Mo/Si AES intensity ratio remained constant and sample morphology was conserved during the whole cleaning procedure.

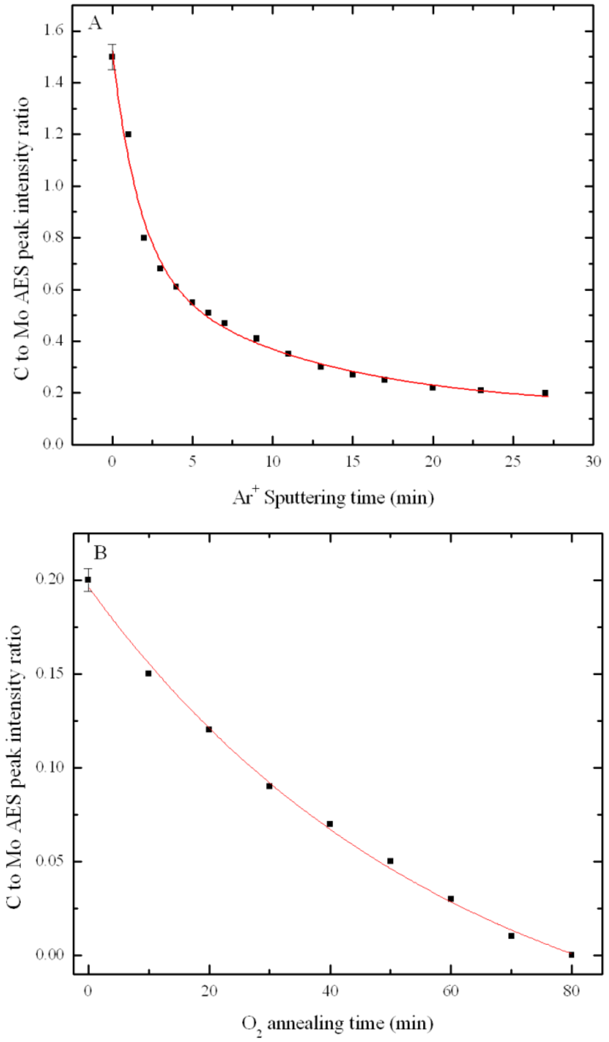

Figure 60 . Cleaning procedure curves of Mo EBL clusters. (A) cleaning with Ar^+ sputtering, (B) cleaning with O_2 annealing. Ref.[247]

Figure 61A depicts AES survey scans of the as received and cleaned Mo EBL sample. The XPS spectra were referenced with respect to the O 1s line at a binding energy of 532.9 eV (see ref.[253]). Besides Si and O AES peaks from the support and Mo AES features, no other structures were evident for the cleaned sample.[139] Similarly, a XPS survey scan of the cleaned Mo EBL sample is shown in Figure 61B which confirms the absence of carbon and other impurities on the surface. The XPS peak positions of Si, O, and Mo agree with reference data.[253]

The inset depicts the XPS of the silica 2p region. Only one peak is evident for fully oxidized silica, whereas two peaks are typical for partially reduced silica.[253] Thus, the cleaning procedure did not reduce the silica support.[254-255] This fact may be important, since silica is non-reactive, but silicon is somewhat highly reactive.[239-240]

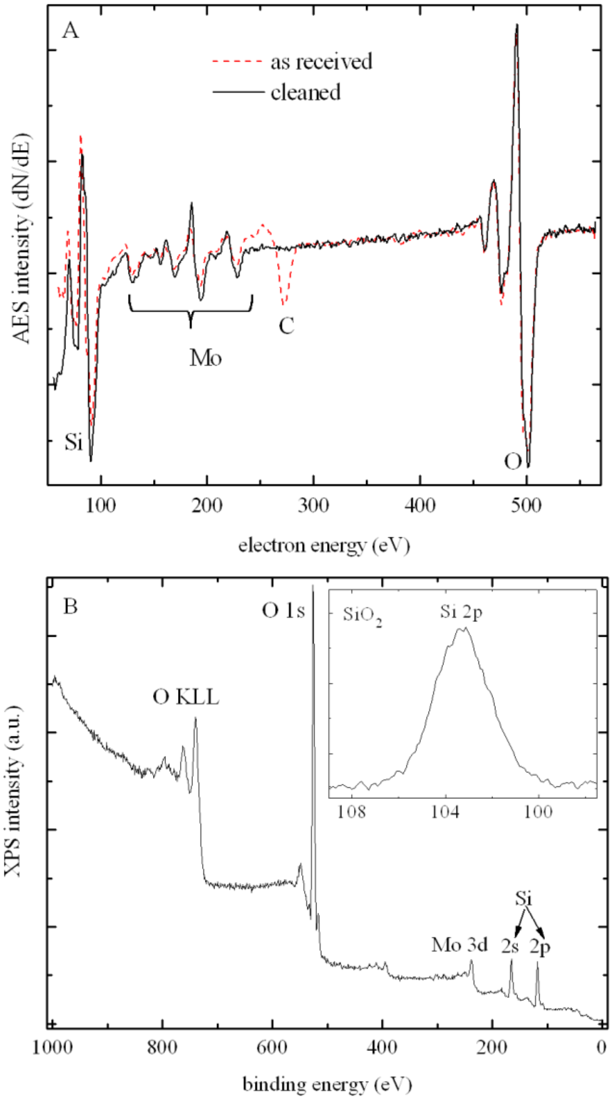

Figure 61. A) AES spectra of the Mo EBL clusters before cleaning (dashed line) and after cleaning (solid line). B) XPS spectra of the Mo EBL clusters after cleaning. The inset shows the XPS Si 2p region. Ref.[247]

Both metallic and oxidic molybdenum have very similar XPS signatures.[229,256-257] However, oxygen and hydrogen annealing can be used to change the oxidation state of molybdenum.[221,224-225,229,251-252,257] Therefore, Mo oxides were reduced in a flux of atomic hydrogen (T_s = 750 K, t = 2 h), while metallic clusters were oxidized in a flux of oxygen ($p = 1 \times 10^{-6}$ mbar, 750 K, 20 min).

4.3.3.3. Adsorption kinetics of n-butane

Figure 62 summarizes butane TDS data on metallic Mo clusters (solid lines) and on oxidic Mo clusters (dashed line). Pure butane was dosed with the molecular beam system at T_s = 90 K and beam flux of $F = (2.0 \pm 0.1) \times 10^{13}$ butane molecules $cm^{-2}\ s^{-1}$ was measured. No desorption of butane was seen for the oxidized Mo clusters. Also, the adsorption of n-butane on the silica support was below the detection level. This is consistent with the adsorption transient of butane on the oxidized sample which is shown in Figure 64. Whereas, two TDS features were evident for metallic clusters at the smallest exposure of χ = 2 s, one centered at 225 K (α peak), and the other centered at 160 K (β peak). With increasing χ, both features shifted to lower temperatures. At the largest exposure χ = 30 s, the α peak shifted to 190 K while the β peak shifted to 140 K. The low temperature onsets of the γ peaks at 105 K lined up which is characteristic of condensed alkanes. It is evident from beam scattering experiment that the surface saturated at exposures around ~10 sec and at about that exposure the γ peak developed in TDS.

The α and β peaks were assigned to the desorption of butane from two different adsorption sites of the metallic Mo clusters. For example, the higher temperature structure was related to desorption from defect sites (such as the rim of the clusters), while the low temperature feature to pristine sites (terrace sites).[255,258] The shift of α and β peak positions with butane exposure were likely due to repulsive lateral interactions among butane molecules. Repulsive interactions among alkanes have been seen before and were described by polarization effects induced by the support.[259] Due to the overlapping peaks, the magnitude of the peak shift was difficult to quantify.

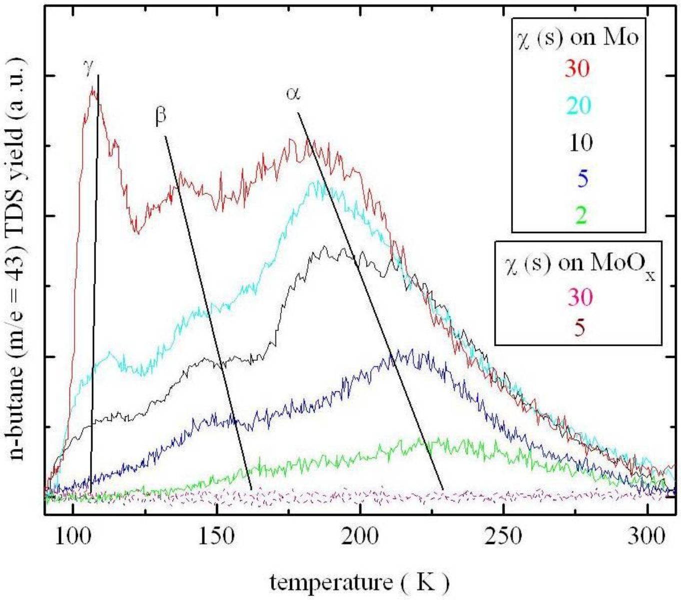

Figure 62. TDS of n-butane on metallic Mo clusters (solid lines), and on oxidic Mo clusters (dotted lines). Ref.[247]

Figure 63 shows multi-mass TDS data of n-butane on metallic Mo clusters (red bar), as well as the mass spectra of gaseous butane (gray bar). In the multi-mass TDS experiments, a constant exposure of χ = 5s was used and the peak intensities in the TDS spectra were normalized with respect to the intensity at m/e = 43. It is obvious from the figure that the mass scans for gaseous butane match those of the multi-mass TDS data. This is the indication of a molecular adsorption pathway. That result is consistent with the absence of carbon in AES/XPS after TDS experiments.

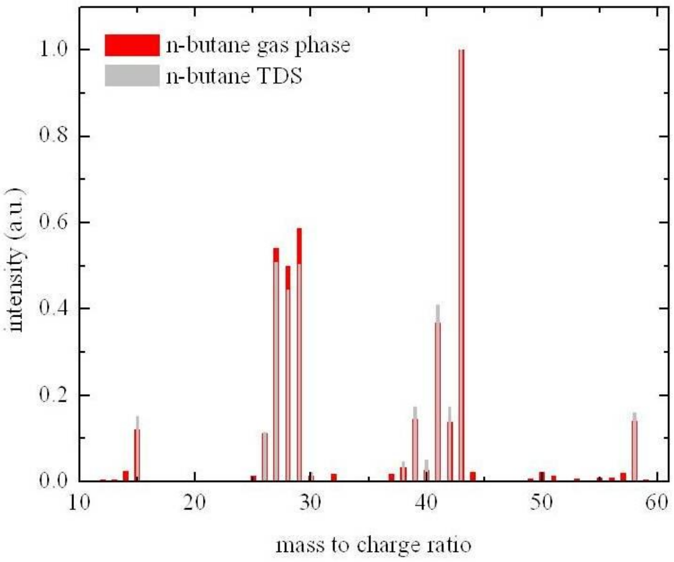

Figure 63. Multi-mass TDS of n-butane on metallic Mo clusters comparing with a mass scan of gaseous n-butane. Ref.[247]

4.3.3.4. Adsorption dynamics of n-butane

The adsorption dynamics of n-butane on the supported Mo clusters were characterized by molecular beam scattering in order to suppress sample holder effects. The impact energy of n-butane was varied within $E_i = 0.1 - 1.2$ eV by using a pure beam or by seeding with helium, combined with a variation of the nozzle temperature in the range of 300 - 750 K. The impact energies of n-butane were measured by TOF. The beam flux was determined to be $F = (2.0 \pm 0.1) \times 10^{13}$ butane molecules $cm^{-2}\ s^{-1}$ for the pure butane beam. The initial adsorption probability, S_0, of n-butane on Mo clusters was obtained by King and Wells type uptake experiments directing the beam perpendicular to the surface plane.[260] The solid lines in Figure 64 show typical adsorption transients of the partial pressure of n-butane against the exposure time (t) on Mo clusters, whereas the dashed lines are transients for oxidic clusters. Results of several experiments at identical measuring conditions are shown in order to illustrate the reproducibility of the measurements. At t = 0 s, a beam flag is opened and n-butane molecules start to strike the surface. If n-butane molecules do not adsorb on the surface, the transient resembles only a step function due to the increase in the equilibrium pressure. However, if the probe molecules adsorb, the alkane’s partial pressure initially increases quickly, but approaches the saturation level slowly hereafter. Once the surface is saturated, all butane molecules will be backscattered since thermal desorption and butane condensation can be neglected at the chosen adsorption temperature (T_s = 115 K). The area above the transient and below the saturation level equals the number of adsorbed molecules. Therefore, it is evident from Figure 64 that the alkane does not build up any significant concentration on the silica supported oxidic clusters, but does adsorb on supported metallic Mo clusters. The crystal structure may be a plausible explanation for this behavior.[261] For example, MoO_3 has an orthorhombic layered structure, consisting of MoO_6 octahedral, forming the basal plane of MoO_3 single crystals. This oxygen terminated surface is expected to be rather inert.

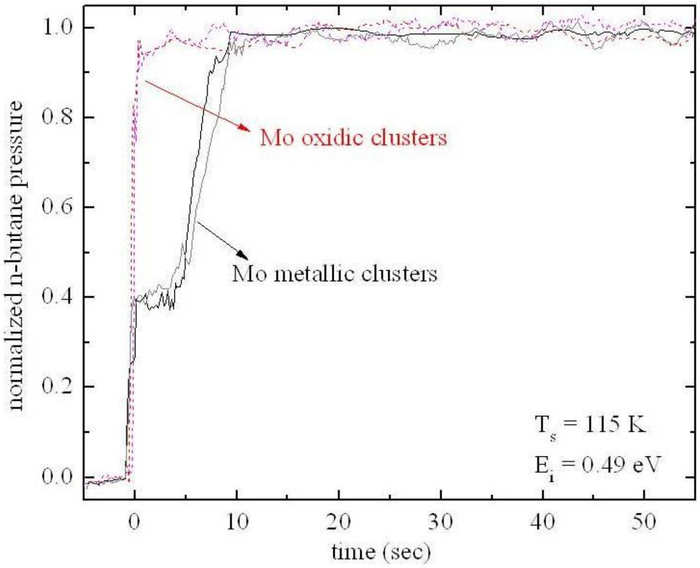

Figure 64. Adsorption transients of n-butane on metallic Mo clusters (solid lines) and on oxidic Mo clusters (dotted lines). Ref.[247]

Considering the known geometrical size of the Mo clusters and the lattice constant of the array catalyst, the Mo coverage (total Mo area vs. support area) was calculated as 0.25 ML. Since the surface density of a typical Mo surface amounts to $1.4e^{15}$ atom cm^{-2} (ref.[262]), the atomic density of the Mo clusters supported on SiO_2 amounted to $3.5e^{14}$ atom cm^{-2}. By integrating the transients shown in Figure 64, the total butane molecular density on the Mo clusters at saturation amounted to $1.0e^{14}$ molecule cm^{-2}. This means, at saturation coverage, the ratio of butane molecules to Mo atoms was only about 0.3, i.e., approximately 3.5 Mo atoms, can accommodate one butane molecule. That result appears reasonable considering the size of n-butane (5.5 Å). Furthermore, the adsorption probability, S(t), of n-butane was obtained from these adsorption transients.[260] In Figure 64, the curves were normalized such that 1- S(t) vs. t was depicted. Thus, the adsorption probability could be directly read from these figures.

Adsorption probability, $S_{0,}$ on metallic Mo clusters as a function of impact energy, E_i, at sample temperature of 115 K is shown in Figure 65. It is evident that S_0 decreased with increasing E_i which reflects the decreasing efficiency of gas-to-surface energy transfer. Simply, the larger E_i means the larger the speed of the molecules when impinging onto the surface and the smaller the interaction time with the surface. Therefore, the efficiency of the energy transfer processes of n-butane molecules decreases with E_i, hence S_0 decreases with E_i. These results were consistent with non-activated and molecular adsorption of n-butane on metallic Mo clusters and were supported by the absence of carbon after several adsorption/desorption cycles, evident from the AES/XPS experiments.

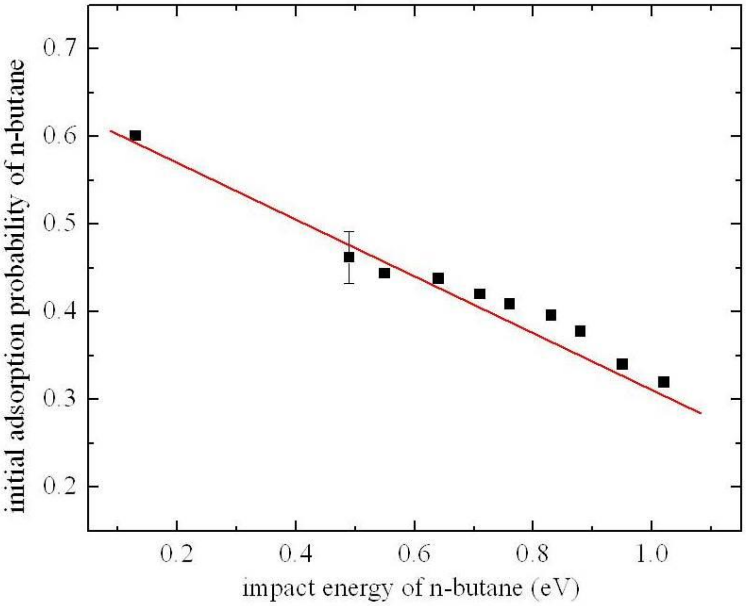

Figure 65. Initial adsorption probability (S_0) of n-butane on metallic Mo clusters as a function of impact energy. Ref.[247]

4.3.4. Summary

The adsorption of n-butane on Mo nanoclusters was found to be molecular and non-activated. Two TDS features were assigned to desorption from two different adsorption sites, namely; pristine sites (terraces sites) and defect sites (rim sites). According to the molecular beam scattering data, n-butane adsorbed on silica supported Mo clusters with initial adsorption probabilities, S_0, within the range of $S_0 = 0.60 – 0.32$, depending on impact energy, whereas on oxidic clusters S_0 was below the detection limit of $S_0 = 0.05$. This result depicts that the metallic clusters were reactive, but the oxidic clusters were not. No bond activation of the alkane was evident resulting only molecular adsorption. Similar results have been reported before where metallic Mo surfaces decompose efficiently methanol[224-225] and thiophene,[221] whereas oxidic Mo surfaces are rather inert. The oxide formation would be one mechanism for catalyst deactivation.

4.4. Overall summary of the chapter

Table 5 summarizes the results obtained from the study of short chain alkanes adsorbed on several model catalysts which includes the TDS peak temperatures, the number of peaks, their corresponding binding energies, and adsorption pathways.

Table 5. Summary showing the results of short chain alkanes on several model catalysts included in this dissertation. Ref. [74,247,263]

Probe molecules	**Model catalysts**	**Lower T_{peak} (K)**	**E_d (KJ/mol)**	**Higher T_{peak} (K)**	**E_d (KJ/mol)**	**Adsorption**
ethane	CaO(100)	168	49.7	223	66.4	Molecular adsorption
iso-butane	CaO(100)	140-150	41.2-44.2	194-215	57.6-64.0	Mol. and dissociative
n-butane	CaO(100)	133-156	39.1-46.0	182-224	53.9-66.8	Mol. and dissociative
n-pentane	CaO(100)	197-200	58.5-59.4	230-247	68.6-73.8	Mol. and dissociative
n-hexane	CaO(100)	177-183	52.4-54.2	210-279	62.5-83.7	Mol. and dissociative
benzene	CaO(100)	224-248	66.8-74.1	290-323	87.0-97.2	Molecular adsorption
n-butane	Sb(111)	118	33.00	123	34.4	Molecular adsorption
n-butane	Mo 77 nm	160	47.2	225	67.3	Molecular adsorption
n-butane	MoO_x	x	x	x	x	No adsorption

CHAPTER 5. SIDE PROJECTS: STUDY OF COAL COMBUSTION GASES ON MODEL CATALYSTS

This chapter is comprised of projects that relate to the study of coal combustion gases adsorbed on the surface of model catalysts. The first project concerns the study of adsorption kinetics and dynamics of CO_2 on MgO(001) by thermal desorption spectroscopy and molecular beam scattering, respectively. Due to the significance of CO_2, motivated by environmental concerns and its utilisation as a feed stock, exploring CO_2 chemistry in general is timely and environmentally pertinent. The second project characterizes the catalytic activity of a non-metal, Se, with probe molecules such as CO_2, NO, CO, H_2, D_2, and H_2O.

5.1. Adsorption kinetics and dynamics of CO_2 on MgO(001)

The significance of carbon dioxide and a brief literature review regarding its interaction with several metal oxide surfaces are presented in the first section below. Then, the adsorption kinetics and dynamics of CO_2 molecule on MgO(100) studied by thermal desorption spectroscopy and molecular beam scattering, respectively, are discussed in the results and discussion section. A summary of the experimental results obtained in this study is given at the end.

5.1.1. Introduction

Carbon dioxide chemistry has become the focus of attention due to its significance motivated by environmental concern and its utilisation as a feed stock. It is a well known fact that the methanol based economy was envisioned[264] for recycling CO_2 from the atmosphere as well as underground CO_2 sequestration[265] based on carbonate formation in geological formations. CO_2 is probably the next more complex traditional probe molecule as compared to CO, in surface science.[107,157-158] CO_2 interacts more weakly with MgO. Due to its easy regeneration, it is considered as a catalyst for CO_2 sorbent. [266] Also, it is considered for the dry reforming of methane. CO adsorption has been studied extensively on MgO;[267-268] but not much work has been done regarding CO_2 adsorption on MgO. CO_2 adsorption kinetics and dynamics have been studied in detail at ultra-high vacuum (UHV) on nearly all model oxide surfaces (listed in Table 6) except on MgO.[122,133-134] Metal oxides are particularly interesting for CO_2 adsorption since oxygen vacancy sites efficiently trap CO_2[153,269] and carbonate formation has been reported for a number of metal oxides. On the other hand, CO_2 physisorbs weakly on most metals.[122,133-134]

5.1.2. Brief literature survey

A literature search reveals several molecular beam scattering studies of CO_2 on various metal oxides.[122,133-134] However, to the best of our knowledge, the only beam scattering studies available for MgO are of NO_x interactions with MgO supported clusters[270] as well as Ar and methane scattering on MgO single crystals.[179] Detailed adsorption probability data or dynamics study of CO_2 on MgO(001) single crystals is still not available. In one of the studies, experimental binding energies for CO_2 on MgO(001) were determined by LASER induced thermal desorption (LITD),[271] which is listed in Tab. 1. Slow diffusion of CO_2 on the surface was seen in this study. Experimental kinetics data are dominated by studies on MgO powders,[272-274] whereas a rather large number of theoretical studies are available in literature. In an early SCF/MP2 level cluster calculation, preferentially CO_2 physisorption perpendicular on Mg^{2+} sites of the MgO(001) surface was observed, although flat adsorbed CO_2 is energetically not much different.[275] Binding energies on low coordinated Mg^{2+} sites (defects) are only slightly larger than on terrace sites. In the same study, carbonate formation on low coordinated O^{2-} defect sites was concluded. CO_2 binding energies on these O^{2-} defect sites were significantly greater than for

Mg^{2+} sites. The chemisorption of CO_2 on the MgO surface was predicted (see Tab. 1). Similarly, theoretical DFT studies confirmed carbonate formation; however, adsorption on Mg^{2+} sites (physisorption) was not considered.[171,276-277] A literature survey reveals the following possible adsorption pathways for CO_2 on MgO surface:

$$CO_2(gas) + Mg^{sur} \rightarrow CO_2(phys) + Mg^{sur} \tag{5.1}$$

$$CO_2(gas) + O^{sur} \rightarrow [CO_2(ads)\text{-}O^{sur}]^{\#} \rightarrow CO_3(chem) \tag{5.2}$$

where, gas, ^{sur}, phys, and chem refer to gas-phase species, surface atoms, physisorbed, and chemisorbed species respectively. Various adsorption configurations of CO_2 have been considered theoretically which are not distinguished in Equations 5.1 and 5.2. Most theoretical studies conclude carbonate formation in the vicinity of defect sites such as steps. However, the decomposition kinetics/dynamics is typically not directly considered. According to these prior researches, carbonates appear to desorb as CO_2 from MgO,[272-274] carbonate decomposition results in O_2 desorption from metallic systems such as silver,[278] and mostly CO desorption was seen on CaO.[156] A number of possible reaction pathways appear plausible for the decomposition of carbonates on metal oxide surfaces such as:

$$CO_2O^{sur}(chem) \rightarrow CO_2(g) + O^{sur} \tag{5.3}$$

$$CO_2O^{sur}(chem) \rightarrow CO_2(g) + 1/2O_2(g) + O^{vac} \tag{5.4}$$

$$CO_2O^{sur}(chem) \rightarrow CO(g) + O_2(g) + O^{vac} \tag{5.5}$$

$$CO_2O^{sur}(chem) \rightarrow CO(g) + 2O^{sur} \tag{5.6}$$

$$CO_2O^{sur}(chem) \rightarrow CO(g) + O^{sur} + 1/2O_2(g) \tag{5.7}$$

$$CO_2O^{sur}(chem) \rightarrow C(a) + O^{sur} + O_2(g) \tag{5.8}$$

$$CO_2(phys) + Mg^{sur} \rightarrow CO_2(g) + Mg^{sur} \tag{5.9}$$

Pathway 5.3 represents the most plausible pathway for decomposition into CO_2 that would sustain the surface structure. The original lattice oxygen (O^{sur}) acts only as an adsorption site of CO_2 forming carbonate-like species. If lattice oxygen is removed during the decomposition process, the defect density of the surface would be affected since carbonates form on oxides via lattice oxygen. Therefore pathways 5.4 and 5.5 are energetically very unlikely and would generate oxygen vacancy sites, O^{vac}, on the surface. Mg-carbonate powders decomposition starts at ~700 K.[279] According to a theoretical study, carbonate formation on MgO is surface defect assisted[275] decomposition pathways which would result in filling oxygen vacancies sites leading to desorption of CO as in pathways 5.6 and 5.7. As per pathway 5.7, oxygen may desorb simultaneously with CO_2 or it may fill oxygen vacancy sites as in pathway 5.6. Also, the formation of carbon is energetically unlikely as shown in pathway 5.8. If present, physisorbed CO_2 would desorb as given in reaction pathway 5.9.

On metal surfaces, carbonates which form in O(a) + CO_2(a) (ref.[280]) or O_2 + CO_2(a) (ref.[278]) coadsorption systems typically decompose at about 600 K according to:

$$CO_3(a) \rightarrow CO_2(g) + 1/2O_2(g) \qquad (5.10)$$

This pathway is similar to pathway 5.7 in the list above. These equations are certainly simplistic since they do not reflect the various adsorption configurations, diffusion, and transition states but do describe the macroscopic processes. In the simplest case, multi-mass TDS experiments (or time resolved spectroscopy) could reveal what decomposition mechanism is active. However, TDS experiments may be obscured by background adsorption. Also, the assignment of infrared (IR) peaks was often controversially discussed in the literature. Moreover, generating well-defined defects on metal oxides is experimentally challenging, which makes the identification of reaction pathways more difficult even for relatively simple model systems.

Experimentally, metastable impact electron spectroscopy (MIES),[281] ultraviolet photoelectron spectroscopy (UPS),[281-282] X-ray photoelectron spectroscopy (XPS),[283] Near edge X-ray absorption fine structure (NEXAFS),[284] and atomic force microscopy (AFM)[283] have been used to confirm the carbonate formation on MgO. According to an early UPS study, physisorbed CO_2 is apparently seen at 77 K and carbonate formation at 123 K.[285] Similarly, in an early IR investigation, the adsorption of distorted physisiorbed CO_2 was concluded (at 82 K on UHV cleaved MgO).[286] Therefore, theoretical studies clearly favor carbonate formation on MgO whereas the experimental database is still not clear yet. Besides CO_2, alkanes,[59] water,[287] and NO adsorption[288] on MgO have been investigated along with the metal cluster growth[289] and the formation of various MgO nano-structures.[290] Our goal is a thorough characterization of adsorption kinetics and dynamics of CO_2 on MgO(001) surface, which has never been done before.

5.1.3. Results and discussion

5.1.3.1. Sample characterization

The MgO(001) sample was obtained from MaTeck (orientation better than 0.3°). Figures 66A-C show AES and XPS spectra for MgO surface and these spectroscopic results are in agreement with reference data.[291-292] Auger peak at electron energy ~272eV for the as received MgO crystal show the presence of carbon as a main impurity. The sample was initially sputtered by the bombardment of Ar^+ (25 min, 2 keV, 1.0 μA sample current, RT) to remove carbon containing impurities. Afterwards, the MgO crystal was cleaned by several annealing cycles at 680 K in $2x10^{-6}$ mbar O_2 ambient for a total of ~80 min. The annealing cycles (~10 min each) were repeatedly applied throughout the project in order to keep impurity levels below the detection limit of the AES/XPS system.

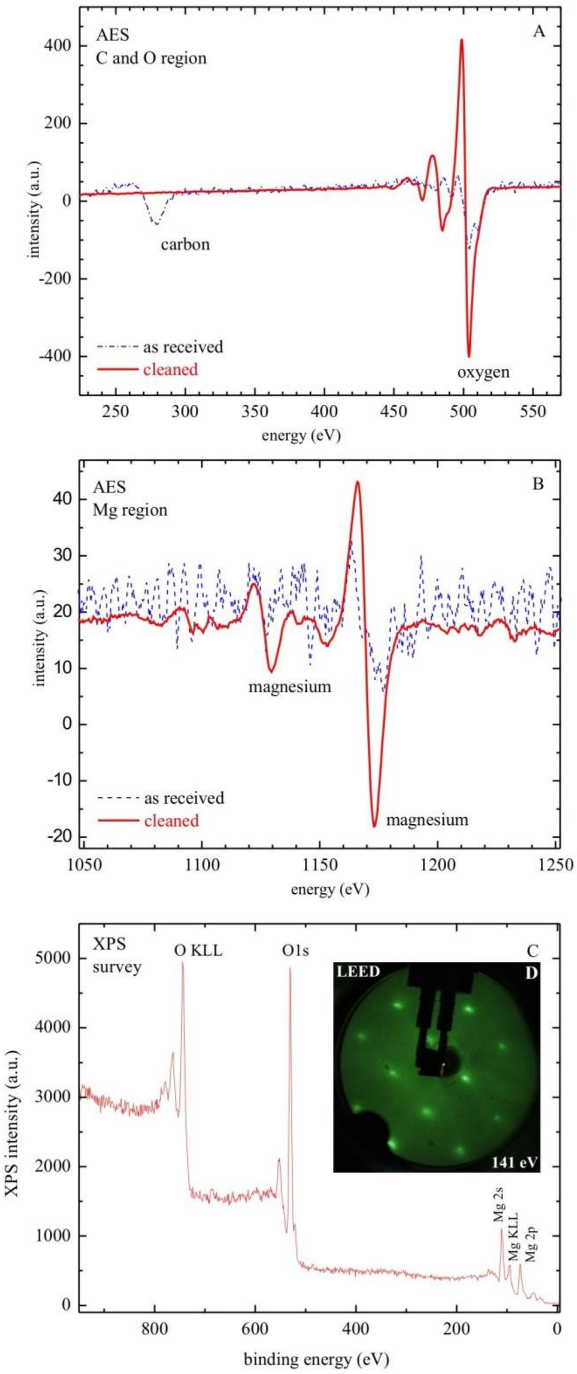

Figure 66. A) and B) AES spectra before and after sample cleaning C) XPS survey scan of clean sample D) LEED pattern.

Ionic MgO crystals have a rocksalt structure with two O and Mg face-centred-cubic sub-lattices. Therefore, the non-polar unreconstructed MgO(001) surface shows a square shaped

LEED pattern[293] as shown in Figure 66D. A large number of experimental/theoretical studies are devoted to characterize the geometrical and electronic structure of surface defects (neutral vs. charged oxygen vacancies).[269,294] Due to the frequent O_2 annealing cycles applied in our study, the surface defect density perhaps should have been reasonably low. Therefore, CO_2 adsorption on MgO(001), unfortunately, did not allow for a direct estimate of the surface defect density, which is discussed later. However, CO_2 TDS allowed the estimation of the defect density in the order of 20% of a monolayer (ML) in ZnO and TiO_2 surfaces which were studied earlier in the same system.[60,153] In the case of ZnO and $TiO_{2,}$ rather extensive sputter cycles were required for cleaning purpose unlike for the MgO surface. Thus, it is likely that the MgO surface considered here must have had a defect density lower than the one reported for ZnO.

5.1.3.2. CO_2 adsorption kinetics

5.1.3.2.1. Parent mass TDS data

CO_2 gas was dosed with a well-collimated supersonic beam reducing sample holder effects to get precise results. CO_2 TDS curves are shown as a function of CO_2 exposures, χ, (at 97 K) using the molecular beam system (E_i = 0.12 eV) in Figure 67. CO_2 TDS for adsorption temperatures down to 85 K (using an in-situ calibrated thermocouple) did not reveal any lower temperature desorption features. TDS results reveal two structures, labeled as α- and β-peaks at (260 ± 5) K and (200 ± 5) K, respectively. No CO_2 desorption was seen without dosing the gas, see dashed line in Figure 67 for $\chi = 0$. The peak positions are independent of χ and the intensities grow with increasing χ. The TDS intensities are small and so is the signal-to-noise ratio. This is expected considering the very small diffusion velocities of CO_2 on MgO(001) at 100 K,[271] since the beam spot at the sample position (~3 mm) is smaller than the size of the crystal (10 x10 mm).

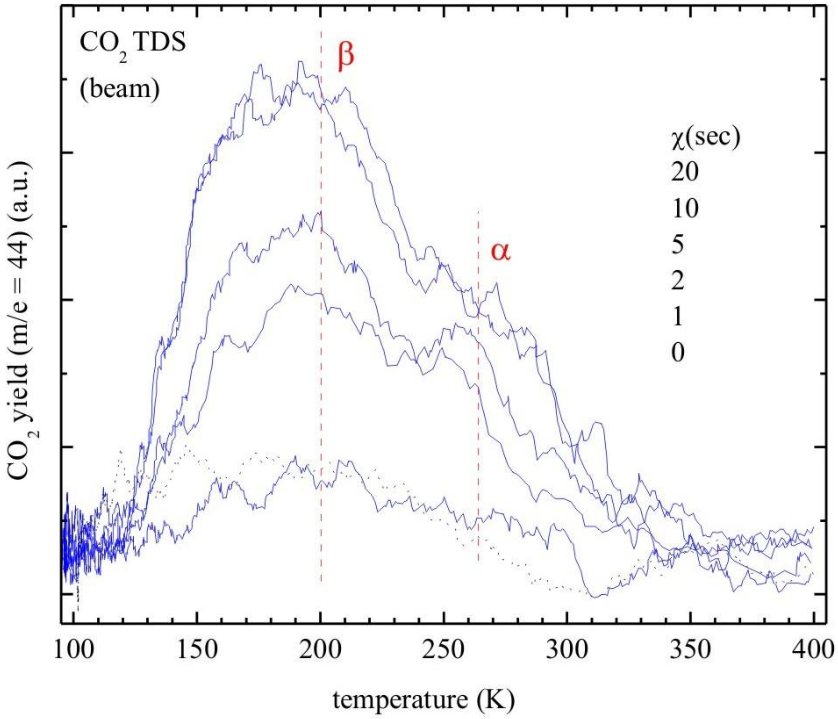

Figure 67. CO_2 TDS on MgO(001). CO_2 was dosed with beam.

Two peaks at desorption temperatures of ~120 K and ~135 K were evident for CO_2 adsorption on ZnO-Zn and TiO_2(110).[60,153] The desorption starts for MgO(001) at much higher temperatures and it is important that the adsorption temperatures were approximately identical in all of these studies. The main difference among these metal oxides is that carbonates form efficiently on MgO.[281-284] In case of the Ti and Zn oxide surfaces, the TDS peaks were assigned to physisorption of CO_2 from pristine and defect sites.[119,153] The resulting desorption temperatures seen for MgO are too large to assign for physisorption of CO_2. Therefore, pathway 5.9 is ruled out from the list of possible interactions given in the introduction section. Similarly, CO_2 condenses at lower temperatures (of ~ 80 K)[295] and can be ruled out. Therefore, we assign the α- and β-peaks shown in Figure 67 to carbonate decomposition resulting from different adsorption sites or configurations of the carbonates. This conclusion is further supported by experimental XPS data. Several kinetics and dynamics parameters of CO_2 adsorption on metal oxides and semiconductors are listed in Table 6.

Table 6. CO_2 adsorption on various system, their binding energies, adsorption probabilities and methods used during the study where SCF means Hartree-Fock self-consistent field, DFT means density functional theory, MP2 means Møller–Plesset perturbation theory, MCS means Monte Carlo simulations, and LITD means LASER-induced thermal desorption. Ref.[296]

System	**E_d** Pristine / Physisorption	**E_d** Defects / Carbonates	**S_0**	**Method**	**Ref.**
ZnO-Zn	34.4	43.6	0.73	TDS	60,114,120,122,297
TiO_2(110)	43.0	48.0	0.56	TDS	153,298
TiO_2 nanotubes	30.4			TDS	299
MgO(001)	38.6 - 28.9		1.0	LITD	271
MgO powder		116 / 203		TDS	274
MgO(001)		51.7 / 67.7	0.74	TDS	This work
MgO(001), Mg^{2+}	16.4 - 32.8	31.8 - 36.7		SCF, MP2	275
MgO(001), O_2^{2+}		164, 68		SCF, MP2	
MgO(001), O_2^{2+}		115 - 154		DFT	171
MgO(001), O_2^{2+}	8.7	145 - 193		DFT	277
MgO(001), Mg^{2+}	29.3			MCS	300
CaO(001)	29.8-47.4	75.1 - 82.9	0.60	TDS	156
CrO_x-on-Cr(110)	30.5	39.5	0.58	TDS	301
Selenium foil	32.3	49.0	--	TDS	302
Silica wafer	< 24		--	TDS	64

To the best of our knowledge, there is one prior study where desorption of CO_2 at lower temperatures, consistent with physisorbed CO_2 on MgO(001), was detected using LASER-induced thermal desorption.[271] However, an apparently non-calibrated temperature reading was given in this study and the adsorption temperatures appear identical to those used here. Condensation of CO_2 starts at relatively great temperatures, i.e., assuming perfect lN_2 sample cooling it may be possible to already condense CO_2 layers and assign this by mistake to physisorbed species (in the monolayer coverage regime). According to quantum chemical calculations, carbonates form entirely on magnesium oxides' defects sites (step sites). Thus, the defect densities of the MgO surfaces may have been different. In both studies, the MgO was cleaved in air, but in the earlier work “oxygen plasma” was used for sample cleaning, which could indeed result in smaller defect densities than in our study. Note, however, that a good LEED pattern was obtained from our sample as shown in Figure 66D. Also, in very rare cases, it has been noted that bicarbonates (HCO_3^-) may possibly form in CO_2 and water coadsorption layers.[119] However, these bicarbonates form on defected surfaces only when both reactants are dosed together. Otherwise, sequential adsorption leads to site blocking effects. On TiO_2, bicarbonates lead to CO_2 desorption at somewhat higher temperatures than desorption from pristine or defect sites.[119] In a kinetics study it may be impossible to rule out completely minor uptake of water from the background. However, it appears unlikely that water adsorption from the background affected our data.

Considering CO_2 TDS in the gas phase as shown in Figure 67, desorption temperatures appear too large to be assigned to desorption of physisorbed CO_2 (ruling out pathway 5.9). Thus, pathways 5.3 and/or 5.4 may be present. However, increasing the surface defect density dramatically in the course of our experiments should have affected the reproducibility of TDS and LEED data, which was not the case. Thus, decomposition along pathway 5.4 can likely be ruled out.

5.1.3.2.2. Multi-mass TDS data

Multi-mass TDS experiments were conducted where masses besides the CO_2 parent mass (m/e = 44) were recorded. Apart from CO_2, desorption signals at m/e =32 for oxygen and m/e = 28 for CO are seen within approximately the same temperature range. The background corrected TDS intensities are given along with the fragmentation pattern of gaseous CO_2 in Figure 68.

Note that the sensitivity factor of the mass spectrometer has been taken into account for this experiment.

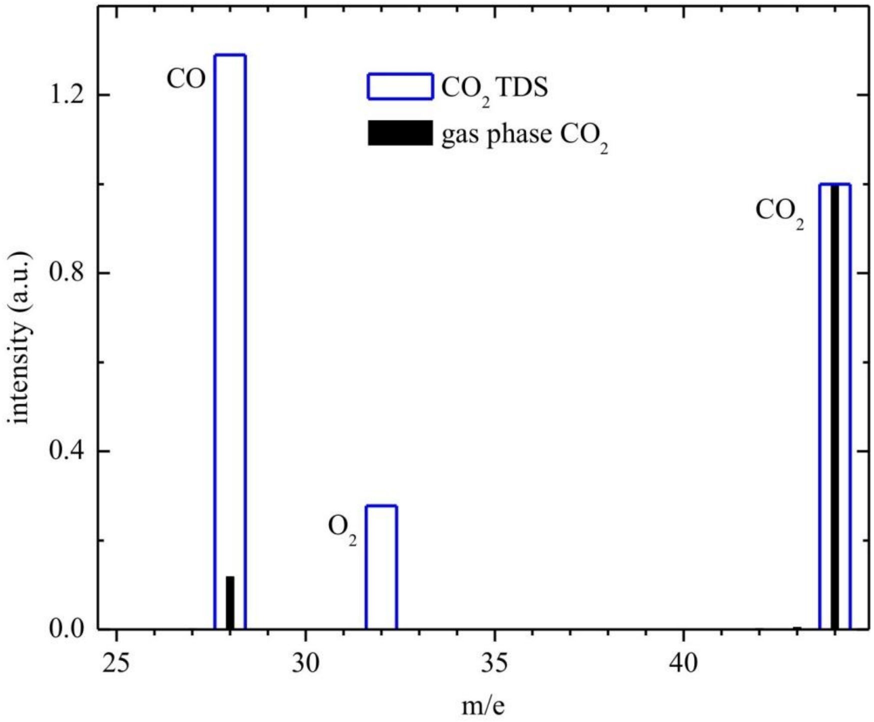

Figure 68. Open bars) Multi-mass TDS of adsorbed CO$_2$ at 90 K. Solid bars) Fragmentation pattern of gas-phase CO$_2$ as determined with the same mass spectrometer.

It is clear that desorption of CO and oxygen favors reaction pathways 5.5, 5.6, and 5.7. The large CO-to-oxygen ratio suggests that formed oxygen atoms heal defects (pathways 5.6 and 5.7) to a larger extent than they desorb into the gas phase (pathway 5.5). On the other hand, it is known that defects can also form thermally on oxides.[153,303] An equilibrium of thermally formed (via TDS) and healed out (via carbonate decomposition) defects would be established. Therefore, the most likely decomposition pathways for the carbonates are reactions 5.3 and 5.6 with a side reaction according to pathway 5.7. The CO$_2$-to-CO ratio amounts to 1.3 calculated in Figure 68, which estimates the branching ratio of pathways 5.3 and 5.6. Similarly, the CO-to-O$_2$ ratio amounts to 4.6, which estimates the branching ratio of reaction pathways 5.6 and 5.7. It is worth mentioning that quite similar results were obtained for CO_2/CaO(001).[156] Carbonate decomposition was accompanied by only CO desorption in this case. A LEED pattern was not observed due to the presence of larger defect density on the CaO surface which might have entirely suppressed any oxygen desorption.

5.1.3.3. XPS of CO_2 / MgO(001)

For XPS, the Mg Kα line (at 1253.6 eV) was used with pass energy of 100 eV (for survey spectrum) and 50 eV (for scans of individual peaks) of the analyzer. The XPS spectra were referenced with respect to the O1s line at a binding energy of 531 eV.[204] The XPS energy resolution is estimated as < 1 eV.

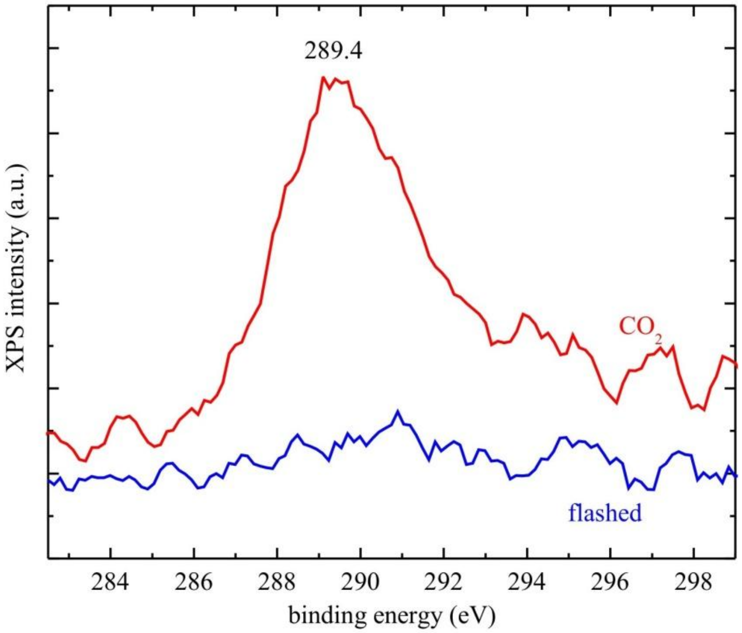

Figure 69. Red line) XPS of C1s region with adsorbed CO_2 (using a pure CO_2 molecular beam, 30 sec) on the surface at 100 K. Blue line) XPS after flashing the surface to 630 K.

In the present study, carbonate formation is further confirmed spectroscopically by the XPS technique. XPS spectra showing the C 1s region of adsorbed CO_2 at 98 K are depicted in

Figure 69. As expected, only one broad structure is seen with a binding energy (289.4eV) matching literature values for carbonates on other systems as shown in Table 7. After flashing the surface to 630 K, the XPS line at 289.4 eV seems to disappear. Thus, we can rule out reaction pathway 5.8 and spectroscopically confirm carbonate formation. The XPS line width is rather broad, which may reflect overlapping structures related to chemical shifts or different adsorption sites.

Table 7. XPS 1s lines for adsorption of CO_2 on several system. Ref.[296]

System	**C(1s)-XPS line position (eV)**	**Carbonates**	**Graphitic carbon**	**Ref.**
CO_2-MgO(001)	290.0	X		[282]
CO_2-MgO(111)	290.1	X		
CO_2-CaO films	291.9	X		[175]
as-received MgO(001)	289.9 285.0	X	X	[283]
CO_2-Cu foil	289.3 284.4	X	X	[304]
CO_2-MgO(001)	289.4	X		This work

5.1.3.4. Adsorption dynamics of CO_2

5.1.3.4.1. Typical example of an adsorption transient

CO_2 adsorption transient is shown in Figure 70. CO_2 is dosed on the surface at T_s = 100 K with the molecular beam (E_i = 0.12 eV) and the CO_2 background pressure is measured simultaneously. At time t = 0, once a beam flag is opened, the transient appears with a steep initial increase in the CO_2 pressure (in the scattering chamber). Then, the signal levels out (here for t > 10 sec) implying the saturation of surface with CO_2 (carbonates). This saturation level (t > 10 sec) is larger than the initial CO_2 background (t < 0 sec) simply due to the increased load on the pumps when opening the beam flag. Normalizing this curve (CO_2 background pressure at t <

0 sec set to zero and CO_2 saturation level at t > 10 sec set to one) allows one to directly read 1 - S(t) from the transient, with S(t) as the time dependent adsorption probability of CO_2. The initial adsorption probability, S_0, is simply obtained at t = 0 sec, i.e., in the limit of negligible CO_2 coverage. The area above the transient and below the saturation level gives the number of adsorbed CO_2 molecules on the surface. Note that the surface saturates at about 10 sec, which agrees with the beam TDS data shown in Figure 67. Integrating these transients results in the coverage, Θ, dependent adsorption probability, S(Θ), which is shown as an inset to Figure 70. Typically, the saturation coverage obtained at low adsorption temperatures is set to one monolayer, just to indicate saturation of the surface. S(Θ)obey the traditional Kisliuk-like shape. Therefore, precursor-mediated adsorption is seen[207,305] where CO_2 is trapped in an extrinsic/intrinsic precursor state before adsorption takes place. The general shape of S(Θ) curves was nearly independent of impact energy and temperature.

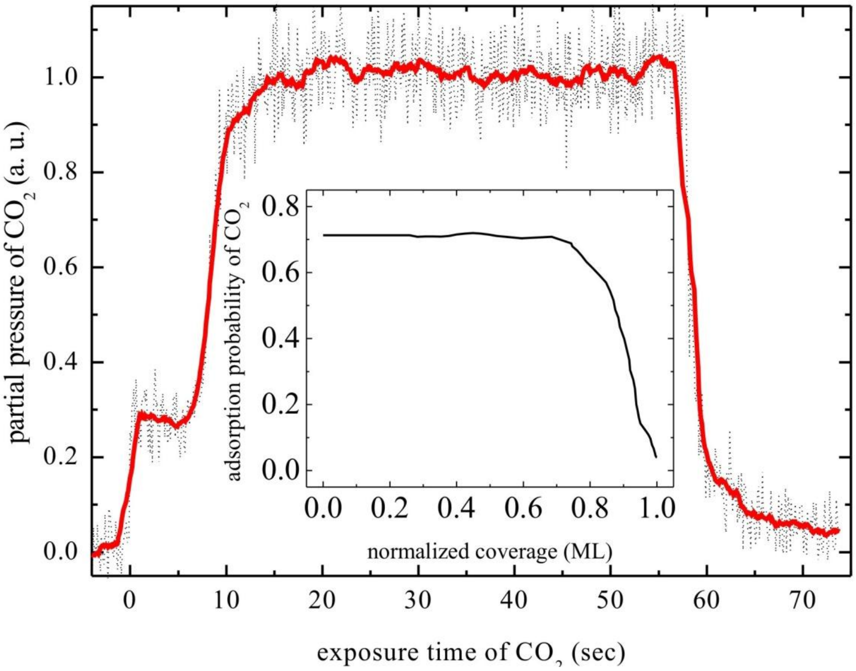

Figure 70. Adsorption transient of CO_2 at T_s = 100 K and E_i = 0.12 eV. The solid line is the smoothed curve given as a guide for the eye. The inset shows the integrated curve.

CO_2 flux of (2.0 ± 1.0) x10^{12} molecules cm^{-2} sec^{-1} was determined by measuring the equivalent (background) pressure of the beam. By integrating the adsorption transient, the saturated surface was found to adsorb (4 ± 1) x10^{13} molecules/cm^2. With a lattice constant of 4.211 Å,[306] the oxygen (Mg) atom density of a defect free MgO(001) surface amounted to 1.128 x10^{15} atoms/cm^2. Therefore, the experimentally determined CO_2 saturation coverage (with respect to the oxygen surface density) amounted to only ~0.04 ± 0.02. Such small coverage may be unexpected; however, it is consistent with theoretical studies[275] concluding carbonate formation occurs solely on defect sites. In addition, a ~4% defect density of MgO(001) appears reasonable as compared with studies on ZnO-Zn and TiO_2.

5.1.3.4.2. Energy dependence of adsorption dynamics

The impact energy (E_i) as a function of adsorption probability (S_0) for CO_2 on Mg(001) at low surface temperature is shown in Figure 71. In addition, CO_2 adsorption data from the literature for other metal oxides and one metal are depicted. At low impact energies, S_0 appears systematically larger for all oxides as compared with copper. Usually, CO_2 binding energies are also larger on metal oxides than for most metals.[107,157-158] On mixed-terminated metal oxides such as MgO, gas-phase species can adsorb on either oxygen or metal sites. However, considering smaller binding energies of CO_2 on Mg sites, [275]the adsorption dynamics should be dominated by adsorption on oxygen sites. In the case of TiO_2(110), considering its geometrical structure, the adsorption dynamics are likely also to be dominated by CO_2-to-surface oxygen adsorption events. Therefore, it is not surprising that at least the low impact energy S_0 values of CO_2 for MgO(001) and TiO_2(110) are basically identical. On the other hand, for systems such as the Zn-terminated surface of ZnO, the adsorption dynamics are relatively different because of CO_2 interacting with metallic sites. Thus, ZnO-Zn may be similar to a metallic system rather than to a metal oxide. Indeed, S_0 (at low E_i) of the Zn-terminated surface of ZnO and copper are nearly identical as are the CO_2-to-Zn (44/65) and CO_2-to-Cu (44/64) mass match.

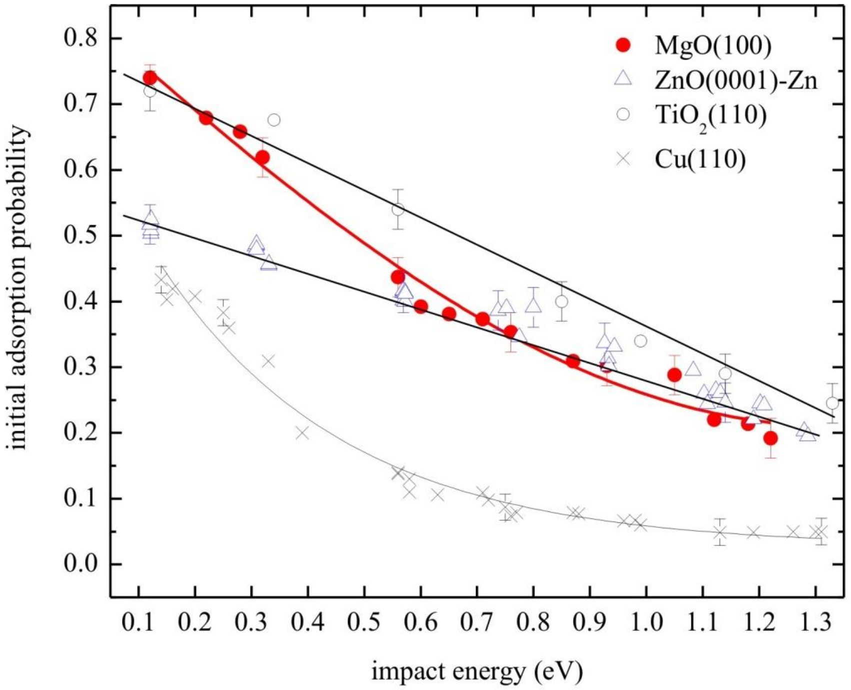

Figure 71. Initial adsorption probability (S_0) of CO_2 as a function of impact energy at 100 K. Also shown are literature data for ZnO, TiO_2 and Copper.

S_0 of CO_2 decreases with increasing E_i for all systems considered, indicating molecular and weakly or non-activated adsorption which is consistent with theoretical predictions. [275] With increasing E_i, more kinetic energy needs to be dissipated to the surface in order for the gas-phase species to adsorb. Therefore, the adsorption becomes generally less efficient with increasing E_i. For $E_i > 0.7$ eV, S_0 is identical for all metal oxides as shown in Figure 71. This result suggests that the adsorption dynamics at greater impact energies are dominated by surface defects (oxygen vacancy, steps, etc.) sites which are present on all metal oxides.

5.1.3.4.3. Temperature dependence of adsorption dynamics

A typical example of the surface temperature, T_s, dependence of S_0 for low impact energies is shown in Figure 72. S_0 is essentially independent of T_s up to 200 K and it decreases linearly with further increase in temperature. A constant S_0 value is consistent with non-activated adsorption of CO_2, as reported before for a number of other metal oxides[114,153,156] and metals.[116] Once thermal desorption/decomposition becomes important, the adsorption probability decreases which reflects a kinetic rather than a dynamic adsorption probability. S_0 starts to drop at about 220 K, which is consistent with the TDS peak maximum at about 200 K as indicated by the arrow in Figure 72.

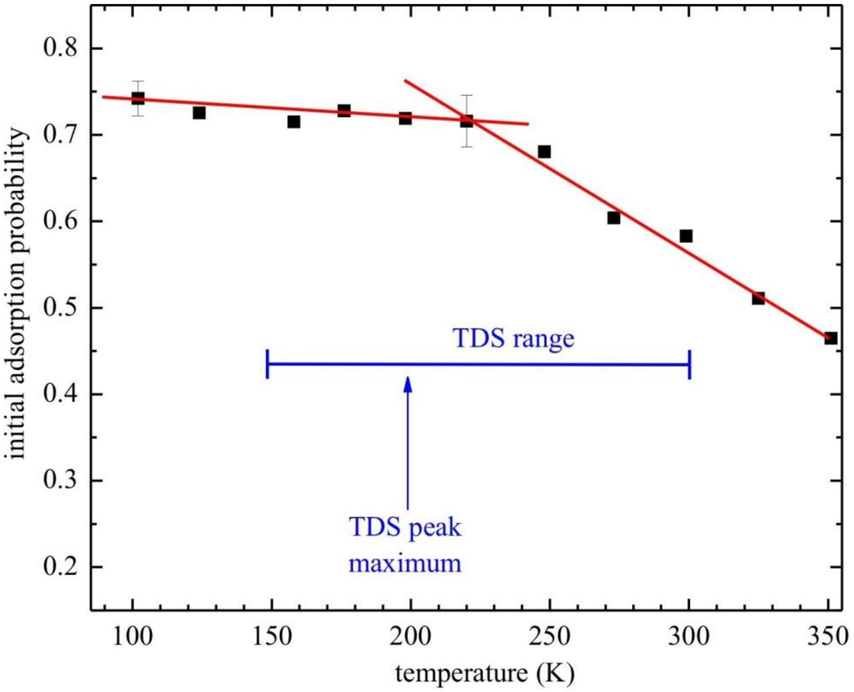

Figure 72. Initial adsorption probability (S_0) of CO_2 as a function of surface temperature and at E_i = 0.12 eV. Indicated is also the TDS temperature range.

5.1.4. Summary

A single crystal of MgO serves as an important support to grow other metal and metal oxide clusters as well as thin films. Therefore, thermal desorption spectroscopy, molecular beam scattering, and other spectroscopic techniques were used to characterize CO_2 adsorption on MgO(001). CO_2 TDS resulted two desorption features at 200 K and 260 K with corresponding binding energies of 51.7 and 67.7 kJ/mol, respectively, assuming pre-exponential of $1x10^{13}$/sec. Interestingly, CO and oxygen desorbed at ~200 K when multi-mass TDS experiment was conducted. XPS of CO_2 (adsorbed at low temperatures) resulted in a C1s line at 289.4 eV which disappeared after flashing the surface to 630 K. Therefore, the kinetics and spectroscopic results consistently reveal carbonate formation at low temperatures. Both the formation and decomposition were likely defect-mediated, which was in agreement with theoretical predictions and these defects were assigned to step sites rather than oxygen vacancies with CO_2 adsorbed in the vicinity of steps. More CO than CO_2 desorbed during decomposition of carbonates along with the small amounts of oxygen. The adsorption was found to be non-activated and temperature independent initial adsorption probabilities of CO_2 decreased from 0.74 to 0.19 within the impact energy range of 0.12-1.22 eV. The coverage dependence of the adsorption dynamics was depicted to be precursor-mediated adsorption (Kisliuk-type) within the temperature and impact energy range studied.

5.2. Adsorption kinetics of coal combustion gases on selenium foil

An introduction about the importance of studying metalloid semiconductors/ non metals is presented first, followed by the brief literature survey regarding the applications of Selenium (Se). A combined results and discussion obtained in this project characterize the catalytic activity of Se with typical combustion gases CO_2, NO, CO, H_2, D_2, and water as probe molecules. A summary of experimental results obtained in this project is listed at the end.

5.2.1. Introduction

Metalloids such as B, Sb, and As or metalloid semiconductor/non-metal, Se, show unusual electronic properties, which make their study interesting from a fundamental perspective. These elements can be present in natural coal and can be released with the plume in coal power plants.[183-184] Most prior studies typically focused on the electronic properties and the growth of thin films of Se. Surface science investigations about the adsorption kinetics of small molecules have apparently not been published for any Se surface. However, an ultra-high vacuum surface science model study presented in this project cannot directly match the conditions present in coal-fired power plants and the formation of flue gas. Very little is known about the adsorption kinetics of gas-phase species. This study at the interface of surface science, catalysis, and chemical engineering attempts to fill this information gap.

5.2.2. Brief literature survey

A literature search revealed hundreds of surface science publications about Se. However, almost all of them reflect the geometrical and electronic properties of supported Se clusters and films, motivated by applications in the electronics/photovoltaic industries. In addition, Se is used in the fabrication of glass and ceramics. The literature on Se appears to focus entirely on Se cluster deposition,[307-308] alloy formation,[309] and thin film growth on semiconductor supports.[310-313] Se forms oxides, hydrides (HSe,[314] H_2Se, ref.[315]), and halides. A surface science literature search about Se reveals only one study about the adsorption of CO on chalcogen modified Pt(111) in which Se basically poisons the catalyst.[197] Several groups have applied vapor depositing Se[195-196] by using crucibles and elemental Se,[316] decomposing H_2Se gas,[197] and using WSe_2 flakes[317] on inert supports such as silica/silicon in order to form non-crystalline thin films or clusters. But, in fact, the safest way to characterize this highly toxic element in a model study is by using single crystals or foils preventing contamination of the entire vacuum system. Unfortunately, Se single crystals are apparently not available which led to the study of a polycrystalline Se foil in this project.

Surface science investigations about the adsorption kinetics of other small molecules have apparently not been published for any Se surface. Therefore, thermal desorption spectroscopy (TDS) was used to characterize the adsorption kinetics of all probe molecules used in this study. In addition, Auger electron spectroscopy (AES) and X-ray diffraction (XRD) were used to characterize the surface cleanliness and structure at ultra-high vacuum (UHV) conditions.

5.2.3. Sample cleaning

The 10 × 10 × 1 mm Se foil (5N) from Princeton Scientific, Corp (USA) was cleaned by ~30 sputter (Ar^+, 2k eV, 30 min, 0.2 μA sample current) and annealing (at 390 K, 5 min) cycles. (Assuming a sputter yield of one, about 2 MLs have been removed within one sputter cycle.) Note that the bulk melting temperature of Se is very low at 494 K. Thus, to avoid unintentionally melting the sample and contaminating the entire vacuum system, low “annealing” temperatures were applied. The liquid phase probe molecules were cleaned by pump-freeze-thaw cycles.

5.2.4. Results and discussion

5.2.4.1. Sample characterization by Auger electron spectroscopy

Figure 73A shows the carbon region of AES spectra collected while cleaning the Se sample. Se was cleaned by the combination of sputtering and annealing for several cycles until the carbon impurity signal was below the detection limit of the AES system. No other contaminations were evident on the sample's surface. The Auger peaks for Se are shown in Figure 73B which are consistent with the reference data.[318] As expected, no LEED pattern was observed since the sample is not a single crystal.

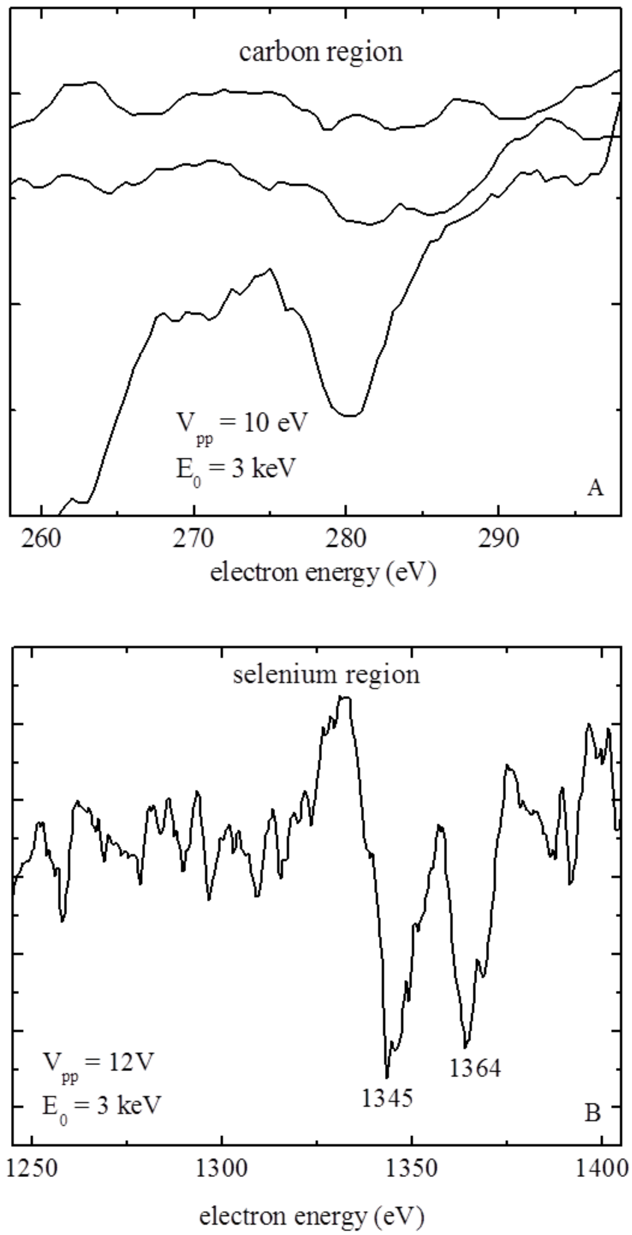

Figure 73. A) Auger spectrum for carbon region B) Auger spectrum for selenium region.

5.2.4.2. Sample characterization by X-ray diffraction

X-ray diffraction (XRD) data were collected at NDSU with a Panalytical X'Pert MPD system equiped with Cu Kα X-ray source (1.54060 Å). Figure 74 depicts X-ray diffraction data of the Se foil. The Se sample being polycrystalline, diffraction patterns are expected, whereas an amorphous system would not result in any structures in XRD. The XRD pattern which is shown in Figure 74 matches the reference scan for selenium.[319]

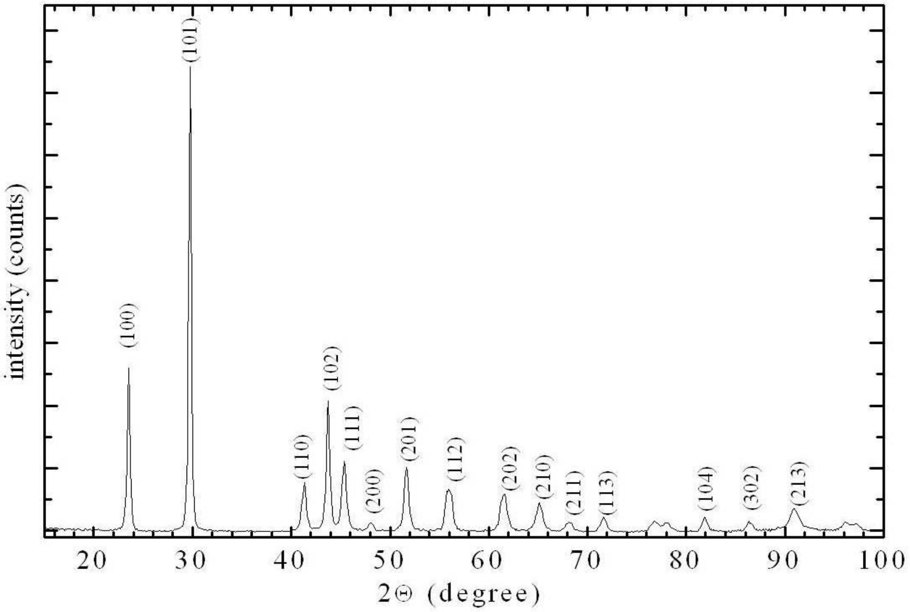

Figure 74. X-ray diffraction scan of the Se foil

5.2.4.3. Adsorption kinetics of CO_2

CO_2 TDS experiments were carried out only after no carbon or other impurities were seen on the surface. A set of CO_2 TDS curves, obtained by varying the exposure, is shown in Figure 75. Two structures, labeled as α and β peaks, are evident at 125 K and 188 K at various CO_2 exposures. At UHV conditions, CO_2 condensation starts at 79 K;[116] therefore, the cooling was not low enough to see the condensation peak in this experiment. Our results show non-activated molecular adsorption and assume a standard pre-exponential factor of 1×10^{13}/s for first order kinetics. With this assumption, the binding energies amount to 32.3 and 49.0 kJ/mol for the α and β peaks, respectively, using the Redhead equation. The TDS peak positions and binding energies are independent of exposure. Thus, the two TDS structures were assigned to different adsorption sites or configurations of CO_2 rather than the effect of lateral interactions. Since sputtering was used for the cleaning purpose, it likely might have generated a rather large defect density. Therefore, it is plausible that the β peak is related to defect sites (e.g., sputter defects, grain boundaries), which are typically characterized by larger binding energies of probe molecules than pristine sites (see e.g., ref.[153]). The TDS peaks overlap very strongly to separate the structures and obtain intensity estimates. The CO_2 binding energies are comparable to those seen on metal oxides/semiconductors (see e.g., refs.[60,153]), but they are larger than typical metals (see e.g., refs.[107,116]). No carbon or oxygen contaminations of the surface were seen as per Auger spectra which were taken after the CO_2 TDS experiments.

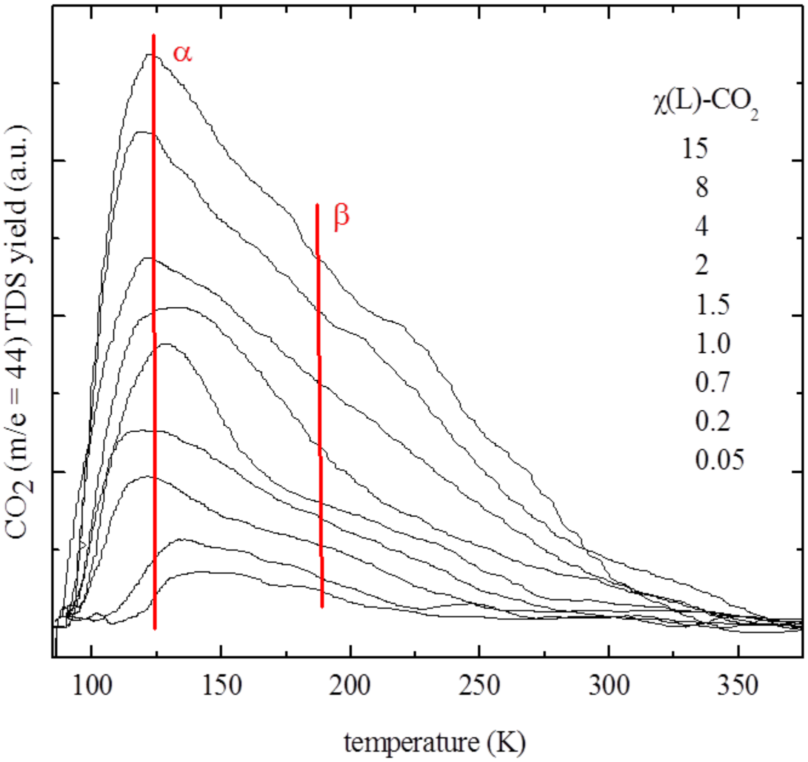

Figure 75. CO_2 TDS data as a function of exposure, χ.

5.2.4.4. Adsorption kinetics of NO

Unlike for CO_2, adsorption of NO at cryogenic temperatures results in only one desorption feature while recording the parent mass (with a mass-to-charge ratio, m/e, of 30). The

TDS peaks shift from 136 K to 179 K with increasing exposure, which is shown in Figure 76A, indicating attractive lateral interactions. This phenomenon is frequently observed for NO (see e.g., ref.[156]). At a quick glance, it appears unusual that the low temperature edges of the TDS curves overlap. However, this is simply the result of the attractive lateral interactions and can qualitatively be reproduced by a simple simulation of the kinetics, as shown in the inset of Figure 76A. For the sake of simplicity, the Polanyi-Wigner equation has been integrated assuming a linear coverage dependence (see inset) of the heat of adsorption (E_d) using computer simulation. Above a given exposure (or initial coverage), the low temperature edges of the TDS curves overlap in the computer simulation similar to the experimental results.

Integrating the TDS peaks and setting the saturation coverage to 1 ML allows one to determine the relative NO coverage. Further, assuming standard first order kinetics (pre-exponential of $1x10^{13}/s$) and using a Redhead analysis of the experimental TDS peak positions results in the E_d vs. coverage curve shown in Figure 76B. The binding energies are characteristic of the molecular adsorption of NO monomers.[320-321]

Multi-mass TDS experiments were also performed to investigate the bond activation of the NO molecules. As a result, a very small fraction of the NO molecules seem to decompose. In addition to the fragments expected for gaseous NO, peaks at m/e = 32 and at m/e = 16 were seen, which is consistent with the decomposition of NO as given by:

$$2NO^{ad} \rightarrow O_2^{gas} + N_2^{gas} \tag{5.11}$$

However, considering the m/e = 32 (from O_2) to m/e = 30 (parent mass of NO) intensity ratio, a decomposition probability of only 7% is estimated. Therefore, a small fraction of NO molecules were decomposed besides the molecular adsorption pathway.

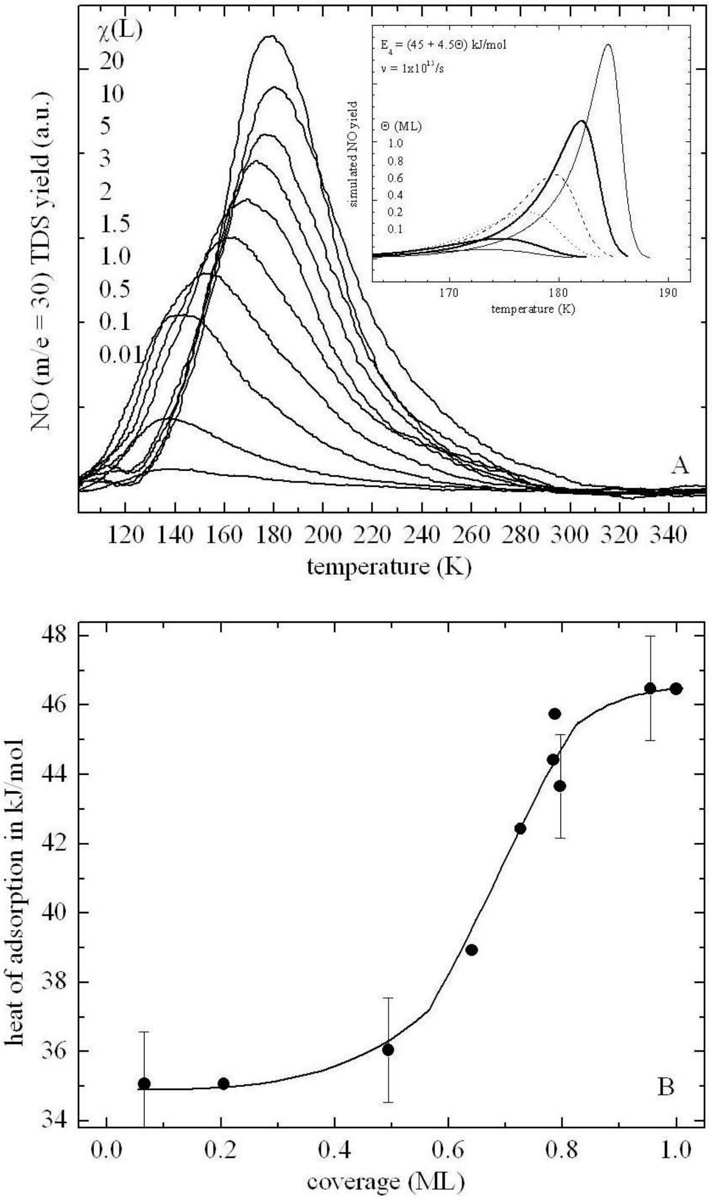

Figure 76. A) NO TDS data of the parent mass, as a function of exposure. The inset shows the result of a simple computer simulation. B) Coverage dependent heat of adsorption as determined for the TDS peak positions using the Redhead equation.

5.2.4.5. Adsorption kinetics of H_2/D_2

The TDS data of atomic hydrogen adsorption are presented in Figure 77. The adsorption of molecular hydrogen (H_2) was not evident, as expected. Therefore, a hot tungsten filament was used to break molecular hydrogen to an atomic hydrogen and was dosed on the surface. Similarly, deuterium TDS curves were also collected, which again are nearly identical to the H TDS curves, as expected. A single symmetric TDS peak at about 173 K, independent of exposure, was detected. The symmetric curve shapes are indicative of recombinative desorption given by:

$$H^{ad} + H^{ad} \rightarrow H_2^{gas} \tag{5.12}$$

Therefore, assuming a second order pre-exponential factor for hydrogen of 10^{21} cm^2/(mol s) (see ref.[322]), a heat of adsorption was found to be 71 kJ/mol. The TDS peak temperatures observed and binding energies calculated are rather low.[323]

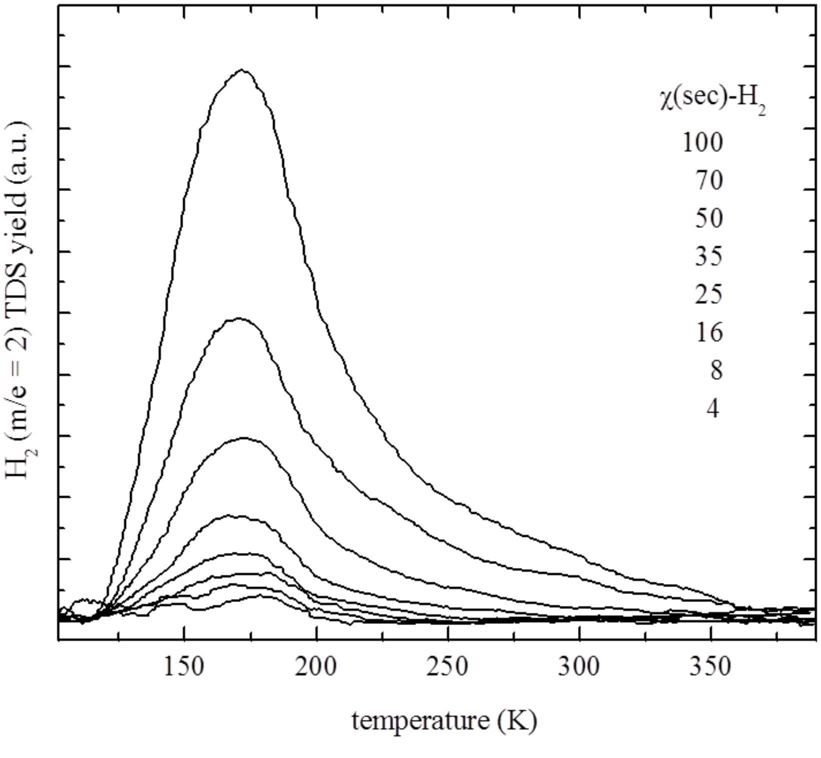

Figure 77. TDS curves of hydrogen as a function of exposure.

It is evident from earlier studies that Se can form hydrates such as HSe and H_2Se (see refs.[314-315,324]). Therefore, multi-mass TDS data were collected after dosing atomic H/D and mass-to-charge ratios of m/e = 80 (corresponding to HSe), 81 (H_2Se or DSe), 82 (HDSe), and 83

(D_2Se) were recorded. When dosing atomic hydrogen, signals were indeed found at m/e = 80 and 81, indicating the formation of HSe and H_2Se, but no signals were detected at m/e = 82 and 83, as expected. All fragments recorded desorb in the temperature range of 150-200 K, i.e., hydrates are formed within this temperature range at ultra-high vacuum conditions, but the actual temperature of hydrates' decomposition is unknown.

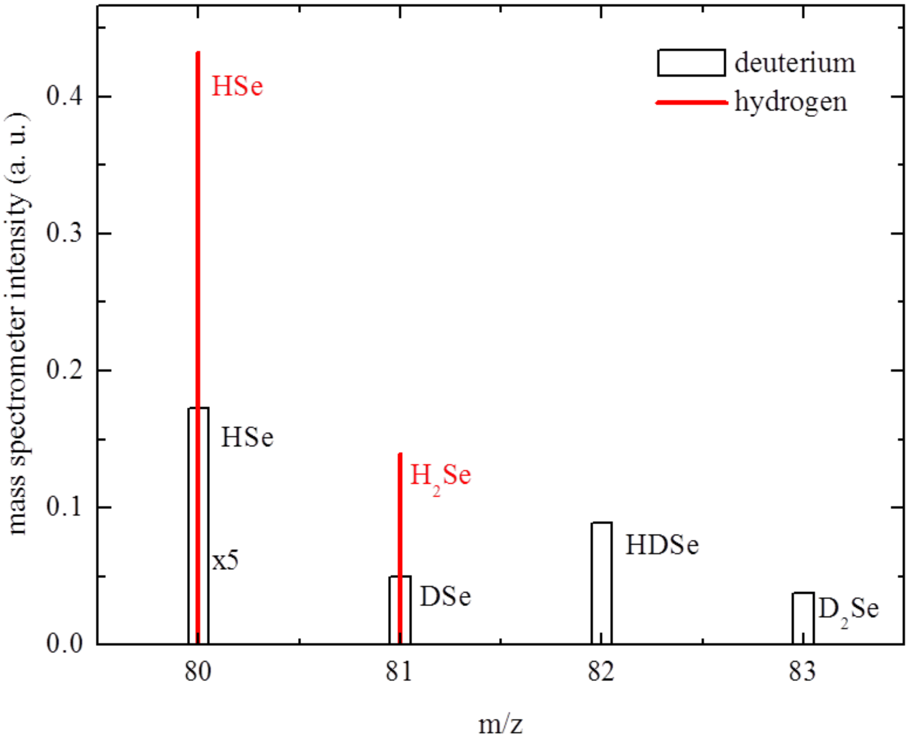

Figure 78. Integrated TDS intensities of multi-mass TDS data obtained after dosing for 100 sec hydrogen (solid lines) or deuterium (open bars) at 1 × 10^{-6} mbar are shown. The intensities of the deuterium data are multiplied by a factor of five.)

The integrated TDS curves are presented in Figure 78. The results obtained from atomic deuterium are more complicated for the reason that not only DSe (m/e = 81) and D_2Se (83) are formed, but also HDSe (82). The latter appears plausible due to the background pressure of hydrogen in any vacuum chamber. In addition, m/e = 80 is evident, which also could originate from the residual hydrogen. It is possible that HSe/DSe may also have formed in the ionizer of the mass spectrometer as a fragment of H_2Se/D_2Se. However, elemental Se was not detected in the gas phase during the entire experiment.

All intensities seen for the deuterated species are smaller by an order of magnitude than those for the hydrogenated species, both are shown in Figure 78. (Note that the D TDS intensities have been multiplied by a factor of five.) The hydrogen-related signal at m/e = 80 (HSe) dominates the multi-mass data. Similarly, the intensity for HDSe at m/e = 82 is also rather large. Reactions involving X–D bond breaking generally have a smaller rate than X–H bond breaking processes due to their higher activation barrier and the lower zero point energy (and zero point vibrational energy) as seen in this equation:

$$\nu = \frac{1}{2\pi}\sqrt{k}/\mu \tag{5.13}$$

For this reason, the smaller intensities are seen for all deuterated species compared to the hydrogenates. Furthermore, reaction such as:

$$D_2Se + H \rightarrow HSe + D_2 \tag{5.14}$$

has been seen in photocatalytic gas phase reactions.[324] It is unclear if this type of process is possible as a thermally activated surface reaction, but it would explain the larger intensities of m/e = 80 in the D multi-mass TDS data (besides the direct formation of HSe from the background). Importantly, the fact that masses 82 and 83 are missing in the hydrogen experiments but are present in multi-mass deuterium TDS experiments clearly shows that a chemical reaction with Se took place. The latter is not unexpected since it is known that atomic hydrogen can “sputter-damage” surfaces.[325] Hydrates will be very unlikely to form at oxidizing conditions of traditional coal combustion plants; they may, however, form at reducing conditions which are present in coal gasification systems.

5.2.4.6. Adsorption kinetics of H_2O

The results of the water TDS as a function of exposure are shown in Figure 79. The data for the molecularly adsorbed water resemble a commonly observed shape:[191-193] a single peak at low exposure and two peaks at higher exposures. It means a low temperature feature appears only at greater exposures. The latter structure shifts to higher desorption temperatures with increasing exposure consistent with zero order kinetics. Therefore, we assign the γ peak to the formation of water clusters in the monolayer range and the c peak to water condensation (amorphous solid water). The heat of adsorption of the γ peak at 200 K would amount to binding energy of 51.1 kJ/mol, assuming a first order process with pre-exponential factor of 10^{13}/s.

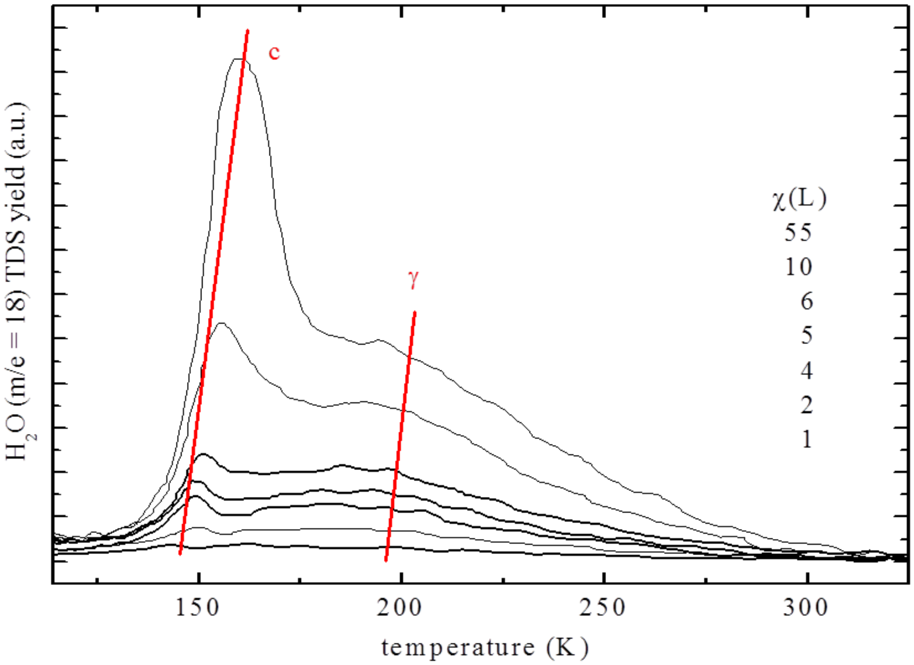

Figure 79. Water TDS curves as a function of exposure.

Water TDS features are fairly common for a large number of systems between 150 K (condensation temperature) and room temperature.[191] The dissociation of water appears very unlikely under the experimental conditions applied in this project and would typically lead to more complex TDS spectra.[191] In addition, dissociative adsorption would lead to higher temperature TDS peaks, which were not observed. However, due to the low melting temperature of selenium foil, TDS curves could only be collected up to surface temperatures of 390 K.

5.2.5. Summary

The chemical activity of a Se foil was investigated at UHV conditions using a variety of probe molecules such as CO_2, NO, H_2, D_2, and H_2O. Auger electron spectroscopy and X-ray diffraction were used to characterize the surface, and thermal desorption spectroscopy was used to characterize the adsorption kinetics of several gases on coal combustion model system. The heat of adsorption was determined from the TDS peak positions. Besides H_2, rather large binding energies were seen for CO_2, NO, and H_2O, but, with desorption temperatures below room temperature. Interestingly, the adsorption of NO and H_2 led to the formation of reaction products such as N_2, O_2, and Se hydrates but with very small rates.

5.3. Overall summary of the chapter

Table 8 summarizes the results obtained from the study of coal combustion gases adsorbed on several model catalysts which includes the TDS peak temperatures, the number of peaks, their corresponding binding energies, and adsorption pathways.

Table 8. Summary showing the results of coal combustion gases adsorption on model catalysts studied in this dissertation. Ref. [42,44,296,302]

Gases	**Model catalysts**	**Lower T_{peak} (K)**	**Higher T_{peak} (K)**	**E_d (KJ/mol)** Pristine	**E_d (KJ/mol)** Defects	**Adsorption/ Formation**
CO	CuO 63 nm	125	195	31.7	50.2	Molecular adsorption on rim and terrace sites
CO_2	CuO 63 nm	x	108	x	27.1	Molecular adsorption on rim site
CO_2	MgO(001)	x	200/260	x	51.7 / 67.7	Chemisorbs, $MgCO_3$ formation
CO_2	Se foil	125	188	32.3	49.0	Molecular adsorption
CO	Se foil	x	x	x	x	No adsorption
NO	Se foil	136-179	x	35.1-46.4	x	Molecular/ dissociatve adsorption, N_2 and O_2 formation
H_2O	Se foil	200	x	51.1	x	Molecular adsorption
H_2	Se foil	173	x	71.0	x	Molecular/ Dissociative adsorption, hydrate formation

Note: Binding energies for all the probe molecules except for H_2 (second order pre-exponential factor) were calculated assuming a first order pre-exponential factor of 10^{15} s^{-1}. The uncertainty in temperature readings amounts to ± 5K, resulting in an uncertainty for binding energies of ± 1.3 kJ/mol.

CHAPTER 6. CONCLUSIONS AND IMPLICATIONS

Surface science investigations of model catalysts have made significant contributions in understanding heterogeneous catalysis. Heterogeneous catalysis is considered the foundation of the chemical industry. Every heterogeneous catalytic surface reaction must always be preceded by adsorption. If the active site for adsorption is known before hand, catalysts can be designed not only to accelerate reactions but also to perform at high selectivity. This dissertation reveals the identification of active sites for methanol synthesis model nanocatalysts, i.e. silica-supported CuO_x nanoclusters. Similarly, bond activation in hydrocarbons has been a major topic of research due to its applications in fuel generation. Such bond activation is studied on several model catalysts and the evidence of bond dissociation in alkanes was presented in this dissertation. The oxide-supported metal cluster model catalyst and other model catalyst studied in this dissertation can provide a suitable replicate for industrial catalysts. The fact that there has been a good correlation between the catalytic activity and selectivity of model catalysts and industrial catalysts for a number of catalytic reactions cannot be denied. Therefore, surface chemistry studies on model catalysts enables one to design structure-activity relationships at an atomic level leading to the development of efficient catalysts.

Thermal desorption spectroscopy (TDS) and molecular beam scattering (MBS) were utilized to study the adsorption kinetics and dynamics, respectively, of coal combustion gases and alkanes on model catalysts. These studies gave rise to the identification of a large number of adsorbed species that help rationalize diverse surface phenomenon such as physical and chemical adsorption, lateral interactions in adsorbed layers, determination of active sites, formation of products, and other chemical interactions on surfaces. Similarly, several surface science techniques such as Auger electron spectroscopy (AES), X-ray photoelectron spectroscopy (XPS), X-ray diffraction (XRD), low energy electron diffraction (LEED), and scanning electron microscopy (SEM) were used for the characterization of model catalysts.

The investigation on adsorption kinetics and dynamics of CO and CO_2 on EBL-fabricated silica-supported Cu/CuO_x clusters led to the identification of active sites. By measuring CO and CO_2 saturation coverages on different cluster sizes, it was experimentally proven that CO_2 adsorbs preferentially along the clusters' rim and CO on both the rim and terrace sites. The non-activated molecular adsorption of CO and CO_2 was concluded. Adsorption probability of CO on metallic Cu clusters was found to be dependent on cluster size as described in the framework of the capture zone model. Furthermore, the adsorption dynamics of CO was found to be different depending on the oxidation state of Cu clusters. S_0 of CO on the metallic clusters was larger than on oxidic clusters. Distinct cluster size effects were only present in the case of metallic clusters, but not in the case of oxidic clusters due to cluster size expansion during the oxidation process and larger binding energies. Identifying the active sites on a catalyst surface forms the basis of systematic catalyst design strategies. Therefore, the implications for catalysis may be to optimize the catalyst synthesis such that the rim length of the supported clusters is maximized to obtain better product formation rates. This methodology reveals a very clear example and a strategy which could also be applied to other catalysts.

Multi-mass TDS experiment was used to study bond activation in alkanes on model catalysts of metal oxide single crystal, semi-metal single crystal, and silica-supported MoOx nanoclusters. In the case of CaO(100) single crystal, two reaction pathways were evident, namely: molecular adsorption and bond activation for the linear alkanes larger than ethane. The molecular adsorption pathway in the monolayer range led to the detection of two features in TDS data that were assigned to different adsorption sites/configurations. Bond activation in longer chain alkanes led to the formation of mostly methane and ethylene via hydrogen abstraction. Bond activation in alkanes is a critical step in the catalytic processing of alkanes in application such as the catalytic combustion of natural gas, exhaust gas remediation, and the selective oxidation of alkanes to high demand products. Bond activation via hydrogen abstraction is an environmentally pertinent process for generating hydrogen gas from natural gases.

Bond activation was not evident in the cases of Sb(111) single crystal and silica-supported MoO_x nanoclusters. The adsorption of n-butane on Sb(111) surface was found to be molecular and non-activated. Two TDS features were assigned to desorption from monolayer and bilayer ranges. In addition, experimental results strongly indicated a distinct hydrophobic character of Sb(111) surface. Moreover, antimony surfaces appeared inert towards the adsorption of small molecules such as H_2, CO, CO_2, and NO. Site blocking for n-butane adsorption by water was evident at exposures greater than 500L of water.

The adsorption of n-butane on Mo nanoclusters was found to be molecular and non-activated. Two TDS features were assigned to desorption from two different adsorption sites, namely; pristine sites (terraces sites) and defect sites (rim sites). Similarly, molecular beam scattering results depicted that n-butane adsorbed only on metallic Mo clusters but not on oxidic Mo clusters which led to the conclusion that the metallic clusters are reactive, but not the oxidic clusters. It is possible that the oxide formation would be one mechanism for catalyst deactivation.

The kinetics and spectroscopic studies of CO_2 on MgO(001) single crystal revealed carbonate formation at low temperatures. Both the formation and decomposition were likely defect-mediated, which was in agreement with theoretical predictions. These defects were assigned to step sites rather than oxygen vacancies with CO_2 adsorbed in the vicinity of steps.

CO_2 TDS resulted two desorption features at 200 K and 260 K with corresponding binding energies of 51.7 and 67.7 kJ/mol, respectively. Interestingly, CO and oxygen desorbed at ~200 K in multi-mass TDS experiments. The coverage dependence of the adsorption dynamics was precursor-mediated (Kisliuk-type) within the temperature and impact energy range studied. Carbonate formation is environmentally relevant as a mean to sequester CO_2 and exploring CO_2 chemistry in general is timely and environmentally pertinent. The chemical activity of a Se foil was investigated at UHV conditions using a variety of probe molecules such as CO_2, NO, H_2, D_2, and H_2O. The heat of adsorption was determined from the TDS peak positions. Besides H_2, rather large binding energies were seen for CO_2, NO, and H_2O, but, with desorption temperatures below room temperature. Interestingly, the adsorption of NO and H_2 led to the formation of reaction products such as N_2, O_2, and Se hydrates but with very small rates.

REFERENCES

1. Kolasinski, K., *Surface Science*. John Wiley & Sons, Ltd: West Sussex, 2002.
2. Blakely, D. W.; Kozak, E. I.; Sexton, B. A.; Somorjai, G. A. *Journal of Vacuum Science & Technology* **1976,** *13* (5), 1091-1096.
3. Campbell, C. T. *Advances in Catalysis* **1989,** *36*, 1-54.
4. Rainer, D. R.; Xu, C.; Goodman, D. W. *J. Mol. Catal. A-Chem.* **1997,** *119* (1-3), 307-325.
5. Chusuei, C. C.; Lai, X.; Luo, K.; Goodman, D. W. *Topics in Catalysis* **2001,** *14* (1-4), 71-83.
6. Askgaard, T. S.; Norskov, J. K.; Ovesen, C. V.; Stoltze, P. *J. Catal.* **1995,** *156* (2), 229-242.
7. Somorjai, G. A., Li. Y. M, *Introduction to Surface Chemistry and Catalysis*. 2nd ed.; Wiley & Sons: New Yorl, 2010.
8. Ertl, G., *Reactions at Solid Surfaces*. Wiley & Sons: 2009.
9. Kelley, R. D.; Goodman, D. W. *Surf Sci* **1982,** *123* (2-3), L743-L749.
10. Goodman, D. W. *Surf Sci* **1982,** *123* (1), L679-L685.
11. Herman, R. G.; Klier, K.; Simmons, G. W.; Finn, B. P.; Bulko, J. B.; Kobylinski, T. P. *J. Catal.* **1979,** *56* (3), 407-429.
12. Busetto, C.; Delpiero, G.; Manara, G.; Trifiro, F.; Vaccari, A. *J. Catal.* **1984,** *85* (1), 260-266.
13. Rainer, D. R.; Vesecky, S. M.; Koranne, M.; Oh, W. S.; Goodman, D. W. *J. Catal.* **1997,** *167* (1), 234-241.
14. Chen, M. S.; Santra, A. K.; Goodman, D. W. *Physical Review B* **2004,** *69* (15).
15. Wu, M. C.; Goodman, D. W. *Journal of Physical Chemistry* **1994,** *98* (39), 9874-9881.

16. Wu, M. C.; Corneille, J. S.; Estrada, C. A.; He, J. W.; Goodman, D. W. *Chem Phys Lett* **1991,** *182* (5), 472-478.

17. Xu, C.; Lai, X.; Zajac, G. W.; Goodman, D. W. *Physical Review B* **1997,** *56* (20), 13464-13482.

18. Komarneni, M.; Shan, J.; Burghaus, U. *J Phys Chem C* **2011,** *115* (33), 16590-16597.

19. Kadossov, E.; Cabrini, S.; Burghaus, U. *J. Mol. Catal. A-Chem.* **2010,** *321* (1-2), 101-109.

20. Lai, X.; St Clair, T. P.; Valden, M.; Goodman, D. W. *Prog. Surf. Sci.* **1998,** *59* (1-4), 25-52.

21. Jacobs, P. W.; Ribeiro, F. H.; Somorjai, G. A.; Wind, S. J. *Catalysis Letters* **1996,** *37* (3-4), 131-136.

22. Suzuki, T.; Okazaki, K.; Suzuki, S.; Shibayama, T.; Kuwabata, S.; Torimoto, T. *Chem. Mat.* **2010,** *22* (18), 5209-5215.

23. Heiz, U.; Vanolli, F.; Trento, L.; Schneider, W. D. *Review of Scientific Instruments* **1997,** *68* (5), 1986-1994.

24. Bromann, K.; Felix, C.; Brune, H.; Harbich, W.; Monot, R.; Buttet, J.; Kern, K. *Science* **1996,** *274* (5289), 956-958.

25. Kleyn, A. W. *Chemical Society Reviews* **2003,** *32* (2), 87-95.

26. Avoyan, A.; Rupprechter, G.; Eppler, A. S.; Somorjai, G. A. *Topics in Catalysis* **2000,** *10* (1-2), 107-113.

27. Schildenberger, M.; Bonetti, Y.; Aeschlimann, M.; Scandella, L.; Gobrecht, J.; Prins, R. *Catalysis Letters* **1998,** *56* (1), 1-6.

28. Swaine, D. J., *Trace Elements in Coal, (M)*. Butterworth, London, 1990.

29. D.J. Swaine, F. G., *Environmental Aspects of Trace Elements in Coal, (M)*. Kluwer, Dordrecht, 1995.

30. Raask, E. *Progress in Energy and Combustion Science* **1985,** *11* (2), 97-118.

31. Chinchen, G. C.; Denny, P. J.; Jennings, J. R.; Spencer, M. S.; Waugh, K. C. *Applied Catalysis* **1988,** *36* (1-2), 1-65.

32. Chinchen, G. C.; Hay, C. M.; Vandervell, H. D.; Waugh, K. C. *J. Catal.* **1987,** *103* (1), 79-86.

33. Chinchen, G. C.; Waugh, K. C.; Whan, D. A. *Applied Catalysis* **1986,** *25* (1-2), 101-107.

34. Fleisch, T. H.; Mieville, R. L. *J. Catal.* **1984,** *90* (1), 165-172.

35. Clausen, B. S.; Steffensen, G.; Fabius, B.; Villadsen, J.; Feidenhansl, R.; Topsoe, H. *J. Catal.* **1991,** *132* (2), 524-535.

36. Behrens, M.; Studt, F.; Kasatkin, I.; Kuhl, S.; Havecker, M.; Abild-Pedersen, F.; Zander, S.; Girgsdies, F.; Kurr, P.; Kniep, B. L.; Tovar, M.; Fischer, R. W.; Norskov, J. K.; Schlogl, R. *Science* **2012,** *336* (6083), 893-897.

37. Klier, K. *Advances in Catalysis* **1982,** *31*, 243-313.

38. Chinchen, G. C.; Denny, P. J.; Parker, D. G.; Spencer, M. S.; Whan, D. A. *Applied Catalysis* **1987,** *30* (2), 333-338.

39. Muhler, M.; Nielsen, L. P.; Tornqvist, E.; Clausen, B. S.; Topsoe, H. *Catalysis Letters* **1992,** *14* (3-4), 241-249.

40. Rasmussen, P. B.; Holmblad, P. M.; Askgaard, T.; Ovesen, C. V.; Stoltze, P.; Norskov, J. K.; Chorkendorff, I. *Catalysis Letters* **1994,** *26* (3-4), 373-381.

41. Millar, G. J.; Rochester, C. H.; Waugh, K. C. *Catalysis Letters* **1992,** *14* (3-4), 289-295.

42. Komarneni, M.; Shan, J.; Chakradhar, A.; Kadossov, E.; Cabrini, S.; Burghaus, U. *J Phys Chem C* **2012,** *116* (9), 5792-5801.

43. Chakradhar, A.; Shan, J.; Komarneni, M. R.; Lu, M.; Burghaus, U. *Chem Phys Lett* **2012,** *544*, 70-72.

44. Shan, J.; Chakradhar, A.; Komarneni, M.; Burghaus, U. *J Phys Chem C* **2012,** *116* (35), 18930-18936.

45. Shan, J.; Komarneni, M.; Burghaus, U. *Chem Phys Lett* **2011,** *517* (1-3), 59-61.

46. Weinberg, W. H.; Sun, Y. K. *Science* **1991,** *253* (5019), 542-545.

47. C.B. Mullins, W. H. W., *Kinetics and dynamics of alkane activation on transition metal surfaces*. Springer Series in Surface Science: 1992; Vol. 34, ch. 7.

48. Weaver, J. F.; Carlsson, A. F.; Madix, R. J. *Surf. Sci. Rep.* **2003,** *50* (4-5), 107-199.

49. Juurlink, L. B. F.; Killelea, D. R.; Utz, A. L. *Prog. Surf. Sci.* **2009,** *84* (3-4), 69-134.

50. Zaera, F. *Catal. Today* **2003,** *81* (2), 149-157.

51. Wodtke, A. M.; Matsiev, D.; Auerbach, D. J. *Prog. Surf. Sci.* **2008,** *83* (3), 167-214.

52. Ding, J. Q.; Burghaus, U.; Weinberg, W. H. *Surf Sci* **2000,** *446* (1-2), 46-54.

53. Larsen, J. H.; Chorkendorff, I. *Surf. Sci. Rep.* **1999,** *35* (5-8), 165-222.

54. J.N. Finch , D. L. R. Catalytic cracking of alkanes 1976 US Patent 3985641.

55. Pant, K. K.; Kunzru, D. *Chemical Engineering Journal* **2002,** *87* (2), 219-225.

56. Koper, O. B.; Wovchko, E. A.; Glass, J. A.; Yates, J. T.; Klabunde, K. J. *Langmuir* **1995,** *11* (6), 2054-2059.

57. Paganini, M. C.; Chiesa, M.; Martino, P.; Giamello, E. *Journal of Physical Chemistry B* **2002,** *106* (48), 12531-12536.

58. McCarty, J. G. *Catal. Today* **1995,** *26* (3-4), 283-293.

59. Tait, S. L.; Dohnalek, Z.; Campbell, C. T.; Kay, B. D. *J. Chem. Phys.* **2005,** *122* (16).

60. Wang, J.; Hokkanen, B.; Burghaus, U. *Surf Sci* **2005,** *577* (2-3), 158-166.

61. Goering, J.; Kadossov, E.; Burghaus, U.; Yu, Z. Q.; Thevuthasan, S.; Saraf, L. V. *Catalysis Letters* **2007,** *116* (1-2), 9-14.

62. Hokkanen, B.; Funk, S.; Burghaus, U.; Ghicov, A.; Schmuki, P. *Surf Sci* **2007,** *601* (19), 4620-4628.

63. Funk, S.; Goering, J.; Burghaus, U. *Applied Surface Science* **2008,** *254* (16), 5271-5275.

64. Funk, S.; Nurkic, T.; Burghaus, U. *Applied Surface Science* **2007,** *253* (11), 4860-4865.

65. Paserba, K. R.; Gellman, A. J. *Physical Review Letters* **2001,** *86* (19), 4338-4341.

66. Kadossov, E.; Goering, J.; Burghaus, U. *Surf Sci* **2007,** *601* (16), 3421-3425.

67. Funk, S.; Burghaus, U.; White, B.; O'Brien, S.; Turro, N. J. *J Phys Chem C* **2007,** *111* (22), 8043-8049.

68. Weaver, J. F.; Devarajan, S. P.; Hakanoglu, C. *J Phys Chem C* **2009,** *113* (22), 9773-9782.

69. Weaver, J. F.; Hakanoglu, C.; Hawkins, J. M.; Asthagiri, A. *J. Chem. Phys.* **2010,** *132* (2).

70. Lorenz, M. P. A.; Fuhrmann, T.; Streber, R.; Bayer, A.; Bebensee, F.; Gotterbarm, K.; Kinne, M.; Traenkenschuh, B.; Zhu, J. F.; Papp, C.; Denecke, R.; Steinrueck, H. P. *J. Chem. Phys.* **2010,** *133* (1).

71. Kadossov, E. B.; Burghaus, U. *Chemical Communications* **2008,** (34), 4073-4075.

72. Yates, J. T., *Experimental Innovations in Surface Science: a Guide to Practical Laboratory Methods and Instruments*. AIP Press Springer: New York, 1988.

73. Weirum, G.; Kratzer, M.; Koch, H. P.; Tamtogl, A.; Killmann, J.; Bako, I.; Winkler, A.; Surnev, S.; Netzer, F. P.; Schennach, R. *J Phys Chem C* **2009,** *113* (22), 9788-9796.

74. Chakradhar, A.; Liu, Y.; Schmidt, J.; Kadossov, E.; Burghaus, U. *Surf Sci* **2011,** *605* (15-16), 1537-1543.

75. M. Asscher, G. A. S., in: G. Scoles (Ed.), *Atomic and Molecular Beam Methods*. Oxford University Press: 1988; Vol. 2.

76. Rettner, C. T.; Auerbach, D. J.; Tully, J. C.; Kleyn, A. W. *Journal of Physical Chemistry* **1996,** *100* (31), 13021-13033.

77. A.W. Kleyn, i. D. P. W. E., *The Chemical Physics of Solid Surfaces (Surface Dynamics)*. Elsevier: Amsterdam, 2003; Vol. 11.

78. Rumpf, F.; Poppa, H.; Boudart, M. *Langmuir* **1988,** *4* (3), 722-728.

79. Henry, C. R. *Surf. Sci. Rep.* **1998,** *31* (7-8), 235-325.

80. Hudson, J., *Surface Science: An Introduction*. John Wiley & Sons: New York, 1998.

81. G. H. Stout, L. J., *X-ray structure determination: a practical guide,*. 1989.

82. Bhuvana, T.; Kulkarni, G. U. *Acs Nano* **2008,** *2* (3), 457-462.

83. Pearson, J. L.; Cumming, D. R. S. *Microelectronic Engineering* **2005,** *78-79*, 343-348.

84. Sun, T.; Pan, Z. X.; Dravid, V. P.; Wang, Z. Y.; Yu, M. F.; Wang, J. *Applied Physics Letters* **2006,** *89* (16).

85. Liu, C.-j.; Burghaus, U.; Besenbacher, F.; Wang, Z. L. *Acs Nano* **2010,** *4* (10), 5517-5526.

86. Ribeiro, F. H.; Somorjai, G. A. *Recueil Des Travaux Chimiques Des Pays-Bas-Journal of the Royal Netherlands Chemical Society* **1994,** *113* (10), 419-422.

87. Wong, K.; Johansson, S.; Kasemo, B. *Faraday Discuss.* **1996,** *105*, 237-246.

88. Ribeiro, F. H.; Somorjai, G. A. *Recueil Des Travaux Chimiques Des Pays-Bas-Journal of the Royal Netherlands Chemical Society* **1994,** *113* (10), 419-422.

89. Johanek, V.; Laurin, M.; Grant, A. W.; Kasemo, B.; Henry, C. R.; Libuda, J. *Science* **2004,** *304* (5677), 1639-1644.

90. Vieu, C.; Carcenac, F.; Pepin, A.; Chen, Y.; Mejias, M.; Lebib, A.; Manin-Ferlazzo, L.; Couraud, L.; Launois, H. *Applied Surface Science* **2000,** *164*, 111-117.

91. Woodward, R. B.; Hoffmann, R. *Angewandte Chemie-International Edition* **1969,** *8* (11), 781-+.

92. Taylor, H. S. *Proceedings of the Royal Society of London Series a-Containing Papers of a Mathematical and Physical Character* **1925,** *108* (745), 105-111.

93. Jaramillo, T. F.; Jorgensen, K. P.; Bonde, J.; Nielsen, J. H.; Horch, S.; Chorkendorff, I. *Science* **2007,** *317* (5834), 100-102.

94. Kibsgaard, J.; Lauritsen, J. V.; Laegsgaard, E.; Clausen, B. S.; Topsoe, H.; Besenbacher, F. *J. Am. Chem. Soc.* **2006,** *128* (42), 13950-13958.

95. Frost, J. C. *Nature* **1988,** *334* (6183), 577-580.

96. Kobayashi, H.; Takezawa, N.; Minochi, C. *J. Catal.* **1981,** *69* (2), 487-494.

97. Ossipoff, N. J.; Cant, N. W. *J. Catal.* **1994,** *148* (1), 125-133.

98. Kadossov, E.; Burghaus, U. *Surface and Interface Analysis* **2008,** *40* (5), 893-898.

99. Kadossov, E.; Goering, J.; Burghaus, U. *Surf Sci* **2008,** *602* (3), 811-818.

100. Hansen, J. B., *Handbook of Heterogeneous Catalysis*. VCH: Weinheim, 1997; Vol. 1.

101. Hara, M.; Kondo, T.; Komoda, M.; Ikeda, S.; Shinohara, K.; Tanaka, A.; Kondo, J. N.; Domen, K. *Chemical Communications* **1998,** (3), 357-358.

102. Newsome, D. S. *Catalysis Reviews-Science and Engineering* **1980,** *21* (2), 275-318.

103. Sadykov, V. A.; Tikhov, S. F.; Bulgakov, N. N.; Gerasev, A. P. *Catal. Today* **2009,** *144* (3-4), 324-333.

104. Chan, G. H.; Zhao, J.; Hicks, E. M.; Schatz, G. C.; Van Duyne, R. P. *Nano Letters* **2007,** *7* (7), 1947-1952.

105. Musa, A. O.; Akomolafe, T.; Carter, M. J. *Solar Energy Materials and Solar Cells* **1998,** *51* (3-4), 305-316.

106. Bednorz, J. G.; Muller, K. A. *Zeitschrift Fur Physik B-Condensed Matter* **1986,** *64* (2), 189-193.

107. Burghaus, U. *Catal. Today* **2009,** *148* (3-4), 212-220.

108. White, B.; Yin, M.; Hall, A.; Le, D.; Stolbov, S.; Rahman, T.; Turro, N.; O'Brien, S. *Nano Letters* **2006,** *6* (9), 2095-2098.

109. Premkumar, T.; Geckeler, K. E. *Journal of Physics and Chemistry of Solids* **2006,** *67* (7), 1451-1456.

110. van den Oetelaar, L. C. A.; Partridge, A.; Stapel, P. J. A.; Flipse, C. F. J.; Brongersma, H. H. *Journal of Physical Chemistry B* **1998,** *102* (47), 9532-9540.

111. Cox, P. A., *Transition metal oxides*. Clarendon Press: Oxford, 1995.

112. Cox, D. F.; Schulz, K. H. *Surf Sci* **1991,** *249* (1-3), 138-148.

113. Sueyoshi, T.; Sasaki, T.; Iwasawa, Y. *Surf Sci* **1995,** *343* (1-2), 1-16.

114. Wang, J.; Burghaus, U. *J. Chem. Phys.* **2005,** *122* (4).

115. Kao, C. L.; Carlsson, A.; Madix, R. J. *Surf Sci* **2002,** *497* (1-3), 356-372.

116. Funk, S.; Hokkanen, B.; Wang, J.; Burghaus, U.; Bozzolo, G.; Garces, J. E. *Surf Sci* **2006,** *600* (3), 583-590.

117. Develyn, M. P.; Hamza, A. V.; Gdowski, G. E.; Madix, R. J. *Surf Sci* **1986,** *167* (2-3), 451-473.

118. Wang, J.; Burghaus, U. *J. Chem. Phys.* **2005,** *123* (18).

119. Henderson, M. A. *Surf Sci* **1998,** *400* (1-3), 203-219.

120. Wang, J.; Funk, S.; Burghaus, U. *Catalysis Letters* **2005,** *103* (3-4), 219-223.

121. Wang, J.; Funk, S.; Burghaus, U. *J. Chem. Phys.* **2005,** *123* (20).

122. Wang, J.; Burghaus, U. *Chem Phys Lett* **2005,** *403* (1-3), 42-46.

123. Wang, J.; Johnson, E.; Burghaus, U. *Chem Phys Lett* **2005,** *410* (1-3), 131-135.

124. Kadossov, E.; Justin, J.; Lu, M.; Rosenmann, D.; Ocola, L. E.; Cabrini, S.; Burghaus, U. *Chem Phys Lett* **2009,** *483* (4-6), 250-253.

125. Golunski, S. E. *Platinum Metals Review* **2007,** *51* (3), 162-162.

126. Kadossov, E.; Burghaus, U. *Catalysis Letters* **2010,** *134* (3-4), 228-232.

127. Poulston, S.; Parlett, P. M.; Stone, P.; Bowker, M. *Surface and Interface Analysis* **1996,** *24* (12), 811-820.

128. Panzner, G.; Egert, B.; Schmidt, H. P. *Surf Sci* **1985,** *151* (2-3), 400-408.

129. Espinos, J. P.; Morales, J.; Barranco, A.; Caballero, A.; Holgado, J. P.; Gonzalez-Elipe, A. R. *Journal of Physical Chemistry B* **2002,** *106* (27), 6921-6929.

130. Moretti, G.; Derossi, S.; Ferraris, G. *Applied Surface Science* **1990,** *45* (4), 341-349.

131. Xu, X. P.; Vesecky, S. M.; Goodman, D. W. *Science* **1992,** *258* (5083), 788-790.

132. Xu, X. P.; He, J. W.; Goodman, D. W. *Surf Sci* **1993,** *284* (1-2), 103-108.

133. Xu, X. P.; Goodman, D. W. *Applied Physics Letters* **1992,** *61* (15), 1799-1801.

134. Xu, X. P.; Goodman, D. W. *Journal of Physical Chemistry* **1993,** *97* (3), 683-689.

135. Pierce, D. E.; Burns, R. P.; Gabriel, K. A. *Thin Solid Films* **1991,** *206* (1-2), 340-344.

136. Dumas, P.; Tobin, R. G.; Richards, P. L. *Surf Sci* **1986,** *171* (3), 579-599.

137. Cechal, J.; Polcak, J.; Kolibal, M.; Babor, P.; Sikola, T. *Applied Surface Science* **2010,** *256* (11), 3636-3641.

138. Zhou, J. B.; Gustafsson, T.; Garfunkel, E. *Surf Sci* **1997,** *372* (1-3), 21-27.

139. Hedberg, C. L., *Handbook of Auger Electron Spectroscopy*. Physical Electronics, Inc.: Minneapolis, 1970.

140. Moulder, J. F. S., W. F.; Sobol, P. E.; Bomben, K. D., *Handbook of X-ray Photoelectron Spectroscopy*. Perkin-Elmer Corporation: Eden Prairie, MN, 1992.

141. Barreca, D.; Bruno, G.; Gasparotto, A.; Losurdo, M.; Tondello, E. *Materials Science & Engineering C-Biomimetic and Supramolecular Systems* **2003,** *23* (6-8), 1013-1016.

142. Wu, C.-K.; Yin, M.; O'Brien, S.; Koberstein, J. T. *Chem. Mat.* **2006,** *18* (25), 6054-6058.

143. Fu, S. S.; Somorjai, G. A. *Surf Sci* **1992,** *262* (1-2), 68-76.

144. Wachs, I. E.; Madix, R. J. *J. Catal.* **1978,** *53* (2), 208-227.

145. Kessler, J.; Thieme, F. *Surf Sci* **1977,** *67* (2), 405-415.

146. Linsebigler, A.; Lu, G. Q.; Yates, J. T. *J. Chem. Phys.* **1995,** *103* (21), 9438-9443.

147. Kadossov, E.; Funk, S.; Burghaus, U. *Catalysis Letters* **2008,** *120* (3-4), 179-183.

148. Lemire, C.; Meyer, R.; Henrich, V. E.; Shaikhutdinov, S.; Freund, H. J. *Surf Sci* **2004,** *572* (1), 103-114.

149. Camplin, J. P.; Clowes, S. K.; Cook, J. C.; McCash, E. M. *Surface Review and Letters* **1997,** *4* (6), 1365-1370.

150. Hansen, W.; Bertolo, M.; Jacobi, K. *Surf Sci* **1991,** *253* (1-3), 1-12.

151. Costantini, G.; de Mongeot, F. B.; Rusponi, S.; Boragno, C.; Valbusa, U.; Vattuone, L.; Burghaus, U.; Savio, L.; Rocca, M. *J. Chem. Phys.* **2000,** *112* (15), 6840-6843.

152. Vattuone, L.; Savio, L.; Rocca, M. *Surf. Sci. Rep.* **2008,** *63* (3), 101-168.

153. Funk, S.; Burghaus, U. *Physical Chemistry Chemical Physics* **2006,** *8* (41), 4805-4813.

154. Hadenfeldt, S.; Benndorf, C.; Stricker, A.; Towe, M. *Surf Sci* **1996,** *352*, 295-299.

155. Wang, G. C.; Ling, J.; Morikawa, Y.; Nakamura, J.; Cai, Z. S.; Pan, Y. M.; Zhao, X. Z. *Surf Sci* **2004,** *570* (3), 205-217.

156. Kadossov, E.; Burghaus, U. *J Phys Chem C* **2008,** *112* (19), 7390-7400.

157. Burghaus, U., In New and Future Developments in Catalysis: Activiation of Carbon Dioxide, Suib, S. L., Ed. Elsevier: 2012.

158. Freund, H. J.; Roberts, M. W. *Surf. Sci. Rep.* **1996,** *25* (8), 225-273.

159. Bonicke, I.; Kirstein, W.; Spinzig, S.; Thieme, F. *Surf Sci* **1994,** *313* (3), 231-238.

160. Bowker, M.; Houghton, H.; Waugh, K. C. *Journal of the Chemical Society-Faraday Transactions I* **1981,** *77*, 3023-3036.

161. Kunat, M.; Boas, C.; Becker, T.; Burghaus, U.; Woll, C. *Surf Sci* **2001,** *474* (1-3), 114-128.

162. Bartels, L.; Meyer, G.; Rieder, K. H. *Surf Sci* **1999,** *432* (3), L621-L626.

163. Haruta, M. *Catal. Today* **1997,** *36* (1), 153-166.

164. Kneitz, S.; Gemeinhardt, J.; Koschel, H.; Held, G.; Steinruck, H. P. *Surf Sci* **1999,** *433*, 27-31.

165. Kunat, M.; Burghaus, U. *Surf Sci* **2003,** *544* (2-3), 170-182.

166. Burghaus, U.; Ding, J. Q.; Weinberg, W. H. *Surf Sci* **1997,** *384* (1-3), L869-L874.

167. Zheng, X. G.; Suzuki, M.; Xu, C. N. *Mater Res Bull* **1998,** *33* (4), 605-610.

168. Kim, T. S.; Gong, J.; Ojifinni, R. A.; White, J. M.; Mullins, C. B. *J. Am. Chem. Soc.* **2006,** *128* (19), 6282-6283.

169. Libuda, J.; Freund, H. J. *Surf. Sci. Rep.* **2005,** *57* (7-8), 157-298.

170. Diaz, C.; Olsen, R. A.; Auerbach, D. J.; Kroes, G. J. *Physical Chemistry Chemical Physics* **2010,** *12* (24), 6499-6519.

171. Jensen, M. B.; Pettersson, L. G. M.; Swang, O.; Olsbye, U. *Journal of Physical Chemistry B* **2005,** *109* (35), 16774-16781.

172. Pacchioni, G.; Ricart, J. M.; Illas, F. *J. Am. Chem. Soc.* **1994,** *116* (22), 10152-10158.

173. Blanco-Rey, M.; Jenkins, S. J. *J. Chem. Phys.* **2009,** *130* (1).

174. Doyle, C. S.; Kendelewicz, T.; Carrier, X.; Brown, G. E. *Surface Review and Letters* **1999,** *6* (6), 1247-1254.

175. Voigts, F.; Bebensee, F.; Dahle, S.; Volgmann, K.; Maus-Friedrichs, W. *Surf Sci* **2009,** *603* (1), 40-49.

176. Hedberg, C. L., *Handbook of Auger Electron Spectroscopy*. Physical Electronics, Inc: 1995.

177. Kadossov, E.; Burghaus, U. *Surf Sci* **2009,** *603* (16), 2494-2501.

178. Chakradhar, A.; Liu, Y.; Schmidt, J.; Kadossov, E.; Burghaus, U. *Surf. Sci.* **2011,** *605,* 1534.

179. Dohnalek, Z.; Smith, R. S.; Kay, B. D. *Journal of Physical Chemistry B* **2002,** *106* (33), 8360-8366.

180. Song, J. H.; Chen, P. L.; Kim, S. H.; Somorjai, G. A.; Gartside, R. J.; Dautzenberg, F. M. *J. Mol. Catal. A-Chem.* **2002,** *184* (1-2), 197-202.

181. Cazorlaamoros, D.; Joly, J. P.; Linaressolano, A.; Marcillagomis, A.; Delecea, C. S. *Journal of Physical Chemistry* **1991,** *95* (17), 6611-6617.

182. Ochs, D.; Braun, B.; Maus-Friedrichs, W.; Kempter, V. *Surf Sci* **1998,** *417* (2-3), 406-414.

183. Seames, W. S.; Wendt, J. O. L. *Proceedings of the Combustion Institute* **2007,** *31*, 2839-2846.

184. Zeng, T. F.; Sarofim, A. F.; Senior, C. L. *Combustion and Flame* **2001,** *126* (3), 1714-1724.

185. Guo, Z.; Liu, W.; Su, B.-L. *Journal of Colloid and Interface Science* **2011,** *353* (2), 335-355.

186. Hodgson, A.; Haq, S. *Surf. Sci. Rep.* **2009,** *64* (9), 381-451.

187. Liu, K.; Zhai, J.; Jiang, L. *Nanotechnology* **2008,** *19* (16).

188. Linderoth, T. R.; Zhdanov, V. P.; Kasemo, B. *Physical Review Letters* **2003,** *90* (15).

189. Shan, J.; Aarts, J. F. M.; Kleyn, A. W.; Juurlink, L. B. F. *Physical Chemistry Chemical Physics* **2008,** *10* (32), 4994-5003.

190. Kay, B. D.; Lykke, K. R.; Creighton, J. R.; Ward, S. J. *J. Chem. Phys.* **1989,** *91* (8), 5120-5121.

191. Henderson, M. A. *Surf. Sci. Rep.* **2002,** *46* (1-8), 1-308.

192. Smith, R. S.; Kay, B. D. *Surface Review and Letters* **1997,** *4* (4), 781-797.

193. Thiel, P. A.; Madey, T. E. *Surf. Sci. Rep.* **1987,** *7* (6-8), 211-385.

194. Michaelides, A.; Morgenstern, K. *Nature Materials* **2007,** *6* (8), 597-601.

195. Ryu, J. T.; Kui, K.; Katayama, M.; Oura, K. *Applied Surface Science* **1997,** *121*, 223-227.

196. Schultz, K. A.; Suni, II; Allen, C. E.; Seebauer, E. G. *Surf Sci* **1992,** *276* (1-3), 40-49.

197. Kiskinova, M. P.; Szabo, A.; Yates, J. T. *Surf Sci* **1990,** *226* (3), 237-249.

198. Sporken, R.; Thiry, P. A.; Xhonneux, P.; Caudano, R.; Delrue, J. P. *Applied Surface Science* **1989,** *41-2*, 201-206.

199. Foo, W. C.; Ozcomert, J. S.; Trenary, M. *Surf Sci* **1991,** *255* (3), 245-258.

200. Stiddard, M. H. B. *Journal of Crystal Growth* **1981,** *51* (3), 394-396.

201. Sporken, R.; Thiry, P. A.; Petit, E.; Pireaux, J. J.; Caudano, R.; Ghijsen, J.; Johnson, R. L.; Ley, L. *Physical Review B* **1987,** *35* (15), 7927-7935.

202. Bengio, S.; Wells, J. W.; Kim, T. K.; Zampieri, G.; Petaccia, L.; Lizzit, S.; Hofmann, P. *Surf Sci* **2007,** *601* (14), 2908-2911.

203. Stegemann, B.; Ritter, C.; Kaiser, B.; Rademann, K. *Physical Review B* **2004,** *69* (15).

204. J.F. Moulder, W. F. S., P.E. Sobol, K.D. Bomben, *Handbook of X-ray Photoelectron Spectroscopy*. Perkin-Elmer Corporation: Minnesota, 1992.

205. Tait, S. L.; Dohnalek, Z.; Campbell, C. T.; Kay, B. D. *J. Chem. Phys.* **2006,** *125* (23).

206. King, D. A.; Wells, M. G. *Surf Sci* **1972,** *29* (2), 454-&.

207. Kisliuk, P. *Journal of Physics and Chemistry of Solids* **1957,** *3* (1-2), 95-101.

208. Topsoe, H.; Clausen, B. S.; Massoth, F. E. *J. Catal.* **1996,** *163*, 409.

209. Lauritzen, J. V.; Nyberg, M.; Vang, R. T.; Bollinger, M. V.; Clausen, B. S.; Topsoe, H.; Jacobsen, K. W.; Laegsgaard, E.; Norskov, J. K.; Besenbacher, F. *Nanotechnology* **2003,** *14*, 385.

210. Burghaus, U., *Carbon nanotubes - Research Trends*. 2009.

211. Burghaus, U.; Zak, A.; Rosentsveig, R. *Isr. J. Chem.* **2010,** *50*, 449.

212. Jaworowski, A. J.; Smedh, M.; Borg, M.; Sandell, A.; Beutler, A.; Sorensen, S. L.; Lundgren, E.; Andersen, J. N. *Surf. Sci.* **2001,** *492*, 185.

213. Lopez-Carreno, L. D.; Heras, J. M.; Viscido, L. *Surf. Sci.* **1997,** *377-379*, 615.

214. Bond, G. C., *Heterogeneous catalysis: principles and applications*. 1974.

215. Evans, U. R., *The corrosion and oxidation of metals: scientific principles and practical applications*. 1960.

216. Kadossov, E.; Goering, J.; Burghaus, U. *Surf. Sci.* **2008,** *602,* 811.

217. Ko, E. I.; Madix, R. J. *Surf. Sci.* **1981,** *109*, 221.

218. Miles, S. L.; Bernasek, S. L.; Gland, J. L. *J. Phys. Chem.* **1983,** *87*, 1626.

219. Sierka, M.; Todorova, T. K.; Sauer, J.; Kaya, S.; Stacchiola, D.; Weissenrieder, J.; Shaikhutdinov, S.; Freund, H. J. *J. Chem. Phys.* **2007,** *126* (23), 234710.

220. Kibsgaard, J.; Lauritsen, J. V.; Laegsgaard, E.; Clausen, B. S.; Topsoe, H.; Besenbacher, F. *J. Am. Chem. Soc.* **2006,** *128* (42), 13950.

221. Komarneni, M.; Kadossov, E.; Justin, J.; Lu, M.; Burghaus, U. *Surf. Sci.* **2010,** *604* (13−14), 1221.

222. Ozkan, U.; Schrader, G. L. *J. Catal.* **1985,** *95* (1), 120.

223. Tong, Y. D.; Lunsford, J. H. *J. Am. Chem. Soc.* **1991,** *113* (13), 4741.

224. Miles, S. L.; Bernasek, S. L.; Gland, J. L. *J. Phys. Chem.* **1983,** *87* (9), 1626.

225. Street, S. C.; Liu, G.; Goodman, D. W. *Surf. Sci.* **1997,** *385* (2−3), L971.

226. Berko, A.; Magony, A.; Szoko, J. *Langmuir* **2005,** *21* (10), 4562.

227. Chun, W. J.; Asakura, K.; Iwasawa, Y. *Chem. Phys. Lett.* **1998,** *288* (5−6), 868.

228. Kitchin, J. R.; Barteau, M. A.; Chen, J. G. G. *Surf. Sci.* **2003,** *526* (3), 323.

229. Kaya, S.; Weissenrieder, J.; Stacchiola, D.; Todorova, T. K.; Sierka, M.; Sauer, J.; Shaikhutdinov, S.; Freund, H. J. *Surf. Sci.* **2008,** *602* (21), 3338.

230. Weaver, J. F.; Carlsson, A. F.; Madix, R. J. *Surf. Sci. Rep.* **2003,** *50,* 107.

231. Weinberg, W. H.; Sun, Y. K. *Science* **1991,** *253*, 542.

232. Juurlink, L. B. F.; Killelea, D. R.; Utz, A. L. *Prog. Surf. Sci.* **2009,** *84*, 69.

233. Wodtke, A. M.; Matsiev, D.; Auerbach, D. J. *Prog. Surf. Sci.* **2008,** *83*.

234. Zaera, F. *Catal. Today* **2003,** *81*, 149.

235. Ding, J.; Burghaus, U.; Weinberg, W. H. *Surf. Sci.* **2000,** *446*, 46.

236. Larsen, J. H.; Chorkendorff, I. *Surf. Sci. Rep.* **1999,** *35*, 163.

237. Tait, S. L.; Dohnalek, Z.; Campbell, C. T.; Kay, B. D. *J. Chem. Phys.* **2005,** *122*, 164708.

238. Wang, J.; Hokkanen, B.; Burghaus, U. *Surf. Sci.* **2005,** *577*, 158.

239. Funk, S.; Goering, J.; Burghaus, U. *Appl. Surf. Sci.* **2008,** *254*, 5271.

240. Funk, S.; Nurkic, T.; Burghaus, U. *Appl. Surf. Sci.* **2007,** *253*, 4860.

241. Kadossov, E.; Goering, J.; Burghaus, U. *Surf. Sci.* **2007,** *601*, 3421.

242. Paserba, K. R.; Gellman, A. J. *Phys. Rev. Lett.* **2001,** *86*, 4338.

243. Funk, S.; Hokkanen, B.; Nurkig, T.; Burghaus, U.; White, B.; O’Brien, S.; Turro, N. *J. Phys. Chem. C* **2007,** *111*, 8043.

244. Weaver, J. F.; Devarajan, S. P.; Hakanoglu, C. *J. Phys. Chem. C* **2009,** *113*, 9773.

245. Goering, J.; Kadossov, E.; Burghaus, U.; Yu, Z. Q.; Thevuthasan, S.; Saraf, L. V. *Catal. Lett.* **2007,** *116*, 9.

246. Komarneni, M.; Shan, J.; Chakradhar, A.; Kadossov, E.; Cabrini, S.; Burghaus, U. *J. Phys. Chem. C* **2011,** *116*, 5792.

247. Shan, J.; Chakradhar, A.; Anderson, K.; Schmidt, J.; Dhuey, S.; Burghaus, U., Butane Adsorption on Silica Supported MoOx Clusters Nanofabricated by Electron Beam Lithography. In *Nanotechnology for Sustainable Energy*, American Chemical Society: 2013; Vol. 1140, pp 295-310.

248. Deiner, L. J.; Chan, A. S. Y.; Sheehy, M. A.; Friend, C. M. *Surf. Sci.* **2004,** *555* (1−3), L127.

249. Deiner, L. J.; Kang, D. H.; Friend, C. A. *J. Phys. Chem. B* **2005,** *109* (26), 12826.

250. Deiner, L. J.; Kang, D. H.; Friend, C. M. *J. Phys. Chem. B* **2005,** *109* (16), 8085.

251. Sasaki, T.; Goto, Y.; Tero, R.; Fukui, K.; Iwasawa, Y. *Surf. Sci.* **2002,** *502*, 136.

252. Kim, B. S.; K, E. Y.; Jeon, H. S.; Lee, H. I.; Lee, J. C. *Mater. Trans.* **2008,** *49* (9), 2147.

253. Moulder, J. F.; Stickle, W. F.; Sobol, P. E.; Bomben, K. D., *Handbook of x-ray photoelectron spectroscopy*. 1980.

254. Komarneni, M.; Shan, J.; Burghaus, U. *J. Phys. Chem. C* **2011,** *115* (33), 16590.

255. Komarneni, M.; Shan, J.; Chakradhar, A.; Kadossov, E.; Cabrini, S.; Burghaus, U. *J. Phys. Chem. C* **2012,** *116* (9), 5792.

256. Marin-Flores, O.; Scudiero, L.; Ha, S. *Surf. Sci.* **2009,** *603* (15), 2327.

257. Schroeder, T.; Zegenhagen, J.; Magg, N.; Immaraporn, B.; Freund, H. J. *Surf. Sci.* **2004,** *552* (1−3), 85.

258. Chakradhar, A.; Shan, J.; Komarneni, M. R.; Lu, M.; Burghaus, U. *Chem. Phys. Lett* **2012,** *544*, 70.

259. Kadossov, E.; Burghaus, U. *Surf. Sci.* **2009,** *603*, 2494.

260. King, D. A.; Wells, M. G. *Surf. Sci.* **1972,** *29*, 454.

261. Henrich, V. E.; Cox, P. A., *The Surface Science of Metal Oxides*. 1994.

262. Zhang, X.; Linsebigler, A.; Heiz, U.; Yates, J. T. *J. Phys. Chem.* **1993,** *97*, 5074.

263. Shan, J.; Chakradhar, A.; Yu, Z.; Burghaus, U. *Chem Phys Lett* **2011,** *517* (1-3), 46-50.

264. G.A. Olah, A. G., G.K.S. Prakash, *Beyond Oil and Gas: The Methanol Economy*. Wiley-VCH: 2003.

265. Marini, L., *Geological Sequestration of Carbon Dioxide in Developments in Geochemistry*. Elsevier: 2007; Vol. 11.

266. Wang, S.; Yan, S.; Ma, X.; Gong, J. *Energy Environ. Sci.* **2011,** *4* (10), 3805-3819.

267. He, J. W.; Estrada, C. A.; Corneille, J. S.; Wu, M. C.; Goodman, D. W. *Surf Sci* **1992,** *261* (1-3), 164-170.

268. Qin, C. *Chem Phys Lett* **2008,** *460* (4-6), 457-460.

269. Sterrer, M.; Fischbach, E.; Risse, T.; Freund, H. J. *Physical Review Letters* **2005,** *94* (18).

270. Piccolo, L.; Henry, C. R. *Surf Sci* **2000,** *452* (1-3), 198-206.

271. Meixner, D. L.; Arthur, D. A.; George, S. M. *Surf Sci* **1992,** *261* (1-3), 141-154.

272. Shen, J. Y.; Kobe, J. M.; Chen, Y.; Dumesic, J. A. *Langmuir* **1994,** *10* (10), 3902-3908.

273. Tsuji, H.; Shishido, T.; Okamura, A.; Gao, Y. Z.; Hattori, H.; Kita, H. *J. Chem. Soc.-Faraday Trans.* **1994,** *90* (5), 803-807.

274. Yanagisawa, Y.; Takaoka, K.; Yamabe, S.; Ito, T. *Journal of Physical Chemistry* **1995,** *99* (11), 3704-3710.

275. Pacchioni, G. *Surf Sci* **1993,** *281* (1-2), 207-219.

276. Allen, J. P.; Parker, S. C.; Price, D. W. *J Phys Chem C* **2009,** *113* (19), 8320-8328.

277. Cornu, D.; Guesmi, H.; Krafft, J.-M.; Lauron-Pernot, H. *J Phys Chem C* **2012,** *116* (11), 6645-6654.

278. Krenzer, B.; Constant, L.; Conrad, H. *Surf Sci* **1999,** *443* (1-2), 116-124.

279. L'Vov, B. V. *Thermochimica Acta* **2002,** *386* (1), 1-16.

280. Ojifinni, R. A.; Gong, J.; Froemming, N. S.; Flaherty, D. W.; Pan, M.; Henkelman, G.; Mullins, C. B. *J. Am. Chem. Soc.* **2008,** *130* (34), 11250-+.

281. Ochs, D.; Brause, M.; Braun, B.; Maus-Friedrichs, W.; Kempter, V. *Surf Sci* **1998,** *397* (1-3), 101-107.

282. Onishi, H.; Egawa, C.; Aruga, T.; Iwasawa, Y. *Surf Sci* **1987,** *191* (3), 479-491.

283. Aswal, D. K.; Muthe, K. P.; Tawde, S.; Chodhury, S.; Bagkar, N.; Singh, A.; Gupta, S. K.; Yakhmi, J. V. *Journal of Crystal Growth* **2002,** *236* (4), 661-666.

284. Carrier, X.; Doyle, C. S.; Kendelewicz, T.; Brown, G. E. *Surface Review and Letters* **1999,** *6* (6), 1237-1245.

285. Fukuda, Y.; Toyoshima, I. *Surf Sci* **1985,** *158* (1-3), 482-489.

286. Heidberg, J.; Meine, D. *Surf Sci* **1992,** *279* (1-2), L175-L179.

287. Odelius, M. *Physical Review Letters* **1999,** *82* (19), 3919-3922.

288. Schneider, W. F.; Hass, K. C.; Miletic, M.; Gland, J. L. *Journal of Physical Chemistry B* **2002,** *106* (30), 7405-7413.

289. Sterrer, M.; Risse, T.; Heyde, M.; Rust, H.-P.; Freund, H.-J. *Physical Review Letters* **2007,** *98* (20).

290. Yan, Y.; Zhou, L.; Zhang, Y. *J Phys Chem C* **2008,** *112* (50), 19831-19835.

291. Briggs, D., *Handbook of X-ray and Ultraviolet Photoelectron Spectroscopy*. W. Clowes, London, 1978.

292. Davis, L. E., *Phys. Electron*. 1996.

293. Heidberg, J.; Redlich, B. *Surf Sci* **1996,** *368*, 140-146.

294. Florez, E.; Fuentealba, P.; Mondragon, F. *Catal. Today* **2008,** *133*, 216-222.

295. http://webbook.nist.gov.

296. Chakradhar, A.; Burghaus, U. *Surf Sci* **2013,** *616*, 171-177.

297. Wang, J.; Burghaus, U. *Surface Review and Letters* **2004,** *11* (6), 521-529.

298. Funk, S.; Hokkanen, B.; Johnson, E.; Burghaus, U. *Chem Phys Lett* **2006,** *422* (4-6), 461-465.

299. S. Funk, B. H., T. Nurkic, J. Goering, E. Kadossov, U. Burghaus, A. Ghicov, P.; Schmuki, Z. Q. Y., S. Thevuthasan, In *ACS Symposium Series 996*, L.V. SarafOxford Uni. Press: Chicago, 2007.

300. Daub, C. D.; Patey, G. N.; Jack, D. B.; Sallabi, A. K. *J. Chem. Phys.* **2006,** *124* (11).

301. Funk, S.; Nurkic, T.; Hokkanen, B.; Burghaus, U. *Applied Surface Science* **2007,** *253* (17), 7108-7114.

302. Chakradhar, A.; Yu, Z.; Ugrinov, A.; Burghaus, U. *Surf Sci* **2011,** *605* (9-10), 898-902.

303. Henderson, M. A. *Surf Sci* **1995,** *343* (1-2), L1156-L1160.

304. Deng, X.; Verdaguer, A.; Herranz, T.; Weis, C.; Bluhm, H.; Salmeron, M. *Langmuir* **2008,** *24* (17), 9474-9478.

305. Kisliuk, P. *Journal of Physics and Chemistry of Solids* **1958,** *5* (1-2), 78-84.

306. V.E. Henrich, P. A. C., *The Surf. Sci. of Metal Oxides*. Cambridge University Press: 1996.

307. Ishikawa, Y.; Kido, O.; Kimura, Y.; Kurumada, M.; Suzuki, H.; Saito, Y.; Kaito, C. *Surf Sci* **2004,** *548* (1-3), 276-280.

308. Park, C.; Kramer, H. M.; Bauer, E. *Surf Sci* **1982,** *115* (1), 1-14.

309. Popov, G.; Bauer, E. *Surf Sci* **1982,** *123* (2-3), 165-172.

310. Ohtake, A.; Komura, T.; Hanada, T.; Miwa, S.; Yasuda, T.; Yao, T. *Applied Surface Science* **2000,** *162*, 419-424.

311. Schmidt, W. G.; Bechstedt, F. *Surf Sci* **1995,** *331*, 557-563.

312. Feng, P. X.; Riley, J. D.; Leckey, R. C. G.; Pigram, P. J.; Hollering, M.; Ley, L. *Surf Sci* **2000,** *468* (1-3), 109-121.

313. Hunger, R.; Schulmeyer, T.; Klein, A.; Jaegermann, W.; Sakurai, K.; Yamada, A.; Fons, P.; Matsubara, K.; Niki, S. *Surf Sci* **2004,** *557* (1-3), 263-268.

314. Stoneman, R. C.; Larson, D. J. *Journal of Physics B-Atomic Molecular and Optical Physics* **1986,** *19* (11), L405-L409.

315. Anil, G.; Reddy, M. R. P.; Prasad, D. S.; Ali, S. T.; Munirathnam, N. R.; Prakash, T. L. *Materials Characterization* **2007,** *58* (1), 92-95.

316. Nagashima, S.; Ogura, I. *Thin Solid Films* **1993,** *228* (1-2), 64-67.

317. Sotiropoulos, A. K.; Kamaratos, M. *Applied Surface Science* **2004,** *229* (1-4), 161-166.

318. Davis, L. E., *Handbook of Auger Electron Spectroscopy: A Reference Book of Standard Data for Identification and Interpretation of Auger Electron Spectroscopy Data*. Physical Electronics: 1996.

319. NDSU, Code 00-006-0362 (International Center for Diffraction Data, Powder diffraction File 1993).

320. Brown, W. A.; King, D. A. *Journal of Physical Chemistry B* **2000,** *104* (12), 2578-2595.

321. R.M. Lambert, M. E. B., *Nitrogen oxides, in: D.A. King, D.P. Woodruff (Eds.), Chapter 8 in The Chemical Physics of Solid Surfaces and Heterogeneous Catalysis*. Elsevier: 1984; Vol. 3B.

322. Waugh, K. C. *Catal. Today* **1999,** *53* (2), 161-176.

323. Christmann, K. *Surf. Sci. Rep.* **1988,** *9* (1-3), 1-163.

324. Dobson, D. C.; James, F. C.; Safarik, I.; Gunning, H. E.; Strausz, O. P. *Journal of Physical Chemistry* **1975,** *79* (8), 771-775.

325. Becker, T.; Hovel, S.; Kunat, M.; Boas, C.; Burghaus, U.; Woll, C. *Surf Sci* **2001,** *486* (3), L502-L506.